



HAL
open science

3D Discrete Dislocation Dynamics simulations of the role of interfaces in confined materials - : application to electronic devices such as LEDs

Hareesh Tummala

► **To cite this version:**

Hareesh Tummala. 3D Discrete Dislocation Dynamics simulations of the role of interfaces in confined materials - : application to electronic devices such as LEDs. Materials. Université Grenoble Alpes; Université catholique de Louvain (1970-..), 2016. English. NNT : 2016GREAI096 . tel-01688611

HAL Id: tel-01688611

<https://theses.hal.science/tel-01688611>

Submitted on 19 Jan 2018

HAL is a multi-disciplinary open access archive for the deposit and dissemination of scientific research documents, whether they are published or not. The documents may come from teaching and research institutions in France or abroad, or from public or private research centers.

L'archive ouverte pluridisciplinaire **HAL**, est destinée au dépôt et à la diffusion de documents scientifiques de niveau recherche, publiés ou non, émanant des établissements d'enseignement et de recherche français ou étrangers, des laboratoires publics ou privés.

THÈSE

Pour obtenir le grade de

**DOCTEUR DE LA COMMUNAUTE UNIVERSITE
GRENOBLE ALPES**

**préparée dans le cadre d'une cotutelle *entre la
Communauté Université Grenoble Alpes et
l'Université catholique de Louvain***

Spécialité : **Matériaux, Mécanique, Génie civil, Electrochimie**

Arrêté ministériel : le 6 janvier 2005 - 7 août 2006

Présentée par

Hareesh TUMMALA

Thèse dirigée par **Marc FIVEL** et **Thomas PARDOEN**

préparée au sein du **Laboratoire SIMaP** et de l'institut **iMMC**
dans **les Écoles Doctorales I-MEP2**

Simulations 3D par dynamique des dislocations du rôle des interfaces dans la plasticité de milieux confinés, et applications aux LEDs

Thèse soutenue publiquement le **12 Décembre 2016**,
devant le jury composé de :

M. Laurent DELANNAY

Professeur, Université catholique de Louvain, Président

Mme. Anne-Marie HABRAKEN

Directeur de recherche FNRS, Université de Liège, Examinateur

M. Marc VERDIER

Directeur de recherche CNRS, Université Grenoble Alpes, Examinateur

M. Alexander HARTMAIER

Professeur, RUHR-Universität Bochum, Rapporteur

M. Stéphane BERBENNI

Directeur de recherche CNRS, Université de Lorraine, Rapporteur

M. Thomas PARDOEN

Professeur, Université catholique de Louvain, Encadrant

M. Marc FIVEL

Directeur de recherche CNRS, Université Grenoble Alpes, Encadrant



THESE

For obtaining the grade of

DOCTORATE OF THE UNIVERSITY GRENOBLE ALPES

**prepared as part of a joint supervision between the
*University of Grenoble Alpes and the Catholic
University of Louvain***

Speciality : **Materials, Mechanical, Civil Engineering,
Electrochemistry**

Ministerial order : 6 January 2005 - 7 August 2006

Presented by

Hareesh TUMMALA

Thesis directed by **Marc FIVEL** and **Thomas PARDOEN**

prepared within the **Laboratory SIMaP** and the **Institute IMMC**
in the **Doctoral School I-MEP2**

3D discrete dislocation dynamics simulations of polycrystalline films and silicon electrostatics

Thesis defended in public on **12 December 2016**,
before the jury composed of :

Mr. Laurent DELANNAY

Professor, Catholic University of Louvain, President

Mrs. Anne-Marie HABRAKEN

Director of Research FNRS, University of Liege, Examiner

Mr. Marc VERDIER

Director of Research CNRS, University of Grenoble Alpes, Examiner

Mr. Alexander HARTMAIER

Professor, Ruhr-University of Bochum, Reviewer

Mr. Stéphane BERBENNI

Director of Research CNRS, University of Lorraine, Reviewer

Mr. Thomas PARDOEN

Professor, Catholic University of Louvain, Supervisor

Mr. Marc FIVEL

Director of Research CNRS, University of Grenoble Alpes, Supervisor



Abstract

Plastic deformation of classical crystalline materials is essentially dominated by dislocations and their mutual interactions. In nanocrystalline (nc) metals, different grain boundary mechanisms may exist in addition to the dislocation-based mechanisms. The dependency on, among others, the grain shape, grain orientation, initial dislocation density, grain boundary structure and external conditions will promote one or two deformation mechanisms over others. These dominant mechanisms dictate the overall response of nc metals. The influence of microstructural features in promoting these dominant mechanisms need to be better understood individually and collectively. In the scope of the thesis, 3D discrete dislocation dynamics (DDD) simulations were performed on three micron-sized single grains of same volume but differing in aspect ratios to understand the influence of grain morphology. A decrease in localization of plastic deformation with increasing grain aspect ratio was observed. Due to the enhanced cross-slip mechanism, grains with higher aspect ratio exhibit a lower strain hardening behaviour. The anisotropic plastic response of elongated grains was quantified in terms of the magnitude of backstress on each slip system. Further, a polycrystalline version of dislocation dynamics code coupled with a finite element method was used to study the mechanical behaviour of free-standing palladium thin films with columnar grains. The initial dislocation density considered in the simulations is close to the one measured experimentally. DDD simulations of a polycrystal with hexagonal grains properly reproduce the strain hardening behaviour. For a heterogeneous grain size distribution of the polycrystal, an increase in strength with decreasing film thickness was observed. The key element is that the probability of smaller grains with no initial dislocations is increasing with decreasing thickness of the film. Finally, by adapting Read's model, the influence of a static, electrically-charged dislocation on electrical properties in semiconductors was studied.

Key words: 3D Discrete dislocation dynamics simulations; Interfaces, grain boundaries, twin boundaries, free surfaces; Crystal plasticity; Mechanical properties; Dislocations and electronic properties

Résumé

En général, la déformation plastique des matériaux cristallins est essentiellement dominée par le mouvement des dislocations et leurs interactions mutuelles. Pour les métaux nanocristallins (nc), les joints de grains influencent le mouvement des dislocations de différentes façons. Ainsi, la forme des grains, l'orientation des grains, la densité de dislocation initiale qu'il contient, la structure des joints de grains et la nature de chargement extérieur sont autant de paramètres qui sont susceptibles de faire varier la réponse du chargement mécanique du polycristal. Dans le cadre de cette thèse, ces effets sont étudiés en réalisant des simulations de dynamique des dislocations discrète 3D (DDD). Dans un premier temps, le rôle de la forme du grain est étudié en réalisant des simulations du comportement en traction uniaxiale de trois grains isolés de taille micrométrique de même volume, mais qui diffèrent par leur facteur de forme. On observe une diminution de la localisation de la déformation plastique avec l'augmentation du rapport de forme du grain. La réponse plastique anisotrope des grains allongés a été quantifiée en terme de contrainte interne développée sur chaque système de glissement. En outre, une version polycristalline du code de dynamique des dislocations couplée avec des éléments finis a été utilisée pour étudier le comportement mécanique des films minces de palladium ayant une structure de grain colonnaire. La densité de dislocations initiale prise en compte dans les simulations est proche de celle mesurée expérimentalement. Les simulations de DDD d'un polycristal reproduisent correctement le comportement d'écrouissage. L'augmentation de la résistance observée avec la diminution de l'épaisseur du film a été atteinte en utilisant une distribution hétérogène de la taille des grains du polycristal. Le résultat principal est que la probabilité d'avoir des grains plus petits sans dislocations initiales augmente avec la diminution de l'épaisseur du film. L'effet de la distribution de tailles des grains voisins sur la contrainte interne développée à l'intérieur du grain central a été étudiée. Enfin, en adaptant le modèle de Read, l'influence d'une dislocation statiquement chargée sur les propriétés électriques des semi-conducteurs a été modélisée.

Mots clés : Simulations de la dynamique des dislocations ; Interfaces, joints de grains, surfaces libres ; plasticité ; Propriétés mécaniques et électroniques

Acknowledgements

If time travel was a reality, I would set the date to 30th April, 2010. As a *nouveau* graduate in Mechanical Engineering, I never knew "Where will I be in 5 years from then?". It is only now (in the year 2016) that I can confidently say that, "I am a determined, goal-oriented person". Today, I am delighted to thank everyone for being part of my academic adventure.

This academic journey of mine would not have started without the funding from **International Doctoral School in Functional Materials (IDS FunMat)**. I sincerely thank the Doctoral committee for selecting the project. I would like to specially thank **Mrs. Audrey Sidobre**, **Mr. Laurent Servant** and **Mrs. Marianne Delmas** for taking care of the administrative stuff and also making our Doctoral training schools educational and memorable. People I met at the training school will remain "friends for life" and I am really grateful for that.

I would like to thank the members of my PhD jury, **Mr. Laurent Delannay**, **Mrs. Anne-Marie Habraken**, **Mr. Marc Verdier**, **Mr. Stéphane Berbenni** for accepting my request even after knowing the European thesis monitoring rules (travel involved for private and public defense at two different places). A small thank you will never be sufficient to my two supervisors, **Mr. Thomas Pardon** and **Mr. Marc Fivel**. They stood alongside me and guided me throughout the course of my PhD. I should also thank Mr. Laurent Delannay for taking time and being as a mentor to me during this course.

I am indebted to **Mr. Christophe Deprés** for sharing his code and introducing me to Matlab. I thank him for his special class on Object Oriented programming using Matlab. Mr. Tran from University of Liege, Mr. Guericc, Mr. Murali and Mrs. Marianne from University of catholique Louvain, Mr. Samir, Mr. Pawel, Mr. Robin, Mr. Anthoney, Mr. Sebastien, Mr. Alexis, Mr. Edi, Mr. Matheiu and Mrs. Camila from University of Grenoble Alpes should receive special cheers for being as good friends and colleagues. I wish them all the best for their future endeavours.

Mrs. Claire, Mrs. Elisabeth at GPM2 and Mrs. Astrid, Mrs. Catherine, Mrs. Rania from UCL are the best at making people feel very comfortable. I am very

happy that I had the chance to meet and interact with them. I wish them the best in all parts of their lives.

Finally, I can not forget the support I received from my family. Especially, my parents for understanding my situation and waiting eagerly for my call every weekend.

Hareesh Tummala

Contents

Abstract (English)	i
Résumé (Français)	iii
Acknowledgements	v
I Introduction and Background	1
0.1 Context	3
0.2 Outline of the thesis	4
1 Overview: Interfaces in metallic materials	7
1.1 Interfaces in crystalline materials	7
1.1.1 Free surfaces in crystalline materials	8
1.1.2 Phase boundary in crystalline materials	9
1.1.3 Grain boundaries in crystalline materials	10
1.1.4 Crystallography of a grain boundary	11
1.1.5 Types of grain boundaries	12
1.1.6 Twins in crystalline materials	13
1.2 Dislocation-grain boundary interaction models	15
1.3 Generic models for grain boundaries	17
1.3.1 Line tension model	17
1.3.2 Dislocation array model	18
1.3.3 Dislocation dissociation model	22
1.4 Remarks	23
2 Experimental investigation of thin films	25
2.1 Overview: On-chip tensile testing method	25
2.2 Microstructure of thin films	28
2.2.1 Stress-strain curve	28
2.2.2 Grain orientation distribution	30
2.2.3 Grain size distribution	30
2.2.4 Density of linear defects	32
2.2.5 Twins in thin films	32

2.3	Remarks	33
3	Numerical modeling of plasticity in metals	35
3.1	Multiscale nature of materials behavior	35
3.2	Challenges in modeling materials behavior	36
3.3	Numerical modeling of polycrystals	37
3.3.1	Atomistic modeling	38
3.3.2	Continuum based models	40
3.4	Purpose for modeling polycrystal using 3D DDD simulations	45
II	Dislocation dynamic simulations: Methodology and Developments	47
4	Methodology of discrete dislocation dynamics simulations	49
4.1	Introduction	49
4.2	Computation of heterogeneous stress field in a volume containing dislocations	50
4.2.1	Discretization of a dislocation	50
4.2.2	Internal stress field due to a dislocation	52
4.2.3	Periodic boundary condition	53
4.2.4	Superposition principle: modification to finite domain	54
4.3	Prediction of the mobility of a dislocation	56
4.3.1	Mobility laws for a dislocation	56
4.3.2	Effective stress on a dislocation	57
4.3.3	Peierls stress	57
4.3.4	Line tension on a dislocation	58
4.3.5	Peach-Koehler force	59
4.3.6	Local hardening rules	59
4.3.7	Dislocation-grain boundary interaction	61
4.4	Numerical implementation of the DDD model	79
4.4.1	DDD algorithm	79
4.4.2	Integration scheme	80
4.4.3	Optimized stress field calculations	80
4.4.4	Convergence of DD solution	87
4.5	Post-processing of DD simulation results	88
4.5.1	Plastic strain calculation	88
4.6	Conclusions	89

III	DDD simulations of plasticity in FCC crystals	91
5	Influence of grain morphology on intragranular backstress predictions	93
5.1	Introduction	93
5.2	Model and setup	97
5.2.1	Modeling spheroidal grains	97
5.2.2	Information imported from crystal plasticity	98
5.2.3	Selection of initial dislocation density	102
5.2.4	Material parameters	104
5.2.5	Loading condition	104
5.3	Results	105
5.3.1	Reference simulation: Spherical grain without cross slip	106
5.3.2	Grain shape effect on strain hardening without cross-slip	110
5.3.3	Influence of grain shape on cross slip	114
5.3.4	Influence of cross slip on dislocation activity	117
5.4	Discussion	120
5.4.1	Implications for CP models: average back stress on slip systems	120
5.4.2	Extension of the pile up model for predicting back-stresses	124
5.5	Conclusions	127
6	Collective influence of grain and dislocation density parameters on plasticity of thin films	129
6.1	Introduction	129
6.2	Modeling polycrystals	133
6.2.1	Generating polycrystal using Voronoi tessellation	133
6.2.2	Modeling grain size distribution in polycrystals	134
6.3	Simulation setup	135
6.3.1	Polycrystalline 3D DDD model	135
6.3.2	Initial dislocation configuration	138
6.3.3	Identification of material parameters of Pd	139
6.3.4	Boundary conditions	142
6.3.5	Problem description: Tensile test in X-direction	144
6.3.6	The DD-FEM coupling: solving a BVP	145
6.3.7	Adapted DD-FEM algorithm	146
6.3.8	Loading condition	147
6.4	Results	149

Contents

6.4.1	Reference simulation: Film with similar grain sizes and same grain orientations	150
6.4.2	Basic comparative simulations	153
6.4.3	Strain hardening behavior of 200nm film	156
6.4.4	Size effects in Pd thin films	157
6.5	Discussion	170
6.5.1	Anisotropic plastic response	170
6.5.2	Distribution of internal stresses	174
6.6	Conclusions	178
IV	DDD simulations in DC crystals	181
7	Modeling electrostatic dislocations	183
7.1	Introduction	183
7.2	Review: Read's electrostatic model	186
7.3	Modelling a charged dislocation	189
7.3.1	Application: charged dislocation in GaN	191
7.4	Solving an electrostatic problem	191
7.4.1	Validation of the PoisFFT solver	192
7.5	Results and discussion	193
7.6	Conclusions	195
V	Conclusions and perspectives	197
8	Conclusions and perspectives	199
A	Appendix: Review of Depres's pileup model	201
A.1	Introduction	201
A.1.1	Idealised double-ended pileup	201
A.1.2	Extension to 2D pileup	202
A.1.3	Extension to 3D pileup	204
A.2	Hardening due to 'n' similar parallel slip planes in a grain	210
A.3	Conclusions	211
B	Appendix: Non-equiaxed shape of dislocation pileups	213
B.1	Introduction	213
B.1.1	Form 4a (ellipse - longest)	213
B.1.2	Form 4b (ellipse - shortest)	216

B.2	Extended pileup theory Vs DD simulations	218
B.2.1	Single dislocation pileup (non-centred)	218
B.3	Hardening due to 'n' non-similar parallel slip planes in a grain	220
B.3.1	Equiaxed (spherical) grain	220
B.3.2	Non-equiaxed (spheroidal) grain	224
B.4	Conclusion	230
Bibliography		249
Nomenclature		251
List of figures		255
List of tables		269
Curriculum Vitae		271

PART - I

Introduction and Background

0.1 Context

‘Innovative’ new materials are key for commercial success of many products developed by the high-tech industry. In the present age of miniaturization, nanoscale materials have attracted a huge attention from the industry. The reason for such a high demand lies in the possibility of producing materials with specific ‘enhanced’ properties by tailoring the structure of the material at nanoscale. Magnetic recording media, electronic semiconducting devices, LEDs, anti-reflexive coatings, thin film solar cells and thin film batteries are few of the non-exhaustive possible commercial applications of nanoscale materials.

A common point among the examples presented is the use of advanced thin film depositing techniques. Controlled synthesis of materials as thin films is mastered by many research groups all around the world. But, the real-world applications of such thin films still requires that the response of thin films is understood completely under the influence of external factors (stress, temperature, pressure etc.). A market share $< 20\%$ of thin film PV solar cells in the photo-voltaic industry highlight the flaws in the commercial adaptation of the thin film technology due to the lack of complete knowledge about the complex behavior of thin films.

Present-day thin film research emphasises on understanding the response of thin film materials. During the last decade, a wide variety of mechanical characterization techniques have been developed to study thin films experimentally (On-chip tensile test by Sharpe and co-workers [162], Nanoindentation by Espinosa and co-workers [56], Bulge test by de Boer and co-workers [38], Beam bending by Florando and Nix [66]). A film is generally categorized as a *thin film* if the thickness is below a few microns. Generally, thin films are polycrystals often involving only a single grain (not always) along the thickness direction. The excellent strength of thin films compared to their bulk counterparts, is due to the presence of high density of interfaces with nanosized grains. In such materials, the mechanical properties are dominated by the collective behavior of interfaces and defects.

For the development of materials with enhanced properties, a better understanding of microstructural features such as, dislocation density distribution, grain size distribution, grain morphology, distribution of interfaces and their influence on elementary deformation mechanisms is needed. Experimental investigation of individual microstructural features is indeed a highly daunting task even with the present-day advanced nano-fabrication techniques. Inspired by the challenge on

providing a better understanding of deformation behavior of metallic thin films, a systematic numerical approach has been set up and carried out during the course of the thesis. A detailed outline of the thesis is presented in the Section 0.2.

0.2 Outline of the thesis

The main objective of the thesis is to investigate the collective influence of microstructural features of the metallic thin films on mechanical properties. Special emphasis has been placed on studying the plastic deformation mechanisms in non-equiaxed (columnar) grains. The thesis comprises *seven* chapters and each chapters is further organized into *four* parts depending on the specific nature of the topic introduced or study carried out during the course of the thesis. The outline of the thesis is presented below.

In **Part I**, *Chapter 1* introduces the topic of interfaces and type of interfaces in crystalline materials. Grain boundary models developed to address interfaces in crystalline materials are reviewed. Experimental technique which has been used for investigation of thin films is reviewed in *Chapter 2*. This chapter also presents experimental results by highlighting the microstructural features in Pd thin films. The highlighted microstructural features are the major topic of interest in the numerical simulations carried out in *Chapter 5* and *Chapter 6*. Finally, *Chapter 3* presents a brief introduction to numerical models at different length and time scales, the reason behind selection of the particular numerical approach is specified.

In **Part II**, *Chapter 4* explains the methodology of the 3D discrete dislocation dynamics simulations used in the thesis. To harness the power of graphical processing units (GPUs), heterogeneous parallel programming of the stress field computation has been implemented and tested for a static dislocation setup. The basic idea behind the implementation of dislocation interaction with grain boundaries in dislocation dynamics code is presented. The implemented dislocation-grain boundary model has been applied to study dislocation interaction with coherent twin boundary in a bicrystal. Selected results of dislocation interaction with coherent twin boundary are presented.

In **Part III**, *Chapter 5* introduces the issues faced by phenomenological crystal plasticity models in predicting plastic anisotropy in elongated grains (with high aspect ratios). Inaccuracies in predicting plastic anisotropy comes from the fact that the pileup behavior is not modelling accurately at single grain level. We perform

discrete dislocation dynamics simulations on single grain of different aspect ratios to predict the influence of grain shape on dislocation slip activity and inturn, back stress. The influence of cross slip mechanism in such predictions is also investigated. Discussions are followed by the proposal of a simple analytical expression to predict changes in the magnitude of back stresses arising due to grain shape (*cf.* Appendix A). Our understanding of the anisotropic plastic deformation behavior in a single grain is now extended by performing DD simulations on a polycrystalline thin films in *Chapter 6*. This chapters presents all the information about the microstructural details which were accounted while modeling Pd thin films. Results of the 3D DDD polycrystalline simulations are presented by addressing the most relevant microstructural features of Pd thin films. The influence of specific microstructural features on strain hardening capacity and ductility of Pd thin films are discussed.

In the final part [**Part IV**] of the thesis, dislocations in semiconducting materials and their influence on electrical properties has been studied in *Chapter 7*. Implementation of Read's electrostatic model creates a bridge between dislocations and electronic properties of semiconductors. Possibilities of extending the present model to study polycrystalline silicon photovoltaics are discussed.

Finally, major conclusions drawn during the course of the thesis are listed. Few possible research directions are suggested for those who are interested in taking advantage of the defect-based material models to study plastic deformation in crystalline materials.

1 Overview: Interfaces in metallic materials

A metallic material is said to be defective when it deviates from a perfect crystal lattice. Among the different category of crystal defects, attention has been primarily drawn towards *interfaces*, which are planar defects in crystalline materials. Establishing a proper understanding of the behavior of different interfaces and their influence on macroscopic properties has become a prime area of research in the 21st century. Materials modeling at different length- and time-scales administered a small revolution in our approach towards understanding their multiscale behavior. However, the assumptions employed while developing/utilising a particular numerical technique should not be overlooked. For example, the earliest 3D DDD models [microMegas] developed during the late 90s were intended to establish a better understanding of the plastic deformation behavior in a micron-sized single grain. Where, assuming grain boundaries of a single grain as strong obstacles to dislocations is justifiable. Such assumptions need to be improved/modified while working with polycrystals.

First chapter of the thesis starts with a brief introduction to the concept of interface. Different types of interfaces generally observed in crystalline materials are reviewed. Dislocation-grain boundary interaction models were developed to establish a better understanding of the materials behavior. Different models employed in the DD community to model dislocation-grain boundary interactions are presented. Advantages and disadvantages of using a particular model are highlighted.

1.1 Interfaces in crystalline materials

In general, crystalline materials may have regions with different chemical compositions (phases), or regions of different lattice structures, or in some cases both. *Interfaces* are common regions which separate the materials of different chemical compositions (phase) or lattice structures. Based on phase and structure, interfaces

in crystals are broadly classified into three categories [130].

1. **Free surfaces** are interfaces between a solid phase material and a vapour or liquid phase material.
2. **Interfaces between crystals** are interfaces among one or more solid phase materials. Depending on whether the interface is in the same solid phase or not, they are further divided into two types:
 - (a.) Hetero-phase interface and
 - (b.) Homo-phase interface
3. **Interfaces within a crystal** generally occur due to the change in atomic arrangement of a previously single crystal. These type of interfaces are generally viewed as stacking faults or anti-phase boundaries. Anti-phase boundaries are often observed in compound materials.

1.1.1 Free surfaces in crystalline materials

Free surfaces are a special type of solid-vapour (or liquid) interfaces. The atomic arrangement of a crystalline material abruptly ends at a free surface. As the name indicates, free surface is a stress-free surface¹. But, if an edge dislocation is placed at a distance d from the free surface, non-zero stresses are exerted on the free surface due to the presence of linear defects in the crystal. These defects are repulsive if the surface is rigid; otherwise they are generally attractive. Linear defects attracted to the free surface, may exit the crystal by leaving behind a step on the surface. Such visible surface steps are generally referred to as *slip traces*. Figure 1.1(a) and 1.1(b) shows slip traces on the surface of a Ni bicrystal which indicate the changes in slip system activities in the two crystals with changing misorientation² ($\Delta\theta$).

In the case of nanocrystalline materials, smaller sized grains in a polycrystal may have very low defect density. The attractive nature of free surfaces may pull the dislocations out these small grain once they are activated and leaving the grain defect-free. This mechanism is called *dislocation starvation* [79]. In order to maintain compatible plastic deformation in the polycrystal, new dislocations

¹**Stress-free** surface is indicated for a surface with zero normal traction. Non-zero in-plane surface stresses may still exists

²**Misorientation** indicates the change in lattice orientation between two grains in a polycrystal

1.1. Interfaces in crystalline materials

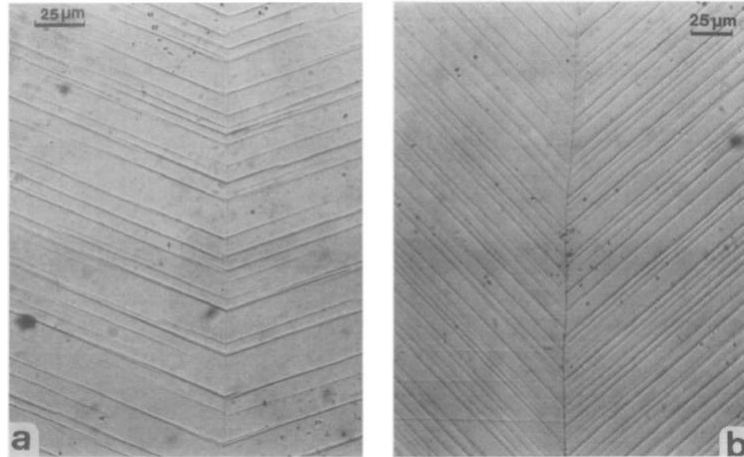


Figure 1.1 – Slip traces on the free surface of a bicrystal with (a) $\Delta\theta = 0^\circ$; (b) $\Delta\theta = 20^\circ$ [122]

can nucleate from the surface steps. Atomic simulations showed that surface steps act as favoured sites for the nucleation of dislocations in Al sample [17]. Such surface dislocation nucleation mechanism can be incorporated as local rules in dislocation dynamics simulations. One example of the use of dislocation nucleation algorithm for nucleating new dislocations from free surfaces was implemented in three-dimensional dislocation dynamic simulations to investigate size-dependent plasticity in sub-micron FCC micropillars under torsion [156].

1.1.2 Phase boundary in crystalline materials

Phase boundaries are planar defects separating two solids in different phases. Due to the presence of more than two phases, they are also called as *hetero-phase boundaries*.

In metallic materials such as iron, along-with the chemical composition, the lattice structure changes with temperatures. Iron shows a BCC structure for temperature up to 912°C . The structure of iron changes from BCC to FCC for temperatures between 912°C and 1395°C and changes back to BCC structure for temperatures above 1395°C . Such changes of phases also depend on the presence of impurities, such as carbon, Ni, Al etc., All the possible phase changes under the influence of specific impurities and temperatures are graphically represented in a *phase diagram*. These *phase diagrams* also predict the co-existence of two phases which are generally separated by a *phase boundary*. Different types of phase

boundaries exist according to their atomic arrangement at the boundary. Consider the lattice structure of the first phase is represented by blue-coloured atoms and the lattice structure of second phase is represented by red-coloured atoms. An interface formed by perfect lattice match between two phases is called *coherent interface* and is shown in the Figure 1.2(a)). Whereas, a semi-coherent interface is formed when there is a partial lattice mismatch. Residual dislocations responsible for the mismatch, are formed from the interaction of a lattice dislocation moving towards a previously coherent interface (cf. Figure 1.2(b)). An interface with no matching lattice is referred to as a *incoherent interface*. A schematic representation of an incoherent interface is shown in Figure 1.2(c).

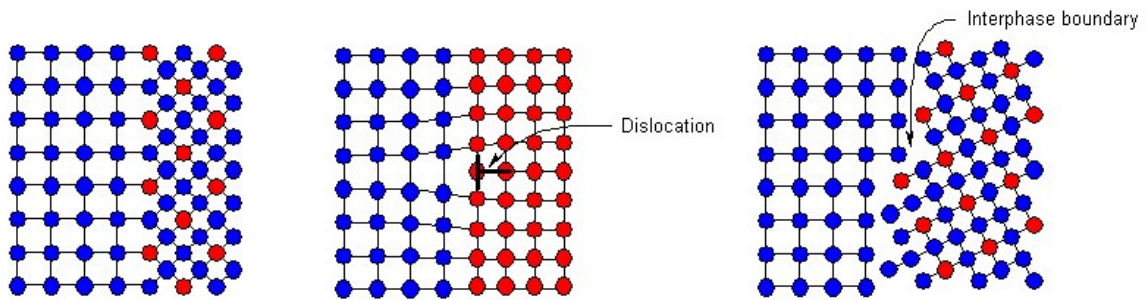


Figure 1.2 – Schematic representation of (a) coherent, (b) semi-coherent and (c) incoherent interfaces, respectively [180]

1.1.3 Grain boundaries in crystalline materials

Grain boundaries separate two crystals of the same phase. They are also called *homo-phase boundaries* due to the presence of only a single phase in the metallic material.

Crystalline materials generally tend to show a highly ordered atomic arrangement. If a crystalline material, on the whole, shows a single highly ordered atomic arrangement, it is then said to be a perfect single crystal. Whereas in a polycrystalline material, every crystal is identified by its own preferential atomic order. The changes in the atomic arrangement among crystals is often seen in polycrystals. *Grain boundaries* can be viewed as the narrow defective (transition) regions highlighting the difference in atomic arrangement among two or more adjacent crystals as shown in Figure 1.3(b).

In a more generalized sense, the atomic arrangements of a single crystal can be represented as a rotation of the crystal lattice about a laboratory/real frame. Such

1.1. Interfaces in crystalline materials

a crystal rotation is generally denoted by Euler angles [21, 103]. Every crystal in a polycrystalline specimen is differentiated by the different lattice rotation they acquire (cf. Figure 1.3(a)). In this case, a *grain boundary* is a two-dimensional (or) planar defect of finite plane thickness separating two or more crystals of different lattice orientations.

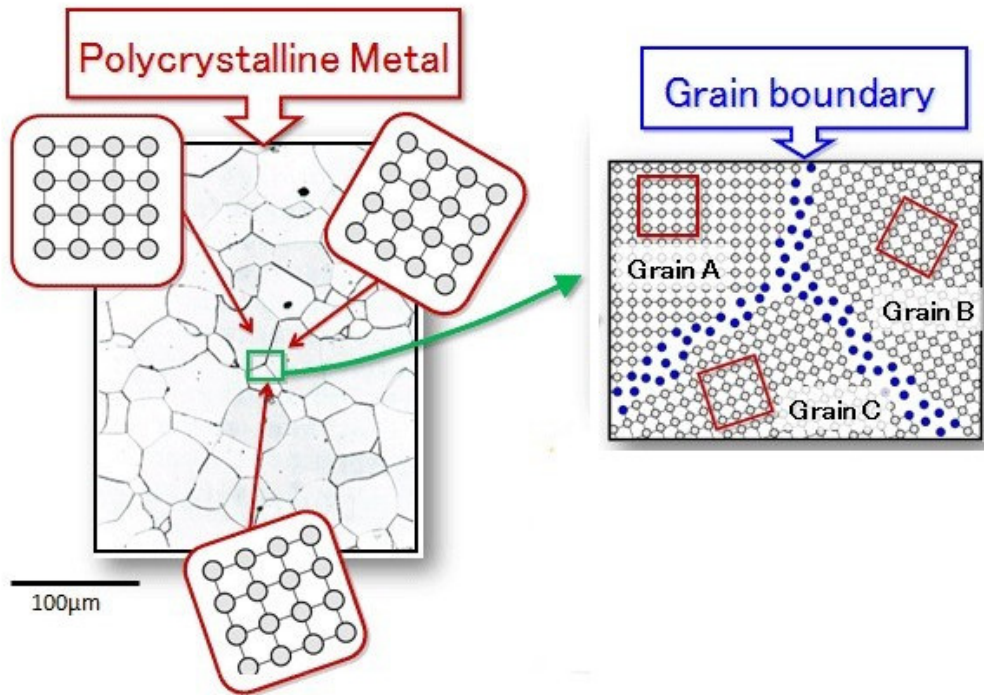


Figure 1.3 – (a) Grain boundaries in a polycrystal; (b) An example atomic arrangement at triple junction [137]

1.1.4 Crystallography of a grain boundary

It has already been established that a grain boundary separates two crystals in same phase and share a common crystal structure. A grain boundary generally possesses nine degrees of freedom (DOF): five macroscopic DOF and four microscopic DOF. The microscopic parameters result from relaxation processes and are not independent of the macroscopic parameters. So, a grain boundary can be fully characterised by its five independent macroscopic parameters [169].

The five independent macroscopic parameters (DOF) are:

- **one** DOF for the rotation angle θ between the two crystals;

- **two** DOF for the rotation axis $\mathbf{o}=[uvw]$ defined by its direction cosines;
- **two** DOF for the orientation of the grain boundary plane defined by its normal \mathbf{n} .

These five parameters provide complete information for the transformation into a bicrystal from a given single crystal. The first three parameters specify mutual misorientation of the adjacent grains A and B (Figure 1.4). This misorientation is defined by the rotation axis $\mathbf{o}=[uvw]$ and rotation angle θ . The final two parameters provide information about the orientation of the grain boundary between the misorientated grains, which is defined by the normal \mathbf{n} .

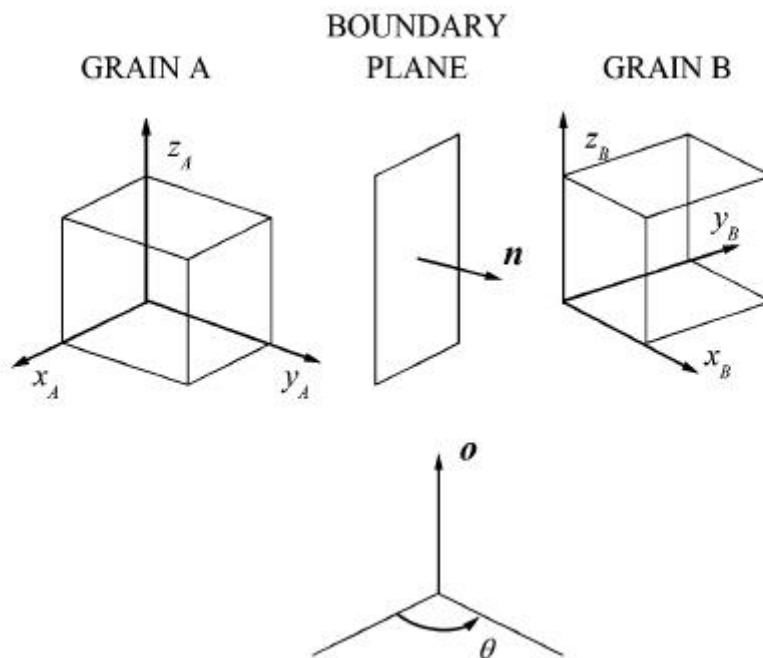


Figure 1.4 – Crystallography of a grain boundary [118]

1.1.5 Types of grain boundaries

The changes in the crystal orientation is generally addressed by *misorientation angle* ($\Delta\theta$) about a common rotation axis. Depending on the measure of misorientation, grain boundaries are segregated as *low-angle grain boundaries (LAGB)* when the $\Delta\theta < 15^\circ$. On the other hand, all the grain boundaries with $\Delta\theta > 15^\circ$ are categorized as *high-angle grain boundaries (HAGB)*.

1.1. Interfaces in crystalline materials

The simplest categories of low angle grain boundaries are tilt and twist grain boundaries. These grain boundaries are categorized depending on their relationship between the rotation axis and the grain boundary normal. Tilt grain boundaries follow the relationship of the rotation axis being perpendicular to the grain boundary normal ($\mathbf{o} \perp \mathbf{n}$). Whereas, twist grain boundaries follow a parallel relationship between the rotation axis and the grain boundary normal ($\mathbf{o} \parallel \mathbf{n}$). Figure 1.5 show a schematic view of the tilt and twist boundaries in a bicrystal. A real grain boundary in a crystal is rarely of a pure tilt or twist nature. Generally, combination of both tilt and twist boundaries in crystalline materials are grouped as *mixed grain boundaries*.

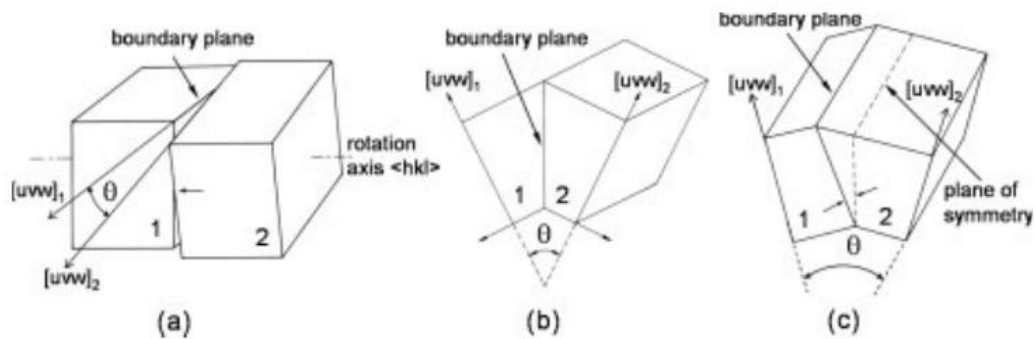


Figure 1.5 – Schematic representation of a pure tilt and a pure twist boundary in a bicrystal [118]

1.1.6 Twins in crystalline materials

Twin boundaries constitute a category of a special kind of grain boundaries which are generally present inside a single crystal. Twin boundaries are formed when the atoms on either side of the boundaries are related by a reflection of $60^\circ/180^\circ$. Twins often show a lowest grain boundary energy due to the attained additional symmetry. Figure 1.6 shows a coherent twin boundary ($\Sigma 3 \langle 111 \rangle$) in Ni with the lowest energy. Apart from a single coherent twin boundary ($\Sigma 3$ boundary), energies of several $\Sigma 3$ boundaries having same misorientation angle but different boundary planes are also shown. The variation in the energies of $\Sigma 3$ boundaries highlight the crucial role of the boundary plane on grain boundary properties. Similar conclusions were drawn from the experimental and computational results for copper [61, 147]. Disorientation angle alone is not sufficient to determine the grain boundary energy. But, the general trend of energies of low angle grain boundaries ($\langle 111 \rangle$ twist and $\langle 100 \rangle$ twist and $\langle 110 \rangle$ symmetric tilt) has been observed to closely align with

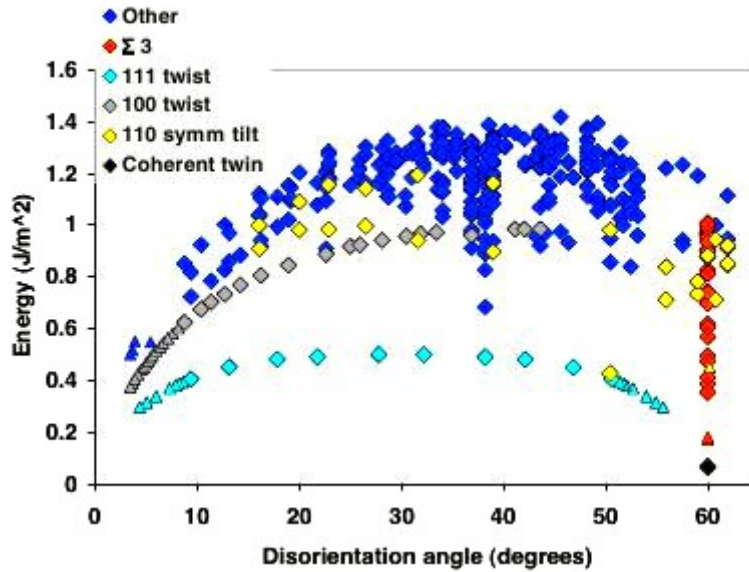


Figure 1.6 – Grain boundary energy versus disorientation angle in Ni [67]

the prediction of the Read-Shockley's dislocation-based grain boundary model.

Twins are of prime importance in nanocrystalline materials. Apart from acting as obstacles to dislocation motion, they also impart additional ductility to the crystalline material. Depending on the formation mechanism, twins in FCC metals are further categorised as annealing twins, deformation twins and growth twins. Deformation twins are formed as a consequence of plastic deformation. Such a deformation mechanism has been observed mostly in low-symmetry crystals, such as magnesium. Christian and Mahajan reviewed deformation twinning in coarse-grained materials [96]. Deformation twinning in nanocrystalline materials has been reviewed by Zhu and co-workers [204]. In contrast, growth twins are formed during the fabrication process. Presence of growth twins in nc-Pd thin films were suggested to be the reason behind increased ductility [189]. Recently, the two classes of twins: growth and deformation twins in metals have been reviewed [13].

Faults in the stacking sequence of FCC crystals are often seen. Twins can also be seen as sequence of stacking faults in a single crystal. Figure 1.7 shows the stacking sequence in a perfect FCC crystal and a crystal twinned about the twin plane.

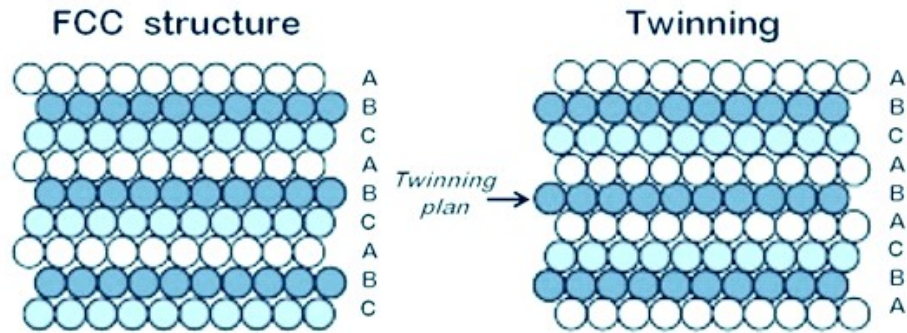


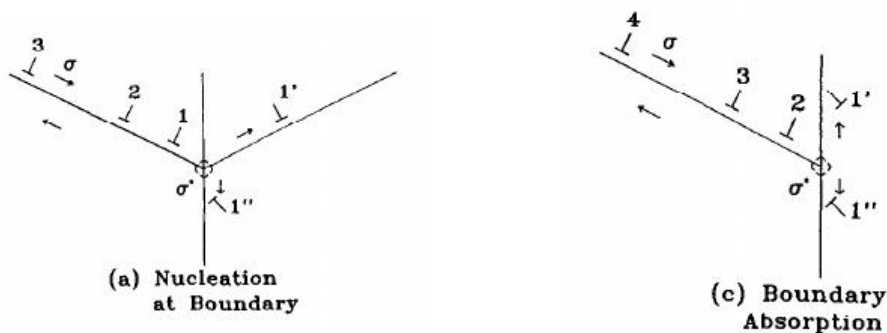
Figure 1.7 – Stacking sequence of a perfect crystal and a twinned crystal *modified from* [157]

1.2 Dislocation-grain boundary interaction models

Grain boundaries (GBs) play an important role in controlling mechanical properties of materials. When polycrystalline metals are deformed at low-temperatures, plastic deformation is proceeded by the motion of dislocations in individual grains and also across the boundaries between neighbouring grains. The four possible mechanisms for slip propagation across a grain boundary as listed by Shen [163] are:

- **Dislocation nucleation** at GB
- **Dislocation absorption** by dissociation in the interface
- **Dislocation transmission** across interface
- **Dislocation absorption** and subsequent **re-emission**

The corresponding sketches for different mechanisms are shown in the Figure 1.8 below.



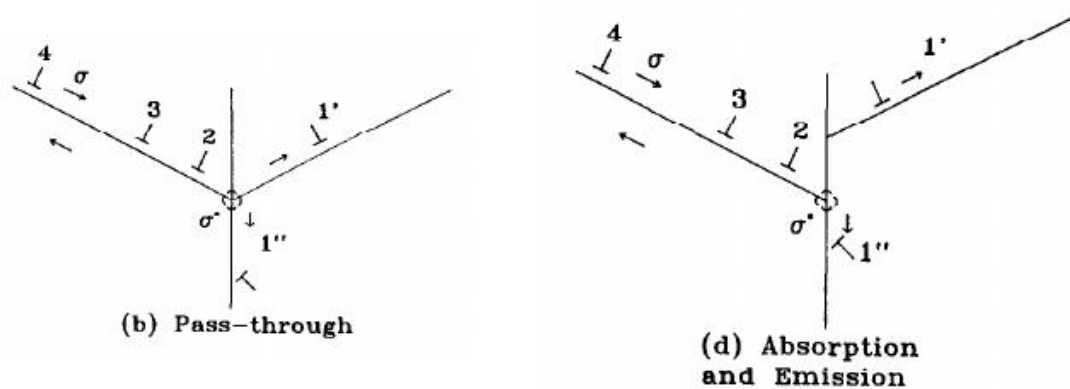


Figure 1.8 – Sketches of possible dislocation mechanisms for slip propagation across interface [163]

In the case of dislocation transmission, the choice of slip system is predictable and several authors proposed criteria for predicting slip system [122, 163]. Among them, *LRB* criteria is widely accepted. As an extension to the *LRB* model, a *modified LRB* models has been proposed [49]. The *LRB* criteria states that the slip transfer across GB depends on:

- a.) Geometry of the GB and lattice slip planes
- b.) Dislocation character
- c.) Stress state

whereas, the *modified LRB* criteria incorporates important details at the GB, such as:

- 1.) Angle between lines of intersection between incoming and emitted slip plane should be small with respect to GB.
- 2.) The residue left at the GB after transmission event should be small
- 3.) Resolved shear stress (RSS) on the slip plane of the transferred/emitted dislocation should be significantly higher than the RSS of the GB plane.
- 4.) The normal compressive stress on the GB should be small

TEM and HVEM experiments on 304 stainless steel revealed that the most frequent deformation mechanism of 60° dislocation pileup is **transmission** and simultaneous **reflection** at the GB [49].

Generally, a grain boundary is modelled as impenetrable by specifying very high barrier strength to the facet ($\tau_{gb} = 1.e^{50} MPa$ for example). Since, dislocations can not physically attain such high stress values, they tend to stop at the facet. This method of modeling grain boundaries accurately represents grain morphology and thereby the pileup behavior in each grain. Chapter 5 of the thesis exclusively addresses the importance of grain morphology on plastic deformation behavior in single grains. Due to the impenetrable facets, dislocations piling up against the grain boundary is shown in Figure 4.10. It should be noted that, apart from the grain boundary labelled in Figure 4.9, all the other facets are generally *Free surface*³. But for simplicity, we assume them also to be as grain boundaries in a bicrystal setup.

1.3 Generic models for grain boundaries

As mentioned before, grain boundaries being impenetrable to dislocations in 3D DDD simulations is a very crude assumption. Different approaches have been followed in the DD community to address this issue. The three widely followed GB modeling approaches are presented in the subsections below.

1.3.1 Line tension model

To essentially capture the features of dislocation transmission across grain boundaries, a *simple line tension model* has been proposed [104].

According to this model, dislocation transmission across a grain boundary occurs at a critical stress τ_{gb}^c . An incoming dislocation \mathbf{b}_1 from Grain1 is being transmitted into Grain2 as outgoing dislocation \mathbf{b}_2 ; whilst leaving a residue $\Delta\mathbf{b}$ at the grain boundary is shown in Figure 1.9. Such transmission events can be modelled by placing a Frank-Read (FR) source⁴ very close to the grain boundary in the corresponding neighbouring grain. When the resolved shear stress exceeds a critical value τ_{gb}^c , the FR source activates and behaves as if the dislocation is being transmitted into the neighbouring grain. Few drawbacks of this model is the necessity in physically placing a FR sources close to the GB to create residual dislocations at GBs.

³Surface from which dislocations can escape the grain by leaving behind a step on it

⁴Source length corresponding to a specific critical stress value

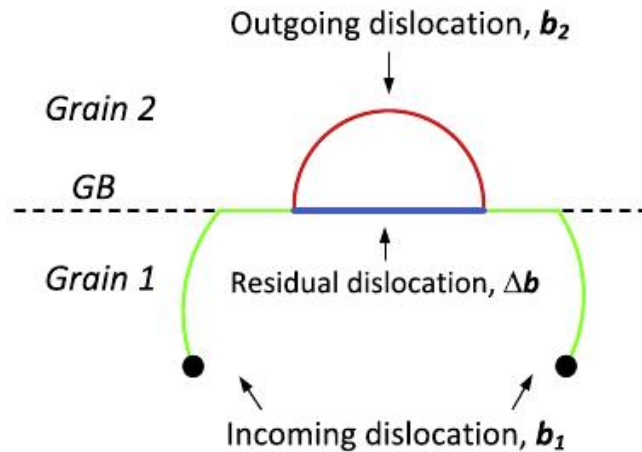


Figure 1.9 – Schematic view of dislocation transmission explained using de Koning’s line tension model [202]

By assuming a very low misorientation between grain (i.e., a similar incoming and outgoing dislocation segments without any residu at the grain boundary), one can avoid physical representation of FR sources near GBs and can simply specify a critical stress value for the GB. Following such a procedure 3D DDD simulations for different critical transmission stress values were carried out to study plasticity in polycrystalline thin films [202].

1.3.2 Dislocation array model

The idea behind dislocation-based models for grain boundary in metals was based on possibility of finding experimental evidence of particular arrays of dislocations constructed as a grain boundaries. Dislocation model of grain boundaries was first suggested by Bragg and Burgers in 1940. The evidence of edge dislocation walls lead to the first quantitative study of the grain boundary models by Read and Shockley [188]. This model was based on a discrete description of edge dislocations as a low angle grain boundary. Read and Shockley further tried to establish a link between grain boundary energies and their misorientation angle for low angle grain boundaries.

1.3.2.1 Discrete approach

Read and Shockley’s dislocation-based GB model was based on description of a symmetric low angle tilt grain boundary as a wall of edge dislocations. Based on

1.3. Generic models for grain boundaries

the experimental evidence, sub-grain boundaries are represented by a network of edge dislocations on the grain boundary plane as shown in Figure 1.10. Further, a relationship between the grain boundary misorientation angle (θ) and the spacing (d) between the edge dislocations of Burgers vector \mathbf{b} was established and is shown in Equation 1.1. An extrapolation of Read and Shockley's formula for high-angle grain boundaries was carried out by substituting θ by $\sin\theta$ (cf. Equation 1.2) [37] leading to Equation 1.2:

$$d = \frac{b}{\theta} \quad (1.1)$$

$$\frac{|\mathbf{b}|}{d} = 2\sin\frac{\theta}{2} \quad (1.2)$$

where θ is the misorientation angle, \mathbf{b} is the Burgers vector of edge dislocations and d is the spacing between edge dislocations in the grain boundary plane.

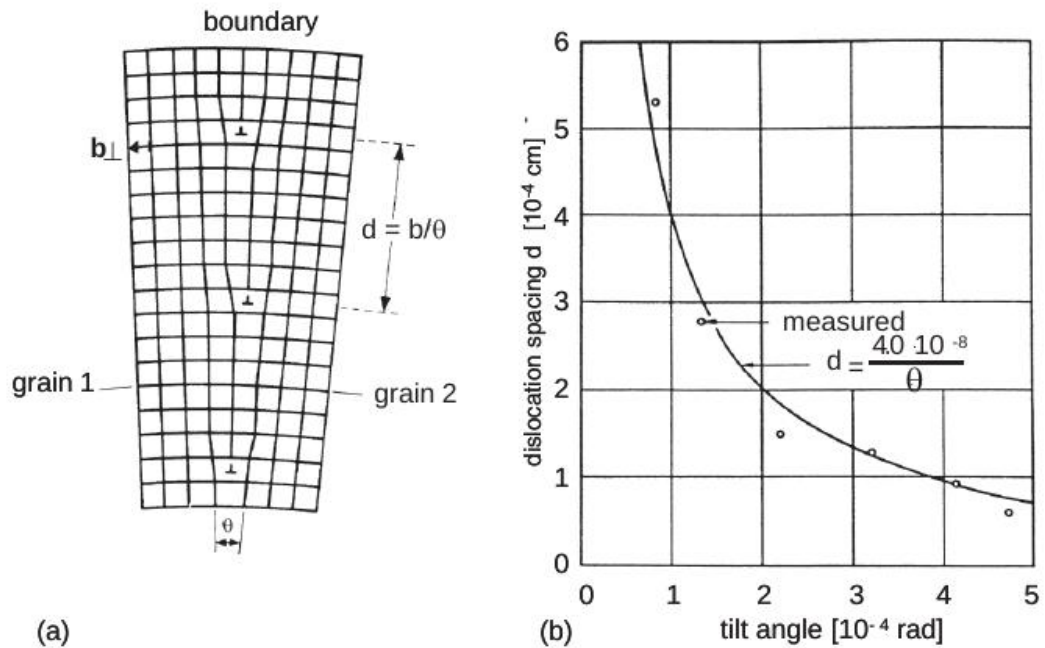


Figure 1.10 – (a) A low angle symmetric tilt boundary represented as a wall of edge dislocations; (b) dislocation spacing vs misorientation angle [188]

In an asymmetric tilt grain boundaries, the grain boundary plane deviates by an angle ψ from its symmetric position. Asymmetric twist grain boundaries require two sets of screw dislocations to represent the grain boundary.

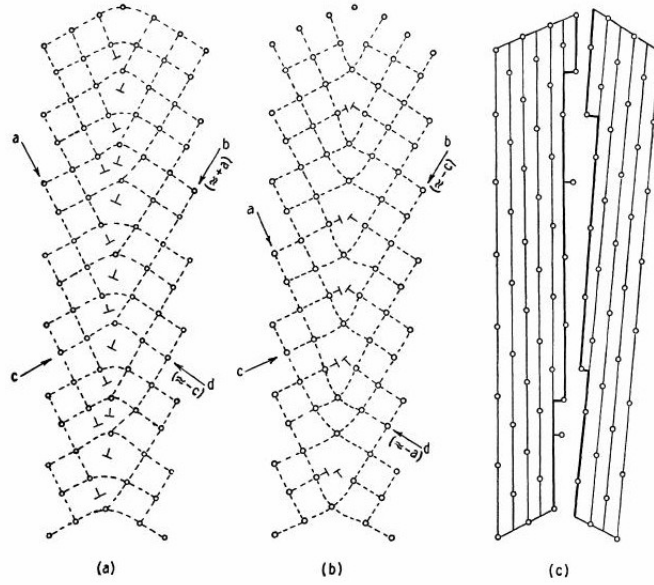


Figure 1.11 – A 60° boundary showing equivalence of $\psi = 0^\circ$ and $\psi = 45^\circ$ models and relationship to imperfect (210) surfaces [188]

Whereas, asymmetric tilt grain boundaries are represented by at least two sets of edge dislocations. The perpendicularity condition between the Burgers vector of the two dislocation sets should be satisfied. The spacing (d_1, d_2 for grain 1 and grain 2 respectively) between edge dislocations of each set will then be:

$$\frac{1}{d_1} = \frac{|\mathbf{b}_1|}{\theta \cos \psi}, \quad (1.3)$$

$$\frac{1}{d_2} = \frac{|\mathbf{b}_2|}{\theta \sin \psi}. \quad (1.4)$$

Equation 1.5 was established to relate interface energy, γ_b^{symm} and misorientation angle, θ . Under the assumption of isotropic continuum elasticity theory, Read and Shockley subdivided the energy per unit length of an edge dislocation, E_d into the contribution of its dislocation core energy, E_c and the energy arising from the strain fields surrounding the dislocations, E_s as in Equation 1.5, leading to

1.3. Generic models for grain boundaries

$$E_d = E_c + E_s \quad (1.5)$$

$$= E_c + \frac{\mu \mathbf{b}^2}{4\pi(1-\nu)} \ln \frac{d}{r_o}, \quad (1.6)$$

where μ and ν are the shear modulus and Poisson ratio of the material, $r_o = b$ is the dislocation core radius, where b is the magnitude of Burgers vector and E_c is the energy of the dislocation core.

The energy per unit area for a symmetric tilt boundary is obtained by substituting Equation 1.1 to account for the number of dislocations per unit length as:

$$\gamma_b^{symm} = \frac{\theta}{\mathbf{b}} \left(\frac{\mu \mathbf{b}^2}{4\pi(1-\nu)} \ln \frac{1}{\theta} + E_c \right) \quad (1.7)$$

$$= \theta \left(\frac{E_c}{\mathbf{b}} - \frac{\mu \mathbf{b}}{4\pi(1-\nu)} \right). \quad (1.8)$$

The grain boundary energies predicted by Read-Shockley's dislocation-based model were verified against experiments. The model remained valid for misorientation angles $\theta < 15^\circ$. For misorientation angles $\theta > 15^\circ$, the dislocation-based models can no longer be applied because of the loss of identity of individual dislocations when the spacing between them is infinitely small. So, grain boundaries with misorientation angle larger than 15° are termed as high angle grain boundaries (HAGB).

Models such as coincidence site lattice (CSL) and displacement shift complete (DSC) lattice construct the structure of the interface on the assumption that the atoms try to remain close to their ideal positions. At certain misorientations, a transition plane exists on which certain atomic positions in the grain boundary coincide with the ideal lattice positions of both the crystals. These atomic positions are termed as coincidence site and the lattice containing these sites are termed coincidence site lattice (CSL). Grain boundary represented accordingly is characterized by the density of coincidence sites, which is defined by the quantity Σ . CSL model is most widely used to differentiate grain boundaries in crystals. Experiments suggest that the CSL grain boundary of low Σ indeed consists of a

low energy configuration. Since, CSL only exists for very special, defined angles; it does not continuously change with misorientation. Drawback of the CSL model is compensated by the introduction of dislocation with DSC Burgers vectors. These dislocations are also called secondary grain boundary dislocations, as they are confined to the grain boundary only. Because of the use of misorientation based approach to represent grain boundaries and their interaction with dislocations (*cf.* Section 4.3.7 of Chapter 4), models based on structure of interfaces are not explained in detail. For more details about these models, a review has been carried out by Sutton and Balluffi [169].

Read and Shockley in their model assumed grain boundaries as single or multiple array of dislocations. A more detailed explanation of the model has already been presented in Section 1.3.2.1 of Chapter 1. Eventhough, this model has a strong limitation to model only low angle grain boundaries (LAGBs), considerable work has been carried out using the model to represent GBs in 3D DDD simulations [123, 167]. One advantage of using such representation of GBs is that no explicit rules are needed to model dislocation-grain boundary interactions. The stress field of the dislocation array acting as grain boundary will define when a subsequent dislocation-grain boundary interaction can take place. This method is useful while working with LAGBs in a simple bicrystal or tricrystal configurations. But, the use of this method is highly constricted for polycrystals. Representing grain boundary as dislocation arrays in a polycrystal will be challenging. So, such a representation of grain boundary has been avoided in the present study.

1.3.3 Dislocation dissociation model

Nodal discretization based DD code provide an advantage of easy representation of dissociation of a dislocation segment at the grain boundary due to the flexibility in the number of degrees of freedom provided to each dislocation segment. Specifying local dislocation-grain boundary rules is significantly easier when compared to that of conventional lattice based codes. Moving ahead in similar direction, implementation of local rules for dislocation interaction with coherent twin boundary in HCP and FCC crystals have been carried out [11, 58].

In spite of these advancements, the use of a physics based numerical model to accurately represent grain boundaries and predict materials behavior is still limited. The use of a physics based model to predict behavior of a polycrystal is one of the motivations of the present thesis.

1.4 Remarks

This chapter provided a short introduction to interfaces and types of interfaces usually seen in crystalline materials. Crystals in single-phase material which are separated by grain boundaries were categorized mainly based on disorientation angle. Edge dislocations were used in modeling grain boundaries of lower disorientations. An example bicrystal simulation with the assumption of grain boundary as an impenetrable obstacle is shown. Different generic approaches followed in the DD community to model dislocation-grain boundary interactions are presented.

2 Experimental investigation of thin films

METALLIC thin films serve as excellent candidates for studying polycrystals with grain sizes in the order of few nanometers. Experimental investigation of nanocrystalline materials would not have been possible without the advancement of different micro- and nano-fabrication techniques, except for the use of nanoindentation which does not involve any fabrication steps (only surface preparation).

This chapter presents an overview on the new on-chip tensile testing method developed at UCL as several test results which will be simulated in this thesis have been obtained with this method. Various steps involved in the micro-fabrication of thin films are presented. Along-side, important results from the experimental observations of Pd thin films are also reviewed.

2.1 Overview: On-chip tensile testing method

The on-chip tensile testing method was developed to deform free-standing thin films [34, 78]. This nano-mechanical technique (cf. Figure 2.1) was developed at UCL to enable characterization of mechanical properties [78] and relaxation/creep behavior [34, 119] of free-standing thin films at a very low strain rate condition ($< 10^{-6} s^{-1}$). The basic concept behind this method is the use of internal stress developed during the micro-fabrication process to deform a thin film. The on-chip test requires no external loading device; hence, it is flexible for testing thousands of structures at the same time under different external conditions (temperature, load etc.). To establish an overview, the technique is now explained for fabrication of *classical structures* in a sequence of five individual steps, for an application to the testing of Pd films.

Step 1: The micro-fabrication process starts with the selection of substrate material. The choice of (100) mono-crystalline silicon wafer (cf. Figure 2.2(a)) as

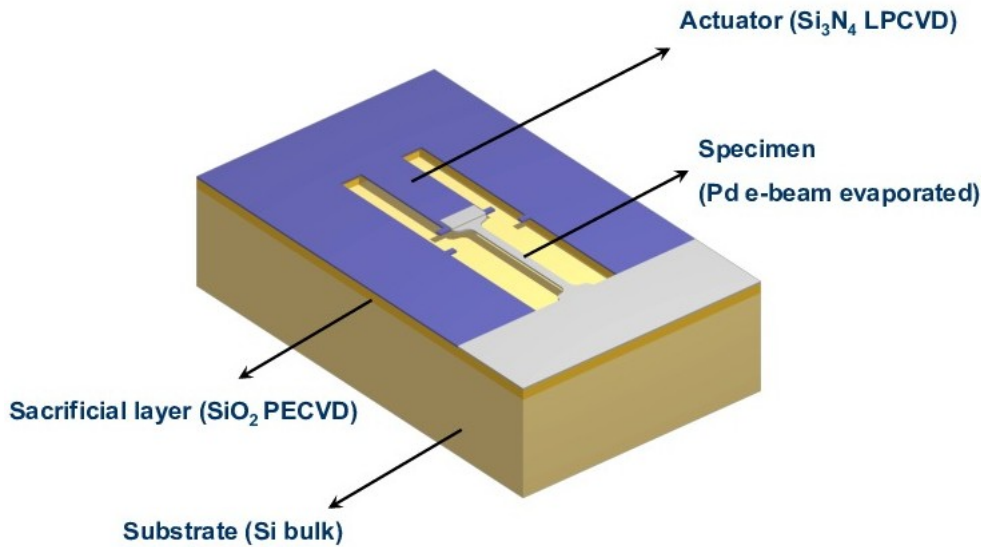


Figure 2.1 – Schematics of on-chip tensile testing technique [33]

a *substrate* is influenced by the type of structure to be studied. Silicon wafers are polished on one side; and are of 3 inches diameter and 180 μm thickness.

Step 2: On top of the substrate, a *sacrificial layer* is deposited as shown in Figure 2.2(b). This layer is generally removed in the later stages to perform the tensile test. So, the material for this layer should be selected in such a way that it does not damage the actuator and the specimen layers. Plasma enhanced chemical vapour deposition (PECVD) was used to deposit the silicon dioxide sacrificial layer at 300°C. The precursor gases were composed of 100 sccm of SiH_4 , 700 sccm of N_2O and 350 sccm of N_2 . The layer gets densified during 20 minutes at 800°C to provide optimum control of etching rate. The typical thickness of the sacrificial layers is 1 μm and compressive stresses of about 100 MPa are internally developed.

Step 3: The material selected as the *actuator layer* should be mechanically stable and also contains high level of internal tensile stresses uniformly distributed through-out the wafer. A low pressure chemical vapour deposition (LPCVD) of Si_3N_4 layer was deposited at 800°C over the sacrificial layer as shown in Figure 2.2(c). The precursor gases were composed of 30 sccm of SiH_2Cl_2 and 120 sccm of NH_3 at a pressure of 35 Pa in the tube. Internal tensile stresses of 1 GPa were introduced in the layer. A layer thickness of almost half that of the specimen thickness was used to create a strong overlap of the two layers and to avoid premature fracture in the area.

2.1. Overview: On-chip tensile testing method

Step 4: Patterning is performed before (cf. Figure 2.2(d)) and after (cf. Figure 2.2(f)) deposition of the specimen (Pd) layer (cf. Figure 2.2(e)) using e-beam evaporation. Pd is deposited on top of a thin Ti or Cr adhesion layer to ensure a good adhesion with the underneath layers. The microstructure of the Pd is varied by changing the deposition rates (0.3 to 10 Å/s). The Pd films were patterned using lift-off photolithography.

Step 5: Figure 2.2(g) shows the final processing steps which allows loading of Pd beams by releasing the structure from the constraint of the substrate by etching the SiO_2 sacrificial layer with hydrofluoric acid (HF 73%) at room temperature.

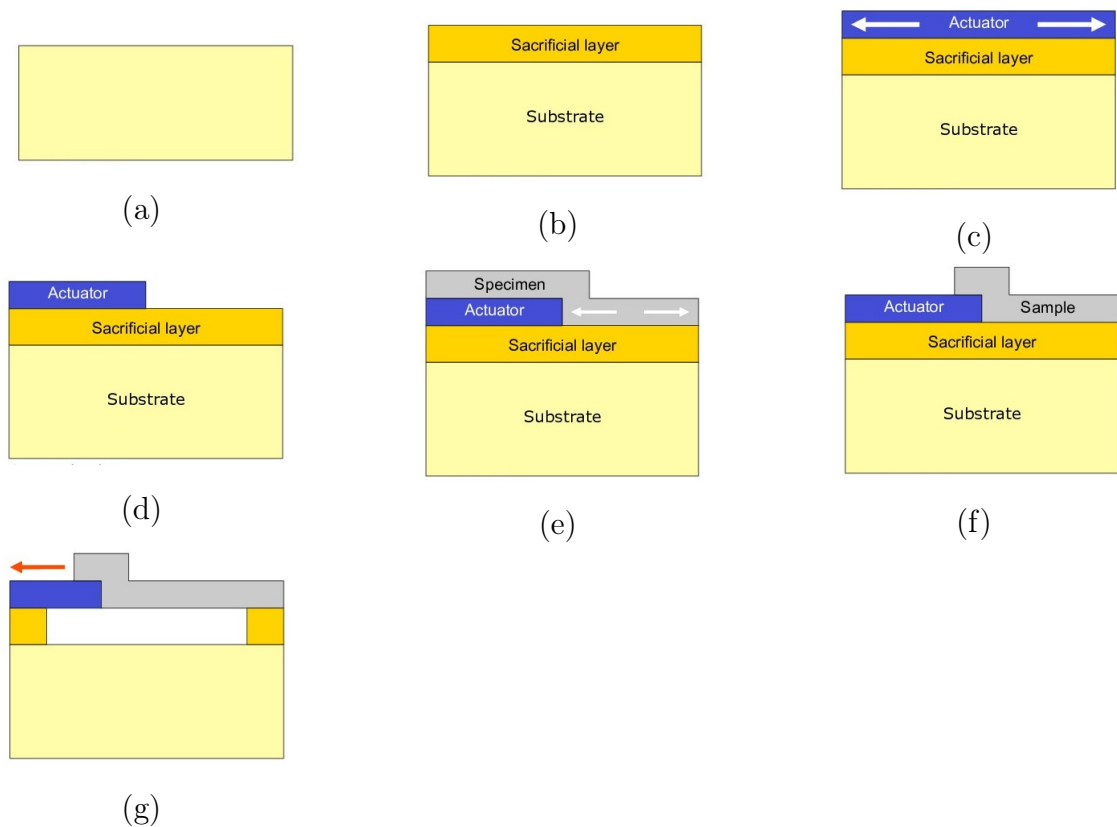


Figure 2.2 – Steps involved in the fabrication of Pd thin film

After every process step, the thickness of the actuator and sacrificial layers were characterized by ellipsometry. Layer curvature¹ and Pd thickness measurements were performed by a profilometer. Displacement measurements were carried out

¹Curvature is estimated by measuring internal stress using Stoney method

using a field emission gun (FEG)². It should be noted that this section is just a brief overview of the on-chip technique. A more comprehensive explanation about the on-chip tensile testing technique can be obtained [32, 126].

2.2 Microstructure of thin films

In contrast to the low ductility generally observed in nc materials, Pd thin films showed an unexpectedly high strain hardening capacity [93]. In nanoscale materials, thermally-activated grain boundary mechanisms [83, 88, 109, 117, 165, 170, 196] were believed to influence the rate sensitivity [76, 158]. The observation of no dominant GB mechanisms [189] highlights the requirement for a more detailed analysis on the microstructural features of the thin film. This section reviews experimental results published on Pd thin films [31, 33, 93, 119, 189, 190].

2.2.1 Stress-strain curve

The complete stress-strain response of thin film is obtained by varying the test specimen size (*cf.* Figure 2.3) using the micro-fabrication technique described in section 2.1.

Micro-tensile tests were carried out on Pd thin films of three different thickness (80nm, 160nm and 310nm). At 0.2% offset strain, the measured yield stresses were 450 ± 39 , 690 ± 86 and 1030 ± 149 MPa for 310, 180 and 80 nm thick films respectively.

The curves T15_2, T10_2 and T10_2 (*cf.* Figure 2.4) of the 80, 160 and 310 nm thick films are represented after smoothing and interpolation in Figure 2.5. The Young's modulus of 120 GPa, measured by nanoindentation, is represented as the slope of the linear elastic region in the curves (black-line in the Figures 2.5 and 2.4).

In order to avoid artefacts such as obstruction of dislocation motion due to substrate and/or passivation layer, further experiments were conducted on free-standing and unpassivated films of 90, 200 and 480 nm thickness (*cf.* Figure 2.6) [119]. The major change was the use of a Ti adhesion layer which was later

²FEG is an ultra-high resolution Schottky field emission scanning electron microscope and is ideal for studying nanoscale materials

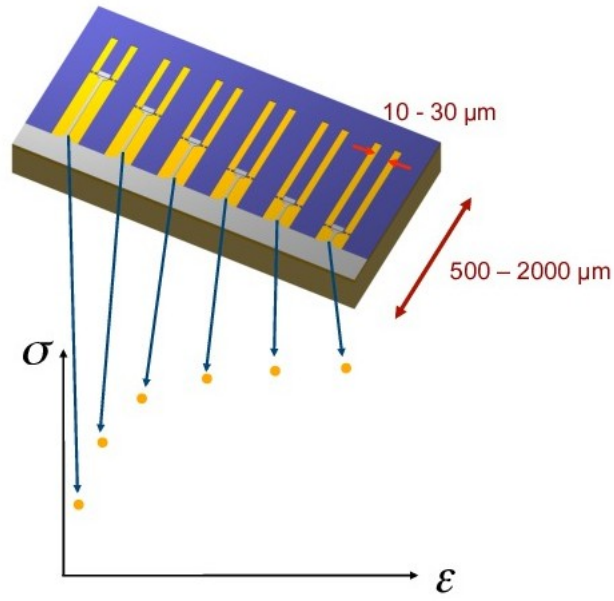


Figure 2.3 – Test specimen of different lengths on a substrate

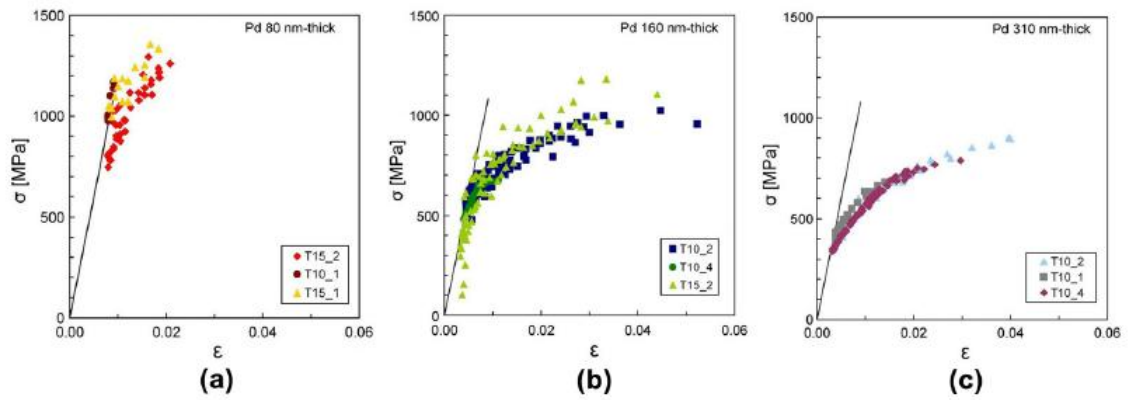


Figure 2.4 – Stress-strain curves of (a) 80nm, (b) 160nm and (c) 310 nm, respectively

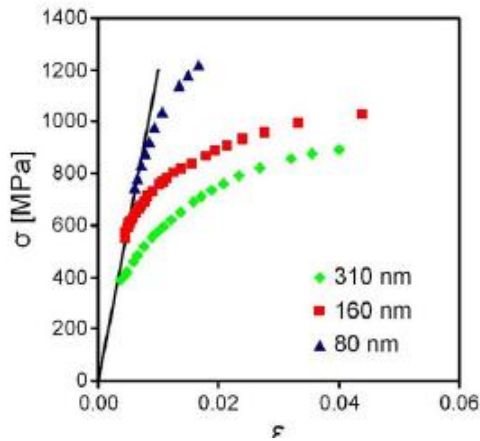


Figure 2.5 – Stress-strain curves after smoothing and interpolation, the Pd films are covered with a few nm thick Cr layer

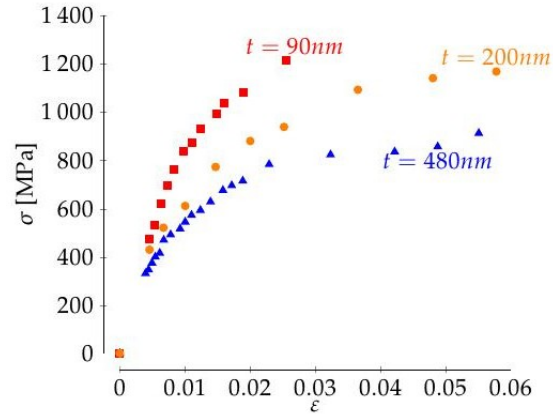


Figure 2.6 – Stress-strain curves of free-standing, unpassivated films (90, 200, 410 nm thickness)

etched away with the sacrificial layer.

2.2.2 Grain orientation distribution

Grain size changes were not observed in ACOM-TEM measurements. The lack of evolution in grain sizes confirmed the absence of GB migrations. GB sliding has not been observed by conventional TEM analysis. Figure 2.7(b) and Figure 2.7(c) shows the texture data with preferential grain orientation in the direction perpendicular and parallel to the thin film respectively. A moderate fibre texture oriented along [110] direction perpendicular to the film was observed in Pd thin films. For this texture, a good balance of tensile strength and ductility was observed. Experimentally, no preferential in-plane orientation was observed in these films.

2.2.3 Grain size distribution

An increase in the strength of the films with a decrease of the film thickness is evident from Figure 2.5. Such a Hall-Petch like effect is often reported in the literature [109, 165]. But, the general notion of a decrease in grain size with decreasing film thickness is not observed in Pd films. The cross-section analysis of three films revealed that the in-plane grain size does not vary with film thickness as shown in grain width distribution of the figure 2.8. The in-plane grain size was

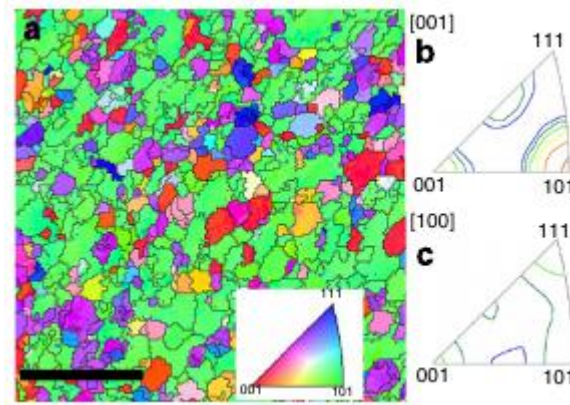


Figure 2.7 – Microstructure of the as-deposited Pd film [31]

observed to be $\sim 30\text{nm}$ in all the three films. Mostly, grains were columnar in shape; with the grain height being in-alignment with the film thickness. Hence, the reason for the size dependent strength must be found in the thickness dimension which will be one of the motivation for our simulations.

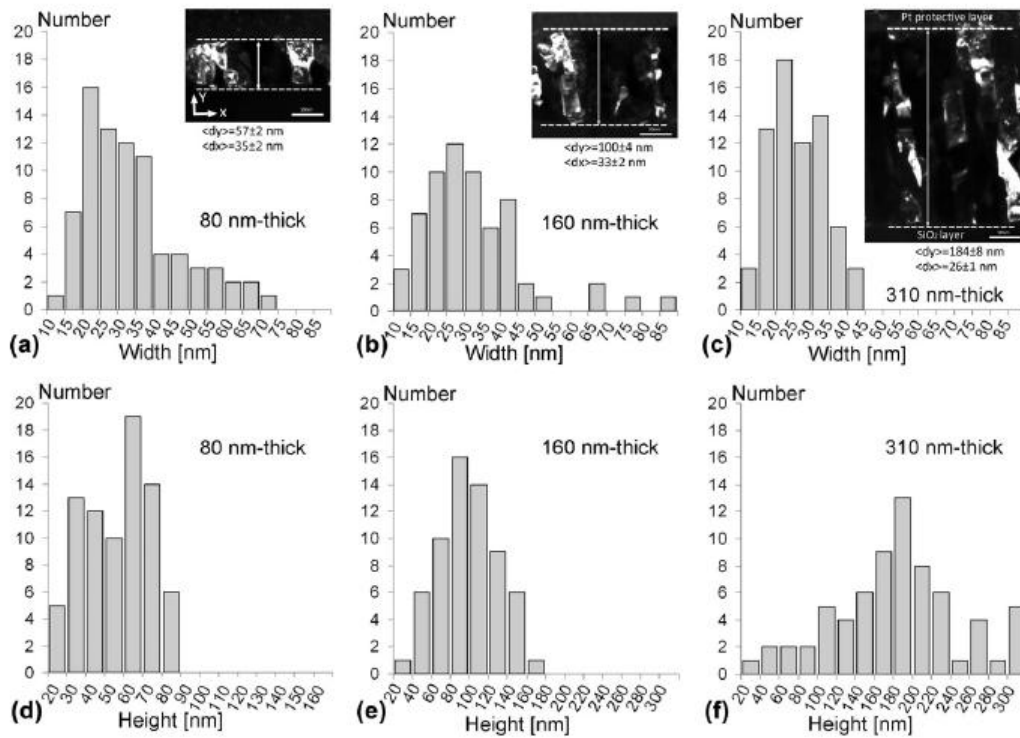


Figure 2.8 – Grain width distribution and grain height distribution derived from the cross-section analysis of three film thickness [31]

found in the Pd films [190].

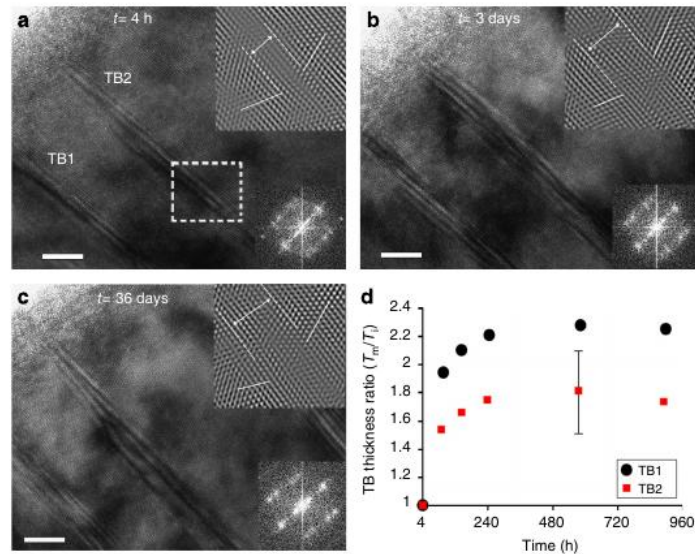


Figure 2.10 – Twin boundary thickness evolution upon relaxation [31]

Reaction of lattice dislocations with perfect coherent twin boundaries resulted in the loss of coherency. This loss of coherency is seen as the progressive increase in TB1 and TB2 thickness in Figure 2.10. Presence of twins was observed to increase the dislocation storage capacity of the film.

2.3 Remarks

In this chapter, an overview of the recently developed on-chip mechanical testing technique is presented. This technique has been extensively used to study behavior of Pd thin films [31, 33, 34, 119, 189, 190]. Ultra-high strength and moderate to high ductility of Pd thin films were observed to arise not from GB mechanism, but from microstructural features of the thin film, such as

- *Dislocation density distribution* in the thin films can be responsible for local and global heterogeneous deformation.
- *Grain morphology*: Columnar grains with aspect ratios ranging from ~ 3.0 in the thinnest film to ~ 16.0 in the thickest film should influence the thermally-activated mechanisms locally in a grain.
- *Grain size distribution*: Evidence of no significant changes in the average

grain size $\sim 30\text{nm}$ among three films highlights the relevance of grain size distribution.

- *Grain orientation distribution:* Experimentally, the improved ductility was observed in films with a preferential [110] texture.
- *Presence of twins* provided evidence to the high dislocation storage capacity of nc-Pd films.

These experimental results provided quantitative understanding of deformation in Pd thin films. But, it is still difficult to correlate a particular deformation mechanism to the macroscopic behavior of the film. For example, the mean dislocation density over four grains in the film provide very little information about the plastic deformation behavior of each individual grain. Heterogeneities of internal stresses may arise due to grain size distribution in the film. The influence of surrounding grains with no preferential grain orientation is to be better understood. The presence of twins contributing to the ultra high strength and ductility of Pd films should be justified. Other questions such as influence of grain morphology on suppressing the GB mechanisms or relevance of a preferential orientation of the grain have not been systematically addressed. More experiments on thin films may provide few answers, but it will be a daunting task to systematically perform such experiments. Numerical modelling of plasticity is a powerful alternative for probing the un-answered questions. Some of the numerical techniques developed especially for predicting the materials behavior at nano-/meso- scale are presented in the next Chapter 3.

3 Numerical modeling of plasticity in metals

DUE to the multiscale nature of metallic materials, their macroscopic behavior closely depend on elementary events at atomic-scale. It has been the goal for many researchers to develop a single concurrent multi-scale model to explain materials behavior at different length and time scales. In an attempt not so far away from the goal, researcher have developed different numerical techniques based on the underlying physics of materials at different length- and time- scales. The underlying physics in a lower-scale model is passed as a local rule to higher-scale models in hierarchical multiscale modeling approaches.

This chapter covers different numerical techniques generally used for modeling of metallic materials at different length and time scales. Starting with an explanation of the multiscale nature of metallic materials, present-day challenges in modeling these materials are highlighted. The basic idea behind different numerical techniques is reviewed. Finally, the approach followed for modeling/predicting thin films behavior is presented.

3.1 Multiscale nature of materials behavior

The reason behind the macroscopic plastic behavior of metals is mostly due to the presence of defective regions in the material. In-fact, linear defects, such as dislocations, were long acknowledged to be the reason behind most of the macroscopic events observed in metallic materials. Dislocations which are the carriers of plasticity, collectively influence the macroscopic properties such as strength, ductility, toughness, strain hardening capacity etc.,

Material behavior is controlled by phenomena over a wide range of length and time scales. An example explaining such an inter-connection is the observation of localized damage due to fatigue (at length-scales < 100 microns); which is linked to the formation of persistent slip bands at length-scale between 1-10 microns; in-turn

has its effect due to dislocation wall formations at the sub-micron regime and the events at atomic level are seen as the base for such macroscopic behavior.

In nanoscale materials, grain boundaries events such as GB sliding, GB rotation, GB growth etc., are considered as the major contributors for the high strain rate capacity. Most of the times, the GB events are initiated due to the interaction of dislocations with grain boundaries or activation of pre-existing GB dislocations. Incorporating such events in advanced numerical models is required to accurately predict the materials behavior. One such attempt has been made during this thesis to incorporate dislocation slip transmission across GBs (*cf.* Section 4.3.7 of Chapter 4). As pointed out in Chapter 2, experimental observations of Pd thin films show no evidence of active GB mechanisms. In such cases, dislocation-based thermally activated mechanisms are believed to drive plasticity in these films. Modeling accurately the grain shape and also accounting for grain size distributions may be vital for predicting size effects or plastic deformation behavior in such cases. The collective behavior of these interfaces may have a pronounced influence on the macroscopic properties of nanoscale materials.

3.2 Challenges in modeling materials behavior

Nanocrystalline materials are throwing new challenges at the materials modeling community. Modeling the overall material behavior using large-scale atomic simulations, without any doubt, would increase the chances in predicting elementary deformation mechanism in nanocrystalline materials. Atomistic simulations are mostly confined to studying a single deformation mechanism [170, 171]. For example, atomic simulations were carried out to understand interaction of a screw dislocation with a coherent twin boundary [28, 81]. Recently, our colleagues have investigated similar problem using quasicontinuum (QC) simulations [177]. The real question is, how important are such detailed deformation mechanisms when modeling materials with high density of interfaces? There is no single answer to this question. But, primarily, it is very important to understand the materials behavior under the collective influence of more than one elementary deformation mechanism; whilst modeling the interfaces accurately. This section addresses few of the major challenges faced by the materials modeling community.

1. Anisotropic response of the material
2. Short-range and long-range effects due to the collective behavior of defects

3. Computational feasibility of the numerical model

3.3 Numerical modeling of polycrystals

Every numerical model has its own advantages and disadvantages. Figure 3.1 shows different numerical techniques which can be used at different scales (length- and time-) to model mechanical response of a material.

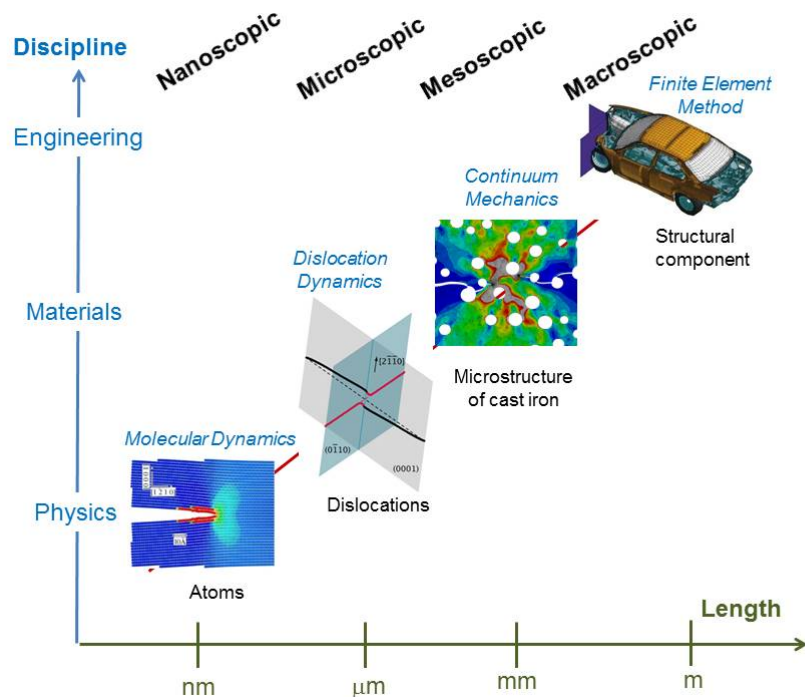


Figure 3.1 – Different numerical tools at different length- and time- scales [80]

The choice of the numerical model should not solely depend on the accuracy in predicting the materials response (the ability to model the experimentally observed trends such as, Hall-Petch effect, strain hardening), but also on the computational efficiency. In Figure 3.2, a region (red-coloured box) is highlighted on a snapshot of the thin film. Assuming that the material in the highlighted region is periodically replicated in the thin film, the setup in different numerical techniques are presented. Figure 3.2 highlights the possibilities of modeling the same problem using different numerical approaches. The concepts behind each of these models is briefly reviewed and the advantages or disadvantages of using a certain numerical model for modeling thin films are highlighted in this section.

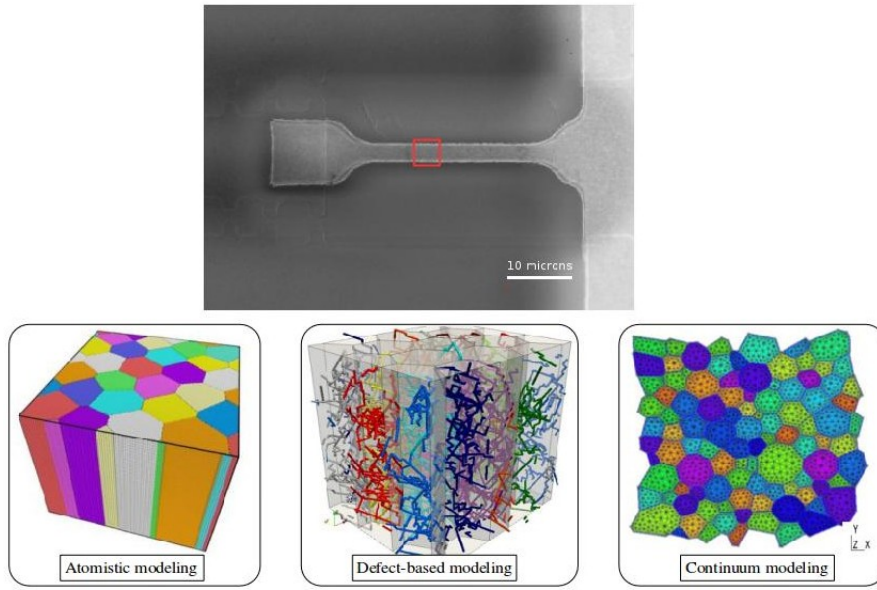


Figure 3.2 – Different numerical models for thin film modeling (a) atomistics [161], (b) dislocation dynamics and (c) 2D crystal plasticity model [119], respectively

3.3.1 Atomistic modeling

Atomic modeling tools such as molecular dynamics (MD) allows prediction of the macroscopic properties of a system through the simulation of particle (atoms in the case of metals) interactions and their evolution with time. The first molecular dynamics simulation of liquid water was done by Rahman and Stillinger [146].

In MD simulations, initial positions and velocities of all the particles in the systems are specified as initial conditions. The force among all the particles is calculated by the selected inter-atomic potential. The time-dependent changes are followed by solving a set of classical equations of motion for all the particles in the system. The algorithm is presented as sequence of steps followed in a basic MD code.

Step 1: Define initial positions ($\vec{r}_i(t_o)$) and velocities ($\vec{v}_i(t_o)$)

Step 2: Force calculation at time (t_n) using $\vec{F}_i = -\vec{\nabla}_i U(\vec{r}_1, \vec{r}_2, \vec{r}_3, \dots, \vec{r}_n)$

Step 3: Solving the equations of motion for all particle using $m_i \frac{d^2 \vec{r}_i}{dt^2} = \vec{F}_i$

Step 4: Update the positions and velocities of all the particles by implicit- or explicit- integration schemes $\vec{r}_i(t_n) \rightarrow \vec{r}_i(t_{n+1})$ $\vec{v}_i(t_n) \rightarrow \vec{v}_i(t_{n+1})$

3.3. Numerical modeling of polycrystals

Step 5: Update the timestep ($t_{n+1} = t_n + \Delta t$) and proceed to Step 1 until the total time is less than certain prescribed value.

The main advantage of this method is the use of a single interatomic potential determining the occurrence of all the elementary deformation processes in the material. A detailed atomic-level information can be obtained by these simulations. The strength of the MD method lies in the ability to study processes which are away from equilibrium (Eg: dynamic fracture, crack growth, elementary mechanism of plastic deformation etc.,).

The limitations of the technique lies in the approximations used for deriving the inter-atomic potential. Due to the typical time-scales (\sim femtoseconds), a serious limitation is laid on many problems involving thermally-activated processes. Like in most of the numerical techniques defining boundary conditions and applying artificial ensemble (NVT, NPT, NST, NVE) constraints to monitor pressure, temperature, stress, energy inhibit the use of this technique at higher scales.

Despite the limitations, MD simulations have largely been applied to predict behavior of crystalline materials. Thermally-activated mechanisms, such as cross-slip are very important process during plastic deformation of crystals. A critical review has been presented on different models for dislocation cross-slip in close-packed crystal structures [145]. By maintaining constant temperature and constant stress, cross-slip of screw dislocations and annihilation of screw dislocation dipoles have been successfully studied in fcc metals such as Cu and Ni [129, 148–150]. In fact, large-scale MD simulations were performed to provide local rules for DD models [19] and were also used for the investigation of hardening mechanisms in metals [18].

MD simulations have been largely performed to capture elementary dislocation-grain boundary mechanisms in nanocrystalline materials. Deformation of nanocrystals using atomistic simulations has been reviewed [112, 194]. Atomic simulations have been applied to investigate the influence of parallel free surfaces on deformation mechanisms in fcc nanocrystals [170]. Simulation of Cu nanowires highlight the events such as, dislocation nucleation from free surfaces during early stages of plastic deformation [25].

Another review on the deformation mechanisms controlling plasticity of fcc nanocrystals captured using atomistic simulations has been carried out [171]. In this article, they highlighted that the inherent high stress and short time restrictions of

atomistic method makes it impossible to determine the true rate-limiting processes. At present, atomic simulations alone are not suited for setting up a deformation map for nanocrystalline metals. As most of the plasticity models based on constitutive relations, studying the influence of applied stress, grain size, strain rates and temperatures are of prime importance while modeling nanocrystal.

3.3.2 Continuum based models

Continuum models for metallic materials are generally based on single crystal plasticity framework. At a single grain level, plastic deformation is carried by dislocations moving on different slip systems. Slip systems constitute a comprehensive set of slip planes and slip directions on which dislocation motion is highly concentrated. The number of slip systems differ with the lattice structure of the materials. In FCC metals, plasticity thrives on 12 densely packed $\{111\}$ slip planes. Whereas, in BCC metals, 12 $\{110\}$ type and 12 $\{112\}$ type slip planes with $\langle 111 \rangle$ slip direction can be potentially active.

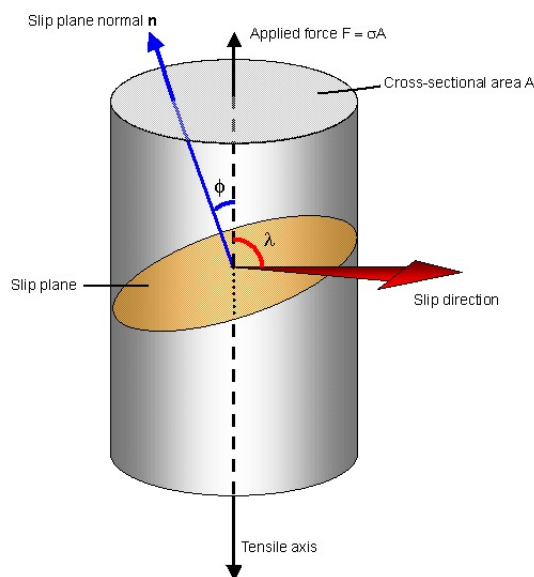


Figure 3.3 – Schmid law explained using a cylindrical grain deformed under tension along the tensile axis [180]

A single crystal deformed under tension yields (*cf.* Figure 3.3) when the resolved shear stress on a slip system exceeds a critical value. This is called Schmid's law [52],

3.3. Numerical modeling of polycrystals

which writes:

$$\tau_c = \sigma_y \cos\phi \cos\lambda \quad (3.1)$$

where τ_c is the critical resolved shear stress, σ_y is the tensile yield strength and $M = \cos\phi \cos\lambda$ is known as *Schmid factor*(M).

Since there are 12 slip systems in a FCC crystal, slip occurs on the system which first exceeds the critical value, τ_c . The slip system hence is known as primary slip system and apparently has the greatest Schmid factor.

3.3.2.1 Elasto-plastic framework

The constitutive formulation of single crystal plasticity is based on multiplicative decomposition of the deformation gradient ($\mathbf{F} = \frac{d\mathbf{U}}{dx}$; where \mathbf{U} is displacement) into elastic (\mathbf{F}_e) and plastic (\mathbf{F}_p) parts [7]. The elastic distortion and rigid-body rotation is described by the elastic part (\mathbf{F}_e) of the deformation gradient. \mathbf{F}_p is the plastic part of the total deformation that is due to crystallographic slip. It should be mentioned that the crystallographic slip, in general, includes a rotational part (\mathbf{R}_p) in addition to the translation part (\mathbf{U}_p).

$$\mathbf{F} = \mathbf{F}_e \cdot \mathbf{F}_p \quad (3.2)$$

$$\mathbf{F}_p = \mathbf{R}_p \cdot \mathbf{U}_p \quad (3.3)$$

The multiplicative decomposition considers the concept of a local intermediate (relaxed or stress-free) configuration. In Figure 3.4, the plastic deformation gradient maps any material point from the reference configuration to the intermediate configuration. The elastic part of the deformation gradient further maps the material points from an intermediate configuration to the current configuration. The decomposition of the *Eulerian* velocity gradient ($\mathbf{L} = \dot{\mathbf{F}} \cdot \mathbf{F}^{-1}$) follows:

$$\mathbf{L} = \dot{\mathbf{F}} \cdot \mathbf{F}^{-1} = \dot{\mathbf{F}}_e \cdot \mathbf{F}_e^{-1} + \mathbf{F}_e \cdot \dot{\mathbf{F}}_p \cdot \mathbf{F}_p^{-1} \cdot \mathbf{F}_e^{-1} = \mathbf{L}_e + \mathbf{L}_p. \quad (3.4)$$

The plastic velocity gradient is determined by accumulative slip rates on all

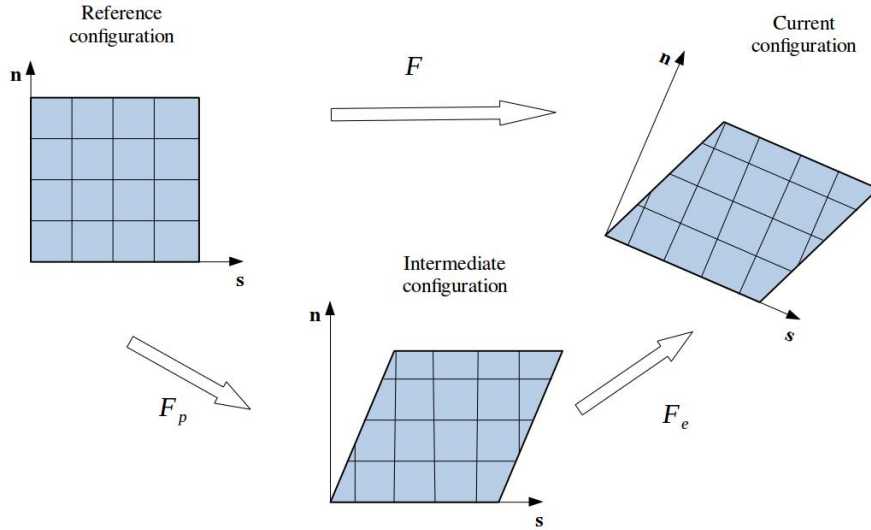


Figure 3.4 – Schematic representation of reference, intermediate and current configurations based on multiplicative decomposition of the deformation gradient tensor

the active slip system as

$$\mathbf{L}_p = \dot{\mathbf{F}}_p \cdot \mathbf{F}_p^{-1} = \sum_{i=1}^{12} \dot{\gamma}^i \mathbf{s}^i \otimes \mathbf{n}^i, \quad (3.5)$$

where \mathbf{s}^i is the slip direction and \mathbf{n}^i is the slip plane normal of slip system i . The rate of plastic shear on slip system i is denoted by $\dot{\gamma}^i$.

3.3.2.2 Constitutive equations

The constitutive behavior of the crystal is specified for both elastic and plastic parts by the stress-strain relation. For the elastic part, the response of the crystal is given macroscopically by:

$$\mathbf{S}^e = \mathbf{C}^e : \mathbf{E}^e \quad (3.6)$$

where \mathbf{E}^e is the elastic Green-Lagrange strain tensor and \mathbf{S}^e is the second Piola-Kirchhoff stress tensor. \mathbf{C}^e represents the elastic moduli in the intermediate configu-

3.3. Numerical modeling of polycrystals

ration, and

$$\mathbf{E}^e = \frac{1}{2}(\mathbf{F}_e^T \cdot \mathbf{F}_e - \mathbf{I}) \quad \mathbf{S}^e = \det(\mathbf{F}_e) \mathbf{F}_e^{-1} \cdot \sigma \cdot \mathbf{F}_e^{-T}. \quad (3.7)$$

At microscopic level, a power law is often used to model the plastic deformation on each slip system:

$$\dot{\gamma}^i = \dot{\gamma}_o^i \left(\frac{|\tau^i|}{s^i} \right)^m \text{sign}(\tau^i) \quad (3.8)$$

where, i is the slip system index and $\dot{\gamma}_o^i, \tau^i, m$ are rate of plastic shear, critical resolved shear stress and strain rate sensitivity coefficient, respectively. For metals $m=100$, a highly non-linear relation between $\dot{\gamma}^i$ and τ^i exists.

3.3.2.3 Hardening rule

Dislocation slip on a particular slip system leads to hardening of the system. The accumulation of dislocations on the slip system leads to resistance for further slip. A higher stress level is required to continue plastic deformation on the slip system. This is referred to as self-hardening. Consequently, a dislocation also experiences the interaction strength due to dislocations on other slip systems. This is called as latent hardening. Such resistance to dislocation slip is highly discrete and leads to anisotropic behavior at single crystal level. The evolution of the shear resistances s^i is defined phenomenologically in CP models by

$$\dot{s}^i = \sum_{j=1}^{12} H^{ij} |\dot{\gamma}^j| \quad \text{with } i = 1, \dots, 12. \quad (3.9)$$

The proportionality coefficients H^{ij} are the hardening moduli, where H^{ii} is the self-hardening term and H^{ij} ($i \neq j$) refers to the latent hardening effects.

The development of a single-crystal plasticity models has been well documented [102, 154]. During this thesis, the working procedure of a Taylor assumption based crystal plasticity code has been used to find new hotspots in the phenomenological CP model.

3.3.2.4 Polycrystalline behavior

To determine the properties of a polycrystalline aggregate, different approaches have been developed. Earliest models were based on local and global assumptions made on stress or strain tensors. Sachs proposed a model based on iso-stress formulation [Sachs 1928]. He assumed that the locally averaged Cauchy stress of each crystal is equal to the macroscopic Cauchy stress of the polycrystalline aggregate. With this assumptions, every grain deforms independently and can lead to overlapping of the grain boundaries. Whereas, Taylor's iso-strain formulation assumed that the local deformation is equal to the macroscopically imposed deformation of the aggregate [173]. According to Taylor, at least five independent slip systems in each grain should operate to maintain macroscopically compatible strain. Because of the complete restriction placed, these models were known as fully-constrained (FC). Taylor's iso-strain approaches was later modified by global relaxation of some strain components. These modifications were categorized as relaxed-constraint (RC) Taylor models [90,101]. Even, RC Taylor models were not imparting the stress heterogeneities which arise at single grain level. Present-day advanced models can be classified into two types based on the employed homogenization schemes:

- a.) Full-field approach
- b.) Mean-field approach

In a full-field approach, both long-range and short-range grain interactions are considered and the micro-mechanical fields are resolved on a discrete grid. For solving this heterogeneous problem using a FEM, at the discrete grid level, equilibrium of forces is achieved and displacement compatibility is maintained by using *principle of virtual work* [60]. Mesh element size in this case should be smaller than the average grain size of the polycrystal. Whereas, in the FFT-based method, the local mechanical response of the heterogeneous medium is calculated as a convolution integral between Green functions associated with appropriate fields of a linear reference homogeneous medium and the actual heterogeneity field [113]. The FFT algorithm transforms the heterogeneous fields into Fourier space and, in turn, gets the mechanical fields by transforming back into real space. A comparative study shows that for an exactly similar problem, FFT-based full-field crystal plasticity approach is more efficient than the FEM-based full-field crystal plasticity approach [114].

In contrast, mean-field approaches deal with the complex stress heterogeneities and continuity of displacement in polycrystal by a finite elements method (FEM). Grain interactions in a cluster are considered in some of the mean-field approaches.

3.4. Purpose for modeling polycrystal using 3D DDD simulations

Bi-crystal grain interactions was considered in LAMEL [181, 182] and ALAMEL models [183]. Another scheme is based on the viscoplastic self-consistent (VPSC) formulation [115]. Based on a generalization of grain interaction (GIA) model, a relaxed grain cluster (RGC) homogenization scheme was proposed [176]. To move from phenomenological CP model to a more advanced physics based CP models, dislocation based hardening rules have been incorporated into crystal plasticity framework [4, 6]. Most CP models accurately predict texture evolution in a polycrystal but fail to capture any size-effects. In an attempt to overcome the restriction on size-effect predictions, strain gradient crystal plasticity theories incorporated intrinsic length scales [65, 69, 140].

3.4 Purpose for modeling polycrystal using 3D DDD simulations

Large scale molecular dynamics simulations are a viable option to study the behavior of metallic thin films. But, the very small time-step ($\sim 10^{-15}s$) and high computational intensity prohibit the use of MD simulations for studying behavior of materials under the collective influence of defects. On the other hand, crystal plasticity models can deal with complex boundary conditions and are specifically developed to deal with anisotropic crystal deformation. Computationally, CP simulations are far effective when compared to MD simulations. But, the phenomenological rules used in a CP model should be validated against a more physics based model or by experiments.

Defect-based models, such as dislocation dynamics can treat size effects with the length scale involved with the dislocation sources. The advanced thermally activated mechanisms such as cross-slip (or) climb can provide answers to rate sensitivity arising from collective dislocation behavior. DD simulations can be coupled with a FEM to treat stress heterogeneities and also to deal with complex boundary conditions. With advanced hardening rules, DD simulations can predict the behavior of metallic thin films with quite few assumptions. The methodology of a three dimensional discrete dislocation dynamics simulations, which is the core method used in this thesis, is provided in detail in Chapter 4.

PART - II

Dislocation dynamic simulations: Methodology and Developments

4 Methodology of discrete dislocation dynamics simulations

THE idea of developing a 3D code to predict materials behavior at mesoscale was first realised by Kubin, Canova, Bréchet in the early 1990s. This meso-scale material model proved vital in explaining the plastic deformation behavior of a single crystal under the collective influence of dislocations. Whereas in a polycrystal, along with dislocations, other types of defects (e.g. grain boundaries) also influence the plastic response of the materials.

This chapter presents the methodology of three dimensional discrete dislocation dynamics (DD) simulations. A polycrystalline version of the DD code has been used during the thesis and it does not differ much from its single version counterparts. The only major difference is the manner in which internal stress field due to a dislocation is computed. The stress tensor calculated is always in the *lab frame* to ensure compatibility of the long-range stress fields due to dislocations in the simulation volume. The different reference frames introduced in the polycrystalline DD code are also explained. Developments in the form of slip transfer mechanism across GBs and optimised stress field calculations are also incorporated in the polycrystalline DD code and are presented in this chapter.

4.1 Introduction

The earliest dislocation dynamics code was co-developed at Onera [16] and at Grenoble INP [62, 185]. This simple lattice-based edge-screw model led to the code *Micromegas* distributed by Onera and the code *TRIDIS* developed in Grenoble. More than two decades after the first 3D discrete dislocation dynamics code, the present-day 3D DDD codes are sufficiently advanced to deal with multiple interfaces in crystalline materials. In this thesis, we use *TRIDIS*, the code which was developed at Grenoble. Some of the noticeable developments in *TRIDIS* are:

Chapter 4. Methodology of discrete dislocation dynamics simulations

1. The application of the box method to treat long-range dislocation stresses in the case of [186];
2. Implementation of the superposition method for solving a boundary value problem; its application to advanced nano-indentation simulations [62];
3. Taking advantage of the MPI parallelism scheme to deal with dislocation-precipitate interaction [27];
4. An easy implementation of the displacement field for modelling fatigue induced plastic steps in 316L steel [43, 63];
5. Accounting for anisotropic elastic stress field and development of the first polycrystal version of the code [92]

Readers are directed to the following HDR thesis [64] for more comprehensive details about the advancements of the *TRIDIS* code being developed and maintained at SiMaP laboratory in Grenoble. During the course of the thesis, generic rules for screw dislocation-grain boundary interaction have been incorporated in the present polycrystal version of the 3D DDD code. The stress field computations was also optimized to run on graphical processing units (GPUs). In spite of these developments, the optimised GB interaction based polycrystalline model has not been used for performing large scale thin film simulations. Before proceeding to the sections presenting developments in the polycrystalline 3D DDD model, the main idea behind the computation of the stress field due to dislocations in a confined volume is presented.

4.2 Computation of heterogeneous stress field in a volume containing dislocations

4.2.1 Discretization of a dislocation

In DD codes, a curved dislocation line is represented by series of discrete dislocation segments following a general discretization scheme. Different discretization schemes were developed to avoid restricting dislocations to a fixed set of orientations. Earliest DD code relied solely on pure edge and pure screw segments to represent a dislocation line. This description limited the possibility of accurately modeling all the elastic interactions between dislocations (junction formations). A mixed

4.2. Computation of heterogeneous stress field in a volume containing dislocations

character for the dislocation segment was additionally used to describe a dislocation lines in the DD code developed [48]. More sophisticated nodal-based discretization schemes [5, 108, 192, 200] were developed to account for complicated dislocation-based hardening mechanisms such as multi-junctions [20], dislocation partials and twin boundary interaction in polycrystalline Mg [58], formation of glissile junctions [167], interaction of dislocations and irradiation defects in Zr [51].

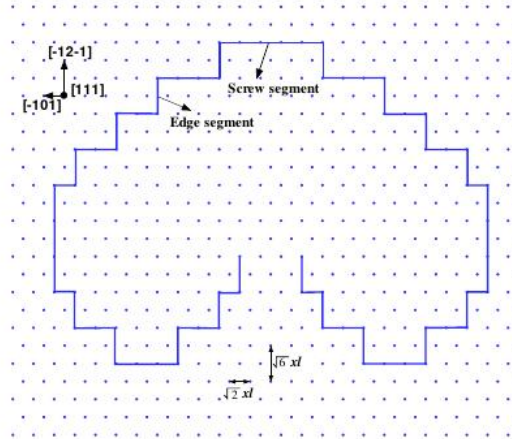


Figure 4.1 – Edge-Screw based discretization of a curved dislocation line [27]

The DD code used in the thesis is based on *Edge-Screw* based discretization scheme [16, 62]. A dislocation line is divided into series of *Edge* and *Screw* segments as shown in Figure 4.1. Each discrete segment moves on a pre-defined lattice network with lattice spacing, xl . A heterogeneous lattice is inherently present due to the different unit lengths of edge ($\langle 112 \rangle$ type with $\sqrt{6}xl$ length) and screw ($\langle 110 \rangle$ type with $\sqrt{2}xl$ length) dislocations. The xl value is generally defined to be $10\mathbf{b}$, where \mathbf{b} is the magnitude of Burgers vector. But, this value can be modified according to the size of the simulation specimen. For example, for the Pd thin films simulations (*cf.* Chapter 6), $xl = 0.1\mathbf{b}$ has been used. In the polycrystal version of the DD code, the lattice network corresponding to every grain is oriented with certain *Euler angles*. The texture objects representing the oriented lattices of the grains are shown in Figure 4.43. The rotated lattice network of the grain can be referred as *crystal frame* and the 3D space in which the polycrystal is setup is hereby referred as *lab frame*.

The family of *Screw* and *Edge* vectors of the Thompson Tetrahedron [175] are used to describe the 12 slip systems of a FCC and DC crystal. Each of the six *Screw* segments can have either *Edge1* and *Edge2* as glide directions with

Chapter 4. Methodology of discrete dislocation dynamics simulations

corresponding 111 plane normals, \mathbf{n} . Whereas, *Edge1* and *Edge2* can only glide along the corresponding *Screw* direction. For a given orientation of the Screw, the two Edges are considered in such a way that the $\text{Edge1} \times \text{Edge2} = 4\text{Screw}$. Such systematic construction is necessary for the description of prismatic loops [64].

4.2.2 Internal stress field due to a dislocation

The stress field of a dislocation of finite length in an isotropic elastic framework is obtained as the difference between the stress field of two semi-infinite dislocations since a closed form expression for the stress field already exists for a semi-infinite dislocation in isotropic elastic framework. If the semi-infinite dislocations with Burgers vector $\mathbf{b} = (b_x, b_y, b_z)$ is placed along the z-axis, then the stress field due to the dislocation [125] at an arbitrary point $\mathbf{r}(x,y,z)$ is given by:

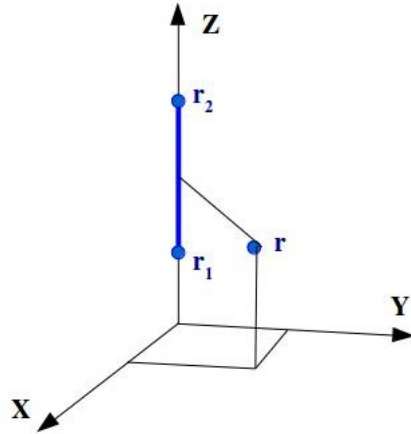


Figure 4.2 – Notation adapted for calculating stress field of a dislocation

The difference of two semi-infinite segments then gives:

$$\sigma_{int}(\mathbf{r}) = \sigma(\mathbf{r} - \mathbf{r}_1) - \sigma(\mathbf{r} - \mathbf{r}_2) \quad (4.1)$$

where $r_1 = (0, 0, z_1)$ and $r_2 = (0, 0, z_2)$ points are shown in Figure 4.2.

4.2. Computation of heterogeneous stress field in a volume containing dislocations

The symmetric second order stress tensor, $\boldsymbol{\sigma}(\mathbf{r})$ reads:

$$\begin{aligned}\sigma_{xx}(\mathbf{r}) &= \frac{-b_x y - b_y x}{r(r-z)} - x^2 \frac{(b_x y - b_y x)(2r-z)}{r^3(r-z)^2} \\ \sigma_{yy}(\mathbf{r}) &= \frac{b_x y + b_y x}{r(r-z)} - y^2 \frac{(b_x y - b_y x)(2r-z)}{r^3(r-z)^2} \\ \sigma_{zz}(\mathbf{r}) &= \frac{z(b_x y - b_y x)}{r^3} - \frac{2\nu(b_x y - b_y x)}{r(r-z)} \\ \sigma_{yz}(\mathbf{r}) &= \frac{y(b_x y - b_y x)}{r^3} - \frac{\nu b_x}{r} + \frac{(1-\nu)b_z x}{r(r-z)} \\ \sigma_{xz}(\mathbf{r}) &= \frac{x(b_x y - b_y x)}{r^3} + \frac{\nu b_y}{r} - \frac{(1-\nu)b_z y}{r(r-z)} \\ \sigma_{xy}(\mathbf{r}) &= \frac{b_x x - b_y y}{r(r-z)} - xy \frac{(b_x y - b_y x)(2r-z)}{r^3(r-z)^2}\end{aligned}$$

where $r = \sqrt{(x^2 + y^2 + z^2)}$ and the stresses are in the units $\frac{\mu}{4\pi(1-\nu)}$, where μ and ν are the shear modulus and Poisson ratio of the material, respectively.

As linear elasticity is not valid in the dislocation core region, the above expression for stress field of a dislocation become singular along the dislocation line. To address the issue, a non-singular formulation has been proposed by Cai and co-workers [23]. Their idea relied on introducing a spread of the Burgers vector, such as to remove the singularity of the core. Apart from singularity issues at the dislocation core, the computational bottleneck in DD code arise mainly due to the long-range effect of dislocation stress field ($\propto \frac{1}{r}$). To tackle this computational issue, different techniques adopted in the DD community and the newly developed GPU based method to tackle the same issue are presented in *cf.* Section 4.4.3. As mentioned in Section 4.2.1, all the discrete dislocation segments move on respective lattic networks (in crystal frame) specific to every grain. The self stress field due to a dislocation segment is computed in the crystal frame and the stress tensor is then transferred/rotated to the lab frame. This way, compatibility of long-range stress field due to dislocations in the simulation volume is maintained.

4.2.3 Periodic boundary condition

Periodic boundary condition (PBC) is an elegant way to predict bulk behavior by simulating a small region of the specimen. If a primary simulation volume is imagined as a two dimensional square box. Periodic simulation volume are

Chapter 4. Methodology of discrete dislocation dynamics simulations

periodic replicas of the primary volume in the directions in which PBC is applied (X- and Y- direction in our 2D case). Due to PBC, the dislocation segments in the primary volume are forced to leave from one side and re-emerge from an equivalent position on the opposite side of the box with the same velocity to ensure conservation of dislocation fluxes (cf. Figure 4.3). A non-cubic (orthorhombic) simulation volume is considered to avoid the self-annihilation phenomenon which creates artificial dislocation microstructures [153]. The segments which leaves the primary volume are also imagined in the twenty six periodically duplicated volumes around the primary. The segments in the primary volume elastically interacts with the segments in the duplicated volumes and vice-versa. The PBC has been implemented in the present DD code [27, 92].

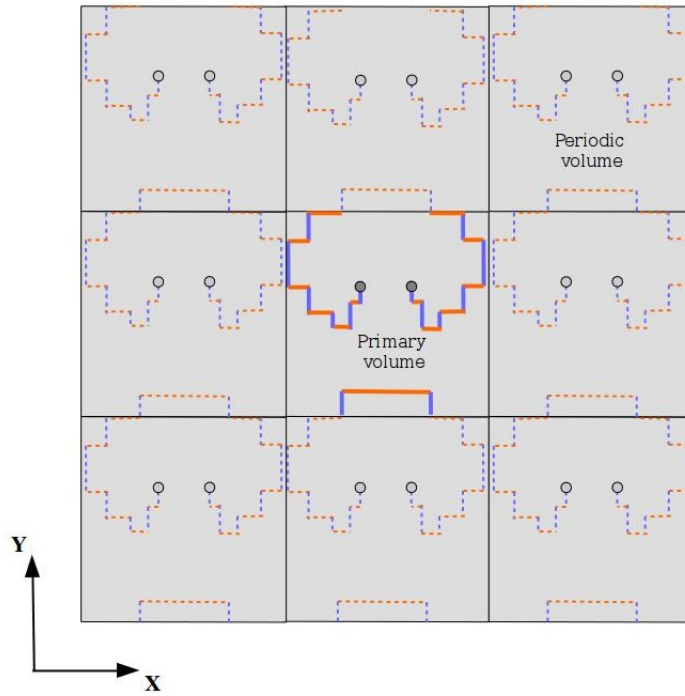


Figure 4.3 – A Frank-Read source in a 2D system with periodic boundary condition

4.2.4 Superposition principle: modification to finite domain

The solution for the 3D stress field of a dislocation segment was given for a homogeneous material in an infinite domain under the assumption of isotropic elastic framework [39, 45, 125]. The use of such stress field expression for thin films is no longer possible for two reasons:

4.2. Computation of heterogeneous stress field in a volume containing dislocations

1. Validity of stress field only in infinite domain
2. Anisotropic nature of a polycrystalline film

The problem involving finite domain (displacement and traction boundary conditions) was addressed based on the *principle of superposition* [134]. According to this principle, any finite domain problem can be calculated by superimposing the solutions of the two sub-problems:

$$\boldsymbol{\sigma} = \boldsymbol{\sigma}_{int} + \boldsymbol{\sigma}_{ext} \quad (4.2)$$

- a. infinite domain sub-problem $\boldsymbol{\sigma}_{int}$ with dislocations and external boundary conditions;
- b. a finite domain boundary value problem $\boldsymbol{\sigma}_{ext}$ with corrected boundary conditions.

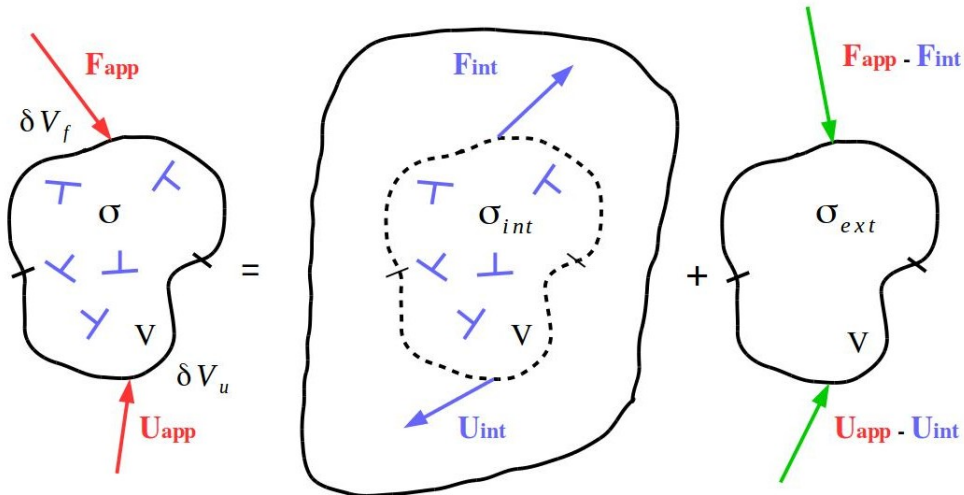


Figure 4.4 – Superposition principle used to deal with complex boundary conditions

If Figure 4.4 represents an original finite domain problem containing dislocations, applied displacement field \mathbf{U}_{app} on the surface δV_u and traction boundary conditions \mathbf{F}_{app} on the surface δV_f . The stress field $\boldsymbol{\sigma}$ at every point in the volume V can be accurately calculated by first calculating $\boldsymbol{\sigma}_{int}$ from the first sub-problem containing dislocations. The classical internal stress field expression of a dislocation in infinite domain, which is the core of all DD codes (TRIDIS), can be used in

Chapter 4. Methodology of discrete dislocation dynamics simulations

this case. Displacements \mathbf{U}_{int} on the surface $\delta\mathbf{V}_u$ and forces \mathbf{F}_{int} on the surface $\delta\mathbf{V}_f$ are produced due to the dislocations in the volume \mathbf{V} . In order to correct the displacement and traction incompatibilities on the boundary surfaces (second sub-problem σ_{ext}), the elastic and continuum boundary value problem with no dislocation and under an effective forces $\mathbf{F}_{app} - \mathbf{F}_{int}$ and effective displacement $\mathbf{U}_{app} - \mathbf{U}_{int}$ on the surfaces $\delta\mathbf{V}_f$ and $\delta\mathbf{V}_u$ respectively is solved using a finite element method (here with the FE code, CASTEM) [26].

The DD-FEM coupling between TRIDIS and CASTEM has been implemented in earlier works to deal with free surfaces during nanoindentation simulations of Cu single crystal [62]. In the present thesis, the DD-FEM coupling was further extended to deal with polycrystalline thin films. With such an extension, it is feasible to accurately account for the anisotropic nature of the polycrystalline materials while performing thin film simulations (*cf.* Chapter 6).

4.3 Prediction of the mobility of a dislocation

4.3.1 Mobility laws for a dislocation

The velocity with which a dislocation can glide is computed by a linear mobility law in FCC crystals. According to the mobility law, velocity of discrete dislocation segment is linearly related with the effective stress on the segment times its Burgers vector and inversely related to the phonon drag coefficient. Due to the constrictions laid by the edge-screw discretization scheme, the direction of the velocity of a dislocation segment is always perpendicular to its line direction.

$$v = \frac{\tau_{eff}b}{B} \quad (4.3)$$

where the phonon drag coefficient, B is a material and temperature dependent parameter. At room temperature, $B = 1.5 \times 10^{-5} Pa.s$ for Cu is used as reference to calculate the B values for which-ever material we use [142]. In the case of Pd, $B = 1.1 \times 10^{-5} Pa.s$ has been used. A maximum value of velocity equal to the speed of sound ($v_{max} = 2000m/s$) is used in the simulations to ensure the segment not to glide over large distances.

4.3.2 Effective stress on a dislocation

The effective stress, τ_{eff} required to move a dislocation segment is given by the following equation

$$\tau_{eff} = \tau' - \text{sign}(\tau') \cdot \tau_{Peierls} \quad (4.4)$$

$$\tau' = \tau + \tau_{lt} \quad (4.5)$$

$$\tau_{lt} = \frac{\mu b}{4\pi(1-\nu)R} (1 - 2\nu + 3\nu \cos^2 \theta) \left[\ln \left(\frac{L}{2b} \right) - \nu \cos(2\theta) \right] \quad (4.6)$$

where μ and ν are the shear modulus and Poisson's ratio of the material respectively. R being the radius of curvature, L is the length of the segment and θ is the angle between Burgers vector, \mathbf{b} and line direction of the dislocation.

4.3.3 Peierls stress

Dislocations generally move by breaking and making bonds at the dislocation core. Dislocations experience certain resistance every time they move an atomic distance. A correspondingly stress value is generally needed to overcome this lattice friction. This stress is called *Peierls stress*, $\tau_{Peierls}$.

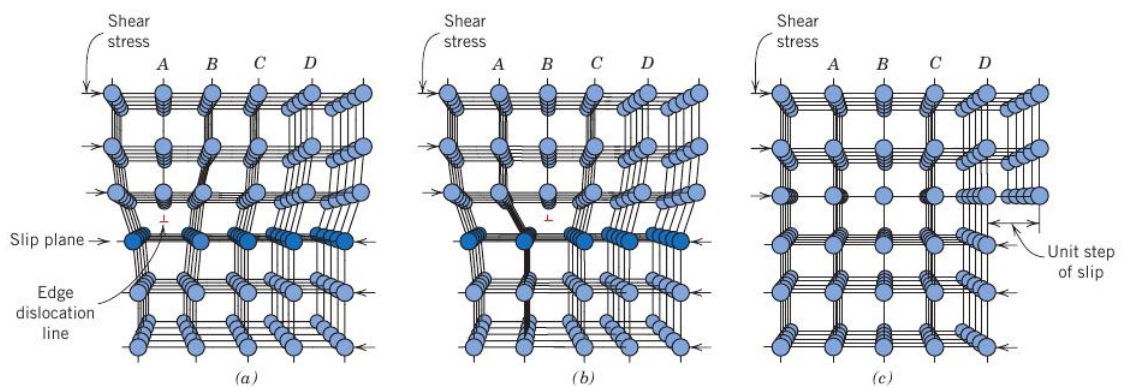


Figure 4.5 – Dislocation motion by breaking and making bonds [36]

The *Peierls stress* is negligible for FCC materials showing no directionality in the bonding (thermal energy at room temperature is way higher). In such

Chapter 4. Methodology of discrete dislocation dynamics simulations

cases, $\tau_{Peierls}$ of the order $10^{-5}\mu$, where μ is the shear modulus of the material; are considered. But, in BCC and DC materials, a certain sense of directionality of bonding is observed at low temperatures. A relatively high stress is required to overcome the lattice friction of these materials. In such cases, dislocation motion to overcome the Peierls barrier is thermally activated and is modelled as kink-pair mechanism. The stress, τ' in Equation 4.4 is generally written as the sum of resolved shear stress, τ from Equation 4.5 and stress due to line tension, τ_{lt} in Equation 4.6.

4.3.4 Line tension on a dislocation

Dislocation being a linear defect, carries a stress field. Because of the self stress field, every dislocation has an energy per unit length or *line tension*, τ_{lt} . A dislocation with no external force acting on it will exhibit a straight line configuration. If an external stress applied is greater than the line tension of the dislocation, then a dislocation bows out of the original equilibrium state and continues to do so by Frank-Read mechanism.

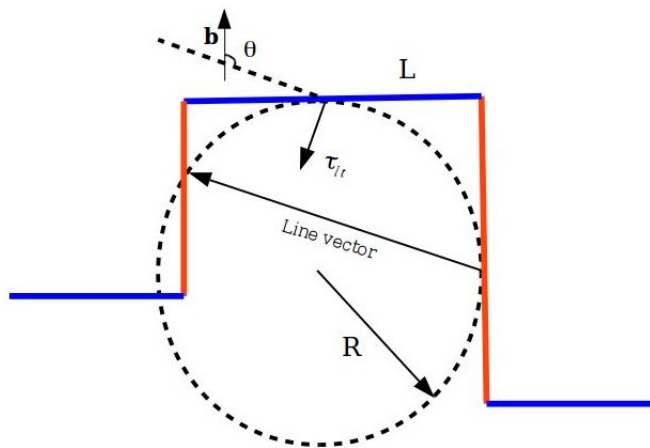


Figure 4.6 – Schematics of neighbouring segments (orange color) used to find the angle between Burgers vector and line vector; which in turn is used for line tension calculating

Accounting for the difference in energies of a screw and edge dislocation, a general formula (cf. Equation 4.6) for line tension has been proposed by Foreman [68]. As shown in Figure 4.6, neighbouring segments (in orange color) are taken into account for the calculation of θ .

4.3.5 Peach-Koehler force

The *resolved shear stress*, τ (cf. Equation 4.5) on the plane is deduced by projecting the force in the glide direction, \mathbf{g} .

$$\tau = \frac{1}{b} \mathbf{F}_{pk} \cdot \mathbf{g} \quad (4.7)$$

Peach and Koehler [127] derived a general expression for determining the force acting on a dislocation segment on a slip plane. If a stress, $\boldsymbol{\sigma}$ is being applied on a dislocation of Burgers vector \mathbf{b} and line vector $\boldsymbol{\zeta}$, then the Peach-Koehler force (\mathbf{F}_{pk}) on the segment is given by

$$\mathbf{F}_{pk} = (\boldsymbol{\sigma} \cdot \mathbf{b}) \times \boldsymbol{\zeta} \quad (4.8)$$

where, $\boldsymbol{\sigma}$ is the sum of external applied stress $\boldsymbol{\sigma}_{app}$; $\boldsymbol{\sigma}_{img}$ which accounts for the image stresses due to dislocation segments leaving the volume through the free surface (cf. Section 4.2.4) and total internal stresses, $\boldsymbol{\sigma}_{int}$ due to all the dislocation segments in the volume. Internal stress field due to dislocations in a simulation volume is the most important point of the dislocation dynamics codes and is discussed in detail in the Section 4.2.2.

4.3.6 Local hardening rules

Dislocation segments moving under effective stress may encounter other dislocations and interact with them to minimize energy. Depending on the Burgers vector and glide plane, dislocations may annihilate, cross-slip or form a junction with the meeting dislocation. These processes will have their influence on the strain hardening.

Annihilation of two dislocations as shown in Figure 4.7 occurs when the dislocation i detects another dislocation j of the same Burgers vector as i , but of opposite sign. Annihilation of dislocations i and j results in a dislocation network as shown in Figure 4.7.

Junctions are formed between dislocations m and n on different slip planes if a simple energetic condition (*Frank's rule*) in Equation 4.9 is satisfied. The

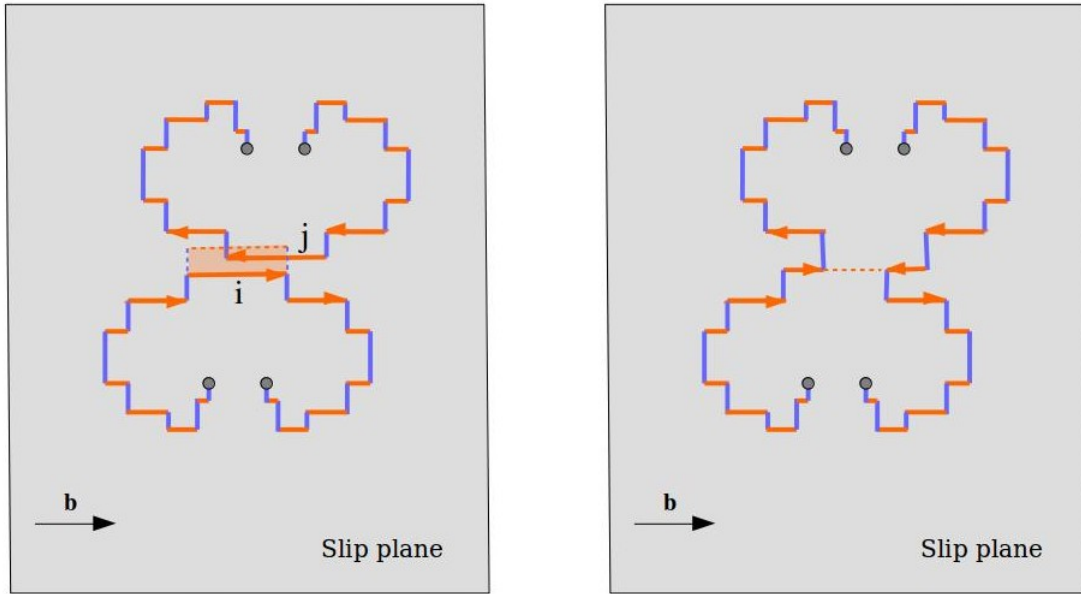


Figure 4.7 – Annihilation: Dislocation i detects dislocation j of same Burgers vector but opposite sign (vice-versa possible)

energetic condition reads:

$$b_m^2 + b_n^2 > (b_m + b_n)^2 \quad (4.9)$$

Four non-coplanar junctions which mainly contribute to the strain hardening behavior of FCC crystals, are accounted in the present DD code.

1. *Collinear junction*: $b_m = b_n$ are on different slip planes
2. *Hirth lock*: $b_m \perp b_n$ and are on different slip planes
3. *Glissile junction*: resultant of $b_m + b_n$ is glissile and lies on either of the slip planes (glissile interaction is not accounted by *TRIDIS*. Nodal code can tackle these types of junctions [51])
4. *Lomer-Cottrell lock*: resultant of $b_m + b_n$ is sessile and lies on either of the slip planes

Cross-slip of a screw dislocation segment is a thermally activated mechanism. The cross-slip model proposed by Bonneville and co-workers [54] has been used in the code. A probabilistic law is used to model the glide procedure on deviate plane. At every time step, the probability for a screw dislocation

4.3. Prediction of the mobility of a dislocation

segment to glide on its corresponding deviatoric plane is calculated using the expression:

$$P_i = \beta \frac{l}{l_o} \frac{\Delta t}{t_o} \exp\left(\frac{\tau_{dev} - \tau_{III}}{kT} V_{act}\right) \quad (4.10)$$

where β is the normalisation coefficient which makes sure $P_i \in [0 - 1]$, $\frac{l}{l_o}$ is the ratio of length of the discrete screw segment to the reference length ($l_o = 1\mu m$), $\frac{\Delta t}{t_o}$ is the ratio of time step to the reference time ($t_o = 1s$), τ_{dev}, τ_{III} are the resolved shear stress on the deviate plane and the reference stress value respectively. k , V_{act} and T are Boltzman constant, activation volume and temperature respectively.

Cross-slip of a screw segment is possible if the computer generated random number $n < P_i$. In the present DD code, numerical implementation of cross-slip has been carried out [186].

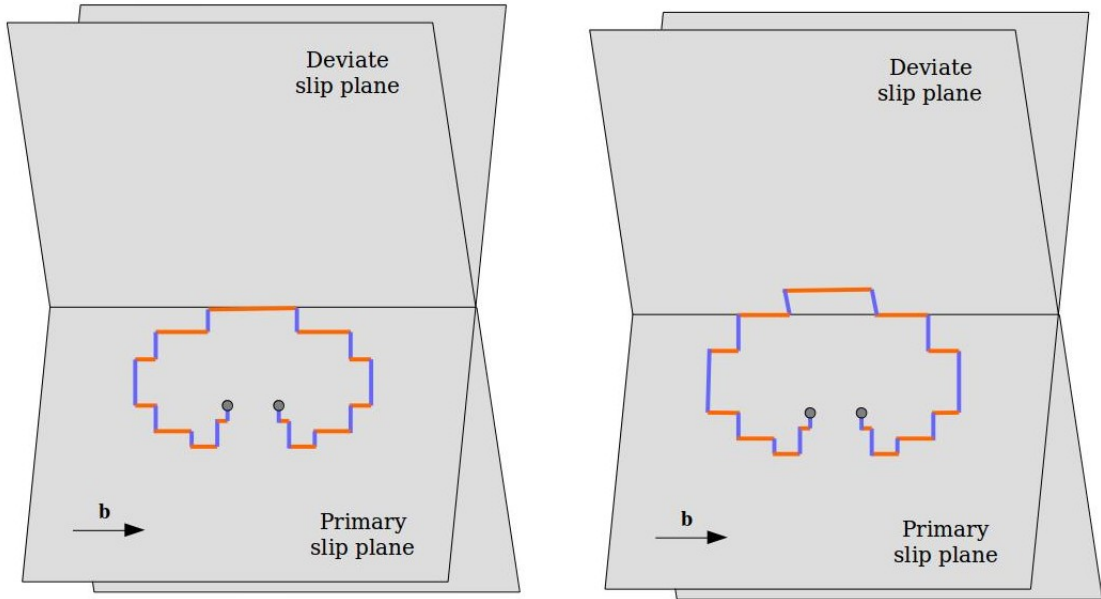


Figure 4.8 – Cross-slip of a screw segment

4.3.7 Dislocation-grain boundary interaction

In addition to the local hardening rules in a grain, dislocation-grain boundary interactions become more important when modeling polycrystals. In the present DD model (TRIDIS), grain boundaries are considered as infinitely strong obstacles (i.e.,

dislocations are stopped at the grain boundary) to dislocations and we employed a similar assumption for the DD simulations carried out in Chapter 5 and Chapter 6.

4.3.7.1 3D DDD modeling of grain boundaries

In the polycrystalline DDD code, grain boundaries are modeled as *facets*. These facets divide grains/crystals of different orientations. A bicrystal is modeled for the present study. A texture object¹ represents the lattice orientation of the grain separated by a grain boundary is shown in the Figure 4.9.

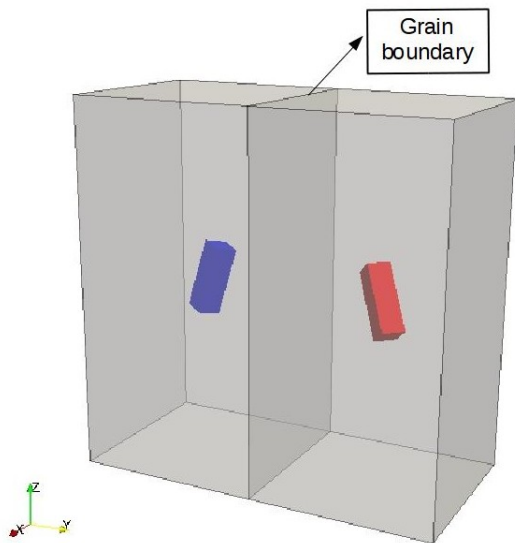


Figure 4.9 – Bicrystal with grains in different orientations separated by grain boundary; lattice orientation being represented by a coloured texture object

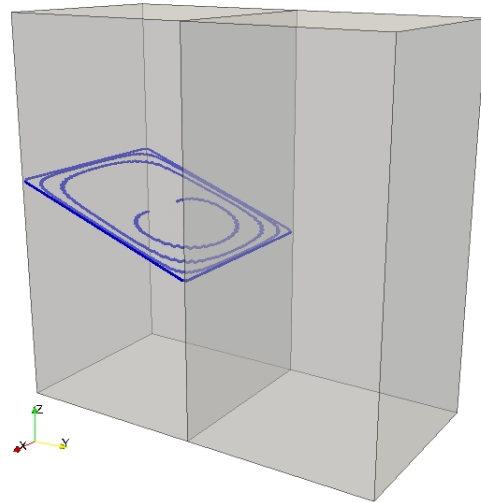


Figure 4.10 – Pileup of dislocations against a grain boundary

In polycrystals, grain of different orientations are separated by grain boundaries. Apart from the influential long range stress field of dislocations across grain boundaries, dislocations can also interact with grain boundaries. Especially in nanoscale materials such as thin films, high density of interfaces will influence the plastic deformation behavior. As a first step in understanding such materials, grain boundaries can be assumed as strong obstacles, similar to the assumptions used for a micron-sized single grain. But, eventually, this assumption need to be replaced/modified with more realistic rules at grain boundaries.

¹the coloured, rotated cuboid present inside each grain

4.3. Prediction of the mobility of a dislocation

The main motivation for this study is to incorporate slip transmission as local rule across grain boundaries in 3D DDD code (TRIDIS). Different approaches followed in the DD community for modeling dislocation grain boundary interactions are reviewed in Section 1.2 of Chapter 1. A *new resultant dislocation loop (RDL) method* is used to model slip transmission as generic rule in TRIDIS. To take advantage of the results from atomistic/quasicontinuum simulations performed by several groups on dislocation-coherent twin boundary interaction [28, 81, 177], a coherent twin boundary configuration in a bicrystal is setup to validate the implementation of the *RDL* method. Finally, the improvements that are planned to the *RDL* model are also presented.

4.3.7.2 Resultant dislocation loop (RDL) method

Dislocation slip transmission across grain boundaries can be incorporated as local rules in conventional lattice based DD codes without dissociating a dislocation at the grain boundary. Slip transmission across any grain boundary can be generally modelled by placing a *glissile loop* of corresponding resultant Burgers vector in the adjoining grain as shown in Figure 4.11. When a dislocation segment $+\mathbf{b}$ in Grain1 carrying a resolved shear stress which is higher than a critical value τ_{gb}^c hits a grain boundary, a resultant glissile loop is inserted at the corresponding lattice coordinate in Grain2. The resultant loop being placed will behave as if the dislocation segment is already transmitted across the grain boundary. One advantage of this method is that the Burgers vector remains always conserved. Further, a compatibility of the stress field at the grain boundary can be easily maintained and verified.

4.3.7.3 Simulation setup for modeling slip transmission across GB

A simple bicrystal configuration had been setup to validate the *RDL* method explained in the above section. Of the two grains in the bicrystals, the first grain is rotated with Euler angles of [0.0 35.264 -135.0] and the second grain with Euler angles of [180.0 35.264 -135.0] and the rotations are represented correspondingly by coloured texture objects in Figure 4.12. For these set of Euler angles, (111) is the common plane (*cf.* Figure 4.15) between two grains and can be addressed as coherent twin boundary.

The three perfect screw dislocations, $\mathbf{b}_1 = \mathbf{BA}$, $\mathbf{b}_2 = \mathbf{CA}$ and $\mathbf{b}_3 = \mathbf{CB}$, on the common plane are as shown in Figure 4.14. A schematic view of slip plane

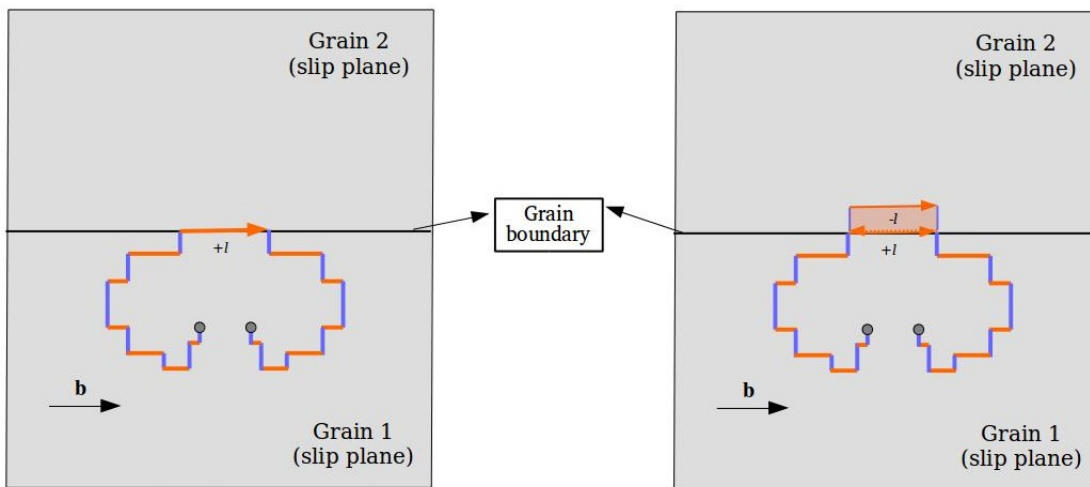


Figure 4.11 – Schematic view of a Glissile loop being placed at corresponding lattice point in Grain2 (to mimic transmission) after hitting the grain boundary

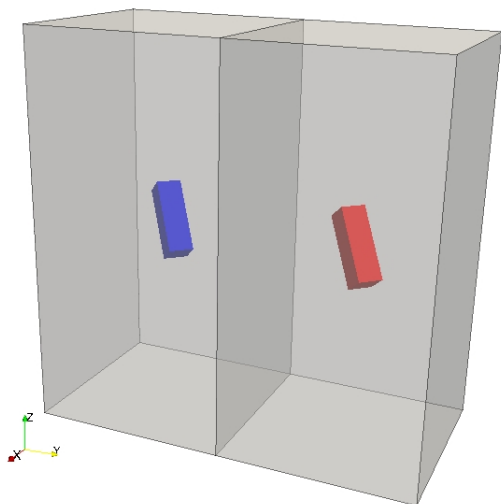


Figure 4.12 – Schematic view CTB setup with texture objects representing the lattice orientation of grains

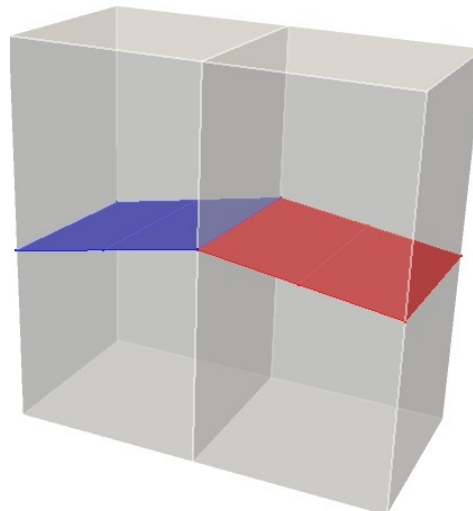


Figure 4.13 – Schematic view slip planes corresponding to \mathbf{b}_1 in Grain1 and Grain2 of the Bicrystal

4.3. Prediction of the mobility of a dislocation

corresponding to \mathbf{b}_1 in both the grains is shown in Figure 4.13. When a dislocation with any of the above three Burgers vectors hits the coherent twin boundary, they can be transmitted without leaving a residu at the twin boundary plane (CTB). Hence, the stress field on the boundary will not have any impact if the *RDL* method is correctly implemented. This configuration is used for validating the implementation of the *RDL* method.

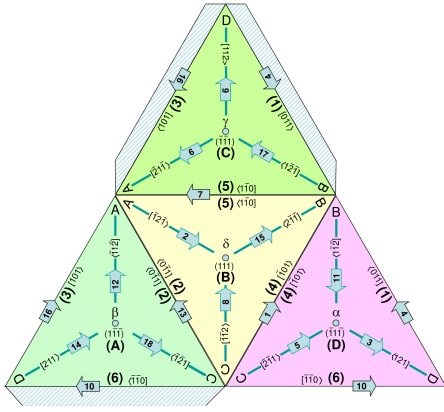


Figure 4.14 – Thompson tetrahedron representing all the slip planes and vectors in a FCC crystal

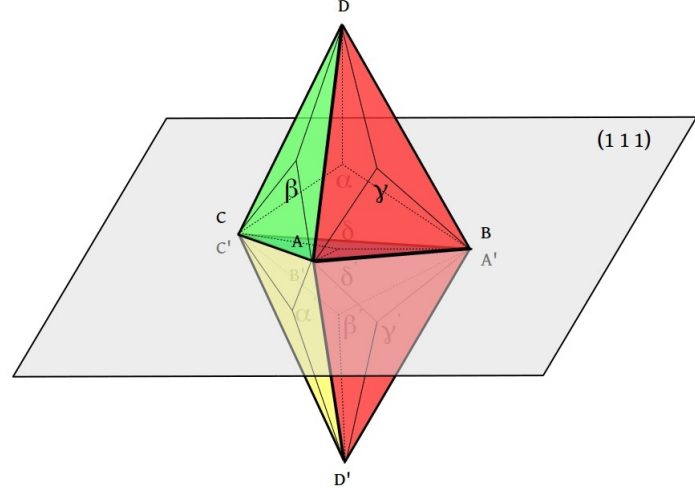


Figure 4.15 – Schematic view of a double Thompson tetrahedron with (111) common slip plane

Material parameters of Ni (*cf.* Section 5.2.4 of Chapter 5) were chosen for all the simulations. A strain rate $\frac{d\epsilon}{dt} = 100s^{-1}$ is monitored during the simulation and the external stress tensor applied is:

$$\sigma_{ext} = \begin{bmatrix} 0 & 0 & \sigma_{yz} \\ 0 & 0 & 0 \\ \sigma_{yz} & 0 & 0 \end{bmatrix} \quad (4.11)$$

4.3.7.4 Validation of the *RDL* method: Stress field at coherent twin boundary

An initial dislocation source of Burgers vector $\mathbf{b}_1 = \frac{a}{2}[1 - 10]$ is placed in Grain1. Once the resolved shear stress on the slip plane exceeds a randomly chosen critical transmission stress $\tau_{gb}^c = 250MPa$, dislocation segment transmits into Grain2 via the *RDL* method. The step for which a dislocation segment still does not

Chapter 4. Methodology of discrete dislocation dynamics simulations

meet the stress criteria and only piles up against CTB is referred to as **step P**. Snapshots at different simulation steps starting from the point when a dislocation segment satisfies the stress criteria are referred to as **step P**+ T_n , where n indicates different simulation step proceeding the pileup (**step P**). Further, the stress field corresponding to the snapshots are also presented.

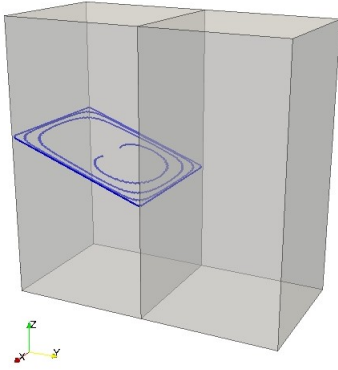


Figure 4.16 – Pileup against the CTB (for $RSS < \tau_{gb}^c$) at **step P**

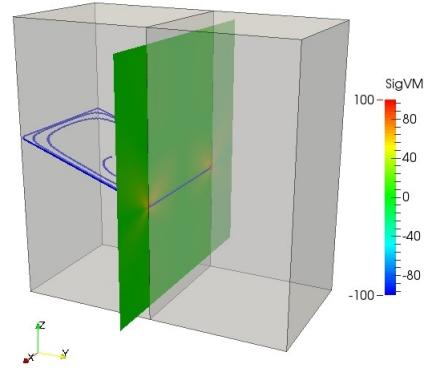


Figure 4.17 – Stress field on the CTB due to pileup at **step P**

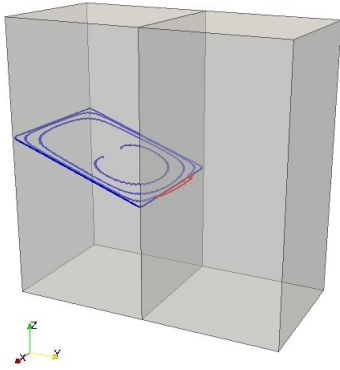


Figure 4.18 – Slip transmission across CTB (for $RSS > \tau_{gb}^c$) at **step P**+ T_1

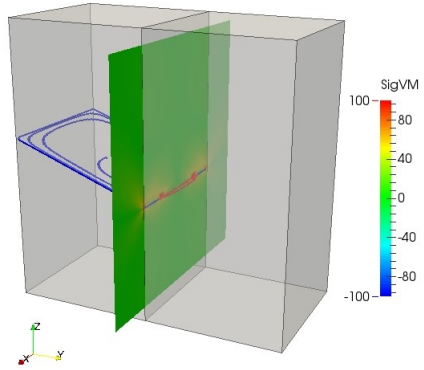


Figure 4.19 – Stress field on the CTB after transmission at **step P**+ T_1

By looking at the stress field at different simulations steps during transmission it is clear that the resultant dislocation loops were placed at the right lattice positions in Grain2. The small discrepancy in the stress field arises at the corner of the Grains as the stress field of the discretized edge segment at the corners is not accounted for in the present implementation of the *RDL* method. This error can be minimized by accounting for the stress field of the edge segments specially at corners of the grains. But, such an edge stress field correction is non-unique due to the dependency not only on the discretization scheme but also on the grain

4.3. Prediction of the mobility of a dislocation

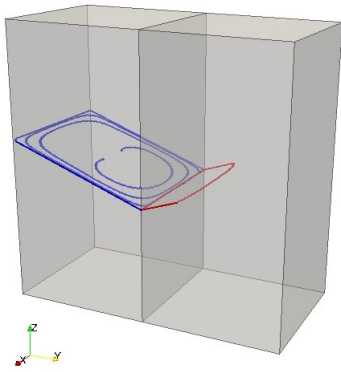


Figure 4.20 – Slip transmission across CTB (for $RSS > \tau_{gb}^c$) at **step $\mathbf{P}+T_2$**

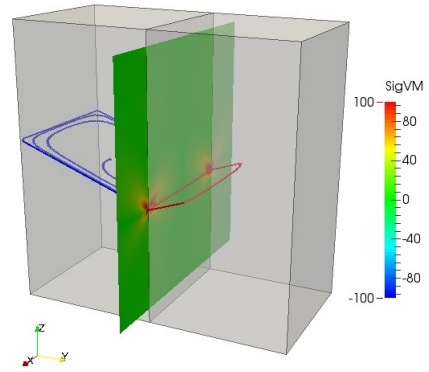


Figure 4.21 – Stress field on the CTB after transmission at **step $\mathbf{P}+T_2$**

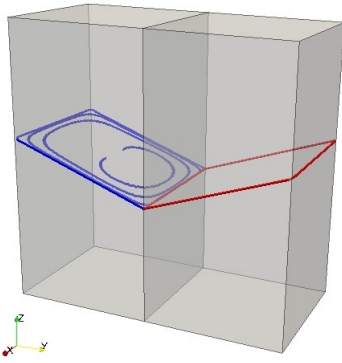


Figure 4.22 – Slip transmission across CTB (for $RSS > \tau_{gb}^c$) at **step $\mathbf{P}+T_3$**

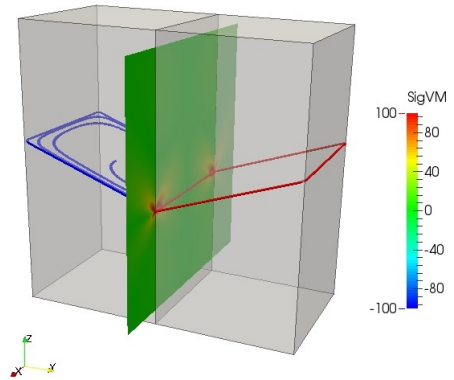


Figure 4.23 – Stress field on the CTB after transmission at **step $\mathbf{P}+T_3$**

Chapter 4. Methodology of discrete dislocation dynamics simulations

morphology. Implementing such stress-field corrections at the corners in TRIDIS (Edge-Screw model) is a tedious job.

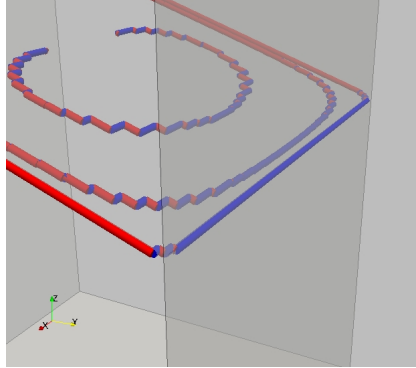


Figure 4.24 – Distance between subsequent loops in a pileup (Edge and Screw segments in red and blue colors, respectively)

The stress field of a dislocation piled up against the boundary create a back stress on the subsequent dislocation loop approaching the primary dislocation loop. Figure 4.24 shows the subsequent dislocation loop being stationed at certain distance due to back stress created by the primary dislocation loop. During the slip transmission via *RDL* method, the stress field created by a dislocation at the grain boundary is cancelled and the subsequent dislocation loops are allowed to reach the grain boundary. These event can be more clearly observed in the below series of zoomed (near grain boundary) images in Figures 4.25, 4.26, 4.27 and 4.28.

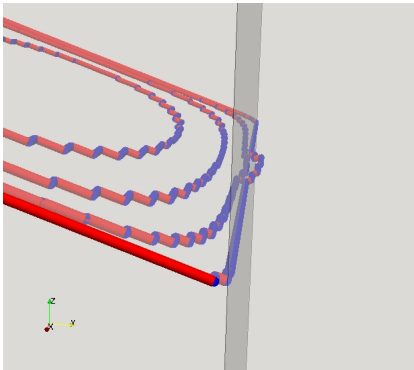


Figure 4.25 – Slip transmission across CTB at step $\mathbf{P}+T_1$



Figure 4.26 – Slip transmission across CTB at step $\mathbf{P}+T_2$

4.3.7.5 Directionality tests for slip transmission

Transmission events across a grain boundary should be independent of the direction of the Burgers vector and also the grain from which the dislocation segment interacts

4.3. Prediction of the mobility of a dislocation

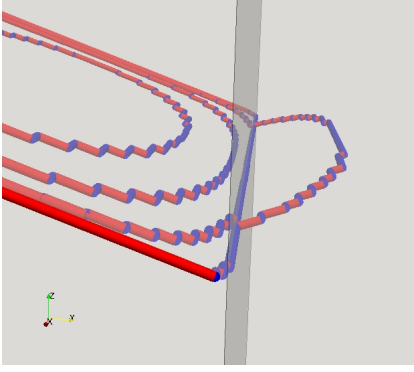


Figure 4.27 – Slip transmission across CTB at **step P**+ T_3

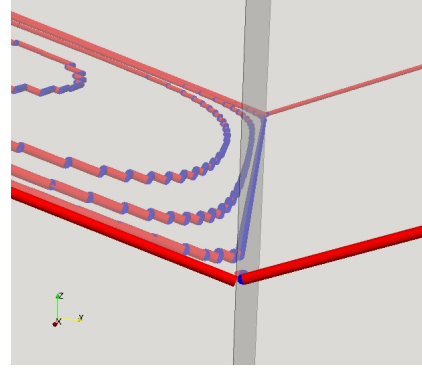


Figure 4.28 – Slip transmission across CTB at **step P**+ T_4

the common grain boundary. In order to test the directionality behavior, dislocation source of same magnitude but different directions are placed as initial dislocation sources in Grain1 first and then in Grain2. Four combinations of the directionality are tested by performing different simulations. The critical transmission stress is specified to be $\tau_{gb}^c = 200MPa$ for this case. Like in the above case, the snapshot of the step during which dislocations only pileup against the grain boundary is referred to as **step P**. All the later snapshots after transmission are referred to as **step P** + T_n , where n indicates n^{th} simulation step after pileup.

In **case 1**, a dislocation source of Burgers vector $\mathbf{b}_1^{(1)} = \frac{a}{2}[1 - 10]$ is initially placed in Grain1. As mentioned, slip transmission event is shown at different steps in Figure 4.29.

In **case 2**, a dislocation source of Burgers vector $\mathbf{b}_1^{(2)} = \frac{a}{2}[-110]$ is initially placed in Grain1. The slip transmission event is shown at different steps in Figure 4.30.

In **case 3**, a dislocation source of Burgers vector $\mathbf{b}_1^{(3)} = \frac{a}{2}[1 - 10]$ is initially placed in Grain2. As mentioned, slip transmission event is shown at different steps in Figure 4.31.

In **case 4**, a dislocation source of Burgers vector $\mathbf{b}_1^{(4)} = \frac{a}{2}[-110]$ is initially placed in Grain2. The slip transmission event is shown at different steps in Figure 4.32.

4.3.7.6 Information exchange between QC and DD

Now that the *RDL* method had been implemented successfully, a correct critical transmission stress value needs to be specified for the coherent twin boundary.

Chapter 4. Methodology of discrete dislocation dynamics simulations

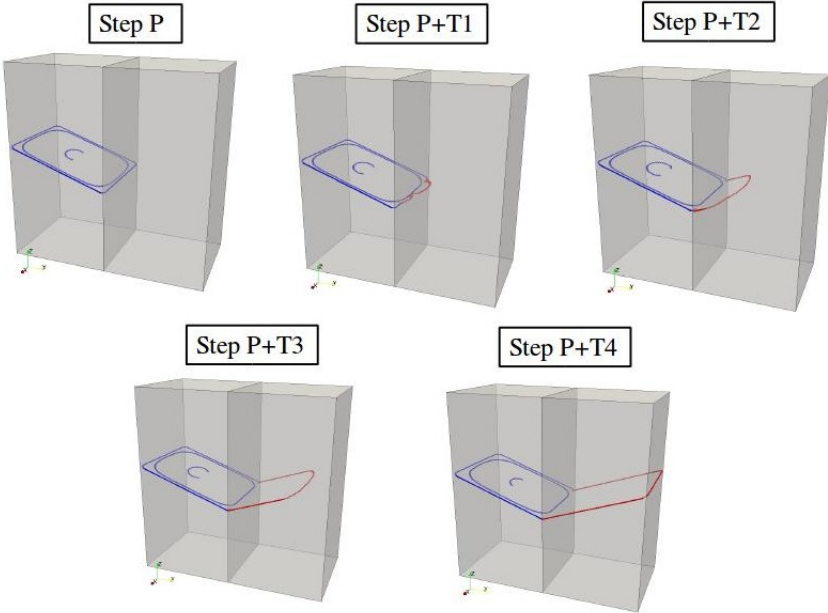


Figure 4.29 – Directionality test with initial dislocation source of Burgers vector ($\mathbf{b} = \mathbf{b}_1^{(1)}$) in Grain1

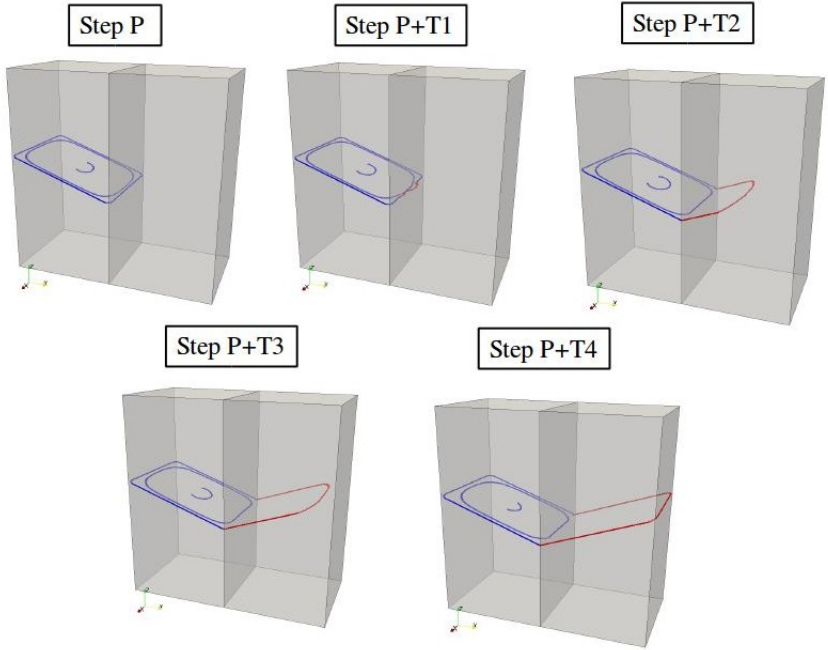


Figure 4.30 – Directionality test with initial dislocation source of Burgers vector ($\mathbf{b} = \mathbf{b}_1^{(2)}$) in Grain1

4.3. Prediction of the mobility of a dislocation

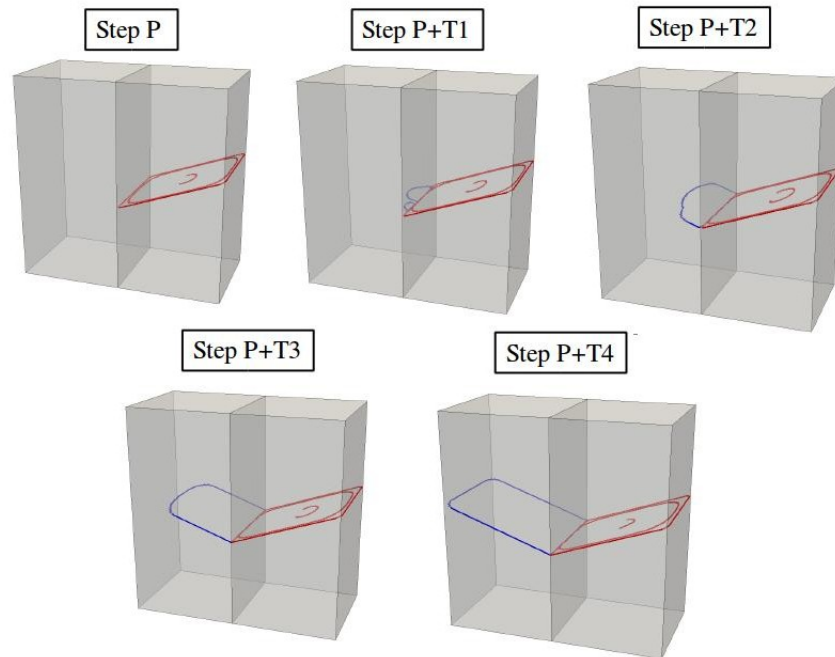


Figure 4.31 – Directionality test with initial dislocation source of Burgers vector ($\mathbf{b} = \mathbf{b}_1^{(3)}$) in Grain2

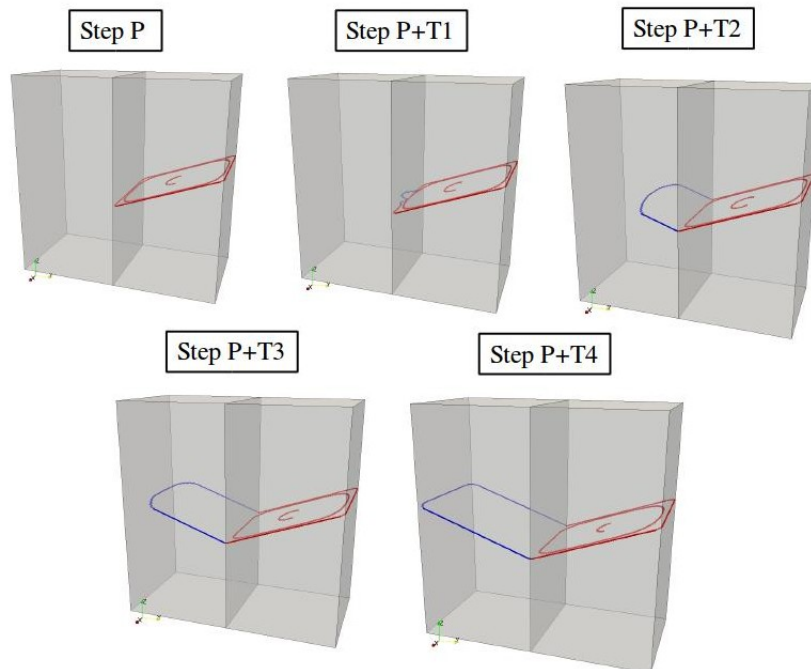


Figure 4.32 – Directionality test with initial dislocation source of Burgers vector ($\mathbf{b} = \mathbf{b}_1^{(4)}$) in Grain2

Chapter 4. Methodology of discrete dislocation dynamics simulations

In general, such a critical transmission stress value is taken from literature or by performing atomistic simulations. Instead of using atomistic simulations to predict the critical transmission stress for a screw dislocation across a coherent twin boundary, firstly, QC simulations were performed. A control box method has been used to extract the resolved shear stress on the slip plane during the first slip transmission event. For complete details about the QC simulation setup and the method used to extract critical stress, readers are directed to the paper [177]. QC simulations predict a critical transmission stress value of $\tau_{gb}^c = 605 MPa$ for a perfect screw dislocation.

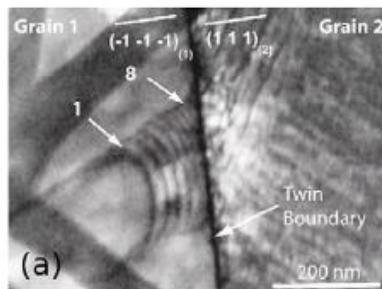


Figure 4.33 – *In situ* TEM image showing the absorption and emission of dislocation across CTB in Cu [28]

A very important task apart from working with numerical materials modeling tools at different length- and time- scales is the *exchange of information between the scales*. In any hierarchical multiscale modeling approach, correction information that needs to be transferred should be identified and then assessed if the direct use of the information in numerical technique at different length scale is valid. In this section, a similar kind of task had been performed for exchanging information (i.e., critical transmission stress across coherent twin boundary) between Quasi-continuum (QC) simulations and dislocation dynamics (DD). Experimentally, it is feasible to count the number of dislocation loops in a pileup by looking at TEM images as shown in Figure 4.33. Eventhough, there have not been any experiments performed during this study, the idea is to develop a simple mathematical expression that can predict number of dislocation loops that should be required to build the stress level in a pileup for the first transmission event to occur. A modified pileup-based formula (developed by Tran [177]) was used to predict the number of dislocation loops before first slip transmission event to take place at a given critical transmission stress value predicted by QC. A critical transmission stress $\tau_{gb}^c = \sim 600 MPa$, as predicted by QC simulations was used in the present DD simulations. For different grain sizes and different dislocation lengths DD simulations predict different number of

4.3. Prediction of the mobility of a dislocation

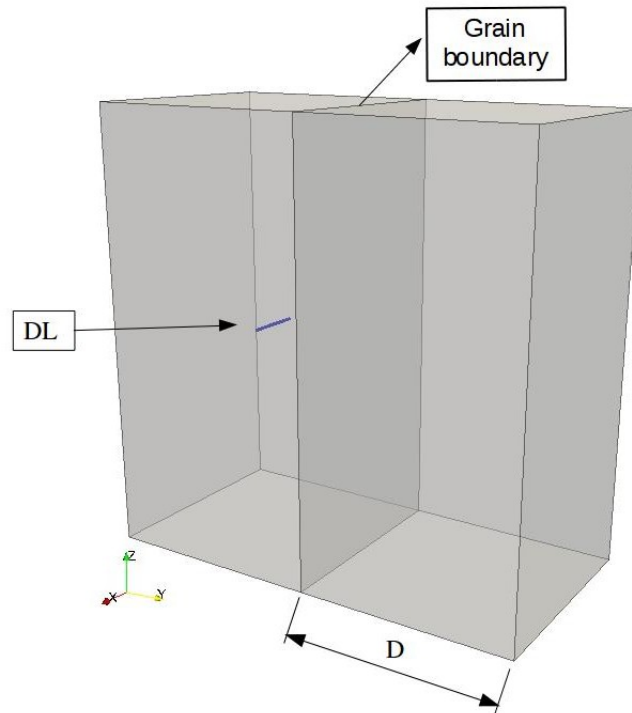


Figure 4.34 – Bicrystal indicating the introduced general convention of the grain size (D) and dislocation segment length (DL)

dislocation loops in a pileup (*cf.* Table 4.1) for initiation of the first slip transmission event. In the table, **GS** indicates grain size (D) information in the first column and **DL** represents *dislocation length* written in terms of the grain size in the first row.

GS/DL (nm)	0.1D	0.15D	0.2D	0.3D	0.5D
D=1000	6	6	5	5	4
D=750	4	5	5	4	3
D=500	3	4	4	3	3
D=250	1	3	2	2	2

Table 4.1 – Number of loops before 1st slip transmission as predicted by DDD simulations

The classical pileup-based formula reads:

$$N_{classical} = \frac{\pi\tau_{trans}L}{\mu\mathbf{b}} \quad (4.12)$$

The derivations for both the classical and modified pileup-based formula used for

predicting number of dislocation loops in the pileup is presented in the paper [177] and the formula reads:

$$N_{modified} = \frac{\pi\tau_{trans}}{\mu\mathbf{b}}L \left[1 - \left(\frac{\tau_a^2}{\tau_{trans}^2} \right) \right] \quad (4.13)$$

where N is the number of dislocation loops in pileup, \mathbf{b} is the magnitude of Burgers vector, μ is the Shear modulus, τ_a is the activation stress for the Frank-Read source of length, L and τ_{trans} is the critical transmission stress predicted using QC simulations.

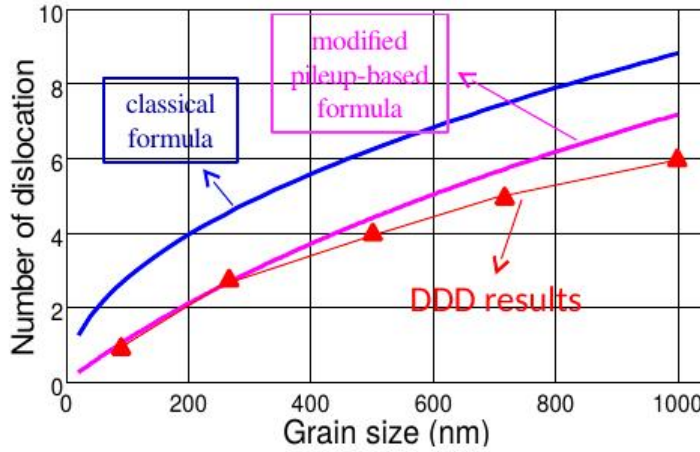


Figure 4.35 – Comparison of number of loops in pileup (modified pileup-based formula Vs DDD results) [177]

The predictions of the number of dislocation loops from DD simulations are compared against the predictions of the modified pileup-based formula for a dislocation source length ($DL=0.15D$) in Figure 4.35. The results predicted by the modified formula are in good agreement with the ones predicted by DDD simulations at a critical transmission stress of $\tau_{trans} = \tau_{gb}^c \approx 600MPa$.

4.3.7.7 Interface padding region: finite width of CTB

So far, implementation of the *RDL* method had been validated for slip transmission of only the first dislocation segment that hits the grain boundary. Figure 4.36 shows experimental evidence of subsequent events after the first transmission [99].

To model such a general behavior as slip transmission across grain boundary, a

4.3. Prediction of the mobility of a dislocation

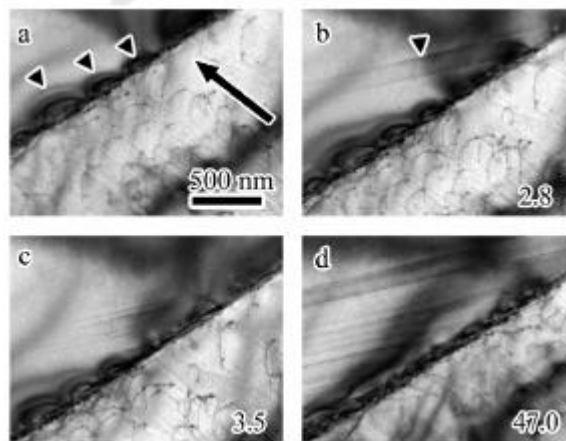


Figure 4.36 – *In situ* TEM image showing dislocation propagation across CTB in $\alpha - Ti$ [99])

finite width is specified for the grain boundary as show in the Figure 4.37. The region (coloured in orange) around the grain boundary is hereby referred to as *interface padding region (iPad)*.

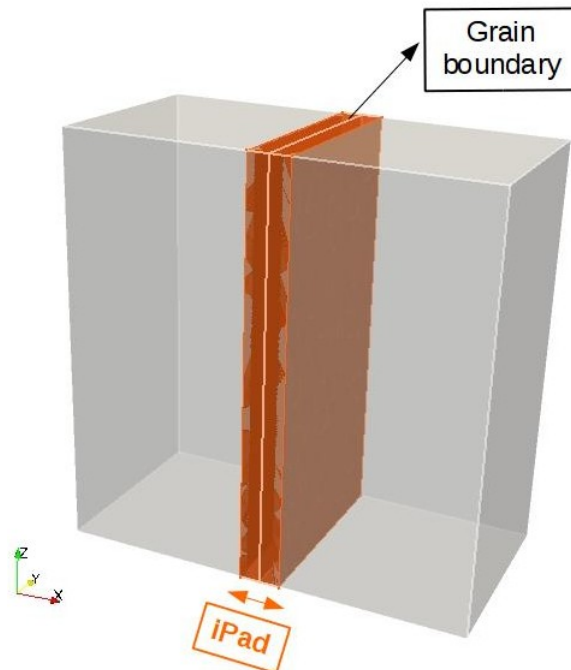


Figure 4.37 – Schematic view highlighting the interface padding region of a general width= $iPad$

Dislocation slip transmission across grain boundary is tested for different widths

Chapter 4. Methodology of discrete dislocation dynamics simulations

of the interface padding regions. DD simulations revealed that the number of emitted/transmitted dislocation loops remained constant (~ 3 or 4) for any $iPad \geq 3.xl$, where xl specifies lattice spacing. Looking at the stress-strain response it is clear that the first and second slip transmission occurred almost at the same stress value. But, a for the third slip transmission to occur, the dislocations had to overcome a much higher stress barrier. The higher stress barrier for the third slip transmission is due to the pronounced contribution of backstress from the already transmitted dislocation loops. The slip transmission as explained above can be seen in the Figures 4.38 and Figures 4.39 in which Von Mises stress and plastic strain are also plotted.

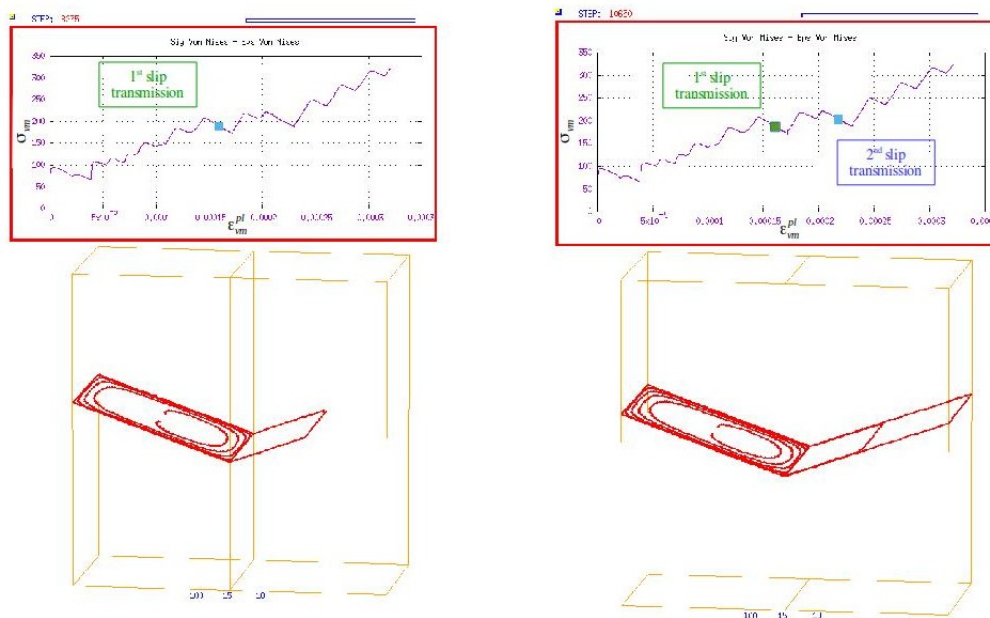


Figure 4.38 – Snapshots taken during first and second transmission (for $iPad=10.xl$) along with the corresponding points on the stress-strain plots are also indicated

4.3.7.8 Slip transmission after subsequent cross slip events

Dislocation piled up against a grain boundary, firstly, tries to relieve the stress concentration at the grain boundary by cross slip mechanism. If the stress still builds up even after subsequent cross slip events, then a slip transmission across the grain boundary may occur. Figure 4.40 highlights the occurrence of such cross slip events inside the grain; preceded by a transmission across grain boundary in 304 stainless steel.

4.3. Prediction of the mobility of a dislocation

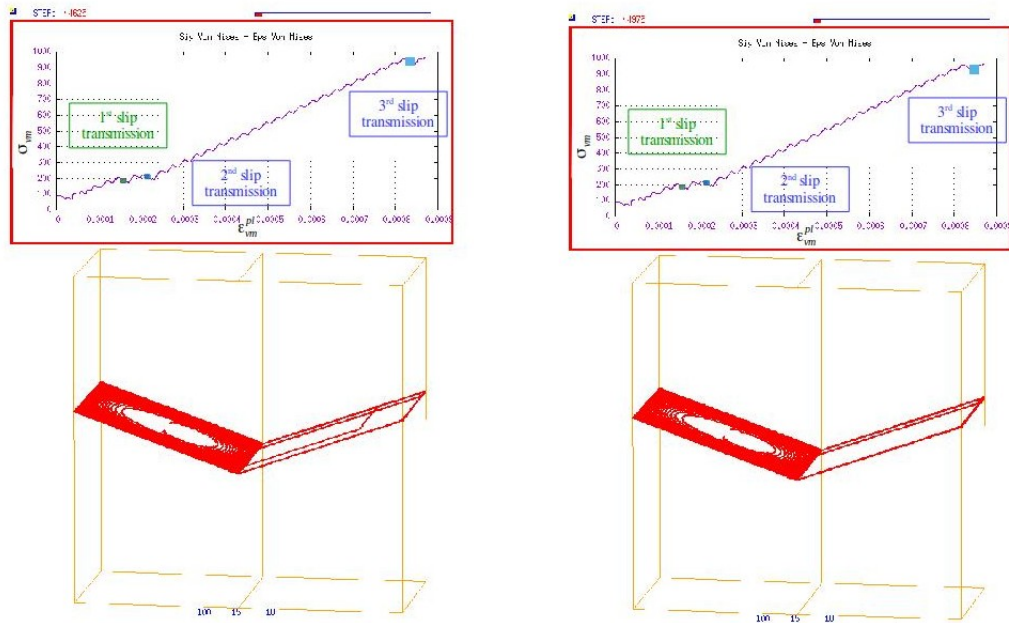


Figure 4.39 – Snapshots taken during and after the third transmission (for $iPad=10.xl$) along with the corresponding points on the stress-strain plots are also indicated

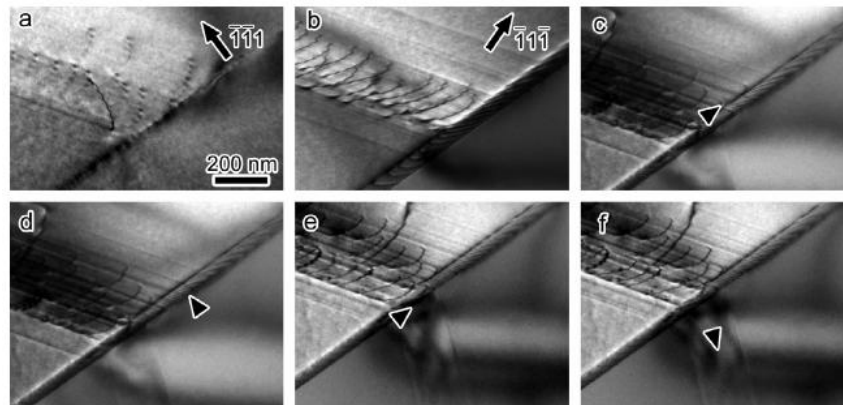


Figure 4.40 – *In situ* TEM image showing succession of cross slip events indicated by directional arrow (a-e) and final transmission across grain boundary in f in $\alpha - Ti$ [99])

Chapter 4. Methodology of discrete dislocation dynamics simulations

In DD simulations, the very first dislocation loop which comes in contact with the grain boundary (coherent twin boundary in our case) will stay put at the grain boundary in the parent grain. Here, parent grain is referred to the grain in which dislocation source is initially present. Subsequent dislocation loops in the pileup are free to relieve the stress concentration by cross slip mechanism as shown in Figure 4.41. Figure 4.42 depicts initiation of the slip transmission into neighbouring grain after subsequent cross slip events in the parent grain.

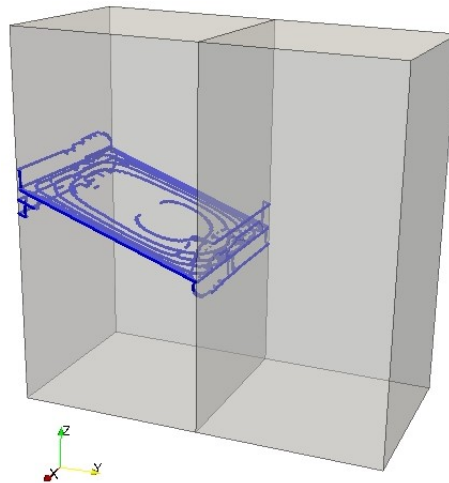


Figure 4.41 – First dislocation loop attached to the grain boundary; whereas the subsequent dislocation loops (2nd and 3rd) begin cross slipped

4.3.7.9 Perspective: Improving the RDL method

The perspective directions to improve this method in the DD codes is by following the list below.

1. Testing the *RDL* method for different misorientations (in bicrystal setup)
2. Improving the resultant stress field at the GB (by accounting also the stress field of edge segments)
3. Extension of the *RDL* method in order to deal with 60° dislocations.
4. Implementing new rules for dislocation nucleation at GB.
5. Large scale polycrystalline simulations to test the compatibility of the *RDL* method.

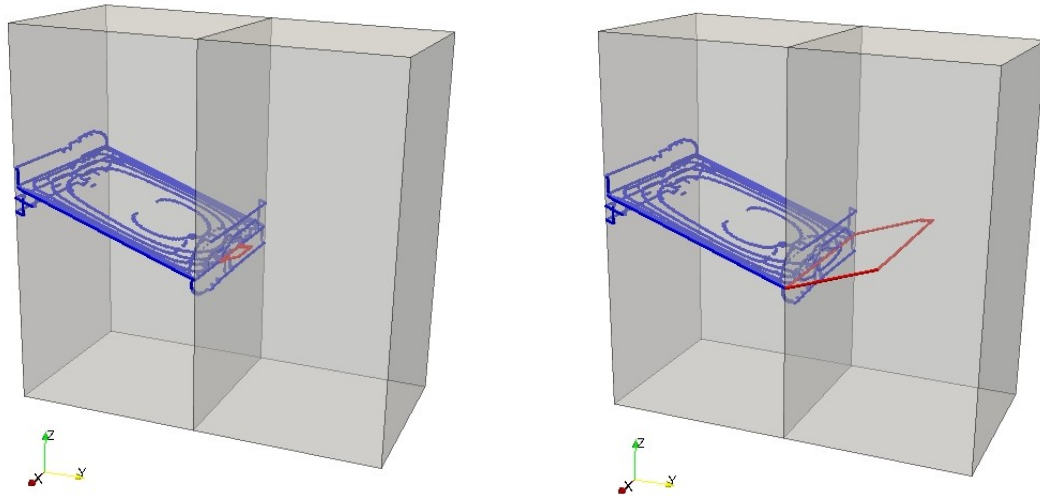


Figure 4.42 – Dislocation transmission across CTB after subsequent cross slip events in the parent grain

4.4 Numerical implementation of the DDD model

4.4.1 DDD algorithm

Except for the realisation of the polycrystal and of the rotated sub-lattice on which dislocation microstructure evolves, most of the steps in the DD algorithm in a polycrystal version remain similar to the single DD version. The complete polycrystalline DD algorithm is shown in a pictographic representation in Figure 4.43. Detailed explanation of the principles involved at each step are presented in different sections.

1. **Generation of the grains/crystals geometry** (grain volume, position, orientation)
2. **Generation of the dislocation microstructure in each grains/crystals** (For each dislocation segment, the properties to define include xyz coordinates, length of dislocation, Burgers vector, Glide plane, iprev connectivity and inext connectivity (-1 pinned), grain/crystal in which the dislocation segment belongs to) After generation of the polycrystal and initial dislocation microstructure, Start of DD STEP at time t)
3. **Discretize each dislocation line into edge and screw segments**
4. **Compute stress field due to each discrete dislocation segment**

Chapter 4. Methodology of discrete dislocation dynamics simulations

5. Motion of dislocation segment via Linear mobility law and Compute the effective plastic strain developed from all the dislocations in the polycrystal
6. Local interaction between dislocations
7. Interaction between dislocations and grain boundaries (Dislocation-Grain boundary rules) Proceed to next DD STEP at time $(t + \Delta t)$.

4.4.2 Integration scheme

Euler forward integration scheme is used to update the position of each dislocation segments. If d_i^t is the position of the dislocation at time t and Δt is the time, from the velocity calculated using the linear mobility law, the position of the dislocation can be updated to a new position $d_i^{t+\Delta t}$ as below:

$$d_i^{t+\Delta t} = d_i^t + v\Delta t \quad (4.14)$$

Time step, Δt should be carefully selected in order to avoid any unnecessary artefacts, such as drastic changes in the dislocation curvature.

4.4.3 Optimized stress field calculations

Several approaches have been proposed to tackle the computational issue of long-range stress field. The most widely used approaches are briefly presented below:

- **Box method** relies on the fact that the dislocation microstructure does not change much at every step in the volume. The simulation volume is divided into equally spaced voxels of side L . A 2D schematic is shown in Figure 4.44. The stress field inside each voxel is assumed to remain invariant for a short interval. Further, the coloured boxes indicate the short range interaction among dislocations which is updated more frequently than the interaction of dislocations in white boxes (long-range), which is updated at prescribed intervals. More information about the speedup using box method and the precision of stress field calculations are presented in detail in [186]. The box-method has been again reviewed and parallelized using a standard message passing interface (MPI) [164].

4.4. Numerical implementation of the DDD model

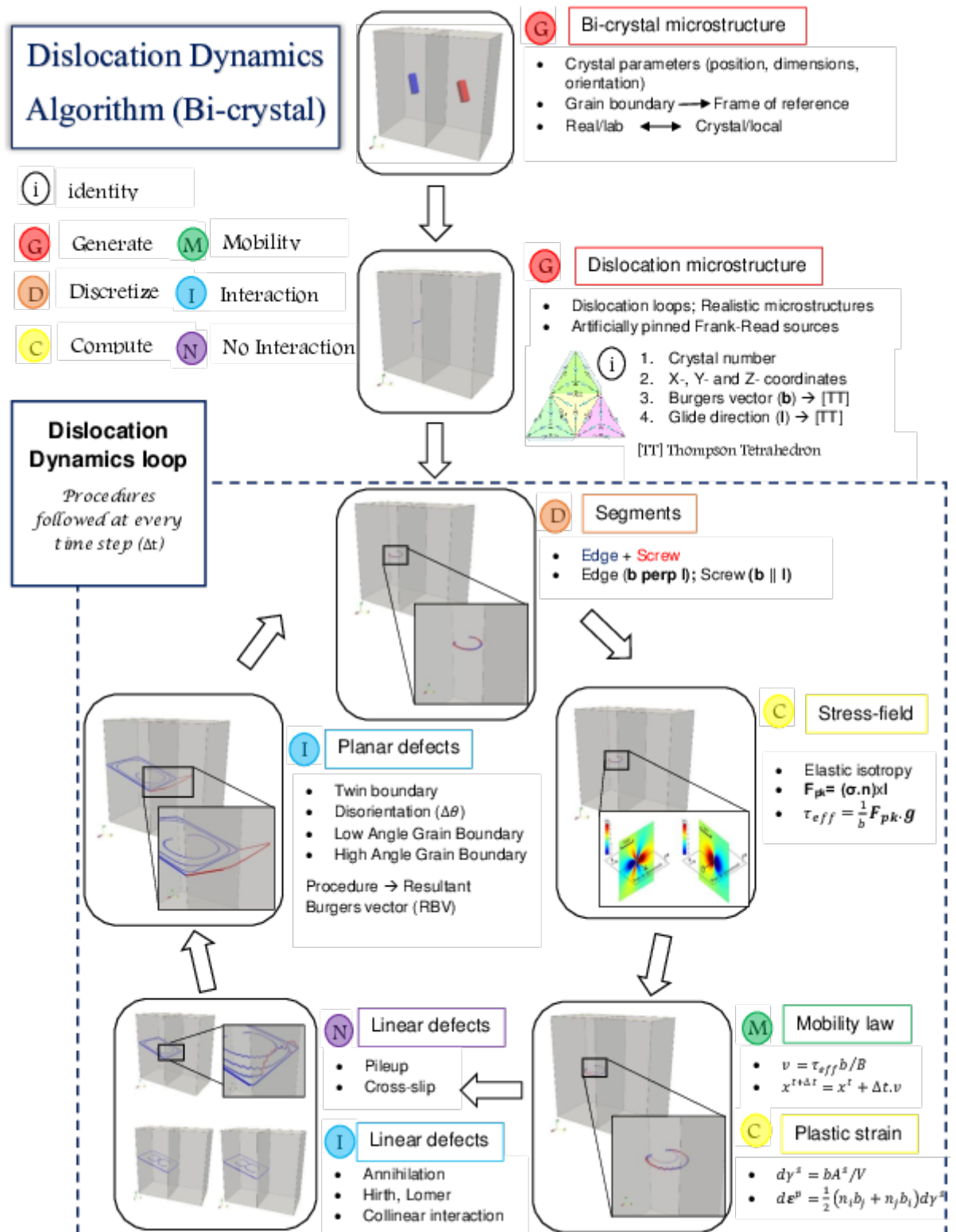


Figure 4.43 – 3D dislocation dynamics algorithm explained based on a bicrystal geometry

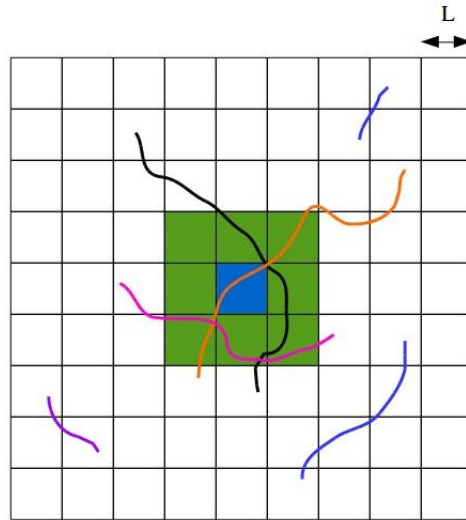


Figure 4.44 – Schematic view of the 2D box approach to segregate short- and long-range dislocation interactions

- **Fast multipole method (FMM)** is currently the most widely used method in DD simulations. It relies on Taylor series expansion to precisely account for the long-range field of dislocations. The expression developed by LeSar and Rickman [120] and Wang [191] were modified and implemented to further increase the computational efficiency [5].
- **DDD-FFT** is a more recently developed Fast Fourier Transforms based formulation for periodic discrete dislocation dynamics [12] to tackle the main issues of anisotropic elasticity and elastic inhomogeneities. Conventional DD codes which rely on a finite element method (FEM) to incorporate elastic inhomogeneities induce a much higher computational burden in-addition to the stress computations of DDD simulations. The main idea of the DDD-FFT approach relies on the computation of strains and stresses in the presence of dislocation segments in a periodic volume directly in the Fourier space. The transformation between the real Cartesian space and Fourier space is performed by the FFT algorithm. The coupled DDD-FFT and DCM (discrete continuous method) [184] approach showed pronounced speedup and inherent incorporation of long-range elastic interactions among dislocations.

In either *Box method* or *FMM*, the use of Application Program Interfaces (APIs), such as Open Multi-Processing (OpenMP) or Message Passing Interface (MPI) are inevitable to distribute/share the computational load among different

4.4. Numerical implementation of the DDD model

processors. Whereas, the DDD-FFT approach can take advantage of the Graphical Processing Units (GPUs) during computations [12]. During this thesis, initiative has been taken up to offload computationally intensive stress calculations to graphical processing units (GPUs). It should be noted that the offloading stress calculations is in no way related to the DDD-FFT approach. Our approach is similar to the use of any of the APIs. Low level APIs for accelerator programming, like OpenACC [35] are still in their early developmental stage. In contrast, the parallel computing platform (CUDA) [135] invented by NVIDIA is robust and requires minimal resources (a CUDA-enabled GPU is the only requirement and CUDA platform is available as open-source, unlike OpenACC) to run computations. GPUs with 1000s of processors are essentially never used during a normal computation on the CPU (single or multi-processor). To take advantage of these unused processors, three important steps need to be followed:

1. Copying relevant data from CPU to GPU
2. Stress computation on GPU
3. Copying back the results from GPU to CPU

Direct implementation of these offloading steps in conventional DD codes has been limited. The only noticeable work which took advantage of heterogeneous parallel programming framework for performing stress calculations on GPUs is carried in the matlab code *DDLlab* [59]. In our Fortran-based DD code, as a first step, GPU functions/subroutines were implemented to tackle a static DD problem (i.e., to compute stress field of a network of dislocations on GPU). Results are presented as different stress components calculated on a dislocation loop using the GPU version. The Side and Top views of the initial static configuration considered are shown in Figure 4.45.

To estimate error due to GPU computation of the stress fields, magnitude of different stress components calculated at the centres of each segment (*cf.* Figure 4.45) in the dislocation loop are plotted against the stress fields computed at the centres of each segment using a single processor version in Figure 4.50.

The correctness of the offloaded stress field calculations can now be extended to a dynamic case and the speedup achieved can be assessed as a second step in the development. This is a perspective development planned for the stress computations using GPUs.

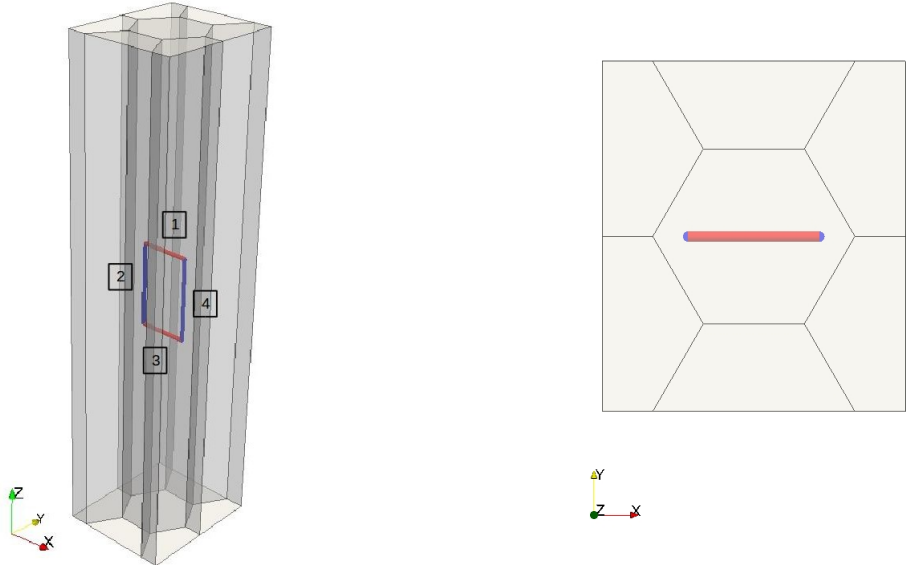


Figure 4.45 – Side and Top views of the initial static configuration considered, respectively

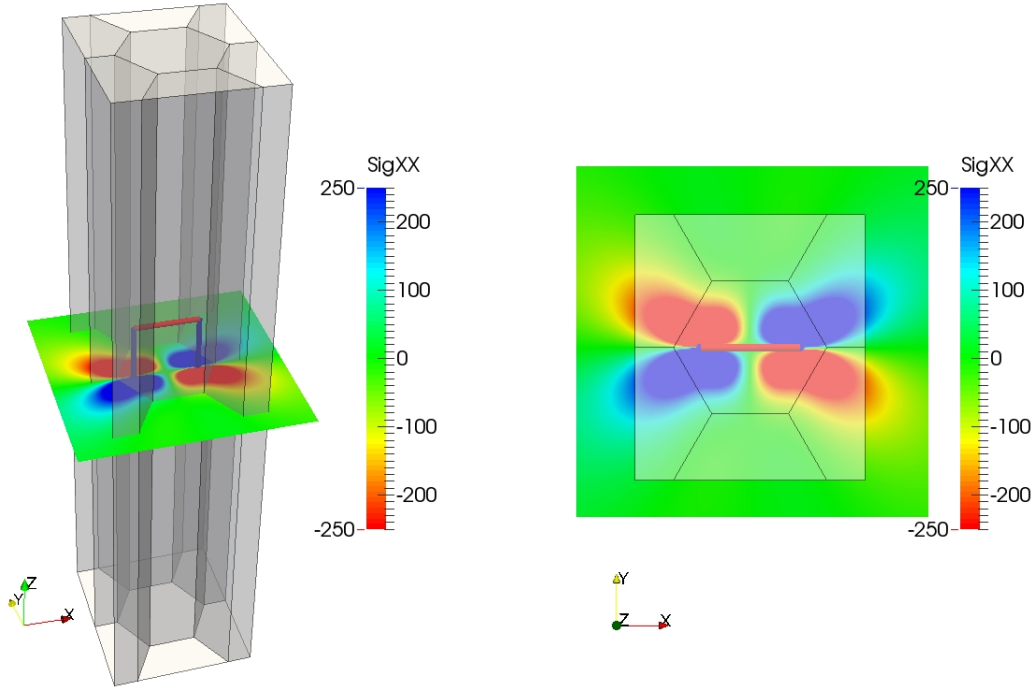


Figure 4.46 – Side and Top views of σ_{xx} component of the internal stress field

4.4. Numerical implementation of the DDD model

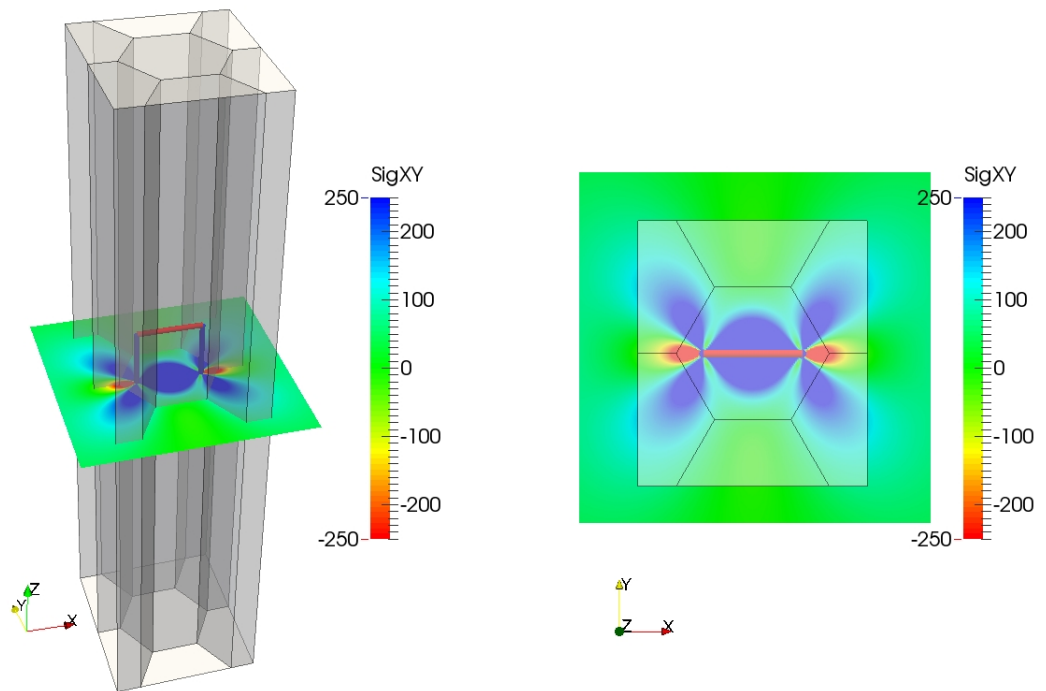


Figure 4.47 – Side and Top views of σ_{xy} component of the internal stress field

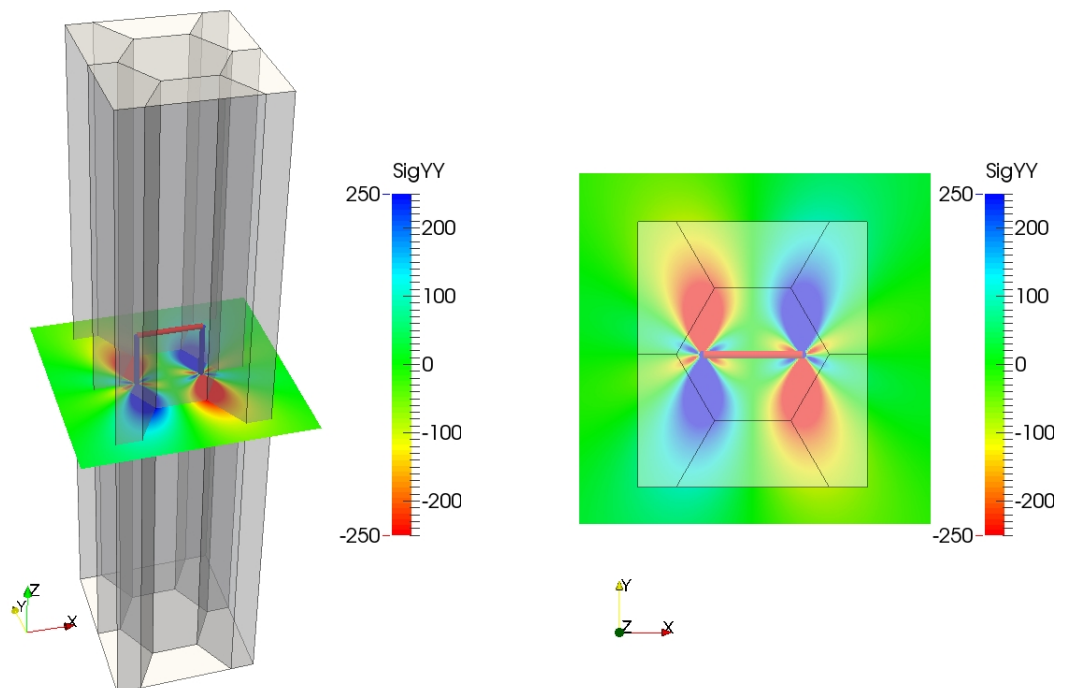


Figure 4.48 – Side and Top views of σ_{yy} component of the internal stress field

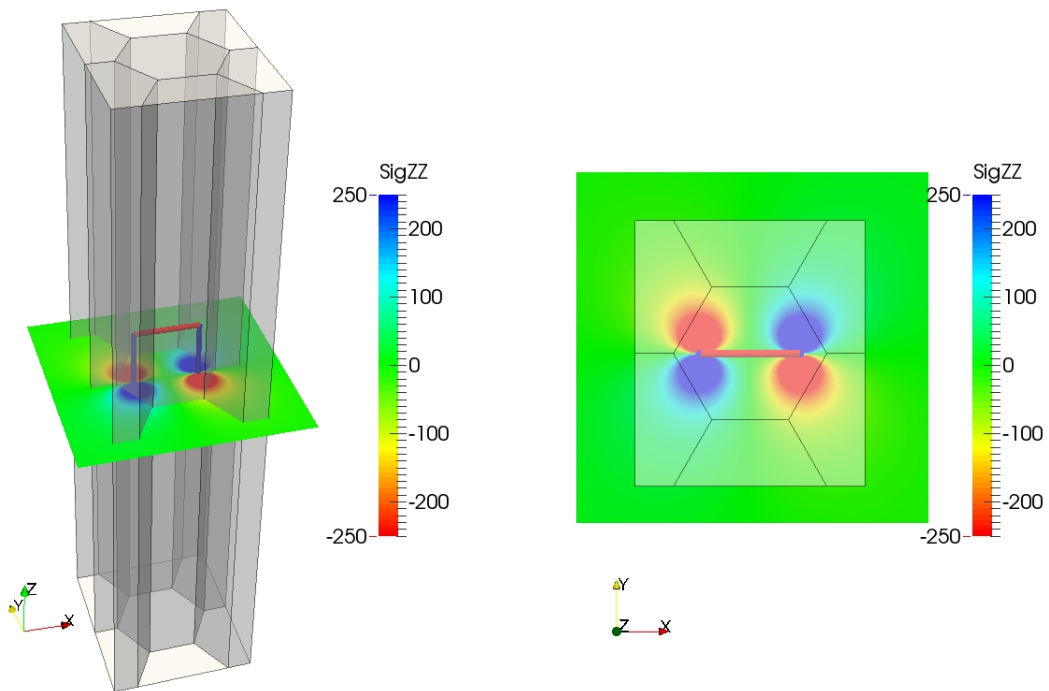


Figure 4.49 – Side and Top views of σ_{zz} component of the internal stress field

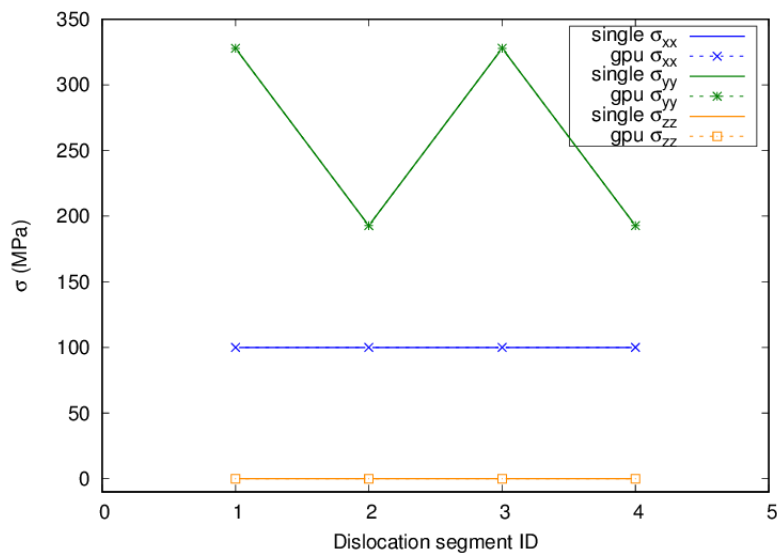


Figure 4.50 – Comparison of different components of stress field calculated at the center of each segments in the dislocation loop shown in Figure 4.45

4.4.4 Convergence of DD solution

In DD simulations, numerical error is introduced due to the discretization of the dislocation line in space and time. Convergence of the solution is ensured by maintaining a reasonably small time step and discretization length. A general approach to check the time step size is to look at the evolution of the Frank-Read source over few time steps. The dislocation structure should not abruptly change from step to step. Discretization of dislocation line segments is generally adjusted in such a way that the ratio of dislocation length to the discretization length is at least 3. This value ensures a limited error arising from spatial discretization.

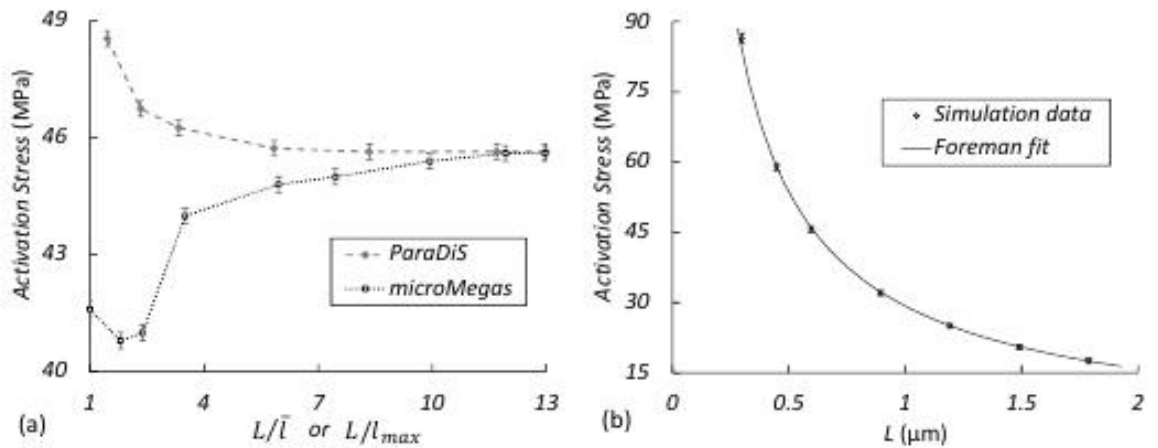


Figure 4.51 – (a) Activation stress of an edge dislocation as a function of the discretization ratio (b) Activation stress as a function of the source length with discretization ratio of 10 [155]

Convergence of two DD code (ParaDIS and microMegas), based on a different dislocation line discretization schemes (nodal and edge-screw schemes, respectively) have been compared for a Frank-Read source of edge character with length ($L=0.59\mu\text{m}$). In Figure 4.51(a), the activation stress of a dislocation source is plotted against the discretization ratios. Here, \bar{l} and l_{max} represent maximum segment length, which is a control parameter in ParaDis and microMegas, respectively. A better convergence is achieved for discretization ratios > 3 [155]. It has already been mentioned that the DD code (TRIDIS) used during this thesis is based on an Edge-Screw type discretization scheme. It was made sure that the discretization ratio is always ≥ 3 in all the DD simulations carried in Chapter 5 and Chapter 6.

4.5 Post-processing of DD simulation results

4.5.1 Plastic strain calculation

Plastic shear strain (γ_i^p) imparted by a dislocation i with Burgers vector magnitude b_i and length l moving on a slip plane is given by

$$d\gamma_i^p = \frac{b_i dA}{V} \quad (4.15)$$

where $dA = l \times \Delta d$ is the area swept by the dislocation in the grain of volume, V (cf. Figure 4.52).

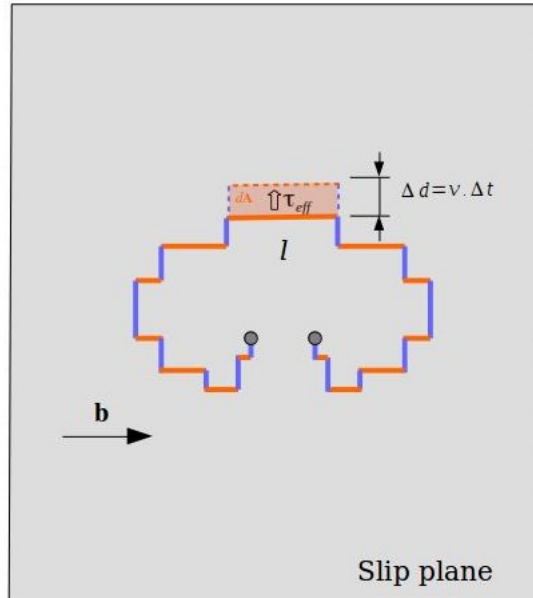


Figure 4.52 – Swept area by a dislocation segment of length l

The increment in plastic strain ($d\epsilon_i^p$) due to this dislocation segment i is:

$$d\epsilon_i^p = \frac{1}{2b} (\mathbf{b}^s \otimes \mathbf{n}^s + \mathbf{n}^s \otimes \mathbf{b}^s) d\gamma_i^p \quad (4.16)$$

where s is the dislocation slip system defined by its normal \mathbf{n}^s and Burgers vector \mathbf{b}^s . In the case of dislocation microstructure with N segments, the increment in

plastic deformation is:

$$d\boldsymbol{\varepsilon}^p = \sum_{i=1}^N d\boldsymbol{\varepsilon}_i^p \quad (4.17)$$

4.6 Conclusions

The methodology of three dimensional discrete dislocation simulation is presented. General approach of using a non-cubic periodic simulation box to mimic the bulk behavior of the material is presented. The superposition principle, which can be used to solve a problem with complex boundary conditions is introduced. DD-FEM coupling code used in the thesis has been extended to deal with anisotropy of a polycrystal. A new method for calculating the internal stress field based on GPU parallel programming is implemented.

PART - III

DDD simulations of plasticity in FCC crystals

5 Influence of grain morphology on intragranular backstress predictions

GRAIN morphology changes plastic deformation behavior. The main objective of this chapter is to address the influence of grain shape on dislocation slip activity. For this, 3D DDD simulations on single grains of different aspect ratios are performed. Based on the results from DD simulations, further implications to the crystal plasticity theory are addressed in the form of average back stresses on the slip systems of interest.

5.1 Introduction

In most metallic films, size effects result from the decrease in the grain size proportionally with the film thickness. Apart from this size effect, another interesting aspects of metallic films is the possibility to understand plastic deformation in grains of varying morphology. Depending on the deposition conditions and on the melting temperatures of the material, the aspect ratio of the grains can vary between pancaked, equiaxed to moderately elongated in the thickness directions [139]. TEM bright field microscopy image in Figure 5.1 shows the cross-sectional view of as-deposited 310-nm-thick Pd film with columnar grains. The influence of grain shape on plastic deformation behavior in a single grain needs to be clearly understood to further model the behavior of metallic thin films.

When the grain size is on the order of a few microns, plastic deformation of crystalline materials is mostly controlled by a limited number of elementary deformation mechanisms. For accurately modeling macroscopic plastic deformation, incorporating if not all, at least the most dominant of the elementary deformation mechanisms at a single grain level is vital. Additionally, grain boundaries should be properly modeled to estimate major changes in the plastic deformation behavior arising due to grain shape. Conventional crystal plasticity (CP) models predict/measure plastic anisotropy of a polycrystalline specimen based on the crystallographic texture [103]. Inaccurate prediction of r -values using both Taylor full constraint [173] and Taylor

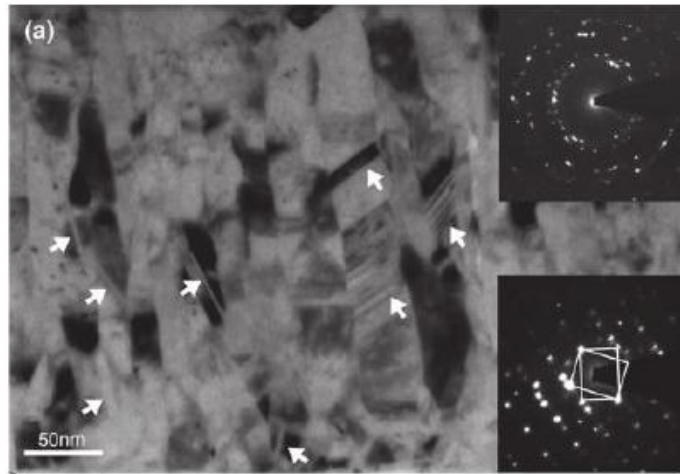


Figure 5.1 – Cross-sectional TEM image of a 310-nm-thick Pd film [93]

relaxed constraint models [101] in electro-deposited pure Fe with sharp γ -fibre texture is suggested to be due to the important role of needle-shape elongated grains in the normal direction [198]. Such examples further stresses on the lack in accuracy of CP models due to the improper treatment of grain boundaries. One of the motivation for studying changes in plastic deformation arising from grain morphology is due to the observation of differing grain shapes attained by Ni under controlled process conditions [109]. Additionally, Ni also carries low stacking fault energy. Generally, in materials with low stacking fault energy, dislocations tend to easily dissociate into partials and interact with the GBs; thereby, activating plastic deformation which is GB and partial dislocation mediated. Interestingly, no such dominant GB or partial dislocation mediated mechanism had been observed in Ni for average grain sizes as low as 30-40nm [109]. This indicates that the grain shape has a non-negligible influence on plastic deformation behavior in a single grain.

CP models rely on generalized Schmid law for modeling plasticity at single grain level. The generalized Schmid law accounts for the different slip resistance term originating from the interaction among different slip systems [70]. Within each grain of a polycrystalline material, grain boundaries act as natural obstacles to gliding dislocations. When dislocation motion is inhibited, they generally pile up against grain boundary. Such pile ups exert a back-stress on the dislocation sources; thereby preventing further activation of the Frank-Read source [124]. Conventional CP models account for such pile up behavior by introducing an average back-stress term corresponding to each slip system. The accuracy in the prediction of plastic anisotropy narrows down to the formulations used for predicting back-stresses in each individual grains. The real question is, how significant is the change in

deformation behavior of a grain with the aspect ratio of the grain? If changes are predominant, how does CP models incorporate the right deformation behavior in these grains? Most of the CP models were developed on the basis of dislocation pile up theory. But, if the pile up behavior is changed by the grain shape, then *so does the back stress influenced by dislocations*.

It has been established that changes in pile up behavior due to grain shape will change the back-stress influenced by dislocations on a slip system. CPFEM simulations were mostly used to study the evolution of grain shape and texture. One such work has been carried out in Mg alloy [144]. To better understand the influence of grain shape on planar anisotropy, a comparative study using CPFEM, VPSC [115] and multisite model [41] was performed on rolled steel sheets [42]. Changes in the activity of slip systems has been observed as the most significant effect of back stress [15]. In the last decade, simple back-stress formulations were developed and were successfully adapted to predict plastic anisotropy of spherical grains [86, 133]. Assuming that the dislocation density gradients being normal to the grain boundary, enriched back-stress formulations have been developed to model resistance due to the pile up of dislocations in elongated grains [40]. Although, these models show improved predictions of plastic anisotropy, the correctness of such enriched back stress formulations needs to be validated, if not modified, accordingly. One way to verify them is by rightfully accounting for the strain gradient that develops at the grain boundary due to the pile ups.

Strain gradient crystal plasticity (SGCP) models were developed with the same idea. These models account for both statistically stored dislocations (SSDs) and geometrically necessary dislocations (GNDs) to describe slip resistance. One advantage of these models is their capability to capture size effects by incorporating only the first order strain gradient within the strengthening term [84, 85]. In the initially developed SGCP models, the back-stress formulations included only the dislocation induced stress component of only the particular slip system [57, 197]. To model intra-granular slip resistance, dislocation-density-based hardening rules have been developed for continuum crystal plasticity to incorporate core concepts of dislocation mechanics [6]. Such rules have been adopted to SGCP models to determine slip system resistance and back stress based on the density of GNDs. A full tensorial nature of dislocation induced back-stress formulation, which accounted also for the stress contribution from all the slip systems, has been developed in SGCP model [9].

Additionally, dislocation slip activity in a grain is significantly changed due

Chapter 5. Influence of grain morphology on intragranular backstress predictions

to thermally activated mechanisms such as cross slip (or) climb. Dislocations which are generally piled-up against the grain boundary, can relieve the high stress concentration by local yielding. Such phenomenon has been experimentally observed in plastically deformed copper single crystals [54]. When a metallic single crystal is deformed past Stage III, the transition to a plastically non-homogeneous material was explained as a two stage behavior [8]. Starting with a general, uniform deformation stage during which an accumulation of statistically stored dislocations is observed. It is followed by a local, non-uniform deformation stage where geometrically necessary dislocations accumulate. The stresses associated with the later exceed the local yield stress. To maintain local strain compatibility, a dislocation array is nucleated.

The well-known two possibilities for the nucleation of a dislocation array in a single grain are briefly described below.

1. **Climb:** During this process the dislocation core is shifted to a plane perpendicular to the present slip plane. This thermally activated mechanism is mostly active at high temperature.
2. **Cross-slip:** A screw dislocation can easily relieve the stress concentration due to the pile up by changing its slip plane [54]. This thermally activated mechanism is called cross-slip.

These two mechanisms which are active upon reaching a ‘local yield stress’; nucleate a new dislocation array. Such mechanisms are vital for predicting the deformation behavior of a single grain; thereby the overall macroscopic response. Changes in the pile up behavior due to cross slip will also have an influence on back stress. In some of the advanced SGCP models, thermally activated mechanisms such as cross-slip and climb have also been included [53].

Full-field solutions of *gradient enhanced* crystal plasticity models have a huge computational cost and are limited so far to two-dimensional analysis of polycrystalline aggregates or to small grain samplings [40]. In contrast, 3D discrete dislocation dynamics (DDD) simulations demonstrate excellent capability in capturing the microstructural features at single grain level. 3D DDD models not only accurately account for the presence of grain boundaries but also are sophisticated to deal with intragranular local yield criteria (such as cross slip). Such advanced tools have been successfully applied to model behavior of single ice crystal [98], fatigue

behavior of FCC single crystal [44] and recently to study plastic deformation of single crystal of Ni based superalloys [74]. Several studies based on dislocation dynamic simulations have also been carried out to address size effects [159, 193], influence on plastic deformation due to size, aspect ratio and initial dislocation configuration [160]. 3D DDD simulations could be the right approach to better understand the influence of grain shape on dislocation activity in order to build improved models at continuum scale.

The main objective of the present work is to examine the role of grain shape on the slip system activity in a single grain using 3D discrete dislocation dynamics simulations. The changes in the dislocation activity which is controlled via the cross slip mechanism is also studied. This chapter is organized as follows. In Section 5.2, following a very brief introduction to the DD model, the setup used for the grain shape study is explained. Results produced during the present work are reported in Section 6.4. Further implications to CP models are discussed in Section 6.5; followed by, conclusion statements on the influence of grain shape on slip system activity and intra-granular back stress predictions.

5.2 Model and setup

3D discrete dislocation dynamics (3D DDD) codes simulate plastic deformation by keeping track of discretized dislocation segments which move under applied external load. For the present study, we use TRIDIS, an *edge-screw* discretization based 3D DDD code developed at SiMaP, Grenoble, France [62, 185]. A detailed explanation about the methodology of the 3D DDD code used was presented in Chapter 4.

5.2.1 Modeling spheroidal grains

The present study has been carried out using an elastic isotropic framework to isolate the influence of grain morphology on plastic deformation behavior. Spheroidal grains, which closely resemble the elongated grain structure are considered. Such elongated grains with different aspect ratios are also found in thin films (*cf.* Chapter 6). Even though, elongated grains with aspect ratio (AR) ≥ 10.0 are sometimes encountered [33, 93, 109, 198]. A clear change in dislocation slip activity was observed in the reference simulation of spheroidal grain with $AR=5.0$. So, the study has been limited to a maximum $AR=5.0$. Three spheroidal grains of same volume (=

Chapter 5. Influence of grain morphology on intragranular backstress predictions

$5000 \mu m^3$) but differing in aspect ratios ($AR = 1.0, 2.5$ and 5.0) were modeled. For the sake of simplicity, we refer to the spheroidal grains with the names which closely resemble their shape. Grain with aspect ratio 1.0, 2.5 and 5.0 are hereby referred to as *Sphere*, *Kacahuete* and *Cigar*, respectively. The exact geometry of the non-similar grains are presented in Figure 5.2. These generalized grain geometries were chosen for two reasons. Firstly, the modeled geometries very closely resemble the non-equiaxed grains generally observed in experiments. The idea of improving the analytical expression developed for predicting back stresses in elongated grains [40] also justifies the choice of spheroidal grain shape considered.

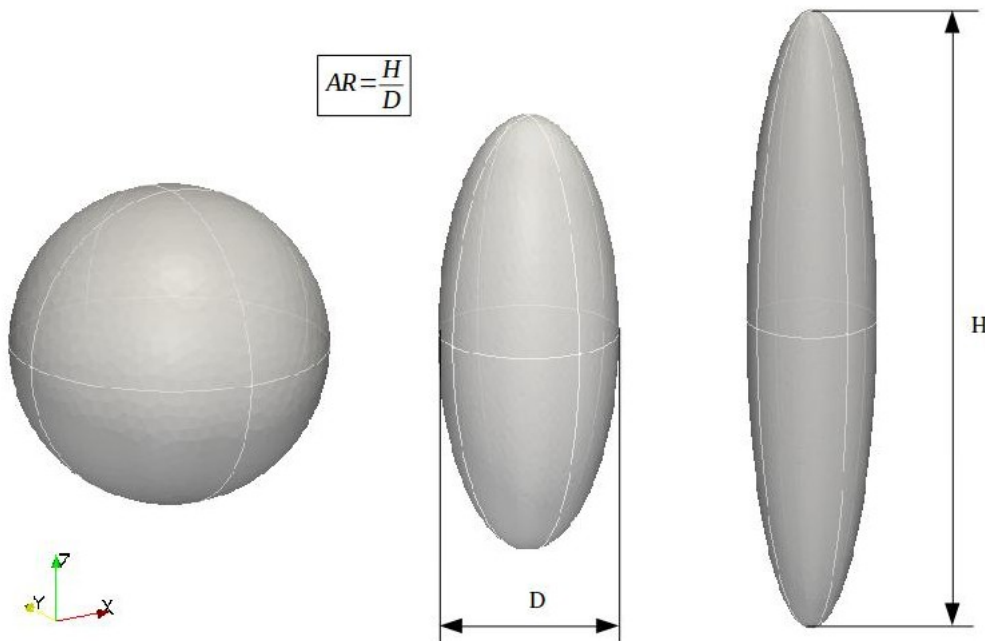


Figure 5.2 – Sphere ($AR=1.0$); Kacahuete ($AR=2.5$) and Cigar ($AR=5.0$)

5.2.2 Information imported from crystal plasticity

The first information imported from crystal plasticity is the columnar and tensile axis of the grain.

Columnar axis: $\{0.5 \ 0.31 \ -0.81\}$ and **Tensile axis:** $\{0.12 \ 0.9 \ 0.42\}$

The columnar and tensile axes pair correspond to Euler angles $[134.4 \ 14.0 \ 58.3]$ in Bunge notation [22]. All the three spheroidal grains are rotated according to the

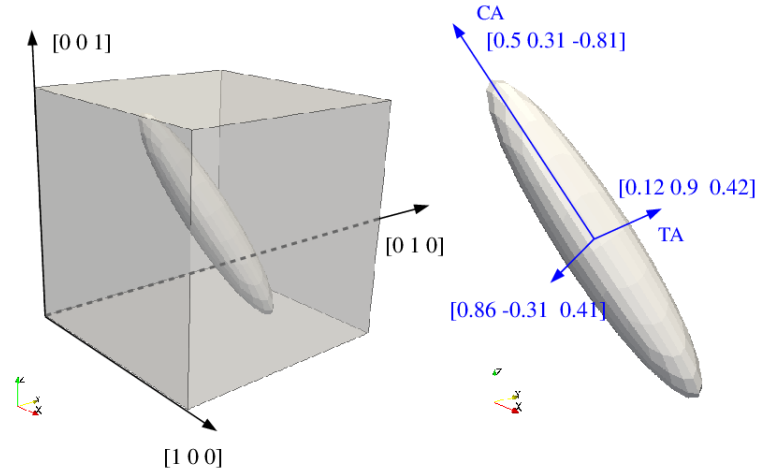


Figure 5.3 – Schematic shows a.) a Cigar grain in rotated configuration inside a cubic simulation volume in reference frame and b.) the Cigar grain with the axes data imported from crystal plasticity

Euler angles and the schematic of a Cigar grain in rotated configuration is shown in Figure 5.3.

The second information imported from crystal plasticity is the stress tensor in reference frame and the corresponding principle stresses ($\sigma_I = 348.25MPa$, $\sigma_{II} = 83.61MPa$ and $\sigma_{III} = -114.04MPa$) along the principle axes are shown in Figure 5.4.

$$\text{Stress tensor: } (\sigma_{ext} \text{ in MPa}) = \begin{bmatrix} \sigma_{11} & \sigma_{12} & \sigma_{13} \\ \sigma_{21} & \sigma_{22} & \sigma_{23} \\ \sigma_{31} & \sigma_{32} & \sigma_{33} \end{bmatrix} = \begin{bmatrix} 317.53 & 82.33 & -79.74 \\ 82.33 & 0.01 & 83.63 \\ -79.74 & 83.63 & -0.02 \end{bmatrix}$$

The orientation of the grain and the external stress applied on the grain are chosen in such a way that the crystal plasticity models predict four highly active slip systems with similar Schmid factors. Table 5.1 gather the slip system information along with their Schmid factors and angle the normal to the plane makes with respect to the long axis of the grain. The long axis is the columnar axis shown in in Figure 5.3.

All the grain boundaries of the grain are kept impenetrable to dislocation (i.e., only pile up at the GBs and no dislocation-grain boundary interactions are considered). The four most active slip systems of interest are indicated in Table

Chapter 5. Influence of grain morphology on intragranular backstress predictions

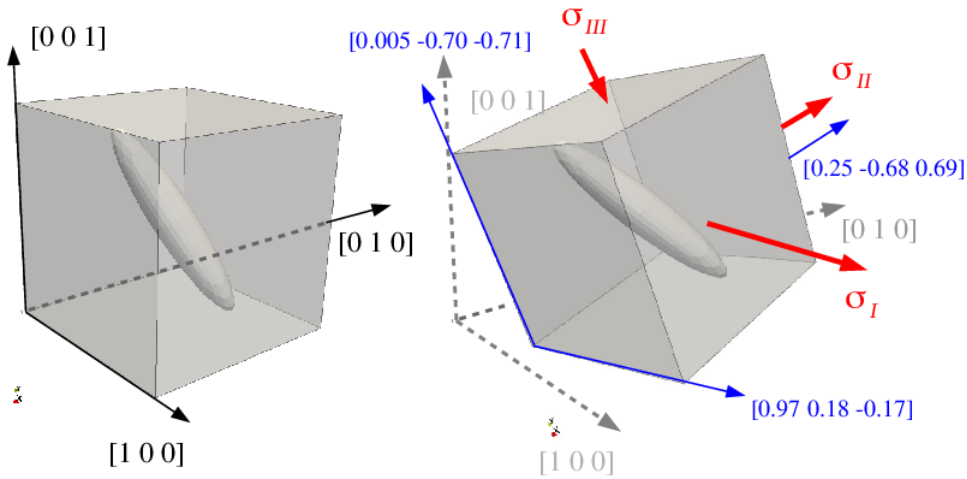


Figure 5.4 – Stress tensor imported from CP model being expressed in principle axes

Slip system no.	Proposed slip system names	Burgers vector (\vec{b})	Slip plane normal (\vec{n})	Schmid factors (M)	Angle w.r.t long axis of the grain
1	SS01	$\frac{a}{2}[\bar{1}01]$	(111)	0.196	90°
2	SS02	$\frac{a}{2}[\bar{1}01]$	($\bar{1}1\bar{1}$)	0.198	69°
3	SS03	$\frac{a}{2}[011]$	($\bar{1}1\bar{1}$)	0.004	69°
4	SS04	$\frac{a}{2}[011]$	($\bar{1}\bar{1}1$)	0.171	21°
5	Long Path (LP)	$\frac{a}{2}[1\bar{1}0]$	(111)	0.368	90°
6	SS06	$\frac{a}{2}[1\bar{1}0]$	($\bar{1}\bar{1}1$)	0.194	21°
7	SS07	$\frac{a}{2}[\bar{1}\bar{1}0]$	($\bar{1}1\bar{1}$)	0.194	69°
8	Short Path (SP)	$\frac{a}{2}[\bar{1}\bar{1}0]$	($1\bar{1}\bar{1}$)	0.363	55°
9	SS09	$\frac{a}{2}[0\bar{1}1]$	($1\bar{1}\bar{1}$)	0.003	55°
10	SS10	$\frac{a}{2}[0\bar{1}1]$	(111)	0.172	90°
11	Collinear1 (CP1)	$\frac{a}{2}[101]$	($\bar{1}\bar{1}1$)	0.366	21°
12	Collinear2 (CP2)	$\frac{a}{2}[101]$	($1\bar{1}\bar{1}$)	0.364	55°

Table 5.1 – Slip system information along with Schmid factors and angle made with respect to the long axis of the grain, respectively

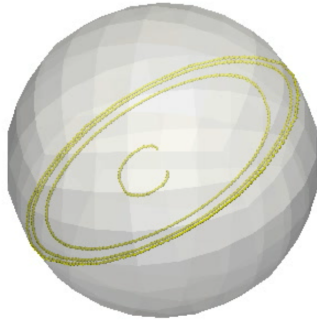


Figure 5.5 – Dislocation activity without cross slip in Sphere



Figure 5.6 – Dislocation activity with cross slip in Sphere

5.2. It should also be noted that for the above stress tensor and Euler angles pair, one of the four active slip systems (Long Path in Table:5.2) is aligned parallel to columnar axis of the grain. Two of the four most active slip systems share the same Burgers vector and hence, screw dislocations on these systems can change their respective glide planes by cross slip mechanism. Figure 5.5 and Figure 5.6 show the change in dislocation activity due to cross slip in a Sphere under single slip condition. Unlike in equiaxed grains, the path a dislocation traces is different on each slip system in non-equiaxed grains (elongated grains in our case). Different names were proposed to indicate the non-similar paths traced by the dislocation on the slip system (*cf.* Table 5.1 and Table 5.2). Along with the proposed names, the same color coding of the slip systems is followed throughout this chapter.

Slip system no.	Proposed slip system names	Burgers vector (\vec{b})	Plane normal (\vec{n})	Schmid factors (M)	Angle w.r.t grain's long axis
5	Long path (LP)	$\frac{a}{2} [1 -1 0]$	(1 1 1)	0.368	90°
8	Short path (SP)	$\frac{a}{2} [-1 -1 0]$	(1 -1 -1)	0.363	55°
11	Collinear ₁ (CP ₁)	$\frac{a}{2} [1 0 1]$	(-1 -1 1)	0.366	21°
12	Collinear ₂ (CP ₂)	$\frac{a}{2} [1 0 1]$	(1 -1 -1)	0.364	55°

Table 5.2 – Four most active slip system

A schematic view of two of the four most active slip systems (*cf.* Table 5.2) in grains of different aspect ratios and different angle (angle made with respect to

Chapter 5. Influence of grain morphology on intragranular backstress predictions

the long axis) are presented in Figure 5.7. The slip plane geometry remains the same for all slip systems in *Sphere* (AR=1.0). In *Kacahuete* (AR=2.5) and *Cigar* (AR=5.0), the slip plane geometry is observed to change according to the angle which the plane normal makes with the long (columnar) axis of the grain. Such variations in plastic deformations can give rise to huge plastic anisotropy influenced by grain shape.

5.2.3 Selection of initial dislocation density

It is common practice in the DD community to consider the initial microstructure as a random distribution of Frank-Read dislocation sources in the simulation volume. We follow the same procedure to generate our initial dislocation microstructure. 132 random sources (11 on each slip system), each of length $2\mu m$; which corresponds to an initial density ($\rho_{initial} = 0.527 \times 10^{11} m^{-2}$) are considered for all our simulations. The choice of the dislocation length was based on the smallest dimension of the grain with highest aspect ratio. In our case, the smallest dimension corresponds to the Cigar grain, where $D = 6.0\mu m$. A dislocation source length of $2\mu m$ is chosen after testing for the minimum influence of GBs on a single dislocation source placed at the center of Cigar. In other words, the minimum length for which a dislocation source can continue the multiplication process when placed exactly at the center of the grain is chosen. This particular value of source length is kept the same even in the case of grains modeled with lower aspect ratios (Sphere and Kacahuete grains). Since the probability of initial dislocation sources being randomly placed close to the grain boundary is higher in the case of Cigar grain, the number of initial dislocation sources has been increased to eleven on each slip system to minimize the effect of initial dislocation sources being placed close to the grain boundary.

Further, the influence of the initial dislocation density can be neglected by analysing only the unloading part of the stress-strain curve during the single loading and unloading cycle. Ten simulations of 10 different random realisations for each grain are considered to further decrease the stochastics due to dislocation positioning inside the grain. One of the random initial dislocation realizations in Sphere, Kacahuete and Cigar grains with only four active slip systems highlighted (coloured; others in white) is shown in Figure 5.8.

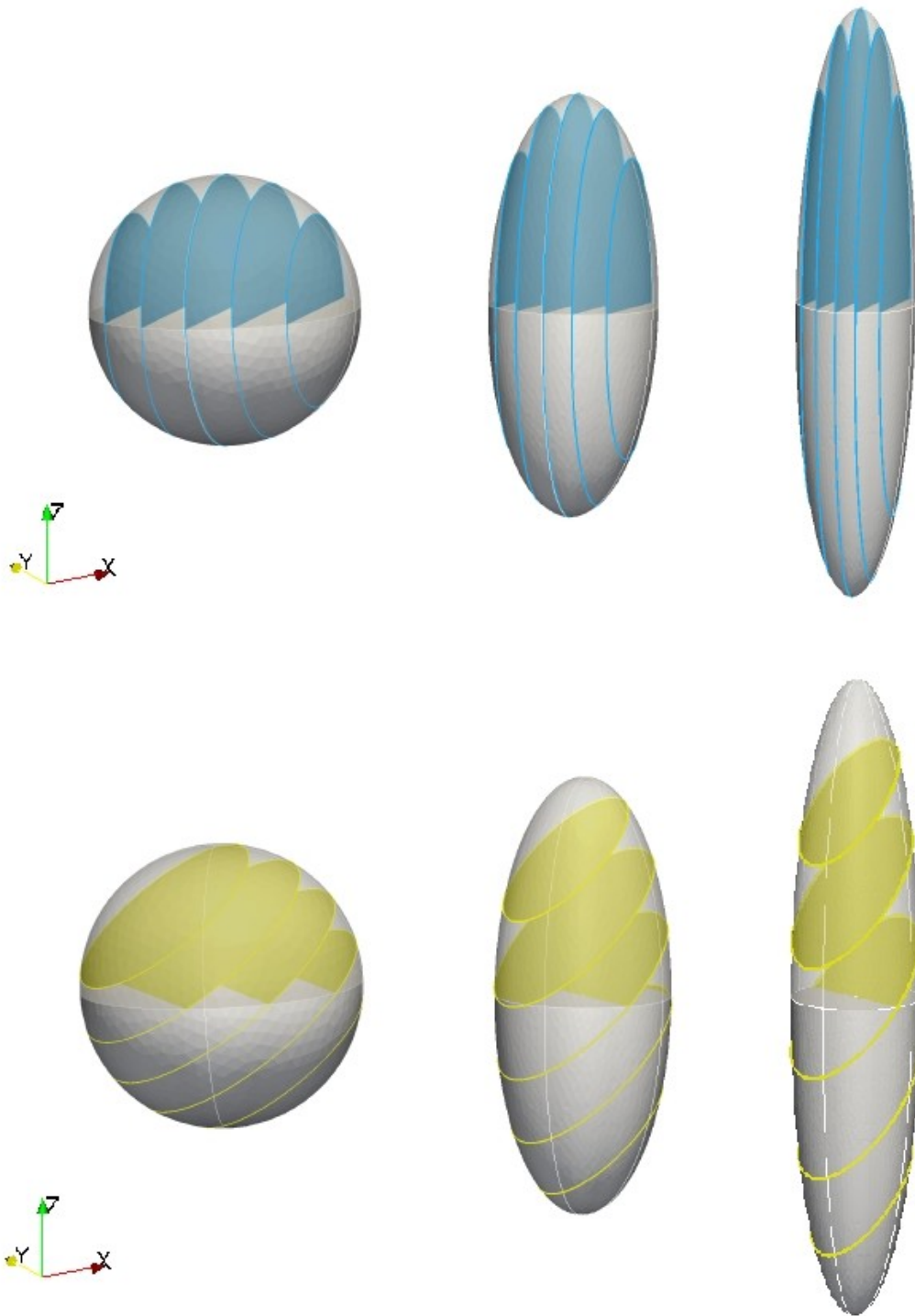


Figure 5.7 – Schematics of slip systems "Long path" (LP) and "Collinear1" (CP1) in Sphere (AR=1.0); Kachete (AR=2.5) and Cigar (AR=5.0) grains, respectively

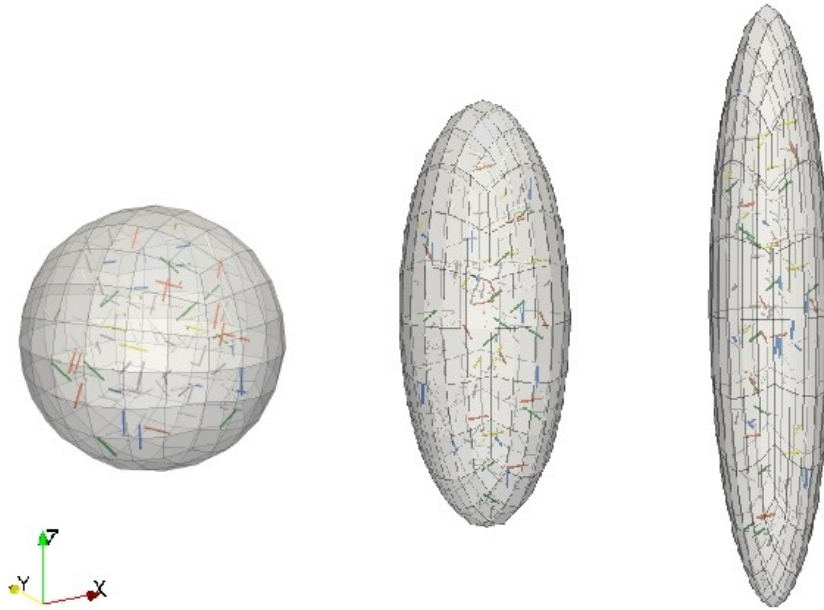


Figure 5.8 – Randomized initial dislocation source realization (RR 05) in Sphere (AR=1.0); Kacahuete (AR=2.5) and Cigar (AR=5.0) grains with only the four most active slip systems being highlighted

5.2.4 Material parameters

The material parameters of Ni, which has a face centred cubic lattice structure, were used for the simulation and are presented in Table 5.3.

Material	Poisson ratio ν	Young's modulus E (GPa)	Shear modulus μ (MPa)	Burgers vector magnitude b (10^{-10} m)	Viscous drag coefficient B (10^{-5} Pa.s)	Density ρ_v (Kg.m^{-3})	Activation volume V_{act}/b^3	Stacking fault energy γ (mj.m^{-2})
nickel	0.31	200	80000	2.489	1.5	1430	350	90

Table 5.3 – Material parameters of Ni

5.2.5 Loading condition

All the simulations were carried out by applying an external stress, σ_{ext} which is taken as an input from CP theory (*cf.* Section 5.2.2). A stress increment of $\Delta\sigma = 10^{-3} \text{MPa}$ at every step is applied. The stress increment is kept low enough

to ensure quasi-static equilibrium before every loading increment.

$$\sigma_{ext}^{new} = \sigma_{ext}^{old}(1 + \Delta\sigma) \quad (5.1)$$

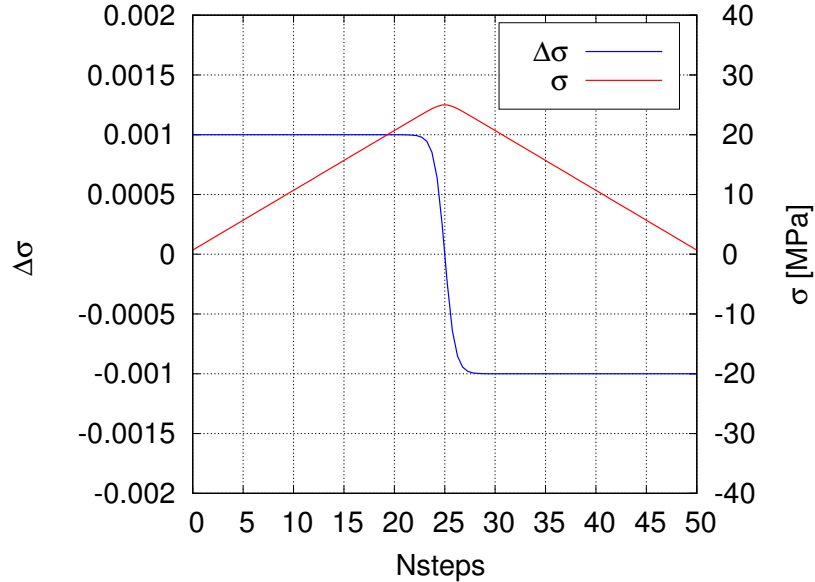


Figure 5.9 – Tangential hyperbolic monitoring (change in stress increment and stress with no.of steps)

Stress increment ($\Delta\sigma$) is not monotonic. It follows a tangential hyperbolic relation. With such monitoring, a systematic decrease of stress is achieved while approaching a prescribed plastic strain at which a load reversal is imposed. If the prescribed plastic strain is reached at step 25, the decrease in stress increment while approaching 25th step in a model plot is shown in Figure 5.9. After reaching the prescribed plastic strain, the stress is decreased by a factor of 75% and the sign of the stress increment is changed. The decrease in the stress by a factor will prevent any overshoot of equivalent plastic strain, ε_{eq}^p (if the dislocations have not reached equilibrium) which is monitored at every simulation step. Loading is reversed by applying a negative stress increment ($\Delta\sigma = -1.10^{-3} MPa$) once the equivalent plastic strain of $\varepsilon_{eq}^p = 4.10^{-4}$ is reached.

5.3 Results

The results of ten simulations with different initial random realisations in Sphere, Kacahuete and Cigar grains are presented in average form in the sections below.

Chapter 5. Influence of grain morphology on intragranular backstress predictions

As our focus is on the influence of grain shape on the prediction of intragranular back stresses, only the plastic regime of the stress-strain curve is plotted. In order to maintain consistency during the comparison of different simulations, Sphere, Kacahuete and Cigar grains are always plotted with similar line types. In all the simulations, loading is reversed when the equivalent plastic strain $\varepsilon_{eq}^p = 4.10^{-4}$ is reached. The choice of the reversal equivalent plastic strain is made after analysing the results from a reference simulations in a Sphere grain. The evolution of plastic deformation on the four most active slip systems is presented by following the same names and color coding as presented in Table 5.2.

5.3.1 Reference simulation: Spherical grain without cross slip

When the Sphere grain is plastically deformed, CP theory, for the specific Miller indices and stress tensor (*cf.* Section 5.2.2) pair, predicts similar dislocation slip activity on the four most active slip systems (*cf.* Table 5.2). But, the DD simulations predict a completely different dislocation slip activity on each slip systems as shown in Figure 5.11.

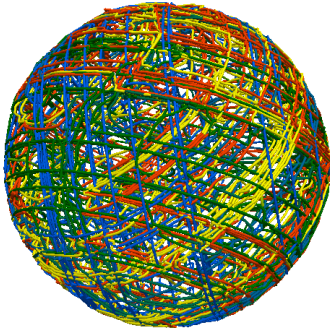


Figure 5.10 – Snapshot of dislocation slip activity on four most active slip systems in Sphere grain at $\varepsilon_{eq}^p = 4.10^{-4}$

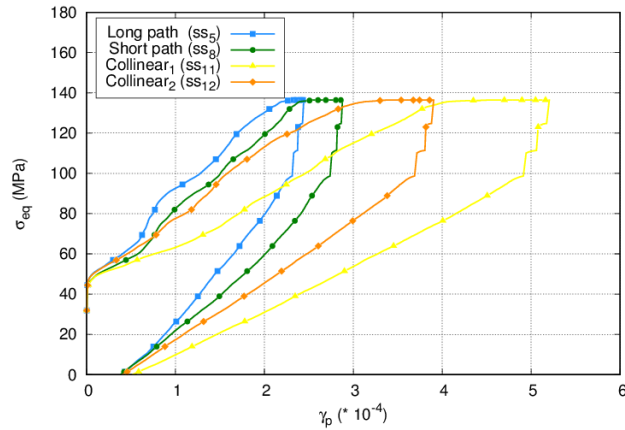


Figure 5.11 – Different dislocation slip activity on four most active slip systems in Sphere grain

In order to probe the origin for the heterogeneities of dislocation slip activities, the contribution of the kinematic and the isotropic hardening parts to the overall strain hardening behavior needs to be better understood. It is still a difficult task to exactly distinguish the contributions of both parts to strain hardening curve even with discrete dislocation dynamics simulations. The reason for these difficulty

comes from the collective contributions of the short-range (σ_i) and long-range stress (σ_d) fields of dislocations:

$$\sigma = \sigma_i + \sigma_d \quad (5.2)$$

where σ_i is the stress required to overcome the resistance of the material (lattice friction) and activation stress of a dislocation segment of length, L ; σ_d is the contribution of long-range effect of dislocations in the simulation volume.

Heterogeneities in plastic deformation in an equiaxed grain (like Sphere grain) is an evidence of the directional nature of long-range internal stresses. Figure 5.12 (b) shows the directional nature of internal stresses during a loading-unloading cycle.

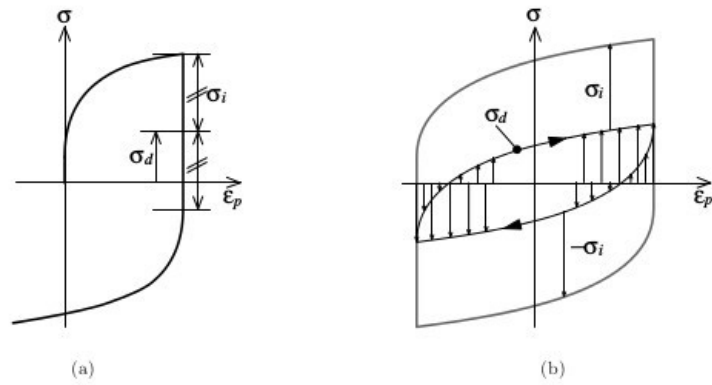


Figure 5.12 – Schematics showing (a) Short-range and long-range contributions; (b) Directionality of long-range interaction [43]

Looking at the DD results in multislip condition (*cf.* Figure 5.11) will only complicate things. In order to first establish a better understanding of the contributions to the overall strain hardening behavior, a DD simulation on a Sphere grain with a single dislocation source (on "Long path") at the center of the grain was performed (*cf.* Figure 5.13). Analysis has been carried out only on the unloading part of a single loading-unloading cycle. During the onset of the unloading cycle, dislocations are in a *piled up dislocation configuration*. Such a pileup configuration is the signature of *kinematic hardening*. So, the contribution of *isotropic hardening* is completely *nullified* by analysing only the unloading part of the single loading-unloading cycle.

During loading, plastic deformation caused by the movement of dislocations

Chapter 5. Influence of grain morphology on intragranular backstress predictions

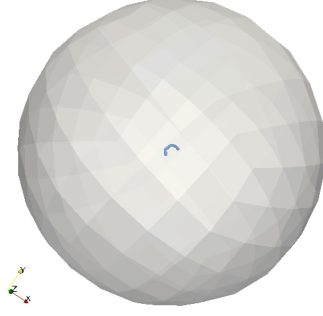


Figure 5.13 – Single dislocation source on "Long path" located at the center of Sphere grain

is hindered by the interaction of dislocations with obstacles (GBs or piled up dislocations). This creates a long-range stress field in the simulation volume and resists further progress of dislocations of similar sign. Snapshots taken at different steps during the DD simulation of Sphere grains are shown in Figure 5.14. But, during unloading, this long-range interaction repels the dislocations from the obstacles (other dislocations in the pile up) and helps to move the dislocations in the direction of reversed strain. Dislocations are reverting (reversed plastic strain) by the same amount of the long-range stress field (also includes external stress) they experience.

So, the kinematic hardening slope measured from the unloading part of the stress-strain curve will be a good measure for the average back stress on each slip system. The formula used for measuring the slope of the unloading part is given in Equation 5.5.

$$\tau^{(s)} = \tau_i^{(s)} + \tau_d^{(s)} \quad (5.3)$$

$$\text{with } \tau_i^{(s)} = \left[\tau_{fr} + \frac{\mu \mathbf{b}}{L} \right] \text{sign}(\gamma_p^{(s)}) \quad (5.4)$$

$$\tau_d^{(s)} = \left[\frac{1}{k_1} \frac{\mu}{(1 - \nu)} \right] \gamma_p^{(s)} \quad (5.5)$$

where the resolved shear stress on the slip system (s), $\tau^{(s)}$ is decomposed into the contributions of short-range $\tau_i^{(s)}$ and long-range $\tau_d^{(s)}$ interactions. The short-range effect $\tau_i^{(s)}$ is arising from the contribution of lattice friction (τ_{fr}) of the material

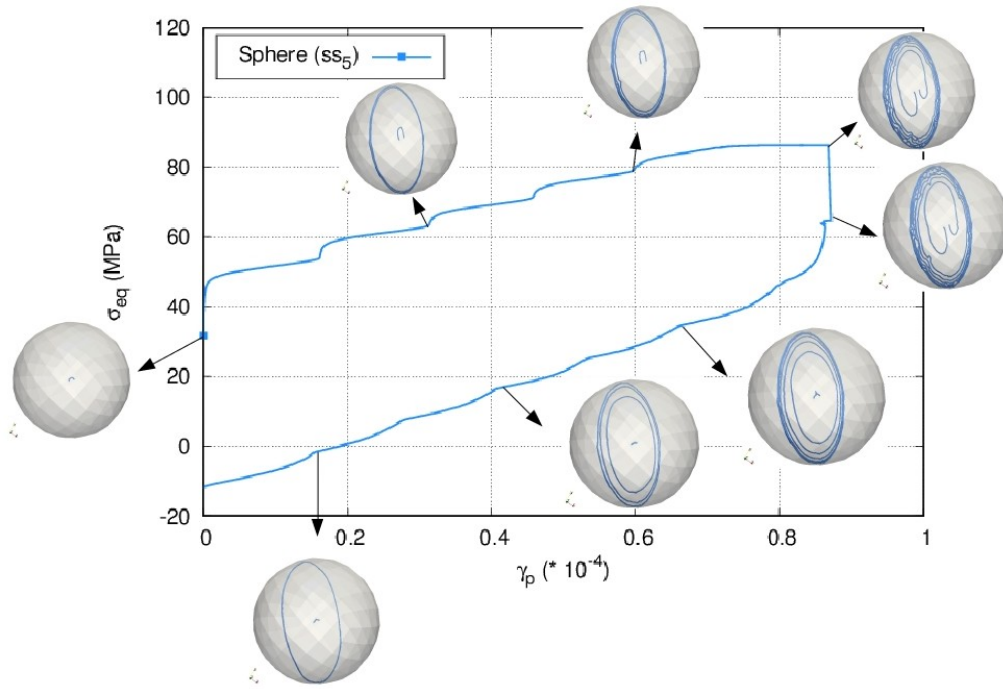


Figure 5.14 – Long-range stress field due to dislocations in the pileup hindering further activation of the initial dislocation source on "Long path" located at the center of Sphere grain

and activation stress of the Frank-Read segment $\frac{\mu \mathbf{b}}{L}$, with μ being shear modulus, \mathbf{b} being the magnitude of Burgers vector and L being the length of the Frank-Read dislocation source. The kinematic hardening due to pile up of dislocations is evaluated as the slope (k_1) of the stress-strain curve. The equation for $\tau_d^{(s)}$ has been modified for the present analysis to:

$$\sigma_d = \frac{1}{M} \left[\frac{1}{k_1} \frac{\mu}{(1 - \nu)} \right] \gamma_p^{(s)} \quad (5.6)$$

where M represents the Schmid factor. An example plot showing the calculation of slope is presented in Figure 5.15. As explained in Section 5.2.5, after reaching a prescribed equivalent plastic strain, the equivalent stress is dropped by $\sim 75\%$ (this value is not constant and can be changed). Dislocations are in a stable configuration at this particular point. So, this point is used as one of the reference points to calculate slope of the curve with the other reference point being at origin.

Chapter 5. Influence of grain morphology on intragranular backstress predictions

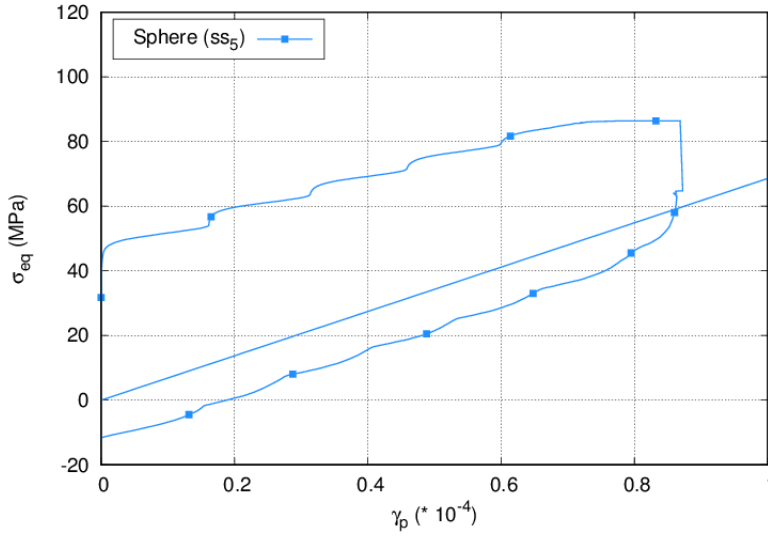


Figure 5.15 – Kinematic hardening slope of the unloading part of the stress-strain curve as a measure of backstress on "Long path" in Sphere grain

5.3.2 Grain shape effect on strain hardening without cross-slip

Simulation results for the Sphere, Kacahuete and Cigar grains when the cross slip mechanism is not active are presented to understand influence of grain shape on plastic deformation. The cross slip mechanism is prohibited by applying a relatively high critical cross slip stress of $CS3 = 160MPa$ in these simulations.

The loading part of the stress-strain curves in Figure 5.16 suggests that plastic deformation in all three grains initiates at the same value of equivalent stress ($\sigma_{eq} \sim 40MPa$) irrespective of the aspect ratio of the grain; owing to the dislocation activation strength of initial dislocation sources of same length prescribed in each grain. In the region $\varepsilon_{eq}^p < 1.10^{-4}$, the similarities in the stress-strain response of Sphere, Kacahuete and Cigar grains are due to the simultaneous dislocation activity on the four slip systems sharing a high, common Schmid factor. The influence of grain shape can be observed as change in the stress-strain reponse for the loading part of the region $\varepsilon_{eq}^p > 1.10^{-4}$. The Sphere grain with an aspect ratio of 1.0 leads to more strain hardening than Kacahuete and Cigar geometries. Results suggest that an increase in the aspect ratio of the grain tends to decrease the strain hardening capacity. The reason for this behavior can be understood by looking at the dislocation microstructure evolution in elongated grain (Cigar (AR=5.0)).

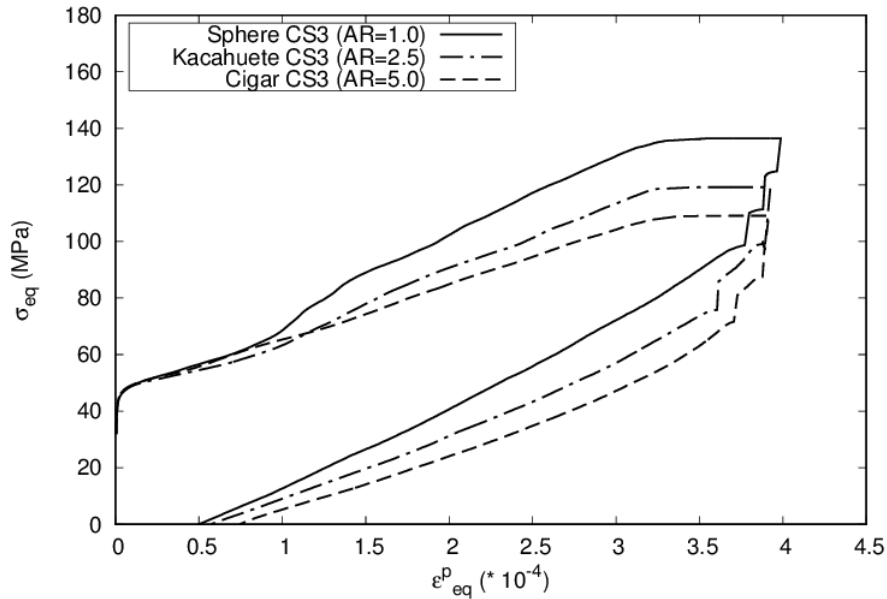


Figure 5.16 – Plastic response of sphere, kachahute and cigar with no cross slip

The lower strain hardening capacity of the Cigar grain shape must be arising from the interaction of dislocations on highly active slip systems with the dislocations on the second highly active slip systems. In order to clearly observe the mechanism responsible for the lower strain hardening in Cigar grain, we look at the dislocation interaction on "long path" and "deviate of long path". The slip system named "long path" is aligned parallel to the long axis of the grain and has a Schmid factor equal to 0.368. Alternatively, the slip system named "deviate of long path" is aligned at 21° with the long axis of the grain and has a Schmid factor equal to 0.194 (second highest Schmid factor). Both these slip systems also share a common Burgers vector. Information related to these two slip systems are presented in the Tables (Table 5.2 and Table 5.4). A schematic view of centred slip plane on "long path" (blue) and "deviate of long path" (red) is presented in Figure 5.17.

Figure 5.18 shows the dislocation activity only on "long path" and "deviate of long path" in Cigar grain at step 1070. Looking at the dislocation microstructure, it is clear that the dislocations on "long path" (blue), having the highest Schmid factors, are already activated. After a certain time, the initiation of dislocation activity on "deviate of long path" (red) should be accompanied by a stress increment as the Schmid factor on this slip system is almost half the highest. But, such an increment in equivalent stress has not been observed in Cigar grain (*cf.* Figure

Chapter 5. Influence of grain morphology on intragranular backstress predictions

Slip system no.	Proposed slip system names	Burgers vector (\vec{b})	Plane normal (\vec{n})	Schmid factors (M)	Angle w.r.t grain's long axis
6	Long path (deviate)	$\frac{a}{2} [1 -1 0]$	$(-1 -1 1)$	0.194	21°
7	Short path (deviate)	$\frac{a}{2} [-1 -1 0]$	$(-1 1 -1)$	0.194	69°
12	Collinear ₂ (CP ₂)	$\frac{a}{2} [1 0 1]$	$(1 -1 -1)$	0.364	55°
11	Collinear ₁ (CP ₁)	$\frac{a}{2} [1 0 1]$	$(-1 -1 1)$	0.366	21°

Table 5.4 – Deviates of four most active slip system

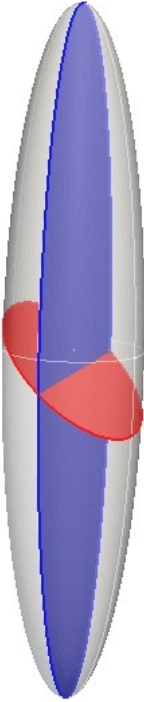


Figure 5.17 – Schematic drawing of a slip plane of "long path" (blue) and "deviate of long path" (red) passing through the center of the Cigar grain

5.16). This is due to the interaction of dislocations on "deviate of long path" (red) with already active "long path" (blue) dislocations.



Figure 5.18 – Dislocation microstructure at step 1070 in Cigar grain

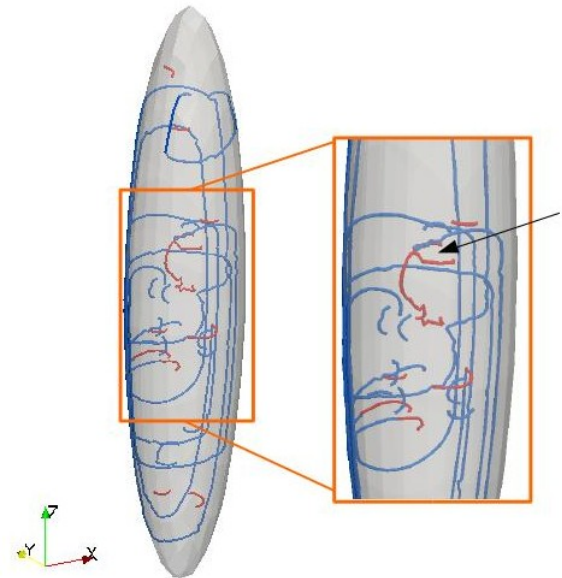


Figure 5.19 – Region of interest at step 1070 in Cigar grain

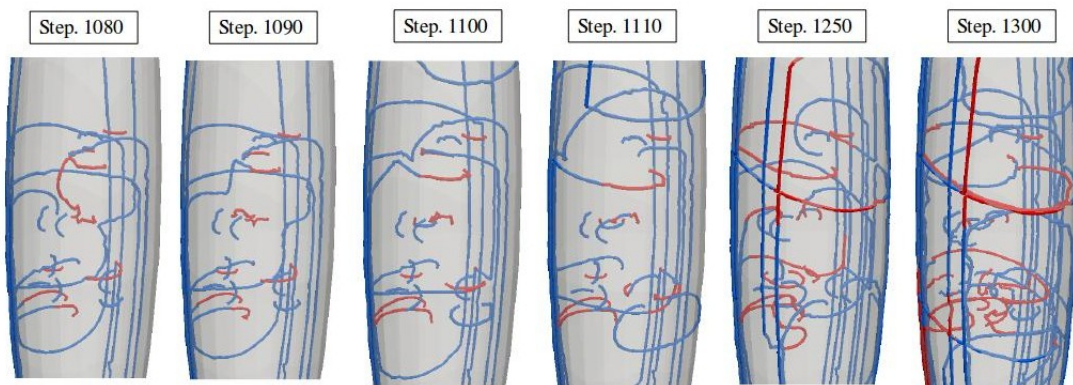


Figure 5.20 – Evolution of dislocation microstructure on "long path" and "deviate of long path" in Cigar grain

Different simulation steps (*cf.* Figure 5.20) of dislocation microstructure evolution highlight the interaction of dislocation on "long path" and "deviate of long path". Due to the confinement of grain size along X- and Y- directions, the dislocations on "deviate of long path" strongly interact with the dislocations on "long path" (*cf.* step 1080 in Figure 5.20) and exchange neighbours mutually (*cf.*

Chapter 5. Influence of grain morphology on intragranular backstress predictions

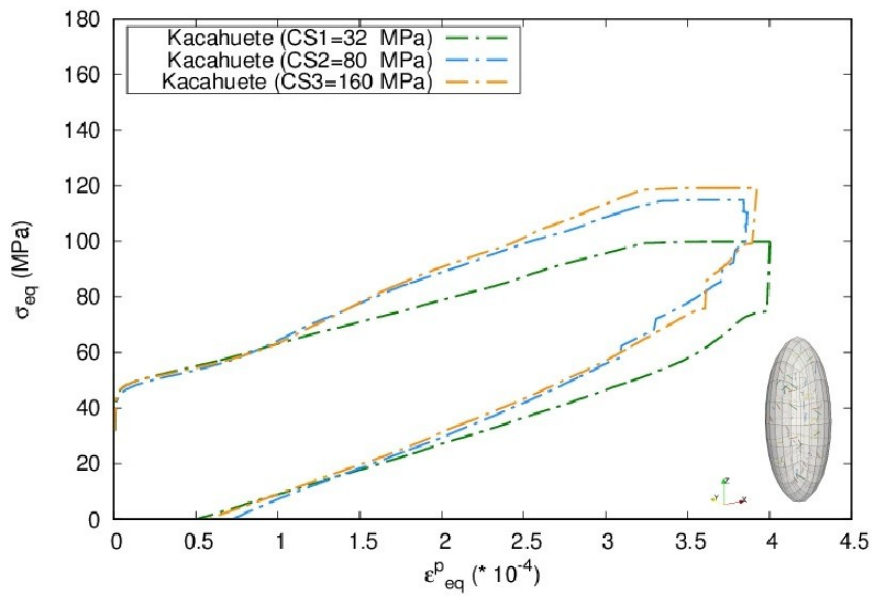
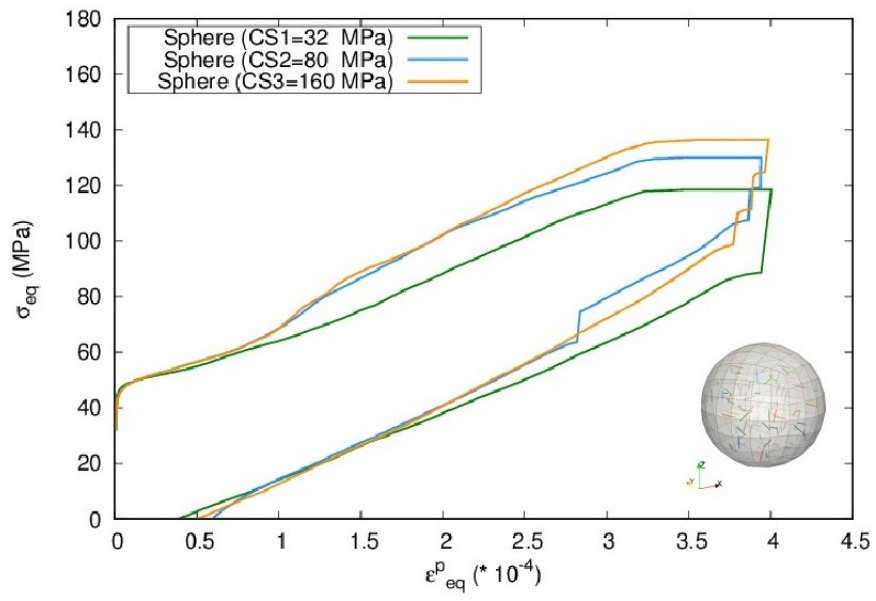
step 1090 and step 1100 in Figure 5.20). This interaction promotes dislocations activity on "deviate of long path" (red) via single arm source (*cf.* step 1250 and step 1300 in Figure 5.20) without much stress increment; thereby leading to less strain hardening, predominantly in Cigar grain which has a higher aspect ratio than Sphere and Kacahuete grains. This type of hardening (single arm sources) is commonly seen in DD simulations on micropillars with aspect ratios of ~ 3 [141, 178, 179].

5.3.3 Influence of grain shape on cross slip

The contribution of dislocation interactions (especially the collinear interaction among cross slip systems) leads to a decrease of strain hardening in elongated grains (*cf.* Section 5.3.2). To emphasize more on the strong collinear interaction, simulation results of Sphere, Kacahuete and Cigar grains at two different critical cross slip stresses of CS2=80MPa and CS1=32MPa were performed and are presented along with the results of the simulations with a critical cross slip stress of CS3=160MPa (i.e., no cross slip) in Figure 5.21 (a).

In all the three comparative plots of Figure 5.21, a low critical cross slip stress CS1= 32MPa is observed to decrease the strain hardening capacity. At the macroscopic level, the critical cross slip stress itself does not show a dominant influence when compared against the grain aspect ratio (*cf.* Figure 5.21). But, this does not mean that cross slip has no influence on the dislocation activity in the grain. The changes in the dislocation activity influenced by the cross slip mechanism and also the aspect ratio of the grain can be analysed by plotting the plastic deformation behavior on each slip system.

The equivalent plastic strain values extracted for the unloading part of Sphere, Kacahuete and Cigar (*cf.* Figure 5.22(b)) at an equivalent stress of $\sigma_{eq} = 50MPa$ for critical cross slip cases CS1 and CS3 are shown in Figure 5.22(a). The equivalent plastic strain is observed to be higher for grain with high aspect ratios. The observation remains intact for the cases with and without cross slip, further highlighting a greater dislocation storage capacity in grains with high aspect ratios.



Chapter 5. Influence of grain morphology on intragranular backstress predictions

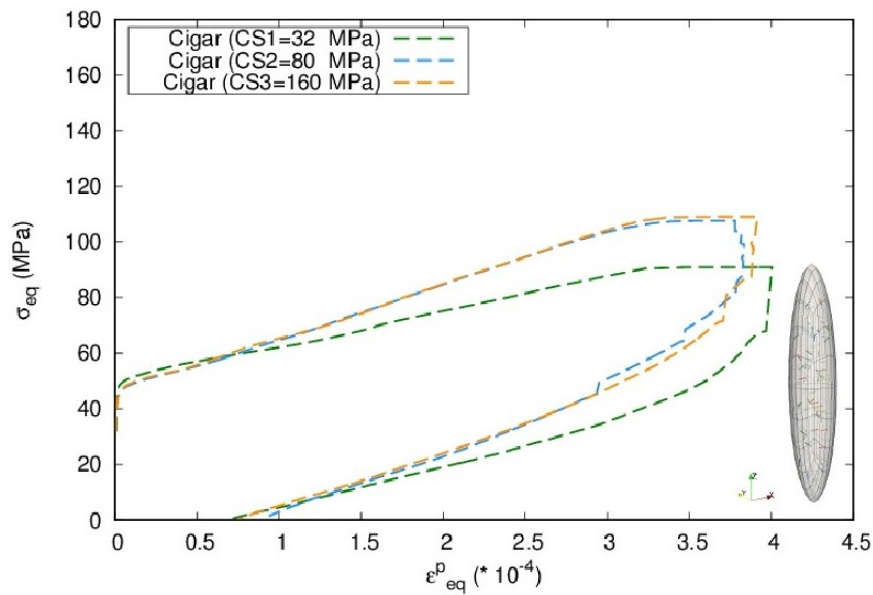


Figure 5.21 – Comparison of equivalent stress versus plastic strain response in (a) Sphere, (b) Kacahuete and (c) Cigar grains, respectively at different critical cross slip stresses (CS1, CS2 and CS3)

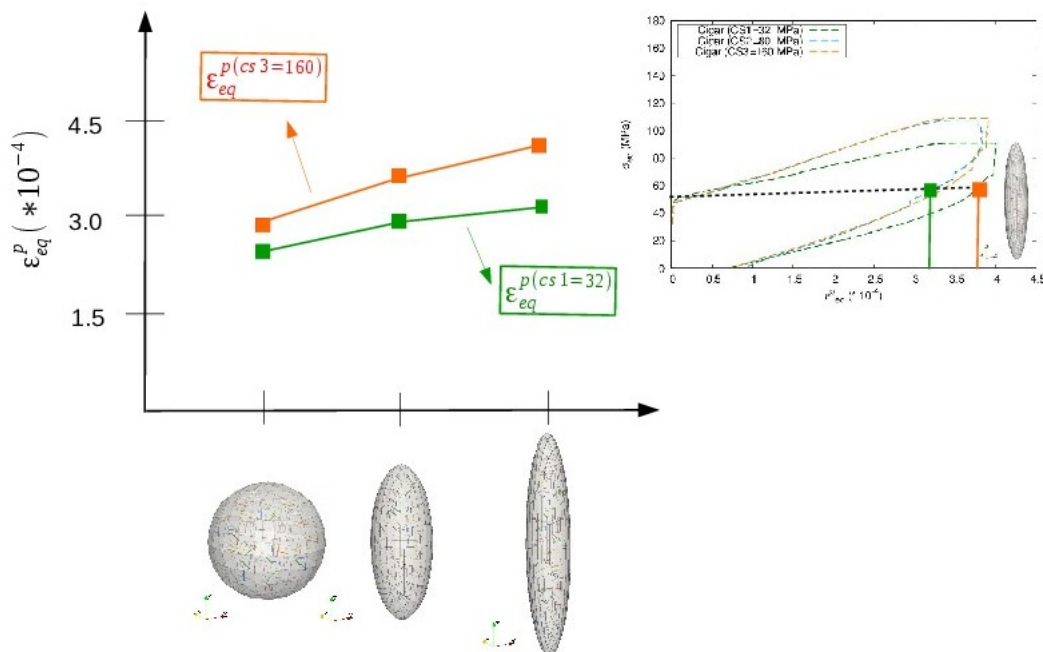


Figure 5.22 – (a) Comparison of equivalent plastic strain of Sphere, Kacahuete and Cigar at equivalent stress $\sigma_{eq} = 50 MPa$; (b) Extraction of equivalent plastic strain values for Cigar grain

5.3.4 Influence of cross slip on dislocation activity

In FCC materials, apart from pile up of dislocations on slip systems, a significant contribution to strain hardening behavior also arise from the mutual interaction of dislocations on different slip systems. A generalized tensor relating the mutual interactions has been proposed [70] as,

$$\tau_c^i = \mu \mathbf{b} \sqrt{\sum_j a_{ij} \rho_j} \quad (5.7)$$

where τ_c^i is the critical resolved shear stress on the slip system (i); μ is the shear modulus; ρ_j is the dislocation density on slip system (j) and the coefficients a_{ij} refers to the components of a matrix that describe the average interaction strength between slip system (i) and slip system (j).

In FCC crystals, four major types of interactions exist, whose coefficients are needed to describe the slip system interactions. The four types of dislocation interactions are already presented in Section 4.3.6 of Chapter 4, but are again listed below:

1. Glissile junction
2. Collinear interaction
3. Lomer lock
4. Hirth lock

DD simulations have been used to extract these coefficients [47, 107, 153]. It has been found that simultaneous dislocation activity on the primary slip system and its corresponding cross slip (or deviate) system is prohibited by the high strength of collinear interaction. The self-interaction coefficient for this interaction is often large and is close to that of a Lomer interaction [106]. Particularly in multislip conditions, the strong collinear interaction favours dislocation activity on the slip system that experiences the weakest global interaction within the microstructure [153]. These observations reveal the importance of collinear interaction on slip system activity. It is interesting to address the importance of such an interaction in elongated grains. Recently, a new dislocation multiplication mechanism based on glissile junctions

Chapter 5. Influence of grain morphology on intragranular backstress predictions

has been found to produce a significant contribution to the plastic deformation within a considered size and density regime [167]. But, the strength of glissile junction in comparison to the already known, collinear interaction is very low. In any case, the new glide system as a consequence of the formation of glissile junction will also change the dislocation slip activity in elongated grains. If the strength of such an interaction is significant, like in the case of collinear interaction, it will in turn influence the backstress experienced by dislocations. It should be noted that, the contribution of glissile junction based new multiplication mechanism has not been accounted for in the present study.

To emphasize only the changes in the dislocation activity influenced by both the cross slip mechanism and the grain shape, plastic deformation behavior on the four highly active slip systems (*cf.* Figure 5.2) and their corresponding deviate systems (*cf.* 5.4) are plotted together for two different critical cross slip stresses equal to CS1=32MPa (cross slip value at 300K) and CS3=160MPa (no cross slip) in the two extreme grain shape cases of Sphere and Cigar grains.

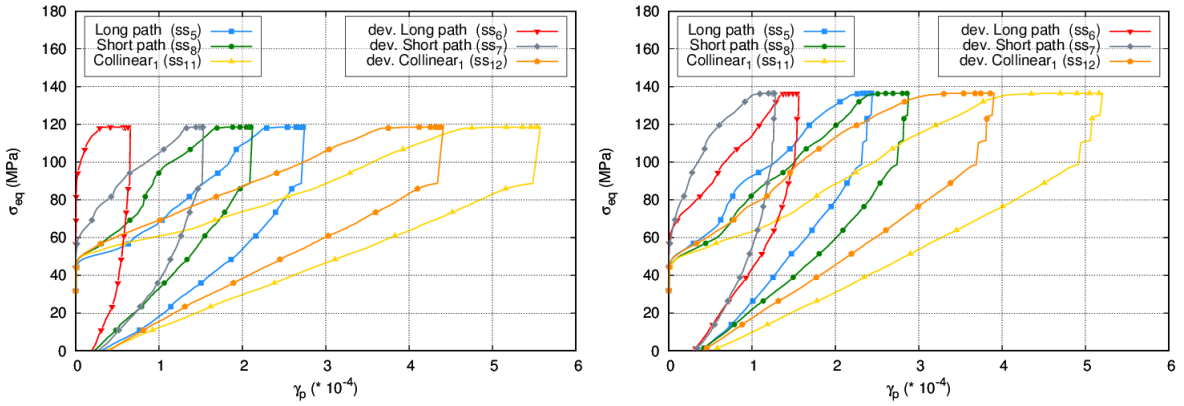


Figure 5.23 – Comparison of plastic deformation behavior on highly active slip systems and their corresponding deviates in Sphere at CS1 and CS3, respectively

In equiaxed (Sphere) grains, with no cross slip (*cf.* plot CS3 in Figure 5.23), DD simulations predict that even the slip systems with similar Schmid factors do not plastically deform at the same rate. As reported by Madec, there is a strong influence of collinear interaction. As the predominant plastic deformation was found to be carried by "Collinear1" (yellow) and "deviate of Collinear1" (orange) in both the cross slip cases of CS1 and CS3, the strong inter-dependency between these cross slip systems is not influenced in the case of equiaxed grains. In other words, Madec's observation of strong collinear interaction promoting either of the cross slip systems is not observed in equiaxed grains. So, in terms of back

stresses developing on the primary slip system and its corresponding cross slip system/s, one can first measure the average back stress developed on both the systems (primary and cross slip systems). Later, the aggregate back stress on primary and its corresponding cross slip systems can be distributed according to the respective Schmid factors, the angle which the primary system makes with long axis of the grain and also the angle which the deviate system makes with the long axis of the grain *triad*. Alternatively, the angles made by primary system and deviate system with the long axis of the grain can also be analysed in terms of the area available for the dislocation to glide on respective slip systems. But, here, we introduce the Schmid factor, primary angle and deviate angle *triad*, which is used for back stress analysis in the Section 5.4.1.

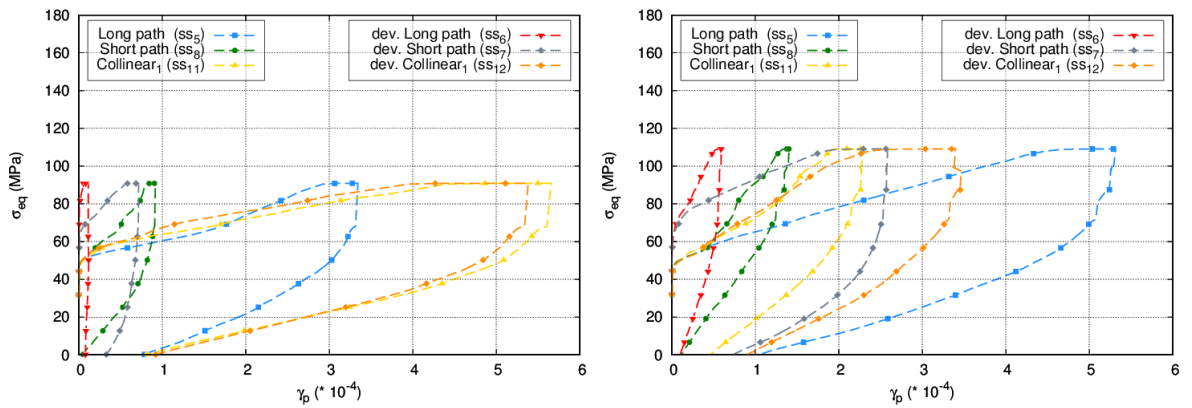


Figure 5.24 – Comparison in terms of plastic deformation behavior on highly active slip systems and their corresponding deviates in Cigars at CS1 and CS3, respectively

A clear justification of the dependency of Schmid factors, primary and deviate angles triad on the dislocation activity is shown in the plastic deformation behavior of CS1 and CS3 in Figure 5.24. The first observation of the shift in the dislocation activity of "Collinear1" (yellow) and "deviate of collinear1" (orange) when CS3 results of Sphere and Cigar grains are compared; the second observation of a change in the dislocation activity of "Short path" (green) and "deviate of short path" (silver) in CS3 results of Sphere and Cigar grains also highlight a systematic change in plastic deformation behavior which may be present. Analysing such trends in the plastic deformation coming from the grain aspect ratio will be useful to build upon enriched back stress formulation for phenomenological CP models.

5.4 Discussion

5.4.1 Implications for CP models: average back stress on slip systems

DD simulation results need to be analysed in such a way that they are useful for enhancing the formulation of continuum crystal plasticity models. Hence, the average back stress on each slip system is determined as the slopes of the stress strain curve. An example of measurement of the average back stress on "Long path" (blue) in Sphere, Kacahuete and Cigar shapes is presented in the Figure 5.25.

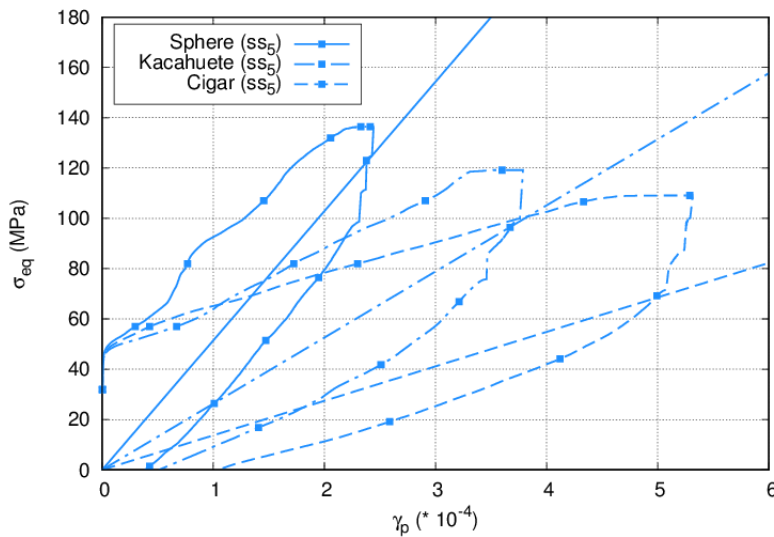


Figure 5.25 – Variation of σ_{eq} with γ_p involving an unloading step to quantify back stress whose magnitude is represented by the slope on "long path" (blue) of Sphere, Kacahuete and Cigar grains

The average back stress values of the four active slip systems and their corresponding deviates are represented for Sphere, Kacahuete and Cigar as shown in Figure 5.26 for critical cross slip stress equal to $CS3=160\text{MPa}$. The four active slip systems along with their deviates are labelled with their proposed abbreviated names. Long path can be read as LP and the deviate of long path as dLP. Short path follows the notation SP and its corresponding deviate as dSP. The highly active cross slip pair follow the same abbreviations according to their names; collinear1 being CP1 and collinear2 being CP2. Along-side the abbreviated names, Schmid factor, primary angle in degrees (angle which the slip plane makes with the long

axis of the grain) and deviate angle in degrees (angle made by the corresponding cross slip plane with long axis of the grain) are also presented.

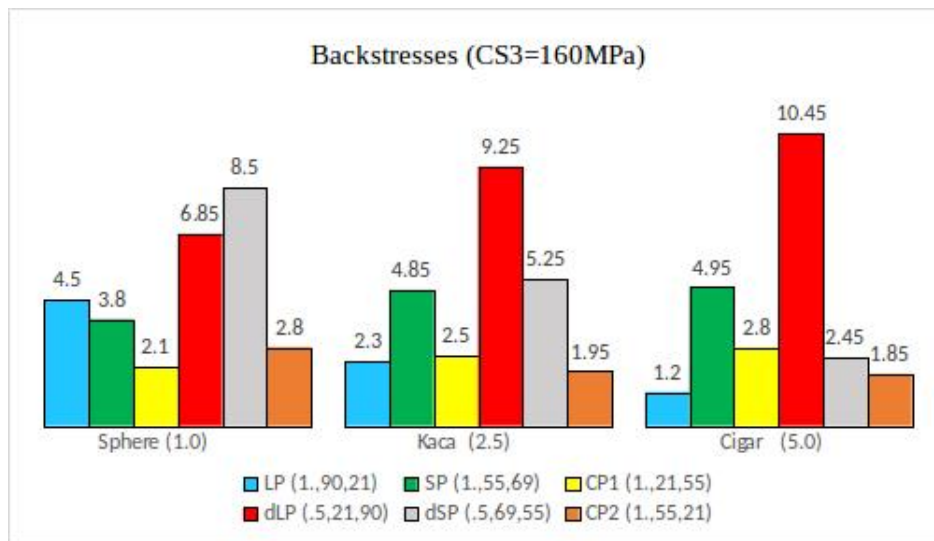


Figure 5.26 – Average back stresses on slip system of interest in Sphere, Kacahuete and Cigar grains at CS3; Labels are presented as abbreviation of the prescribed new names along with the Schmid factor, primary and deviate angles triad

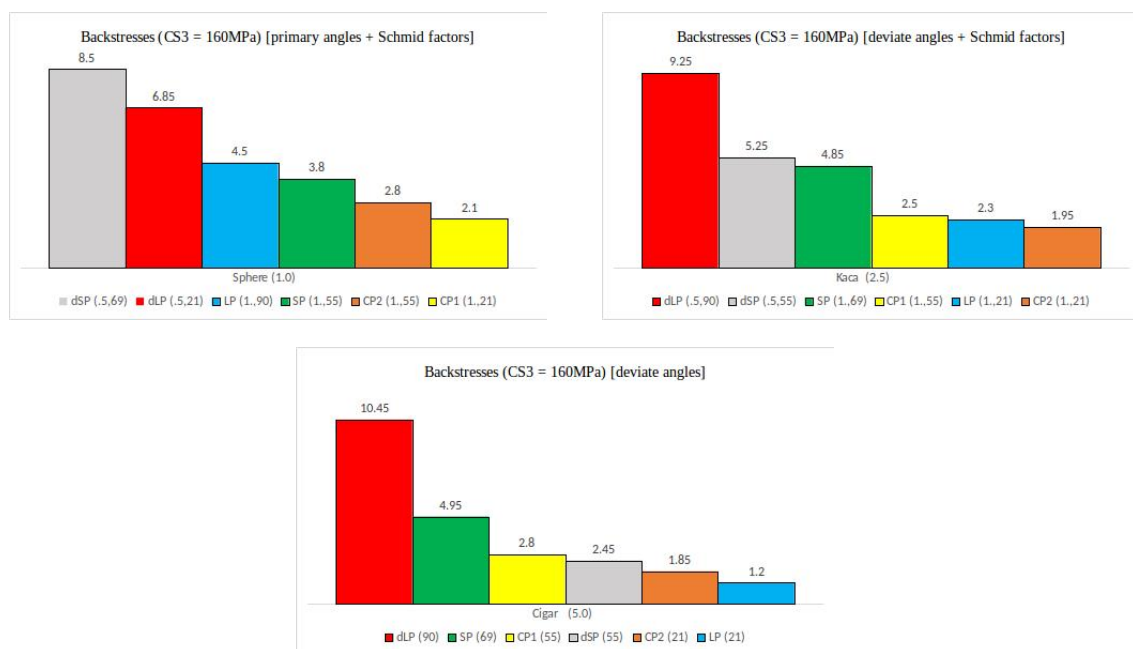


Figure 5.27 – Rearranged average back stresses on slip system of interest in Sphere, Kacahuete and Cigar grains at CS3

As measured average back stress values on the four most active slip systems and their corresponding deviates are presented in Figure 5.26. Average back stress

Chapter 5. Influence of grain morphology on intragranular backstress predictions

systematically increase with increasing aspect ratio of the grain. In Sphere shape, the trend in the evolution of the magnitude of back stresses decreases with an increase of the primary angles as shown in the Figure 5.27. The measured back stress values still were based on Schmid law in Kacahuete, but were not influenced by the primary angles any more. They decrease with a decrease in the deviate angles. In Cigar, a complete change in the trend of average back stresses is observed. The dependence of Schmid factors is over-powered by the strong collinear interaction among the primary and cross slip systems. An increase in the back stress is only dependent on the increase of the deviate angles. The complete shift to the dependence on only the deviate angles is highlighted in the Figure 5.27. Validating the dependence on only the deviate angles is the dislocation microstructure of primary and deviate system sets in Cigar at CS3 (*cf.* Figure 5.28). Concentration of plastic deformation on a particular slip system is prevented in elongated grains (Cigar) by the cross slip mechanism. This effect is strong when the primary and deviate systems are sharing a common Schmid factor, like in the case of collinear1 (yellow) and deviate of collinear1 (orange) as shown in the Figure 5.28.

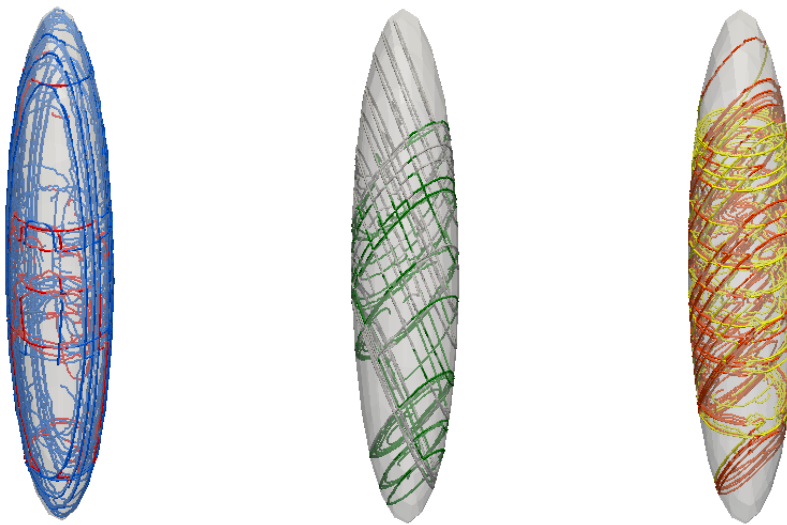


Figure 5.28 – Dislocation microstructure in Cigar grain at critical cross slip stress of CS3=160MPa in "long path", "short path" and "collinear1" and their respective deviates

Increase in the aspect ratio of the grain shows a systematic transition in the back stress values from a Schmid factor and primary angles based behavior in equiaxed grain to only deviate angles dominated behavior in elongated grains. This trend also highlights the strong role of collinear interaction in spheroidal grain with high aspect ratios. The strong collinear interaction also has its influence on

the Schmid law based behavior of elongated grains. Non-Schmid type behavior, which is presently observed in Cigar grain, is commonly evident in BCC crystals. Plastic anisotropy in BCC crystals is mostly linked to deviation of the $\frac{a}{2} \langle 111 \rangle$ screw dislocation from the $(1 - 10)$ average glide plane. Recent, DFT calculations, apart from validating that the origin of plastic anisotropy from the screw dislocation; were also successful in explaining the underlying physics behind the non-Schmid behavior in BCC metals at low temperatures [50]. A modified parameter-free Schmid law proposed can be adopted to mesoscale models to predict non-Schmid behaviors atleast for BCC crystals.

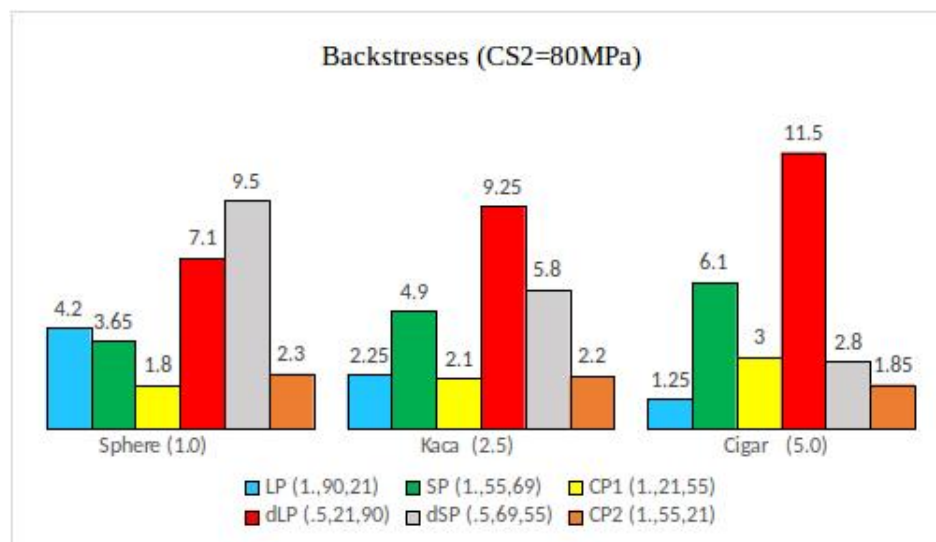


Figure 5.29 – Average back stresses on slip system of interest in sphere, kachuete and cigar at CS2; Labels are presented as abbreviation of the prescribed new names along with the Schmid factor, primary and deviate angles triad

The trend in the changes of average back stress values with an increase in the grain aspect ratio are also observed for the critical cross slip stress, CS2=80MPa as depicted in Figure 5.30. According to these observations, the grain aspect ratio itself has a more dominant influence than the grain orientation on the magnitude of the back stresses. But, this also had to be tested for various other sets of Miller indices in order to be adapted as an enriched local rule in phenomenological crystal plasticity models.

Chapter 5. Influence of grain morphology on intragranular backstress predictions

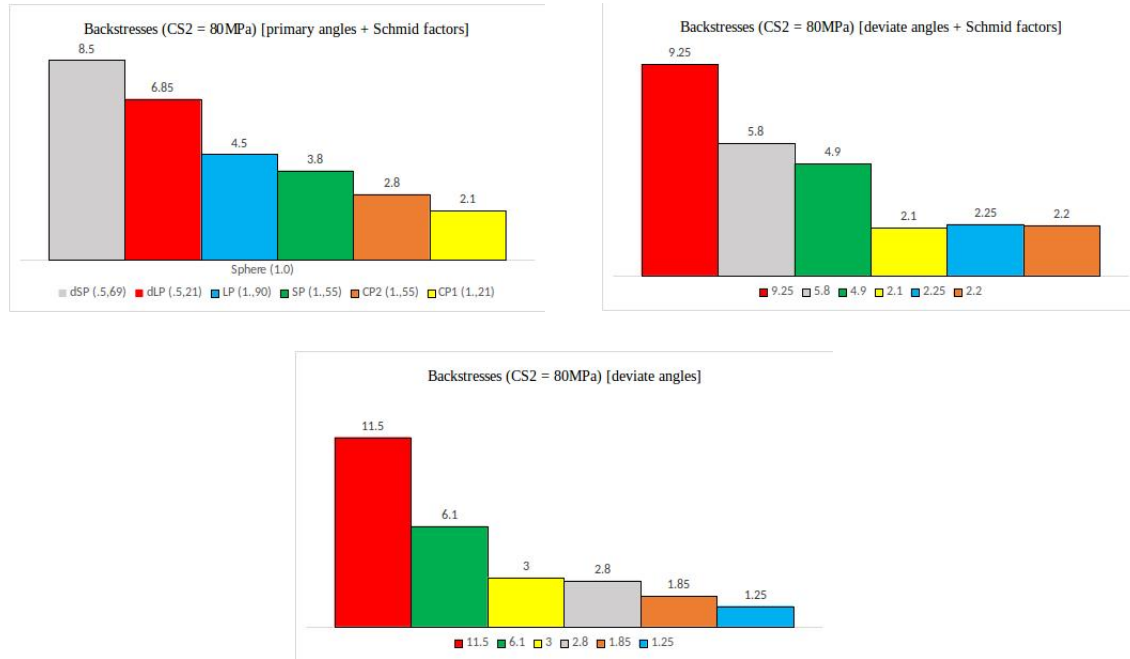


Figure 5.30 – Rearranged average back stresses on slip system of interest in sphere, kacahuete and cigar at CS2

5.4.2 Extension of the pile up model for predicting backstresses

Adapting the continuous-dislocation method ¹, analytical expressions for dislocation distribution and strain fields of double-ended and single-ended pile ups have been already developed for a 1D scenario [124]. The idealized 1D analytical expression for dislocation distribution in a pile up has been extended to a more generalized 3D case by Depres [43]. Depres's work on the extension of the continuous pile up model to 3D case has been reviewed in Appendix A. Further, as an extension to Depres's work, an analytical expression for non-equiaxed shape of dislocation pile up has been derived in Appendix B. Back stress predictions of the formula are compared against DD simulation results for single slip condition.

5.4.2.1 Validation of single (centred) dislocation pileup

When the shape of the grain is a cube, all the slip planes passing through the center of the cubic grain will have a unique slip plane dimension (length of the slip plane

¹continuous dislocation method assumes the pile up behavior being continuous and not discrete inside a grain

= side of the cube). One encounters a similar situation with a spherical grain. All the slip planes when passing through the center of the grain will have a unique slip plane dimension (length of the slip plane = diameter of the sphere). But, in spheroidal grains, the dimension of each slip plane is different and will depend on the angle between the slip plane normal and the long axis of the grain. This angle is referred as *primary angle* of the slip plane. The extended pileup theory derived in Appendix B also accounts the primary slip plane angles and can predict magnitude of back stress in non-equiaxed shaped dislocation pileups.

In this section, the extended theory is validated against results from 12 independent DD simulations. DD simulations were performed under the assumption that hardening in grains of different aspect ratios (Sphere, Kacahuete, Cigar) are coming only as the contribution from a single dislocation source at the center of the grain. A single dislocation was placed on four different slip systems (LP, SP, CP_1, CP_2) to understand how hardening in each grain is influenced with respect to the angle between the slip plane normal and long axis of the grain.

The plastic deformation Υ_{3d}^{pu} before substituting V and l is

$$\Upsilon_{3d}^{pu} = \frac{\pi}{6} \beta_s \frac{(1-\nu)}{\mu V} l^3 \tau_{app}$$

where,

$\beta_s = \frac{\beta}{\sqrt{(\sin\theta)^2 + (\beta\cos\theta)^2}}$, is the aspect ratio of the slip plane.

μ and ν are Shear modulus and Poisson's ratio

β is the aspect ratio of the grain

θ is the angle made by the slip plane normal with respect to the long axis of the grain

Υ_{3d}^{pu} is the plastic strain developed due to pileup when a shear stress τ_{app} is applied on the slip plane. Substituting the volume of the grain, V , and length of the slip plane, l , in the above expression can provide us a theoretical estimate of the magnitude of back stress on the slip system.

In the case of single dislocation pileup, the analytical expression accurately predicts the back stress developed in the grain when cross-slip is not activated. It is evident from Figure 5.31(a.) that the improved formulation accurately captures the back stress values changing with the aspect ratio of the grain and also the primary angle. Whereas, when cross-slip is activated, the analytical formulation tends to under- or over- estimate back stress (*cf.* Figure 5.31(b.)). The effect of

Chapter 5. Influence of grain morphology on intragranular backstress predictions

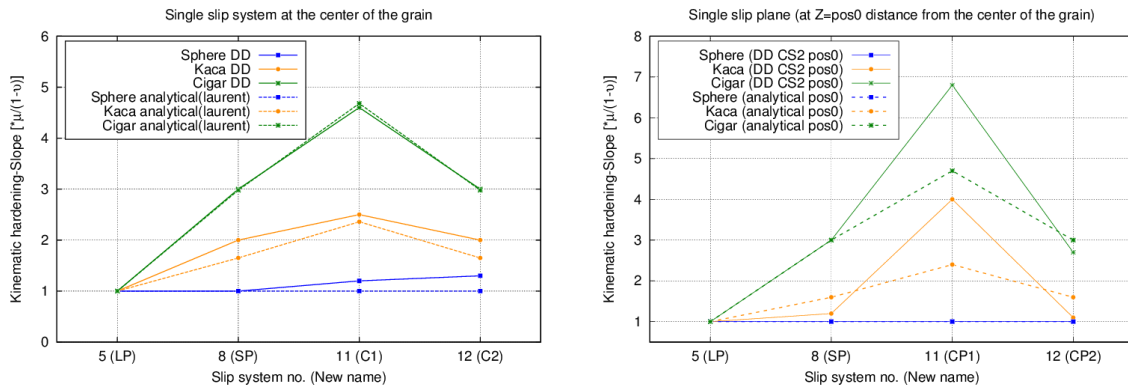


Figure 5.31 – Comparison of DD (centred) results against extended pileup model a.) without cross-slip and b.) with cross-slip

cross-slip can be accounted into the analytical formula by incorporated the area of the deviate system along-side the primary system. This requires more rigorous study of cross-slip at the slip system level in a single grain. This part has not been carried out in the present study.

5.4.2.2 Validation of non-centred single dislocation pileup

It has been shown in Section 5.4.2.1 that the derived analytical expression predicts back stresses accurately when the slip plane is centred in the grain.

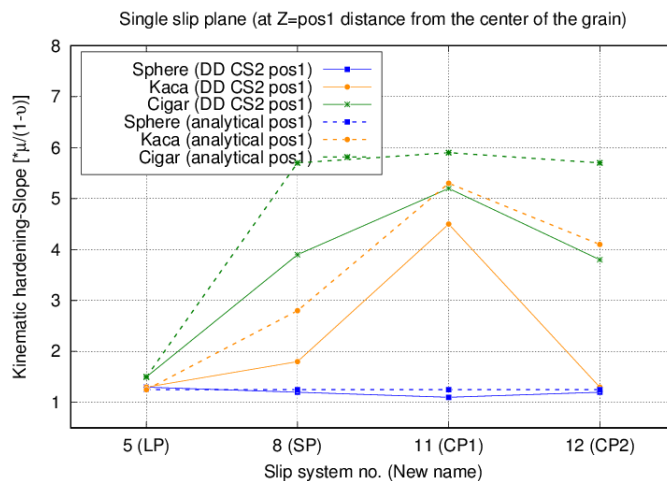


Figure 5.32 – Non-centred plane with cross-slip(CS2=80MPa)

Figure 5.33 – Comparison of DD (non-centred) results against extended pileup model

To tackle multi-slip condition, non-centred slip planes should also be considered. The derivation of analytical expression for a single non-centred slip plane is carried in Section B.2.1 of Appendix B. Results from DD simulations are now compared against the predictions of the analytical formula for a dislocation on a non-centred slip plane inside the grain. Figure 5.32 shows that the enriched pileup based formula slightly under- estimates the back stresses when the slip plane is non-centred. The single dislocation pileup formula is further extended to predict back stresses during multi-slip condition. As there is still work to be done on the multi-slip formulation, the concerned derivation and validation procedure are presented in Appendix B.

5.5 Conclusions

The important conclusions made in the present chapter on grain shape are presented here:

1. Increasing the aspect ratio of spheroidal grain decreases the strain hardening capacity of the grain. The elongated grain shape enhances the dislocation storage capacity of the grain; thereby imparting slightly more permanent deformation in the grain.
2. Collective contribution of single arm sources and double ended FR sources to plastic deformation was observed in grains with higher aspect ratios.
3. A decrease of the aspect ratio of the grains, which enhances the collinear interaction among slip systems, influence the slip system activity in the grain.
4. The slip system activity and the corresponding magnitude of back stresses changes to a non-Schmid behavior. The dependence shifts to the angle the deviate system makes with the long axis of the grain.

6 Collective influence of grain and dislocation density parameters on plasticity of thin films

SIZE effects in polycrystalline thin films are generally a consequence of a decrease in the average grain size with film thickness. In Pd thin films, the average in-plane grain size $d \approx 30\text{nm}$ remains unchanged for films of different thicknesses [31]. One or more dominant deformation mechanisms along with the microstructural features are believed to play an influential role in dictating the macroscopic response of thin films. In this chapter, 3D DDD simulations on polycrystals are performed to probe the fundamental mechanisms behind plastic deformation behavior of Pd thin films.

6.1 Introduction

Metallic thin films are based at the core of many MEMS/NEMS devices [94, 166], flexible electronic systems [168] and in thin membrane technology. These nanocrystalline (nc) metals present *excellent strength* but often suffer with the critical issue of *low ductility* [128]. Enhanced strength of nc metals is attained by controlling the grain size (Hall 1951 and Petch 1953) to be a bit larger than the transition value around 10nm to 30nm [201]. In very small grains $d < 10\text{nm}$, an inverse relationship (negative slope) is observed between strength and grain size. The change in the Hall-Petch slope at 10nm is not abrupt and can be envisaged by linear decrease of slope in the transition region ($d = 10 - 30\text{nm}$ to $100 - 300\text{nm}$) (*cf.* Figure 6.1). The slope in the transition region is not unique and depends on the magnitude and distribution of grain size [3].

Such changes in the Hall-Petch slope can be manifested by differing deformation mechanisms that control plasticity. For grain sizes $d > 100\text{nm}$ to 300nm , plastic deformation mostly occur due to dislocation-based mechanism, such as dislocation slip, dislocation pile up, junction formation, annihilation, forest hardening etc.,. In contrast, very small grains $d < 10\text{nm}$ show low strain hardening capacities due to the confinement of grain size. In such cases, different thermally activated mechanisms

Chapter 6. Collective influence of grain and dislocation density parameters on plasticity of thin films

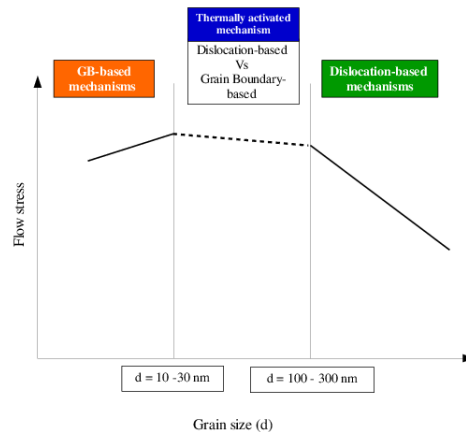


Figure 6.1 – Model plot showing transition in deformation mechanisms when changing the grain size

involving GB rotation [199], GB sliding [170], GB migration [88,117] and nucleation at GBs [109,165] start to dictate the overall response of the material. In addition to GB-based thermally activated mechanisms, dislocation-based thermally activated mechanisms can be simultaneously present when grain size is in the transition regime between 10-30nm to 100-300nm. Depending on the microstructure details and external conditions (temperature, loading etc.), either GB-based or dislocation-based thermally activated mechanisms (sometimes both can work together) will dictate the materials response. Thermally activated mechanisms which lead to high rate sensitivity [158] along with with strain gradients can help in restoring ductility [139].

Moderate to high ductility has been observed in pure Al films [34], Au films [97] and Cu films [203] with nano-sized grains. The high rate sensitivity of these metals in most of the cases is expected to be dominated by GB mechanisms [83,109,165,170]. In contrast, moderate to high ductility (upto 12%) in Pd thin films with growth nano-twins does not show any evidence of plasticity dominated by grain boundary mechanisms [190]. In such cases, the ductility is believed to be driven by thermally-activated dislocation mechanisms. Dislocation mobility when thermally activated showed a more uniform dislocation microstructure; in-contrast, a non-uniform microstructure was obtained in conditions where athermal dislocation-dislocation interactions govern plastic flow [153]. Thermally activated mechanisms can be highly influenced by the microstructural features (grain size, grain shape, grain orientation etc.) of thin films.

Additionally, recent experimental investigations reported significant dislocation

accumulation in nc Pd thin films [31], nc Ni [116, 195] and Pt [190]. The initial dislocation density in as-deposited nc Pd films is one order of magnitude higher than the ones generally observed in nc metals [31, 93]. The fine microstructure of these films along with typical deposition processes can lead to a high density of defects. The presence of pre-existing dislocations and growth twins will further enhanced the dislocation storage capabilities. In addition to the reported increasing strength with decreasing film thickness, a significant grain size distribution was reported in these films [33]. The presence of sufficiently small and large grains in the polycrystal will generate stress heterogeneities. Corresponding strain gradients will influence the plastic deformation behavior as well. Plastic deformation was reported to be affected not only by the mean grain diameter but also by the grain size distribution [105].

Discrete dislocation dynamics (DDD) simulations demonstrate excellent capability to reproduce the strain hardening response of the material when the plastic deformation is still mediated by collective motion of dislocations. Earlier, the use of DD simulations to predict polycrystalline thin film behavior has been mostly limited to two-dimensional simulations. Dependence of film thickness on the tensile strength in free-standing passivated and unpassivated copper films was studied by Nicola and co-workers using 2D DDD simulations [111, 136]. The yield strength of unpassivated films with sufficiently larger grains was reported to be independent of film thickness. But, for thin unpassivated films and for films passivated on one side, the yield strength increases with decreasing thickness. Additionally, passivated and unpassivated film showed difference in Bauschinger effects [111]. Hartmaier and co-workers performed 2D DD simulations to investigate the time-dependent irreversible deformation of a thin film constrained by a substrate. In their simulations, both climb and glide has been together accounted. Despite the 2D limitations, film thickness dependent transition between creep dominated and dislocation glide dominated deformation were in good agreement with experiments [87]. Li and co-workers introduced a dislocation-grain boundary penetration model in 2D DDD simulations to model polycrystal behavior. It was observed that the Hall-Petch relation still holds true for both penetrable and impenetrable GBs. The Hall-Petch slope was observed to be dependent on the applied strain, grain misorientation angle, grain arrangement pattern etc., [121]. Kumar and co-workers used a line tension approach [104] to model slip transfer across tilt grain boundaries. In their 2D simulations, Bauschinger effect was observed to decrease when the dislocation transmission across GBs was enabled [110]. Results from these 2D DD simulations provided interesting perspectives on polycrystal behavior.

Chapter 6. Collective influence of grain and dislocation density parameters on plasticity of thin films

However, 2D DD models cannot accurately capture the exact three dimensional nature of dislocation interactions. Following a 3D approach, the plastic deformation of a polycrystalline thin film of a FCC metal was simulated by considering the dislocation motion in a single columnar grain. Grain boundaries were considered to be either impenetrable obstacles or free surfaces. Further, the inverse dependence of flow stress on film thickness was reported [187]. Such works (based on a single grain to represent the polycrystal behavior) cannot accurately predict the plastic deformation mechanisms as influenced by the long-range effects of dislocations. 3D DDD codes with improved computational efficiencies make it possible to model polycrystal behavior using 3D DDD simulations. Under the assumption that all dislocation sources are located at grain boundaries, a new interpretation of size-dependent plasticity of thin films based on the probability of activating grain boundary dislocation sources was proposed using 3D DD simulations [55]. More recently, Zhou and co-workers [202] performed 3D DD simulations to investigate the plasticity of free-standing polycrystalline thin films. Permitting cross-slip of dislocations and accounting for dislocation transmission across GBs using line tension model, the yield strength of films was observed to scale inversely with film thickness. Further, the influence of grain shape in changing the yield stress dependence with grain size was addressed. In films with pancake-like grain, dependence of yield stress on grain size gradually becomes weaker for decreasing film thickness. In contrast, the strength of needle-like grains in films with high aspect ratios show increased dependence on grain size [202]. For accurately predicting the behavior of polycrystals with nano-sized grains, modeling accurately the grain size distribution is necessary. None of the 3D DDD studies performed on polycrystals accounted for the grain size distribution in their simulations. With this core idea of accurately incorporating the grain size distribution in polycrystals, 3D DDD simulations performed will be directly compared to experimental results on Pd submicron films [31, 33].

The main objective of this chapter is to address the collective influence of grain parameters (such as grain morphology, grain orientation and grain size) and dislocation density distribution on the overall response of polycrystalline thin films. This chapter is organised as follows. In Section 6.2, the modeling environment established with Gmsh [75] to generate polycrystals of different grain size distributions is explained. After describing the simulation environment in Section 6.3, results of 3D DDD simulations on polycrystals of different film thicknesses performed by varying grain size distributions, grain orientations and initial dislocation densities are presented in Section 6.4. Further discussion on the importance of

grain size distribution in Section 6.5 is followed by conclusions on the influential microstructural features and deformation mechanisms responsible for size effects in Pd thin films in Section 6.6.

6.2 Modeling polycrystals

Grain morphology has been observed to influence the dislocation slip activity in single grain (*cf.* Chapter 5). This emphasizes on modeling interfaces (GBs and free surfaces) correctly in polycrystals as first priority. Details at the GBs (like, dislocation-GB interactions) which may also influence the overall mechanical behavior of the film will only follow later (second priority). So, the DD simulations in this chapter were performed under the assumption that dislocation-GB interactions have a minimal/negligible influence on the plastic deformation behavior of thin film.

6.2.1 Generating polycrystal using Voronoi tessellation

To model a representative volume element of the highlighted region in Figure 6.2(b) with columnar grain morphology (*cf.* Figure 6.2(a)), an interface has been created with the Voronoi tessellation-based microstructure generator available in Gmsh [75] and DD polycrystal setup generator.

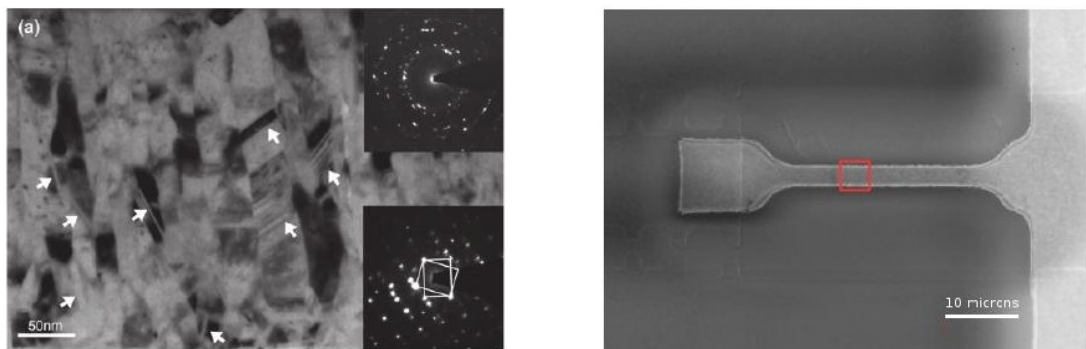


Figure 6.2 – (a.) Bright field image obtained on the cross-sectional FIB sample; (b.) Region of interest for modeling thin film behavior being highlighted in red [31, 93]

Depending on the position (X-, Y- and Z- coordinates) of the seeds in a box and the growth rate specified, a polycrystal microstructure can be easily generated via voronoi tessellation in Gmsh. Taking advantage of this tool, the Side and Top views of the generated polycrystal in Gmsh are shown in Figures 6.3(a) and 6.3(b),

Chapter 6. Collective influence of grain and dislocation density parameters on plasticity of thin films

respectively. Grains attained hexagonal shape owing to the positioning of seeds and similar growth rates specified to each seed.

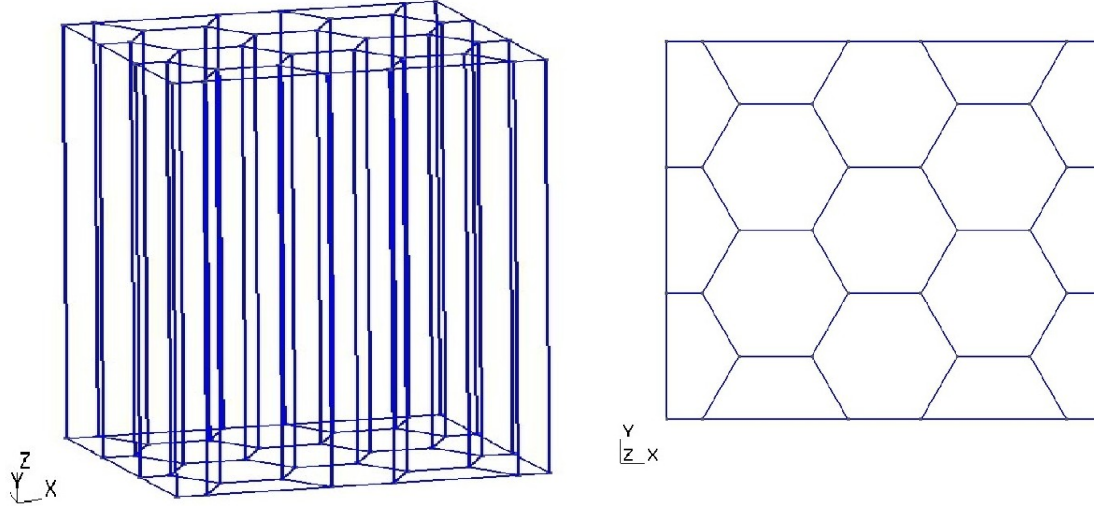


Figure 6.3 – (a.) Side view and (b.) Top view of the periodic (X- and Y- directions) polycrystal microstructure generated by Gmsh using Voronoi tessellation

Then, the interface developed is invoked to replicate the generated polycrystal as an actual 3D polycrystal that is compatible with the DD code. Figures 6.4(a) and 6.4(b) shows the corresponding side and top views of the DDD polycrystal where each GB is represented as a *Facet*. As already mentioned in Chapter 4, a very high stress value ($\tau_{facet} = 10^{50} MPa$) is given to each facet as its property. This method is used to model GBs as infinite obstacles to dislocation motion.

Another important advantage of the created interface is the ease with which a *refined periodic mesh* can be generated for any arbitrary polycrystal. The use of refined polycrystal mesh as shown in Figures 6.5 (a) and 6.5(b) will decrease the computational burden while solving the boundary value problem to account for free surfaces in the simulation volume. A detailed explanation of the procedure followed to account for free surfaces is presented in Section 6.3.6.

6.2.2 Modeling grain size distribution in polycrystals

The Gmsh-DD interface developed also provides an unique advantage to model grain size distribution in a polycrystal. Variation of grain size in the polycrystal was possible by modifying the initial position of seeds and also the growth rate in Voronoi tessellation-based microstructure generator introduced in Section 6.2.1.

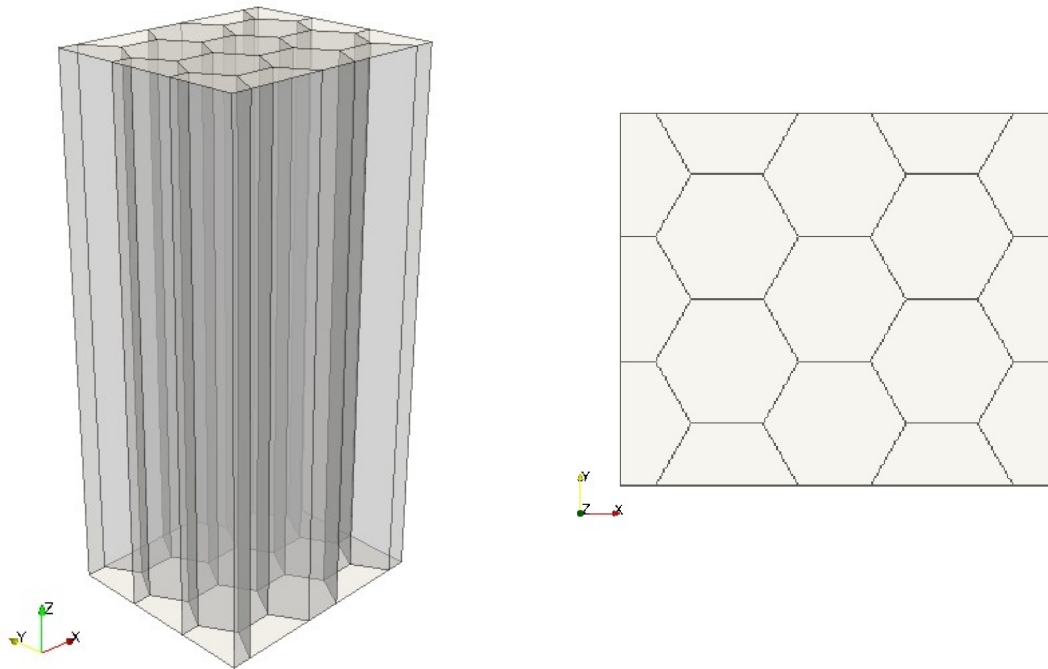


Figure 6.4 – (a.) Side view and (b.) Top view of the periodic (X- and Y- directions) polycrystal representing GBs as *facets*

Figures 6.6(a),(b) and 6.7(a),(b) show Side and Top views of the films with a larger and smaller grains in the center of the film, respectively.

6.3 Simulation setup

6.3.1 Polycrystalline 3D DDD model

A polycrystal version of the 3D discrete dislocation dynamics (DDD) code has been used for this study. In the polycrystal version of DDD code, dislocations in each grain move on their specific rotated lattices. The orientation of the lattice in each grain is represented by a cuboid-shaped texture object as shown in Figure 6.8. Complete details about the methodology of the 3D DDD code has already been presented in the Chapter 4. Even though no dislocation-grain boundary interactions were accounted for in the present study, it is worth mentioning that the long-range stress-field of dislocations will have an influence across grain boundaries. Due to this, the plastic deformation behavior of the polycrystal will be significantly different when only a single grain is modeled.

Chapter 6. Collective influence of grain and dislocation density parameters on plasticity of thin films

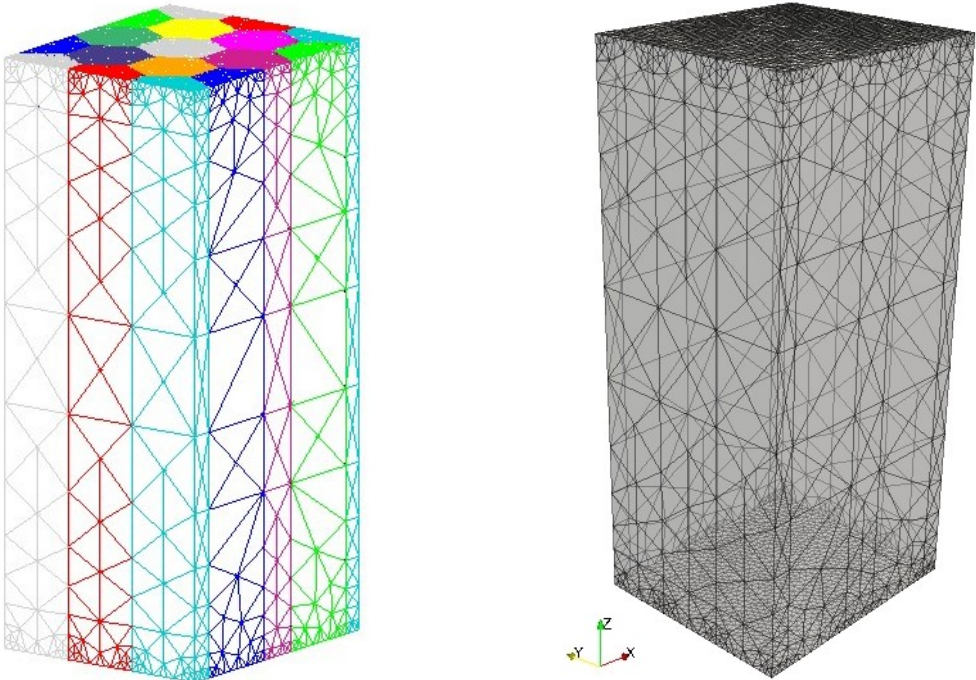


Figure 6.5 – Refined mesh created by Gmsh shown (a.) after importing to CASTEM (snapshot of the mesh from CASTEM) and (b.) corresponding mesh viewed using Paraview

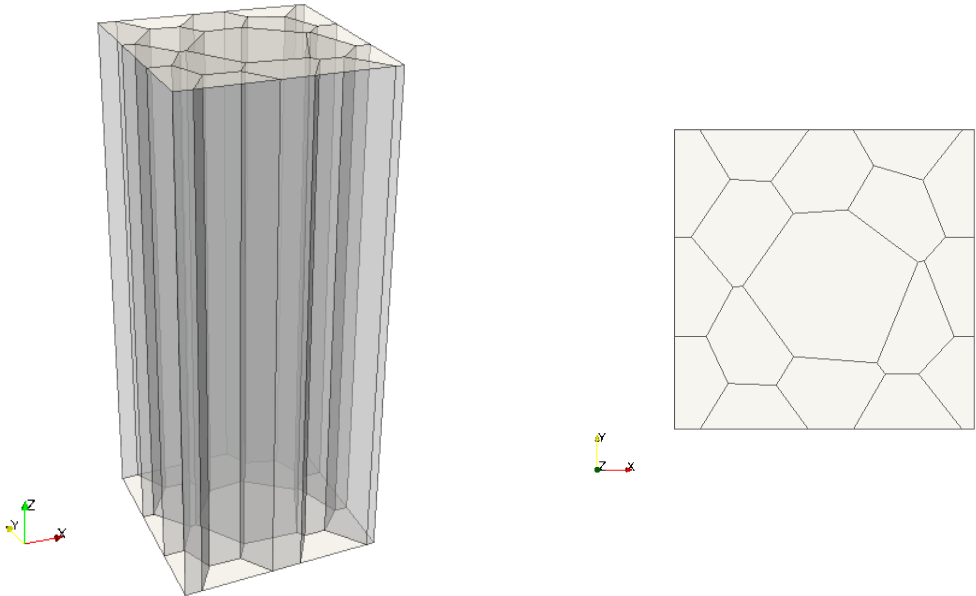


Figure 6.6 – (a.) Side view and (b.) Top view of the polycrystal with larger grain at the center of the film

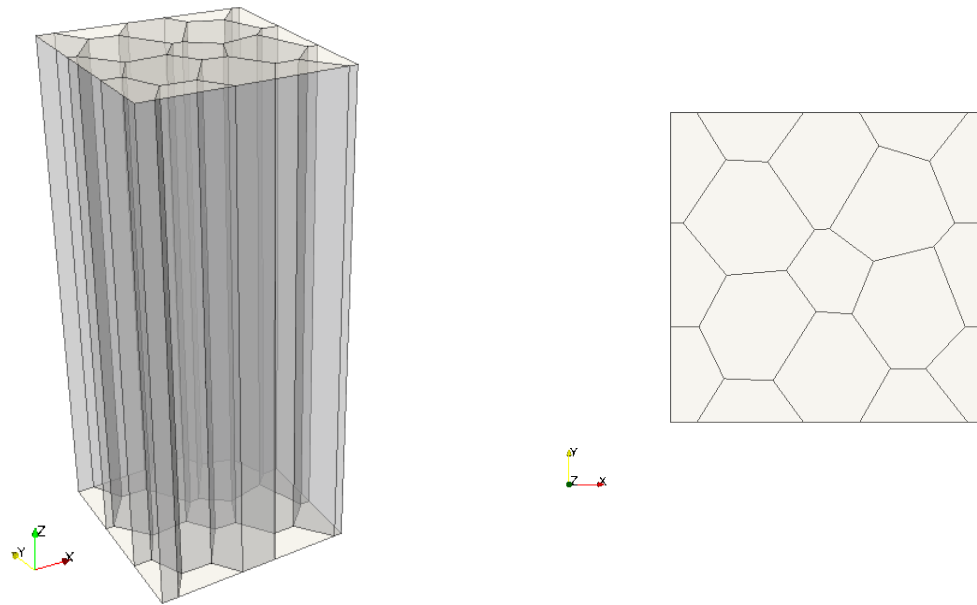


Figure 6.7 – (a.) Side view and (b.) Top view of the polycrystal with smaller grain at the center of the film

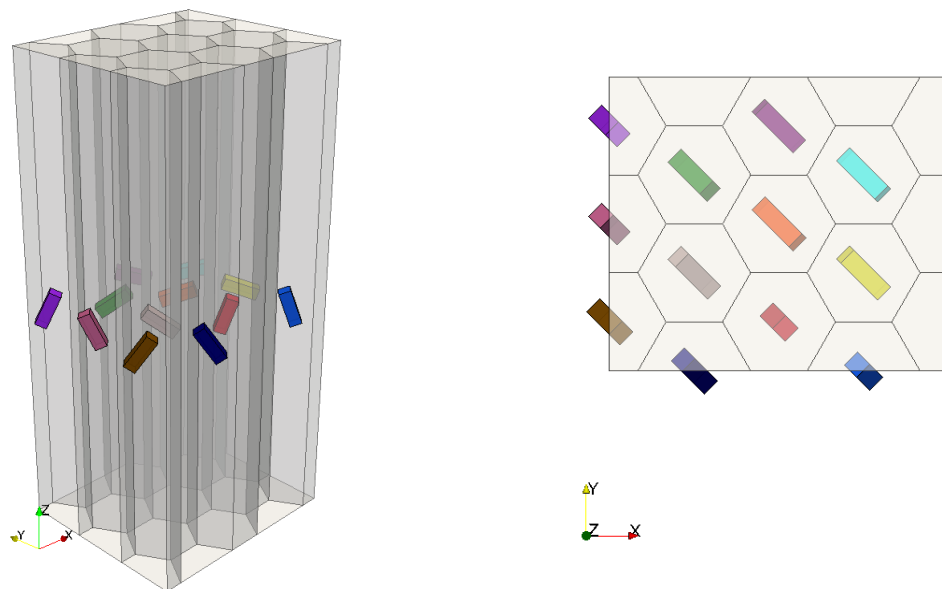


Figure 6.8 – (a.) Side view and (b.) Top view of the polycrystal with cuboid-shaped texture objects representing the lattice orientation of each grain on which respective dislocations move

6.3.2 Initial dislocation configuration

In 3D DDD simulations, Frank-Read sources (FRs) with different size distributions on each slip system are often used as initial dislocation topologies. Such configurations are widely used owing to the ease of generation and also for the sake of mathematical simplicity. For each FRs generated, its position (X-, Y- and Z- coordinates), orientation, length, Burgers vector, glide plane and the grain identity needs to be specified. The side and top views of the initial dislocation configuration generated as FRs in a polycrystal are shown in the Figures 6.9(a) and 6.9(b), respectively. When working with polycrystals with nano-sized grains of very high aspect ratios ≥ 5.0 , it becomes increasingly difficult to avoid influence of GBs during the activation of artificially pinned FRs. In such cases, directing towards a more stochastic approach (i.e., average of many simulations with different initial random FRs distributions) will be a computationally demanding task.

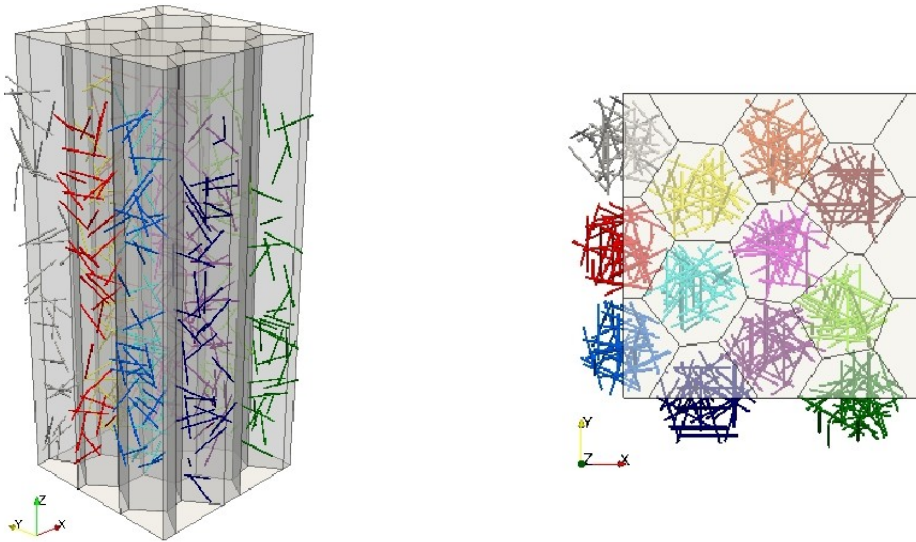


Figure 6.9 – (a.) Side view and (b.) Top view of the polycrystal with initial dislocation configuration as Frank-Read sources of same length

Complex initial dislocation configurations obtained by the relaxation of dislocation loops will not introduce artificial pinning points [131]. Administering almost a similar approach, instead of using image forces to drive the initial FRs, a constant external stress which is slightly higher than the activation stress of the FRs is applied (along the loading/X- direction) until a physical evidence of the bowing out of dislocations is observed. After which, simulation is still continued under zero external stress until an equilibrium configuration for dislocations is reached. The

total initial dislocation density (with FRs in the simulation volume) which was found to be $\rho_{initial} = 9.2 \times 10^{+14} m^{-2}$, rapidly increases due to the applied external load and stabilizes based on the dislocation configuration in the polycrystal. The total density plotted against number of simulation steps in Figure 6.10 shows evidence of equilibrium/relaxed dislocation configuration for simulations step ≥ 100 .

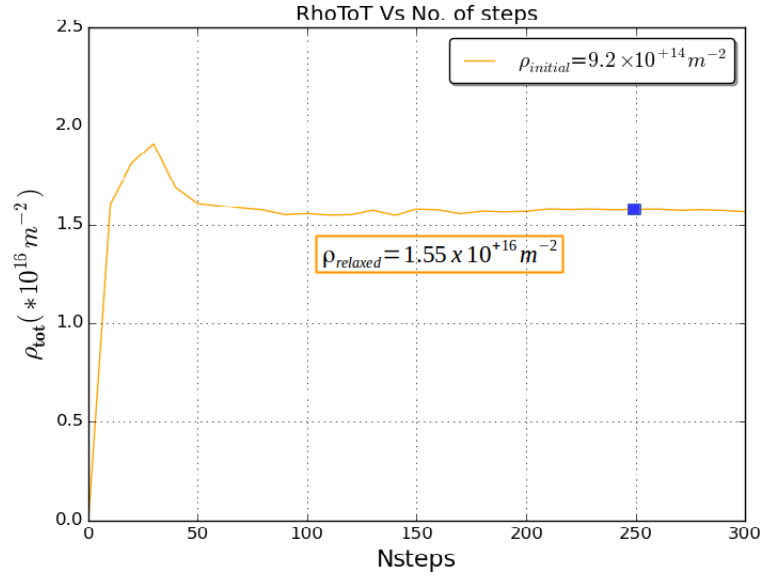


Figure 6.10 – Total dislocation density plotted against number of steps during relaxation test

The dislocation microstructure shown in Figure 6.11 has been extracted at simulation step 250 (*cf.* highlighted in blue in Figure 6.10). Corresponding total dislocation density $\rho_{relaxed} = 1.55 \times 10^{+16} m^{-2}$ is close to the experimental value measured by TEM in the Pd films [31]. The dislocation topology obtained will have a minimum density of artificially pinned sources. Further, a realistic dislocation configuration with dislocation loops, junctions, single arm sources and dislocations pinned at the free surfaces or GBs can be seen. Such relaxed dislocation configurations are used as initial dislocation arrangements for all the simulations performed during the study.

6.3.3 Identification of material parameters of Pd

Numerous control parameters pertaining to a specific material are used in discrete dislocation dynamics codes. For Pd, the material parameters obtained from the

Chapter 6. Collective influence of grain and dislocation density parameters on plasticity of thin films

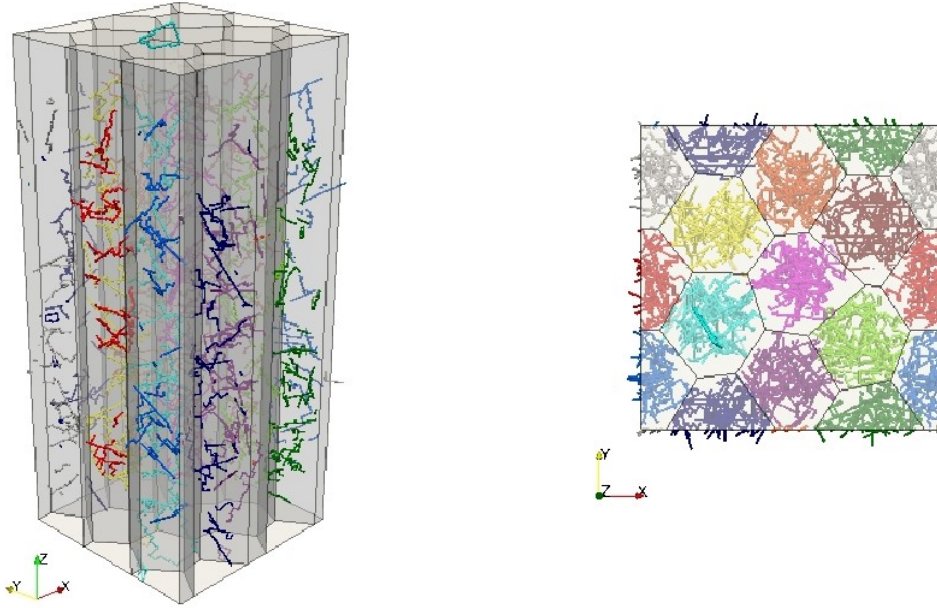


Figure 6.11 – (a.) Side view and (b.) Top view of the polycrystal with relaxed dislocation configuration extracted at relaxation simulation step no.250 (*cf.* highlighted in Figure 6.10)

literature and the ones that need to be identified are listed in Table 6.1.

Symbol	Quantity	Value	Source
E	Young's modulus	121000 MPa	[24]
μ	Shear modulus	44000 MPa	[24]
ν	Poisson ratio	0.39	[24]
$ b $	norm of Burgers vector	-	to be identified
γ	Stacking fault energy (SFE)	180 mJ.m^{-2}	[1]
V_{act}	Activation volume	$\sim 20.b^3$	[31]
B	Phonon drag coefficient	-	to be identified
τ_{III}	critical resolved cross slip stress	-	to be identified

Table 6.1 – Material parameters of Pd

The norm of the Burgers vector of Pd is identified on the basis of crystallography. In FCC metals, lattice parameter relates to norm of Burgers vector as:

$$|b| = \frac{a_o}{2} | \langle 110 \rangle | = \frac{a_o}{\sqrt{2}}$$

where the lattice parameter $a_o = 0.389 \text{ \AA}$ [1], $\langle 110 \rangle$ is the common slip direction

6.3. Simulation setup

in FCC and the norm of the Burgers vector becomes $|b| = 2.75\text{\AA}$.

On the basis of copper as reference material, materials parameters of 316L stainless steel were already identified in [43]. Following a similar approach, phonon drag coefficient of Pd is calculated using:

$$B^{Pd} = \frac{\left[b \sqrt{\frac{\rho\nu}{\mu}} \right]^{Pd}}{\left[b \sqrt{\frac{\rho\nu}{\mu}} \right]^{Cu}} B^{Cu} \quad (6.1)$$

where $B^{Cu} = 1.5 \times 10^{-5} Pa.s$ at $300K$. Equation 6.1 is constructed based on the proportionality relation of the phonon drag coefficient with $b \sqrt{\frac{\rho\nu}{\mu}}$ [142]. Here, ρ is the volume mass density, μ is the shear modulus and ν is the Poisson ratio, specific to a material. After substituting corresponding values, the phonon drag coefficient of Pd is $B^{Pd} = 2.088 \times 10^{-5} Pa.s$.

τ_{III} signifies the stage where the strain hardening rate starts decreasing due to relaxation of internal stress by the onset of thermally activated cross slip mechanism. In DD simulations at nanoscale, this value does not have any significance as the flow stress already has a considerably high value. Due to this, the control over thermally activated mechanism in DD simulations is limited. This is one drawback when working with DD simulations at nanoscale. Recently, based on results from atomistic simulations [149], three newly identified cross-slip mechanisms, namely surface, bulk and intersection cross-slip types were hierarchically informed into DD simulations [91]. In any case, for the present simulations, $\tau_{III} = 32MPa$ ¹ has been used.

All the materials parameters of Pd are presented in Table 6.1.

Material	Poisson ratio ν	Young's modulus E (GPa)	Shear modulus μ (MPa)	Burgers vector magnitude b ($10^{-10}m$)	Viscous drag coefficient B ($10^{-5}Pa.s$)	Density ρ_v ($Kg.m^{-3}$)	Activation volume V_{act}/b^3	Stacking fault energy γ ($mJ.m^{-2}$)
palladium	0.39	121	44000	2.75	2.09	12023	20	180

Table 6.2 – Material parameters of Pd

¹This is the default critical cross slip stress value used for Cu at 300K in DD simulations

Chapter 6. Collective influence of grain and dislocation density parameters on plasticity of thin films

The Zener ratio (*cf.* Equation 6.2) calculated using the elastic constants of Pd suggests that the material is highly anisotropic.

$$A = \frac{2C_{44}}{C_{11} - C_{12}} = 2.45 \quad (6.2)$$

where A indicates Zener ratio, $C_{11} = 234GPa$, $C_{12} = 176GPa$ and $C_{44} = 71GPa$ are anisotropic elastic constants for Pd [95].

To predict correctly the anisotropic response of a polycrystal, apart from considering elastic anisotropy in FEM, the stress field of dislocations in DD simulations should also be in the same anisotropic framework. Unlike the stress field expression in elastic isotropic framework, a closed-form expression does not exist for the stress field of a dislocation in an anisotropic elastic medium. DD simulations will be at least 100 times slower when anisotropic stress field calculations are performed. Moreover, the difference between the two formulations decreases with increasing distance between the dislocation loops and increase in calculation point ² [92]. So, it is justified to use the stress field expression for dislocations in isotropic elastic framework and still estimate the anisotropic response of the polycrystal by considering an elastic anisotropy framework only while solving the boundary value problem using CASTEM.

6.3.4 Boundary conditions

To model the bulk behavior of the polycrystalline thin film, periodic boundary conditions (PBC) can be invoked along X- and Y- directions. The present implementation of PBC in DD code is confined to deal only with flat surfaces in the periodic directions. This is the main reason for modeling the specific configuration of the polycrystal with half grains at the boundaries and full grains in the interior of the thin film. Special care has been taken while prescribing grain identities either for half or full grains. The grain numbering scheme employed has already been explained with the help of a polycrystal model with four hexagonal grains in Section ?? of Chapter 4. Further, to verify the implementation of the grain numbering scheme, Frank-Read sources have been placed at the centres of each of the four hexagonal grains in the model polycrystal setup used in Section ?? of Chapter 4. Top view of the initial configuration with FRs in the model polycrystal

²the number of points on a regular 2D grid

setup is shown in Figure 6.12.

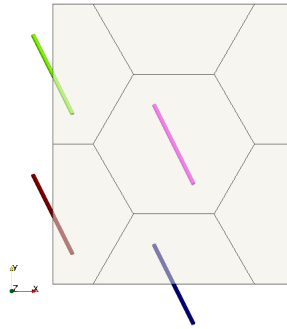


Figure 6.12 – Top view of the initial FRs configuration in polycrystal with four hexagonal grains

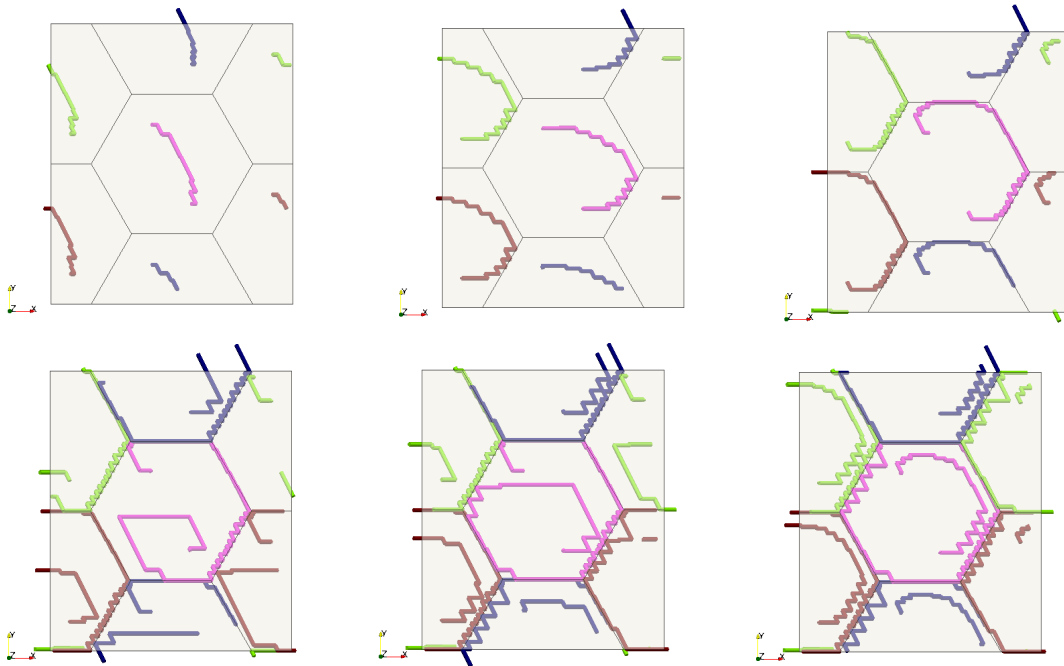


Figure 6.13 – Top view snapshots at different simulations steps showing validity of the grain identity scheme (PBC) in DD simulations

Upon pulling in tension along the X-direction, due to PBC, dislocations leaving a half grain from one side enters to the half grain on the opposite side as shown in series of snapshots at different simulation steps in Figure 6.13. A color coding scheme has been followed to indicate dislocations in different grains.

A zero traction is applied as boundary condition along Z-directions to represent *Free surfaces*. Figures 6.14(b) and 6.14(c) differentiates the two types of interfaces,

Chapter 6. Collective influence of grain and dislocation density parameters on plasticity of thin films

GBs and Free surfaces, modeled in the polycrystal (*cf.* Figure 6.14). GBs are modelled as impenetrable to dislocations and Free surfaces are given directionality (i.e., dislocation can move out, but can not come back into the simulation volume)

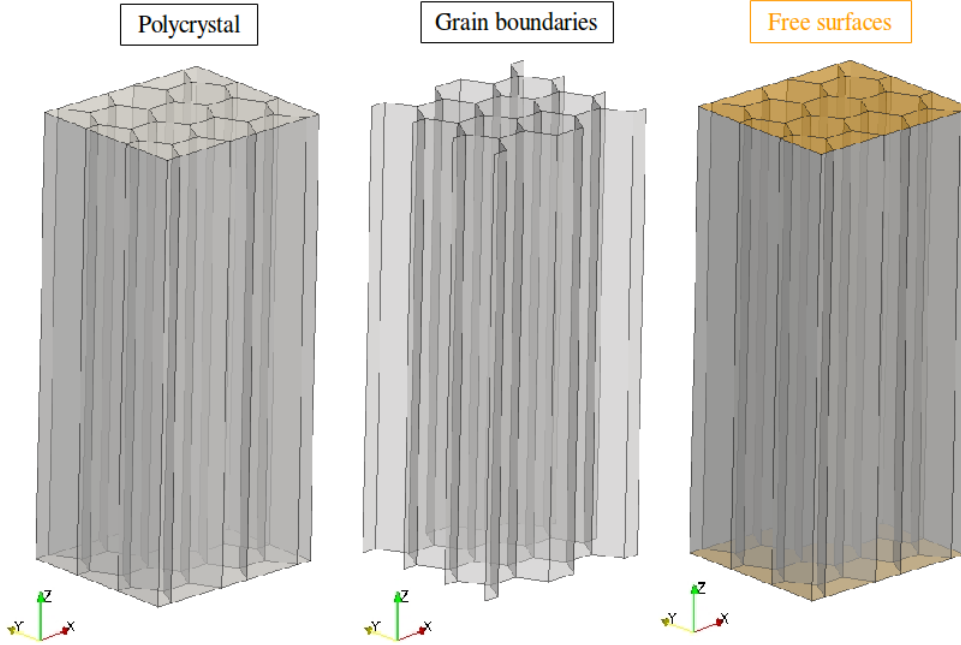


Figure 6.14 – Side view of the (a) Actual polycrystal, (b) Showing only GBs in the polycrystal and (c) Free surfaces in the polycrystal being highlighted in orange color

Dislocation segments which escape the simulation volume through free surfaces will create disturbances on the free surface (i.e., non-zero traction on surface). These errors are corrected by using a DD-FEM coupling based on Superposition principle [134]. Before going into the details about the DD-FEM coupling used for modeling thin films behavior, the actual problem is completely described in Section 6.3.5.

6.3.5 Problem description: Tensile test in X-direction

The main object is to simulate an *uniaxial tensile test* on the polycrystal volume in the presence of dislocations, involving thus zero traction applied on the free surfaces (top and bottom surfaces; Z-direction). The full finite domain DD problem that needs to be solved is presented in Figure 6.15(a). In the actual problem, a homogeneous displacement is applied along the X-direction and is represented by

the vector \mathbf{U}_{app} in blue color. Further, the traction boundary condition imposed on the free surfaces is represented by the vector \mathbf{O} in red.

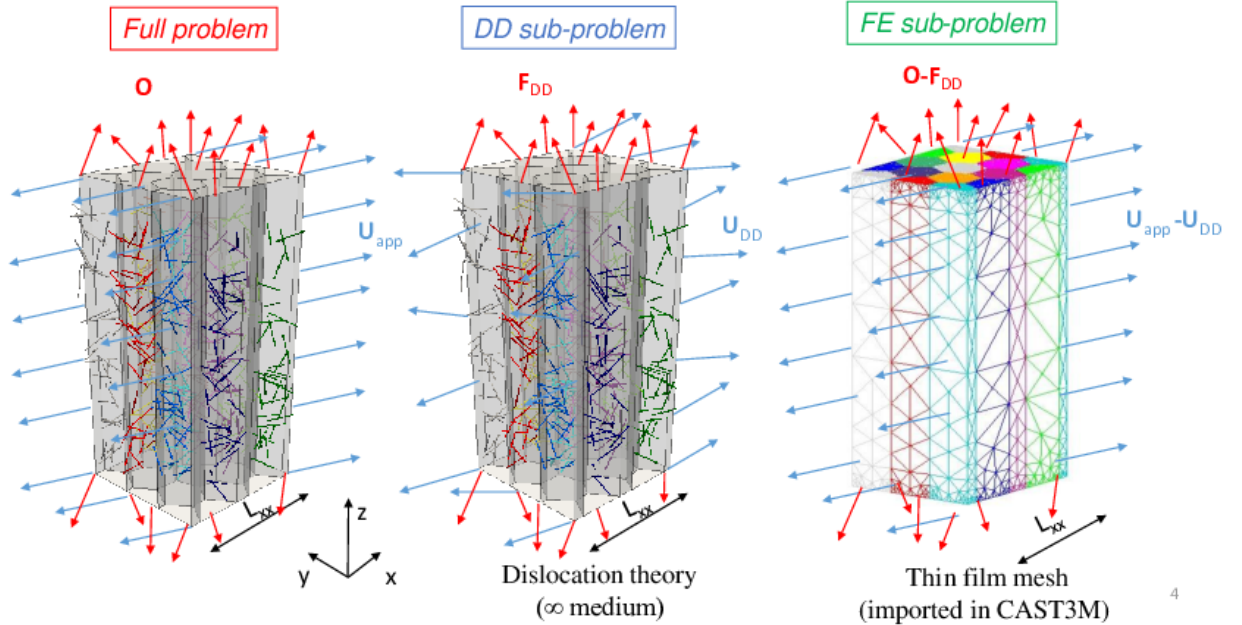


Figure 6.15 – Description of the (a) Full problem; Applying superposition principle to solve (b) DD sub-problem and (c) FE sub-problem

The closed-form expression for the stress field of a dislocation in elastic isotropic framework in DD code (TRIDIS) is valid only in infinite domain. That is, the use of this stress field expression while performing a tensile test on thin films will not yield correct results. This is due to the fact that the displacement (\mathbf{U}_{DD} in DD sub-problem) and force (\mathbf{F}_{DD} in DD sub-problem) fields generated on the boundaries by the dislocations are not taken into account. Hence, the displacement and force fields on the boundaries need to be accounted for by solving the full problem.

6.3.6 The DD-FEM coupling: solving a BVP

Using the superposition principle, the *Full problem* is solved by decomposing into two sub-problems.

1. In the first DD sub-problem (*cf.* Figure 6.15(b)), the DD code under only externally applied displacement and no other boundary conditions is used

Chapter 6. Collective influence of grain and dislocation density parameters on plasticity of thin films

to compute the stress field of the dislocation ensemble in the polycrystalline film. As mentioned above, this sub-problem does not yield the final solution.

2. In order to correct for the errors generated while solving the DD sub-problem, a second FE sub-problem (*cf.* Figure 6.15(c)) is simultaneously solved with the corrected (respective force and displacement fields created by dislocations on the boundary) boundary conditions.

When the solutions from the two sub-problems are superimposed, an accurate solution for the full problem is achieved.

Apart from presence of free surfaces in the simulation volume (*cf.* Figure 6.14(c)), elastic anisotropic behavior of the polycrystals is also accounted for via the DD coupling with an open source finite elements software, CASTEM. Different stages involved while solving the boundary value problem are clearly explained in Section 6.3.7 using an adapted DD-FEM algorithm.

6.3.7 Adapted DD-FEM algorithm

The adapted DD-FEM algorithm has been divided into four stages as shown in Figure 6.16. The stages entitled *Boundary conditions* and *Finite element method* are performed by the finite element software (CASTEM). The *Dislocation dynamics* stage is self explanatory (solved by TRIDIS). Finally, the stage entitled *Boundary corrections* is the actual coupling between DD code and CASTEM. The sequence of steps followed while solving the BVP using superposition principle are presented in this section.

- **Boundary condition** in the form of homogeneous displacement (\mathbf{U}_{app}) on periodic X-surface of the thin film generates the loading.
- **Boundary corrections** are needed due to the presence of dislocations. The dislocations in a finite simulation volume will generate heterogeneous displacement (\mathbf{U}_{DD}) and force (\mathbf{F}_{DD}) fields on the periodic and free surfaces, respectively. In the present adapted DD-FEM algorithm, only homogeneous displacement fields are accounted on the periodic X- surface. For the first few loading increments, it is reasonable to assume that the material is only elastically deformed, allowing to skip/avoid this correction stage.

- **Finite elements sub-problem** is solved with the effective boundary conditions accounting for the displacement and force fields created by dislocations on the surfaces. The solution of the FE sub-problem is a heterogeneous stress field at the integration points. These stresses are further transferred to the middle of each dislocation segment σ_{ext} using the DD-FEM coupling.
- **Dislocations** generate a plastic strain by moving in the simulation volume under the influence of the effective stress field, $\sigma_{int} + \sigma_{ext}$ at the centres of each dislocation segment. Accumulation of plastic strain continues for 'N' DD simulations iterations during every loading increment.
- **Equilibrium configuration** is generally achieved after 'N' DD simulations steps. If so, this is proceeded by another loading increment and the corresponding stages to be followed. If equilibrium configuration is not attained, a correction in the boundary conditions is performed to account for changes in the dislocation configuration and the process is continued without any loading increment.

6.3.8 Loading condition

Simulations were performed under quasi-static loading condition. In order to explain how the loading is monitored during the simulations, the results from a base simulation are presented. A relaxed initial dislocation configuration $\rho_{initial} = 1.55 \times 10^{+16} m^{-2}$ is considered (*cf.* Section 6.3.2). Figure 6.17 shows the stress values σ_{11} corresponding to the externally applied displacement increments and the Von Mises plastic strain monitored along Y1 and Y2-axes, respectively being plotted against the number of simulations steps on X-axis. For the first loading increment, $\sigma_{11} = 495 MPa$, a small amount of plastic strain is accumulated in the simulations volume. But, an equilibrium configuration has not been attained by the dislocation ensemble in the polycrystal. This is reflected by a stress drop down to $\sigma_{11} = 475 MPa$ and still resulting in small amounts of plastic strain. The stress drops in DD simulations essentially arise as a consequence of dislocations motion towards free surfaces (Image forces) during plastic deformation. After series of stress drops (two for the first loading increment), an equilibrium configuration of dislocation is attained and dislocations in the polycrystal cannot generate anymore plastic strain if the external load is not increased.

At larger plastic strains, due to the increasing number of mobile dislocations, it

Chapter 6. Collective influence of grain and dislocation density parameters on plasticity of thin films

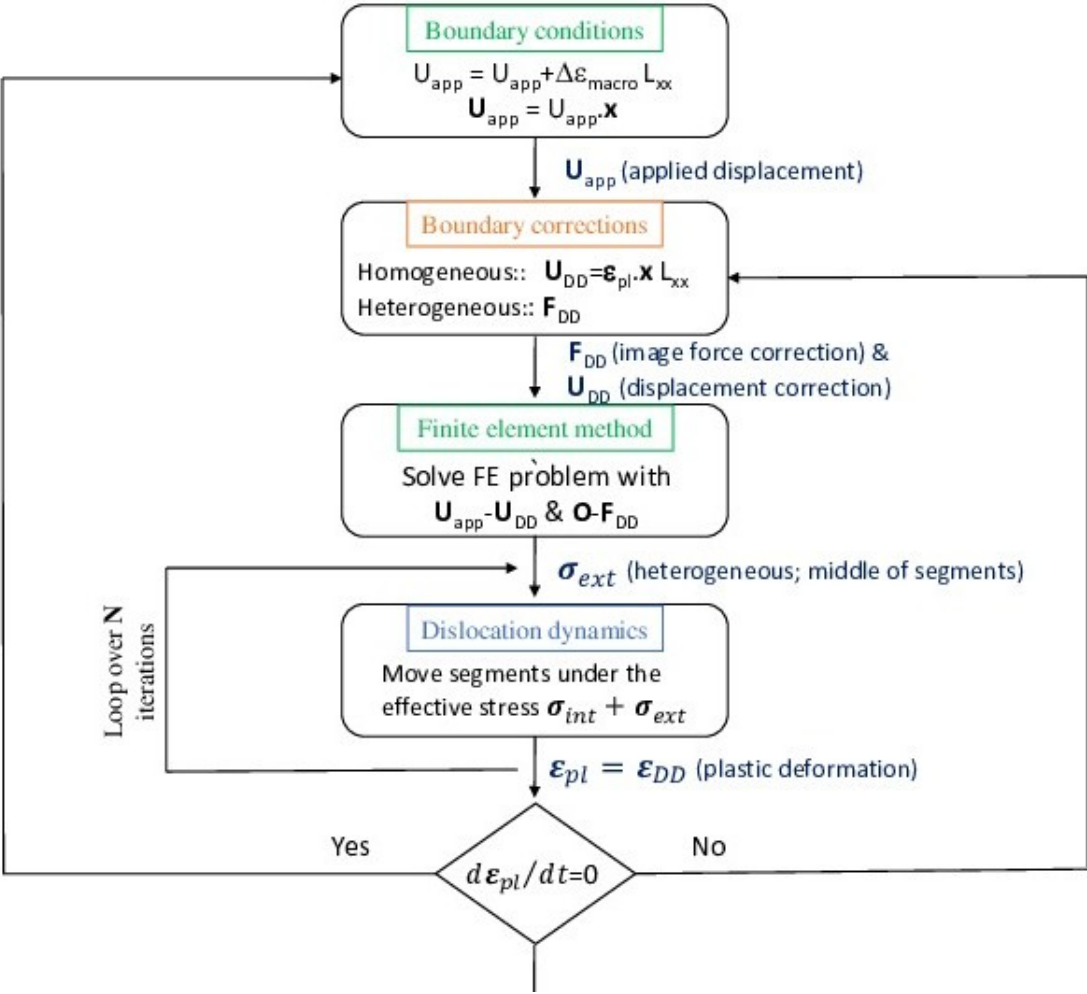


Figure 6.16 – Adapted DD-FEM algorithm using superposition principle

COUPLING

CASTEM

TRIDIS

becomes increasingly difficult to attain an equilibrium configuration of dislocations. More simulation steps are needed to equilibrate the system. Such an increase of number of simulation steps to reach equilibrium can be seen for simulation steps ≥ 1700 . It should be noted that, equilibrium configuration of dislocations is specified when no further contribution is made by the dislocations to the overall plastic strain. In other words, the increment in plastic strain for the last N iterations is almost zero ($d\varepsilon^{pl} \sim 0.0$). Due to vibration of dislocations in the simulation volume, it is never possible to arrive to the exact zero value of plastic strain increment.

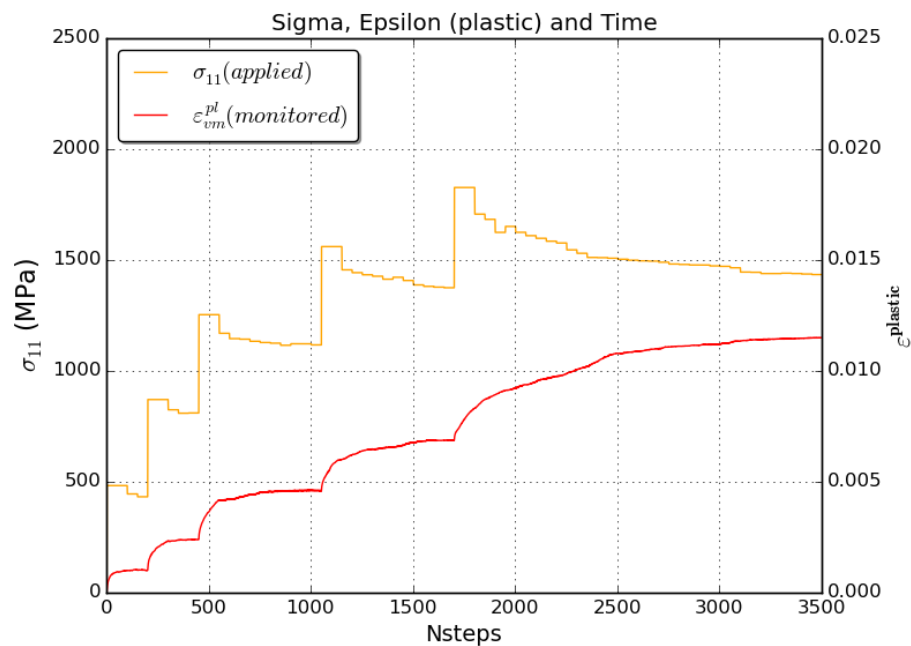


Figure 6.17 – Von Mises plastic strain monitored for every stress increment during the simulations

6.4 Results

Firstly, results from a reference simulation are presented. Details of the polycrystal setup (grain size, grain orientation and dislocation densities) are indicated wherever necessary. Basic comparative simulations were performed to test the influence of different parameters in DD simulations. After analysing the basic simulations, further simulations are carried out to directly compare the results with experiments.

Chapter 6. Collective influence of grain and dislocation density parameters on plasticity of thin films

6.4.1 Reference simulation: Film with similar grain sizes and same grain orientations

A polycrystal of 200nm thickness with similar grain size and same grain orientation is considered as the reference case. Side and Top views of the polycrystal with cuboid-shaped texture objects are shown in Figures 6.18(a) and 6.18(b), respectively. Corresponding to each grain in the polycrystal, the grain sizes and columnar axis along which each grain is aligned are color-coded and are presented in Figure 6.19. Such details are necessary while representing internal stresses contribution of a particular grain of the polycrystal. One such analysis has been carried out and will be presented in the discussion section of this chapter. For this reference simulation, all the grains are rotated with the same Euler angles (corresponding to the columnar and tensile axis).

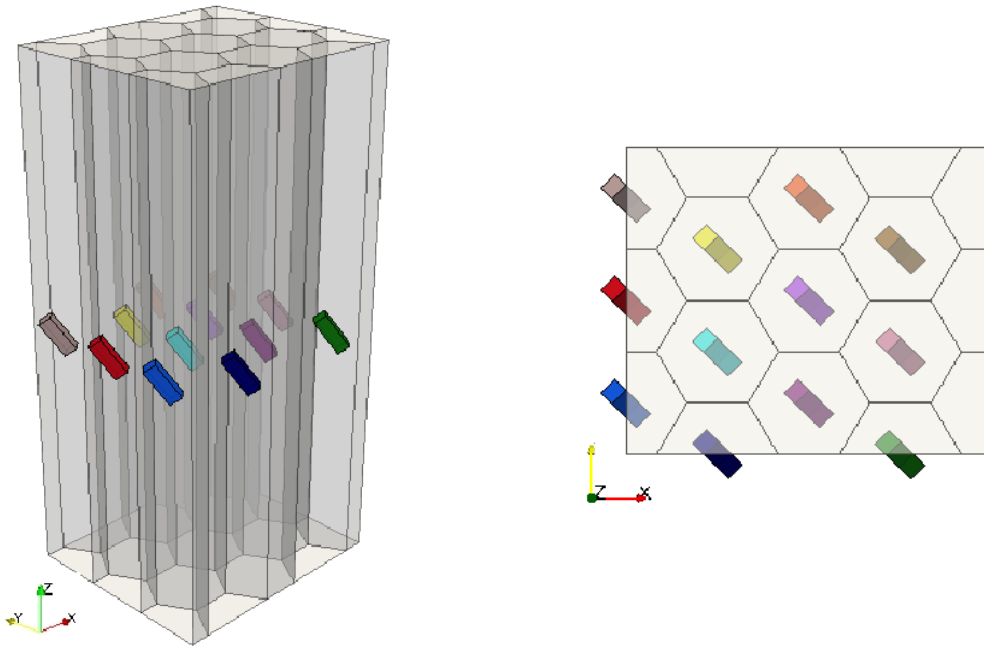


Figure 6.18 – (a.) Side view and (b.) Top view of the polycrystal with cuboid-shaped texture objects representing the oriented lattices of each grain

The stress-strain curve of the reference polycrystal simulation is shown in Figure 6.20(a). A constant strain increment of $\Delta\varepsilon = 2.5 \times 10^{-3}$ has been imposed to generate the loading. Four loading increments were needed to reach a total equivalent strain of $\varepsilon_{11} = 1\%$. The stress level drops by certain value after every loading increment. The point to which the stress drops signifies the actual resultant stress-strain response of the material. The resulting stress-strain response after

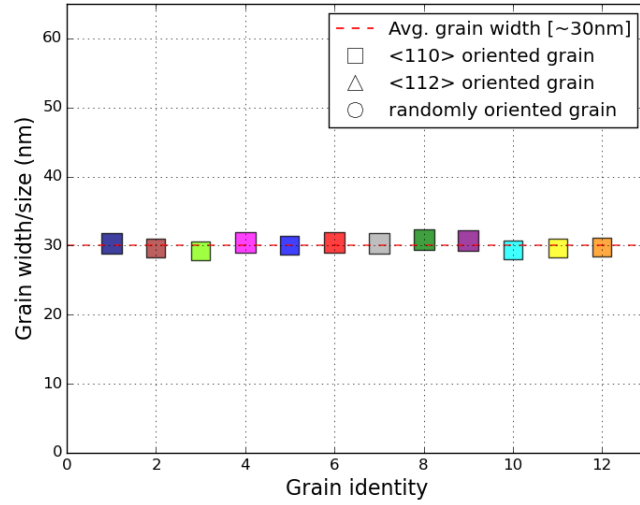


Figure 6.19 – Plot representing size and orientation details about each grain in the polycrystal

highlighting the relaxed stress is shown in Figure 6.20(b). For all further analyses, the highlighted resulting stress-strain response is only plotted.

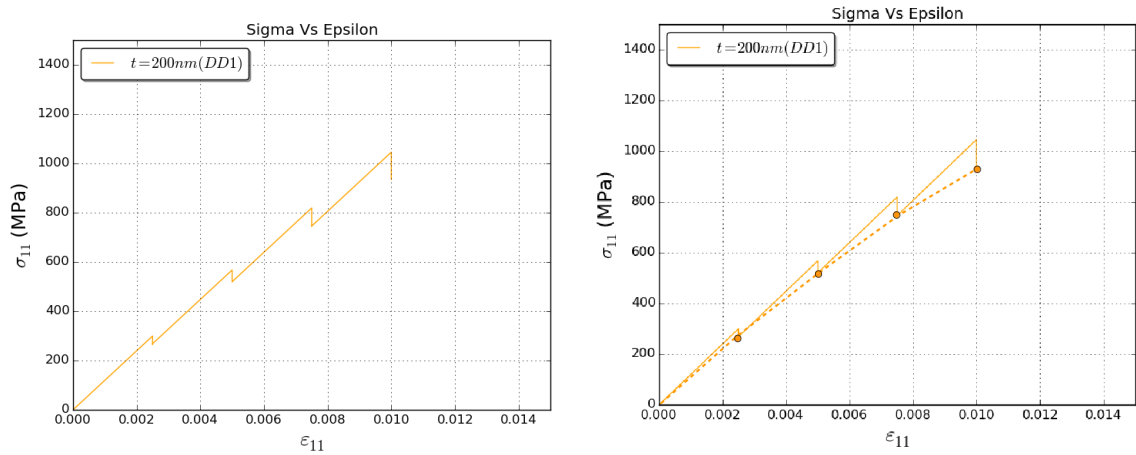


Figure 6.20 – (a.) Stress-Strain curve (original) and (b.) Stress-Strain curve (resultant) for the reference simulation of the polycrystal

The Top and Side views of initially relaxed dislocation configuration in the polycrystal are shown in Figures 6.19(a) and 6.19(b), respectively. Starting with a initial dislocation density of $\rho_{initial} \sim 1. \times 10^{+16}m^{-2}$, the dislocation density in the polycrystal almost quadruples and reaches a value of $\rho \sim 3.8 \times 10^{+16}m^{-2}$ as observed in Figure 6.22(b). The dislocation density has been observed to increase at a higher rate from $\varepsilon_{11} \geq 6.5 \times 10^{-3}$. At $\varepsilon_{11} = 6.5 \times 10^{-3}$, the corresponding

Chapter 6. Collective influence of grain and dislocation density parameters on plasticity of thin films

stress value of $\sigma_{11} \sim 610 \text{ MPa}$ is identified from Figure 6.22(a). The significance of such an abrupt increase in dislocation density and its relation with the equivalent stress value must be analysed with more realistic simulations results (i.e., when all the grains are not oriented exactly with the same Euler angles).

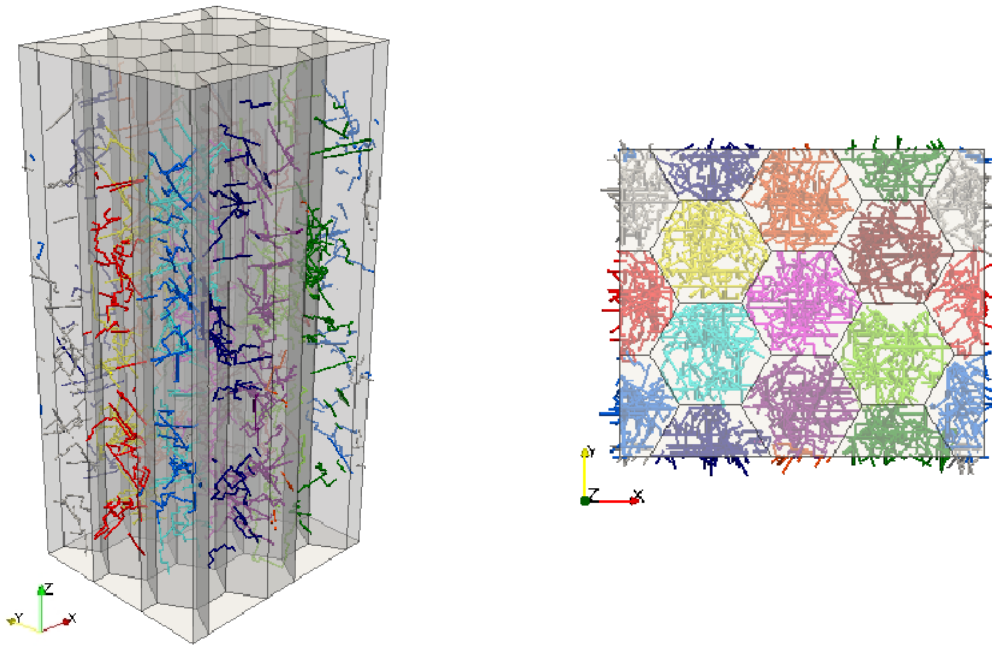


Figure 6.21 – (a.) Side view and (b.) Top view of the polycrystal with initial relaxed dislocation microstructure

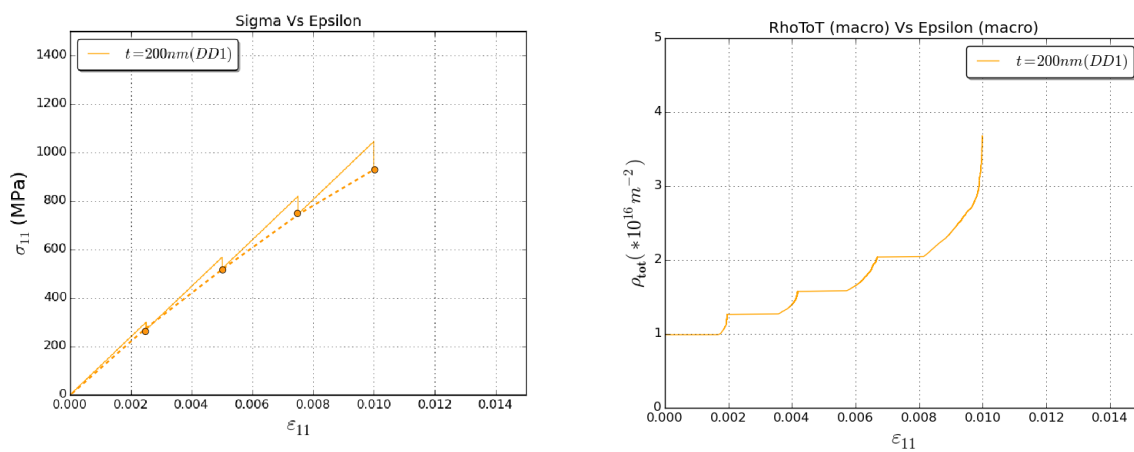


Figure 6.22 – (a) Stress-Strain curve (resultant) and (b) Evolution of total dislocation density during the reference simulations of the polycrystal

6.4.2 Basic comparative simulations

6.4.2.1 Periodic Vs Free surfaces in Z-direction

To understand the influence of the boundary conditions on the overall strain hardening behavior, two different simulations with polycrystal setup involving four grains were performed. In the first simulation, periodic boundary conditions (PBC) are imposed along all three directions of the thin film. This setup would require no coupling with a finite elements method (i.e., no image forces are accounted here). For the second simulation, the general setup with traction boundary condition along the Z-directions is used. Here, the free surface are accounted in the simulations via the coupled code with CASTEM. The stress-plastic strain response of the two simulations are presented in Figure 6.23.

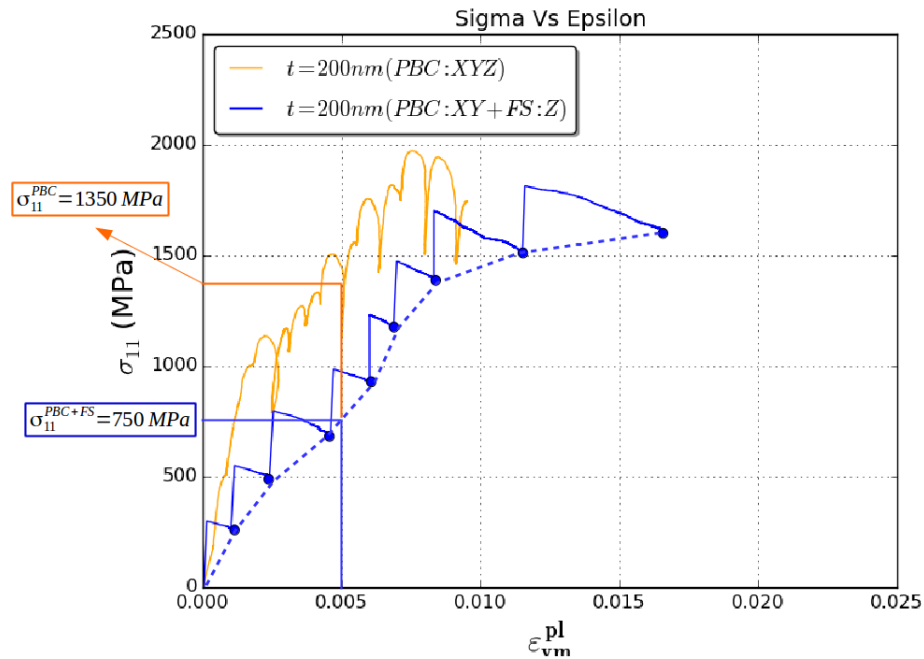


Figure 6.23 – Stress-plastic strain response of two simulations with different boundary conditions

Even-though a tensile test (X-direction or 11) has been performed in both simulations, the loading schemes are quite different. For the first simulation with PBC in all three directions, a constant strain rate (strain rate= $100s^{-1}$) has been imposed. Parameters for loading increment have not been perfectly adjusted (i.e., equilibrium configuration is not achieved before every loading increment). This is evident in the abrupt changes in the stress-strain curve. On the other hand, in the

Chapter 6. Collective influence of grain and dislocation density parameters on plasticity of thin films

coupled simulation, a more dynamic approach is followed. An increment in external load is imposed only after an equilibrium dislocation configuration is reached. As explained in Section 6.4.1, the number of simulation iterations required to achieve equilibrium configuration will solely depend on the internal dislocation interactions. The resultant stress-plastic strain response is highlighted in blue.

Upon neglecting the influence of the load monitoring scheme, the strain hardening response of both the simulations are observed to be quite different. This change is mainly arising from the different boundary conditions. In the simulation result with free surfaces in Z-direction, a stress value of $\sigma_{11}^{PBC+FS} = 750MPa$ was sufficient to accumulate a plastic strain of $\varepsilon_{vm}^pl = 5. \times 10^{-3}$. To reach a similar plastic strain, the simulation setup with PBC in all three directions required a much higher stress value of $\sigma_{11}^{PBC} = 1350MPa$. This highlights the significant influence of free surfaces on the overall response of the material.

6.4.2.2 Effect of number of grains in the films

Simulation results of a polycrystal will depend on the selected number of grains in the representative volume element (RVE). In this section, the number of grains in the RVE is varied and its influence on the stress-strain response is assessed. Simulations were carried on two polycrystals, one with 4 grains and the other with 12 grains. In both cases, the same boundary conditions were applied (PBC in X- and Y- directions and zero traction in Z- direction). Further, grain size, grain orientation and initial dislocation density in each grain and the loading conditions were also kept the same. The stress-strain response of two simulations is shown in Figure 6.24(a).

The initial dislocation density in both the simulations is $\rho_{initial} = 1. \times 10^{+16}m^{-2}$. the results indicate that the two simulations with different numbers of grains in the RVE show a relatively different strain hardening behavior. The observed variation is expected to vanish at very high dislocation densities. The reason behind such observations can be attributed to the change in total number of dislocation segments in the respective RVEs, which in turn is related to difference in long-range internal stresses. Corresponding evolution of dislocation density shown in Figure 6.24(b) also support the previous argument.

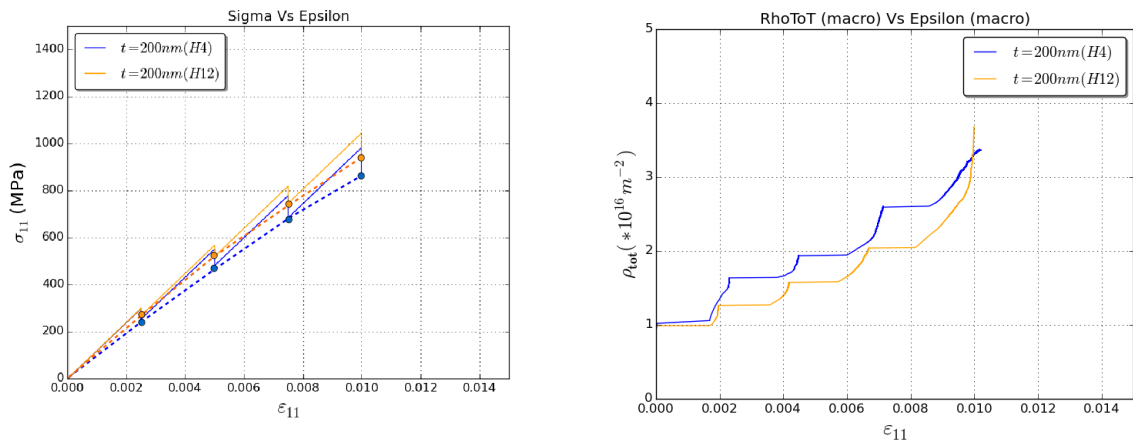


Figure 6.24 – (a) Stress-Strain response and (b) Dislocation density evolution of two simulations with different numbers of grains in the RVE, respectively

6.4.2.3 Response to different loading increments

The use of high loading (strain) rates in DD simulations is a matter of debate even today. The influence of applied strain rate on the tensile stress was studied for a single copper grain. In DD simulations of micron-sized grains, an increase in the strain rate is typically equivalent to an increase in average dislocation velocity when the density of mobile dislocations is not significantly modified. As a consequence, the effective stress governing dislocation mobility is also increased and finally resulting in considerable changes in the dislocation arrangements. In agreement with the above discussion, yield stress was observed not to be strain rate sensitive at low strain rates. Since, in this regime, the dislocation mobility is governed by athermal forest interactions [62]. Above a critical strain rate (specific to a dislocation density), the flow stress was observed to linearly increase with imposed strain rate [46].

In contrast, in DD simulations with nano-sized grains the dislocation mobility has an upper limit (maximum velocity of sound in metals = $2000m.s^{-1}$) and in most cases, dislocations move at this extreme value. This nullifies any changes arising from higher strain rates or different loading increments. This is justified from the simulation results at different loading increments in Figure 6.25.

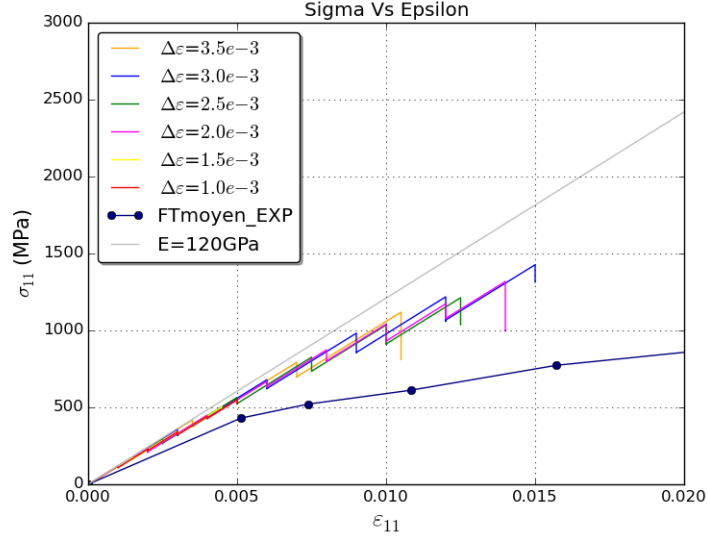


Figure 6.25 – Stress-Strain response for different loading increments

6.4.3 Strain hardening behavior of 200nm film

Incorporation of the right physics and minimal assumptions in DD codes provides the unique advantage of allowing direct comparison with experiments. In this section, DD simulations were performed for different initial dislocation densities to investigate if the experimentally observed strain hardening response of the 200nm thick Pd film can be captured. As it was already observed in Section 6.4.2.2 that the number of grains in RVE has only a small influence on the overall response, a polycrystal setup with four equally sized grains is considered during the simulations. Columnar axis of all the four grains are aligned along the [110] direction which is also the most favoured direction in experimentally observed Pd films.

The initial dislocation density $\rho_{10} = 3.5 \times 10^{+16} m^{-2}$ (*cf.* Figure 6.26) used in DD simulations closely represents the experimental strain hardening response of the 200nm thick film. Interestingly, this particular initial dislocation density value used in DD simulations is in very close agreement with the experiments (*cf.* Figure 6.28).

Experimental evidence of GB-based mechanism driving plastic deformation in Pd thin films is limited [93]. In such cases, the possibility of dislocation-based thermally-activated mechanism dictating the strain hardening response was highlighted [31, 33, 109]. Present DD results confirm the argument of almost one or two deformation mechanisms being dominant in Pd films with average grain size

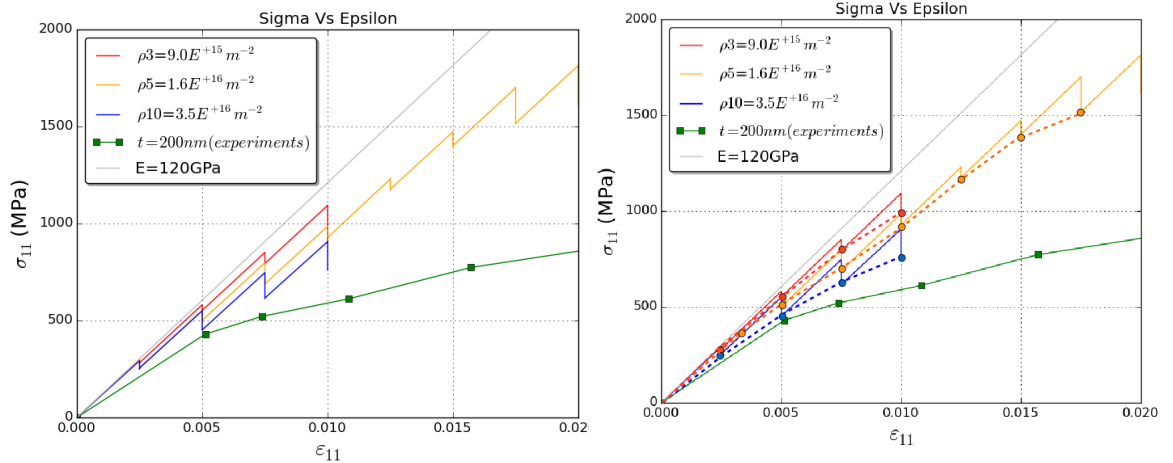


Figure 6.26 – Strain hardening behavior (actual and resultant) of thin film with different initial dislocation densities

$\sim 30nm$ [119, 139]. The plastic deformation mechanism in these nano-sized grains is still dislocation-mediated.

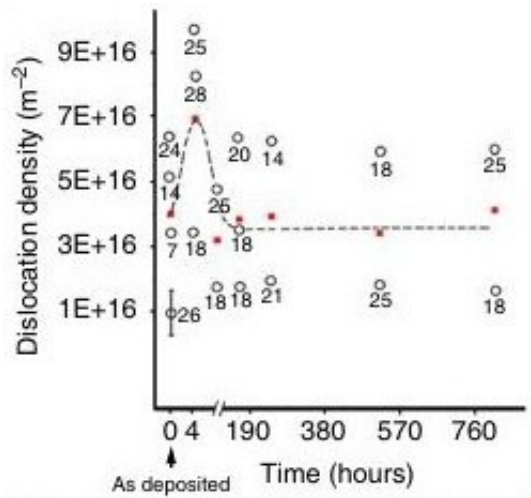


Figure 6.27 – Evolution of dislocation density in thin film with initial dislocation density $\rho_{initial}^{exp} \sim 3.5 \times 10^{+16}m^{-2}$ [31]

6.4.4 Size effects in Pd thin films

6.4.4.1 Influence of grain orientation

With the assumption of having only one grain along the thickness direction of thin film, every grain in the thin film corresponds a specific aspect ratio depending

Chapter 6. Collective influence of grain and dislocation density parameters on plasticity of thin films

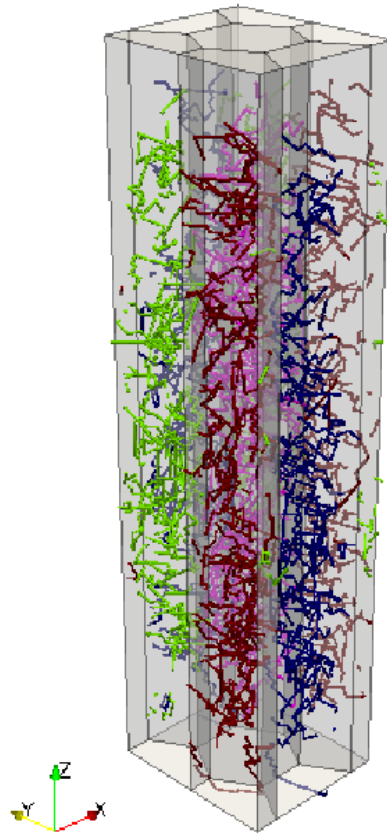


Figure 6.28 – Initial dislocation microstructure corresponding to $\rho_{initial}^{sim} = \rho_{10} = 3.5 \times 10^{+16} m^{-2}$ in 200nm thick film with four grains

on grain size distribution. In an ideal case with no grain size distribution in the film, the aspect ratio of each grain is also approximately (grain size is not exactly the same!) the same. This ideal case with no grain size distribution in the film is used for studying grain orientation influence on films of different thicknesses. Instead of using experimental dislocation density, a lower initial dislocation density is specified to speed-up the calculations. The initial dislocation density in the films is scaled to $\rho_{initial} = 1. \times 10^{+16}m^{-2}$ and the corresponding initial dislocation microstructures in 90nm, 200nm and 480nm thick films are shown in Figure 6.29.

Two extreme grain orientation cases are presented in Figures 6.30(a) and 6.32(a). The stress-strain response and the corresponding microstructure plots are always presented side-by-side. Microstructure details presented in Figure 6.30(b) and 6.32(b) indicate that the grains in the polycrystal have the same size and their columnar axes are aligned along $\langle 110 \rangle$ and $\langle 112 \rangle$ directions, respectively. In other words, polycrystals exhibit $\langle 110 \rangle$ and $\langle 112 \rangle$ textures.

When the corresponding stress-strain responses for films of different thicknesses are compared in Figure 6.30(a) and Figure 6.32(a), it is hard to differentiate among the curves (*cf.* Figure 6.30(a) and Figure 6.32(a)). So, corresponding stress-plastic strain response and dislocation density evolution in all three films are plotted in Figures 6.31 and 6.33, respectively.

Looking at the stress-plastic strain it is clear that when grains in the polycrystal have a preferred orientation (in our case, either $\langle 110 \rangle$ or $\langle 112 \rangle$), they accumulate large amount of plastic strain. Approximately at $\sigma_{11} = 1250MPa$, plastic strain of $\varepsilon_{vm}^pl = 5. \times 10^{-3}$ is accumulated in 90nm thick film in both cases. The same is not true when the grains are randomly oriented. Figure 6.34(a) indicates that only a plastic strain of $\varepsilon_{vm}^pl = 2. \times 10^{-3}$ is developed at approximately the same stress value. Interestingly, when the behavior of 90nm and 200nm thick films is compared, all the three grain orientation cases show a size effect. At any particular value of plastic strain, corresponding stress is always higher in 90nm thick film. But the trend is not followed by the 480nm film motivating further analysis.

6.4.4.2 Larger grain at the center of the film

Now, to understand the influence of grain size distribution and see if it has an impact on the size effect, a polycrystal with a larger grain at the center is considered. Figure 6.35(a) and (b) show the Top and Side views of a 200nm thick film with

Chapter 6. Collective influence of grain and dislocation density parameters on plasticity of thin films

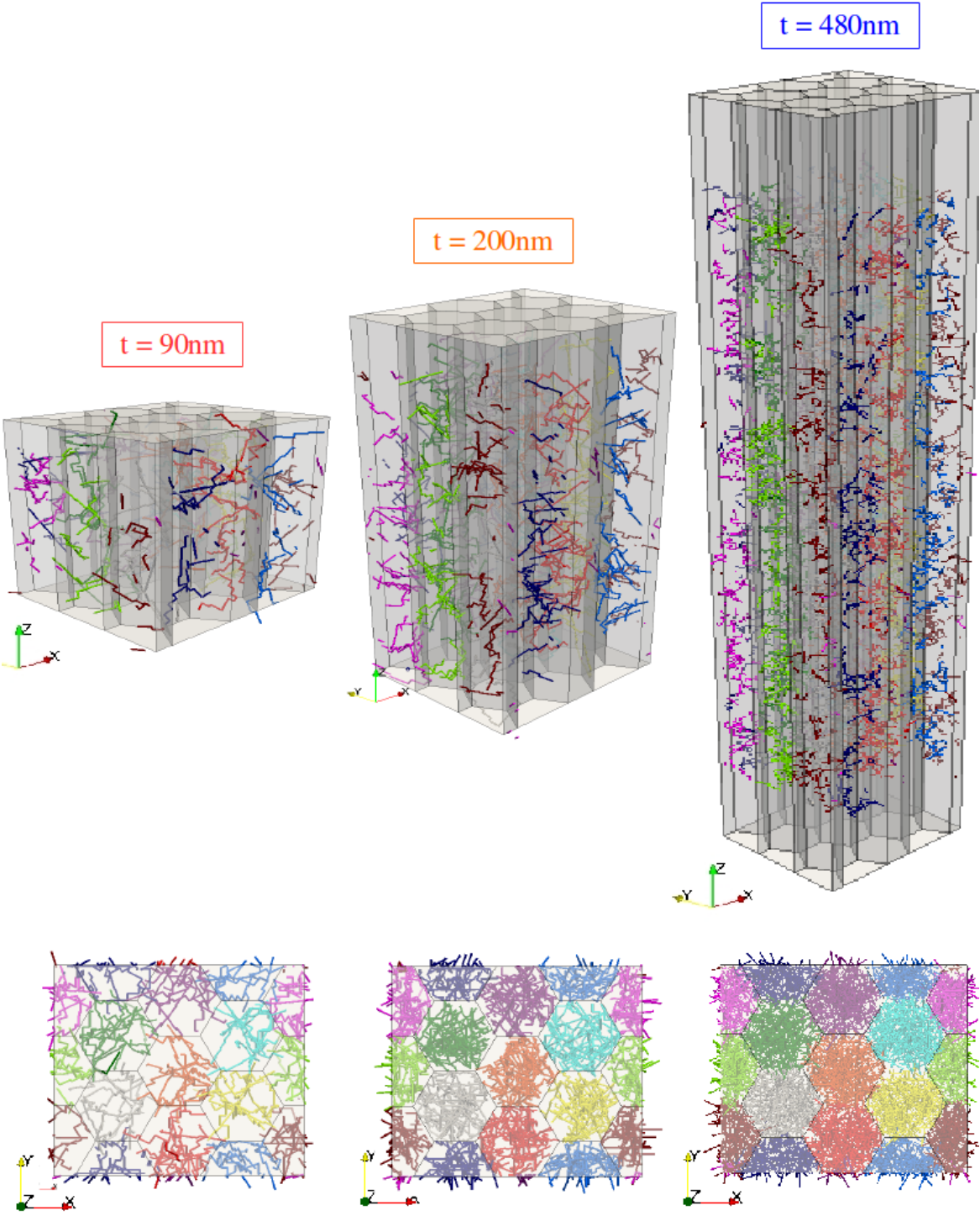


Figure 6.29 – Side and Top views of 90nm, 200nm and 480nm thick films with respective initial dislocation microstructures

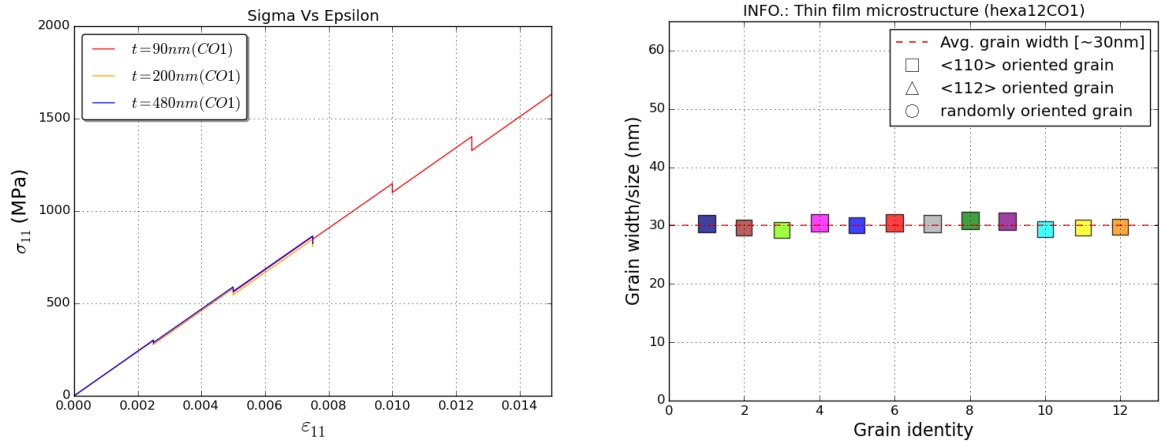


Figure 6.30 – (a) Comparison of stress-strain (actual) response in 90nm, 200nm and 480nm thick films (b) Corresponding microstructure details of the polycrystal configuration (color coding followed for grains)

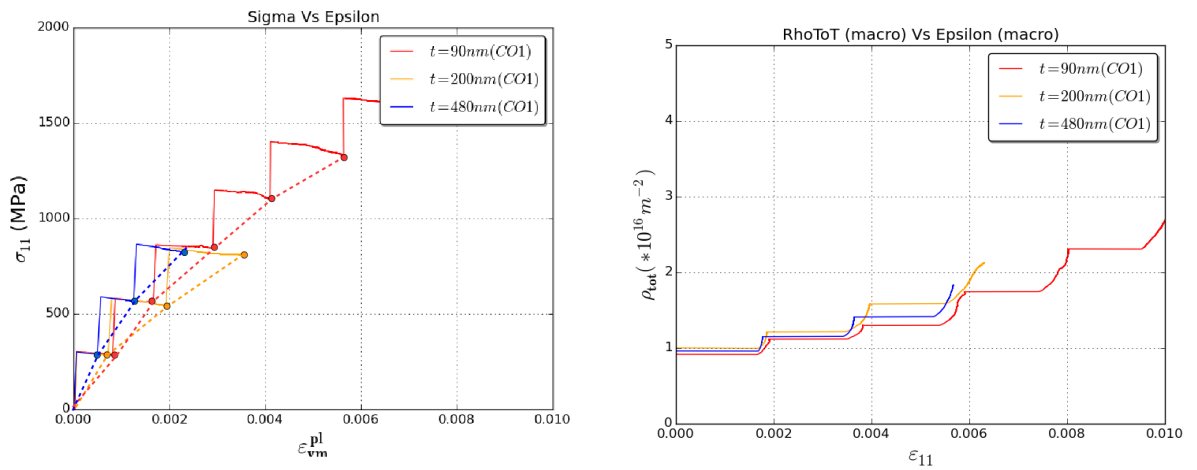


Figure 6.31 – (a) Comparison of stress-plastic strain response and (b) Total dislocation density evolution in 90nm, 200nm and 480nm thick films with <110> texture

Chapter 6. Collective influence of grain and dislocation density parameters on plasticity of thin films

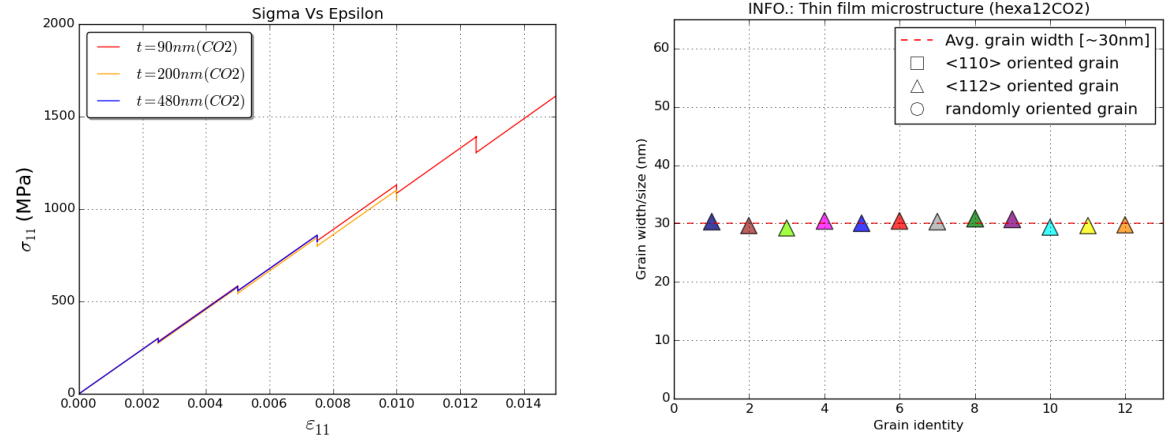


Figure 6.32 – (a) Comparison of stress-elastic strain response and (b) Total dislocation density evolution in 90nm, 200nm and 480nm thick films with <112> texture

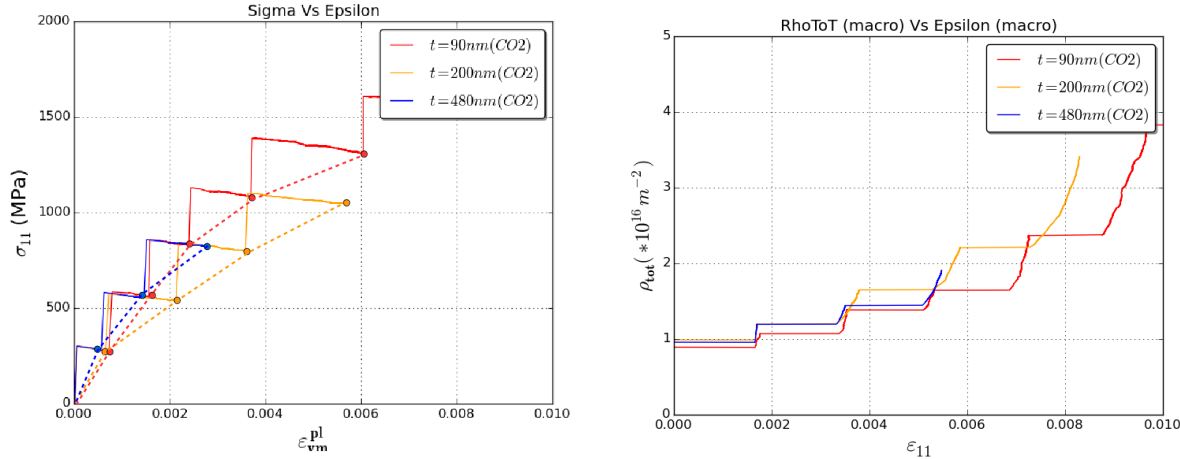


Figure 6.33 – (a) Comparison of stress-plastic strain response in 90nm, 200nm and 480nm thick films (b) Corresponding microstructure details of the polycrystal configuration (color coding followed for grains)

6.4. Results

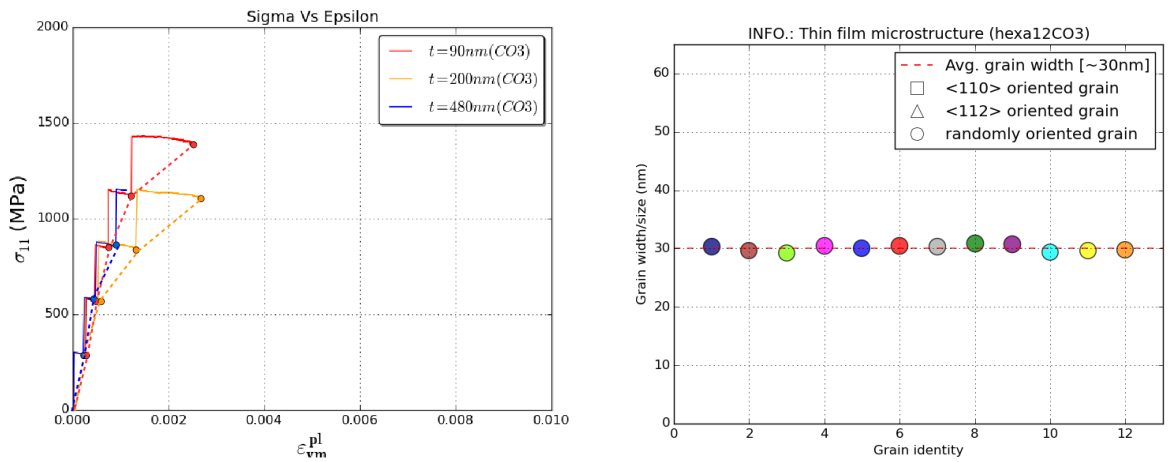


Figure 6.34 – (a) Comparison of stress-plastic strain response in 90nm, 200nm and 480nm thick films (b) Corresponding microstructure details of the polycrystal configuration with $\langle 110 \rangle$ texture (color coding followed for grains)

initial dislocation configuration.

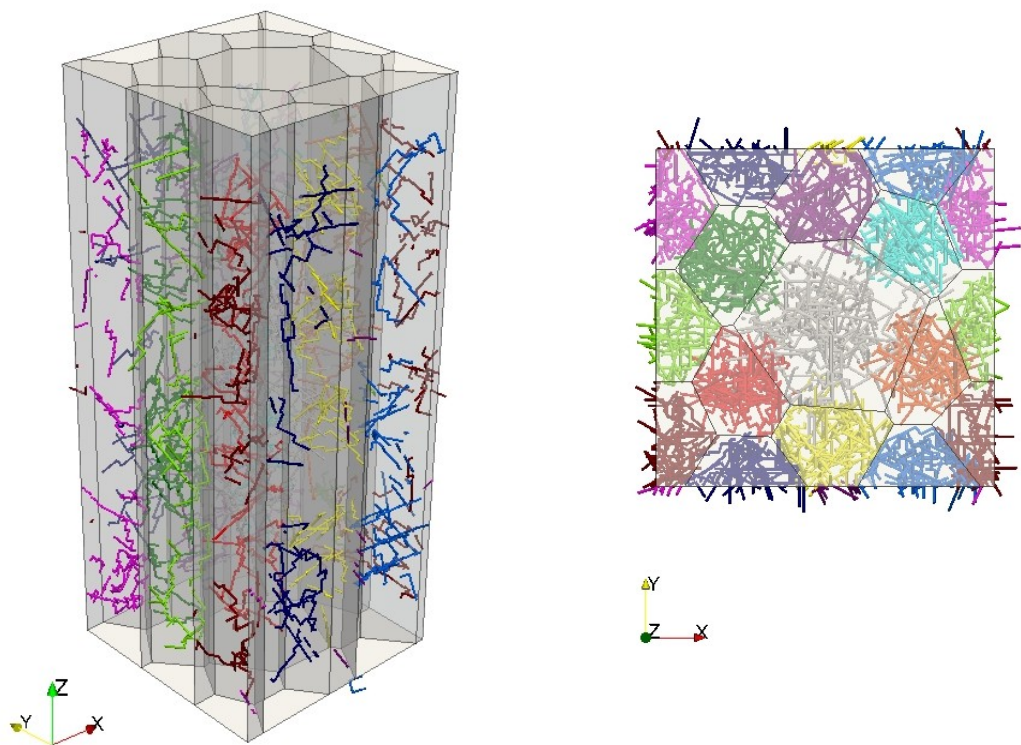


Figure 6.35 – (a) Side and (b) Top views of 200nm thick film with a large grain surrounded by small grains in the polycrystalline film

The stress-strain response is shown along with the microstructure details of

Chapter 6. Collective influence of grain and dislocation density parameters on plasticity of thin films

the polycrystal in Figure 6.36(a) and 6.36(b). Unlike the case with no grain size distribution, changes in the stress-strain response are observed for different film thickness with grain size distribution. But, to understand the impact of a larger grain at the center of the polycrystal, a more detailed analysis has to be carried out.

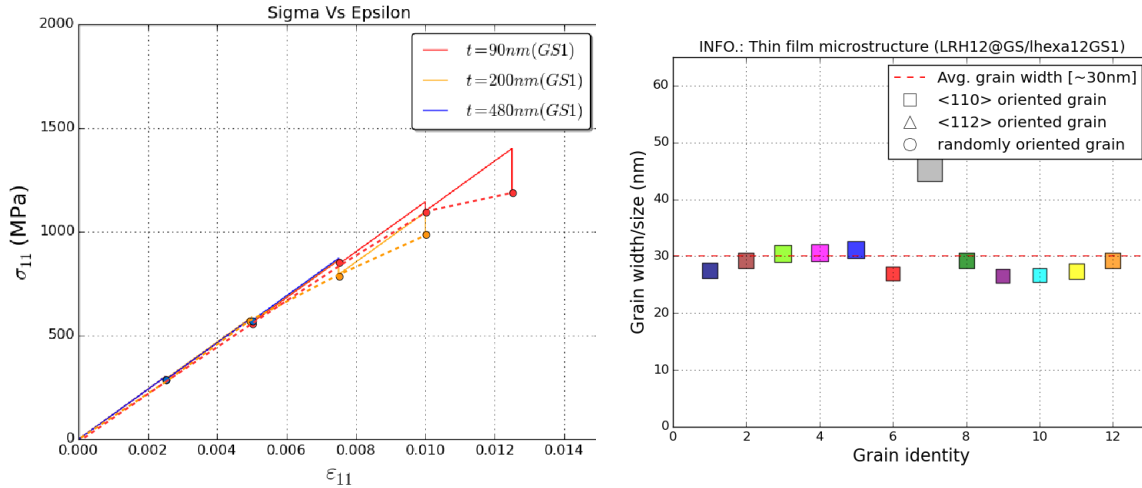


Figure 6.36 – (a) Stress-strain response and (b) Microstructure details of polycrystal with a large grain surrounded by small grains in the polycrystalline film

The total dislocation density evolution in each grain of the 90nm and 200nm thick films is individually plotted in Figures 6.37 and 6.38, respectively. The dislocation density evolutions do not look the same in both the films. In the 90nm thick film, the dislocation density is concentrated mostly in the central larger grain (*cf.* GR07(silver) in Figure 6.37). Whereas in the 200nm thick film, smaller grains act as dislocation storage sites first before any effect on the larger grain.

To validate that the observation of 90nm film promoting dislocation concentration in larger grains, simulation results of polycrystal with same grain size distribution but different texture are also analysed in Figure 6.39(b). Corresponding microstructure is shown in Figure 6.39(a).

Like in the previous case, the dislocation activity is concentrated in the largest grain at the center of the film. It is now evident that larger grains in the smallest film concentrate more plastic strain. For this particular polycrystal setup, the grain size/width of the largest grain is $\sim 45\text{nm}$ and that of smallest grain is $\sim 25\text{nm}$. Such variance of grain sizes in films can be addressed via aspect ratio of the grains. Table 6.3 presents details about the minimum and maximum aspect ratios of the grains in different films.

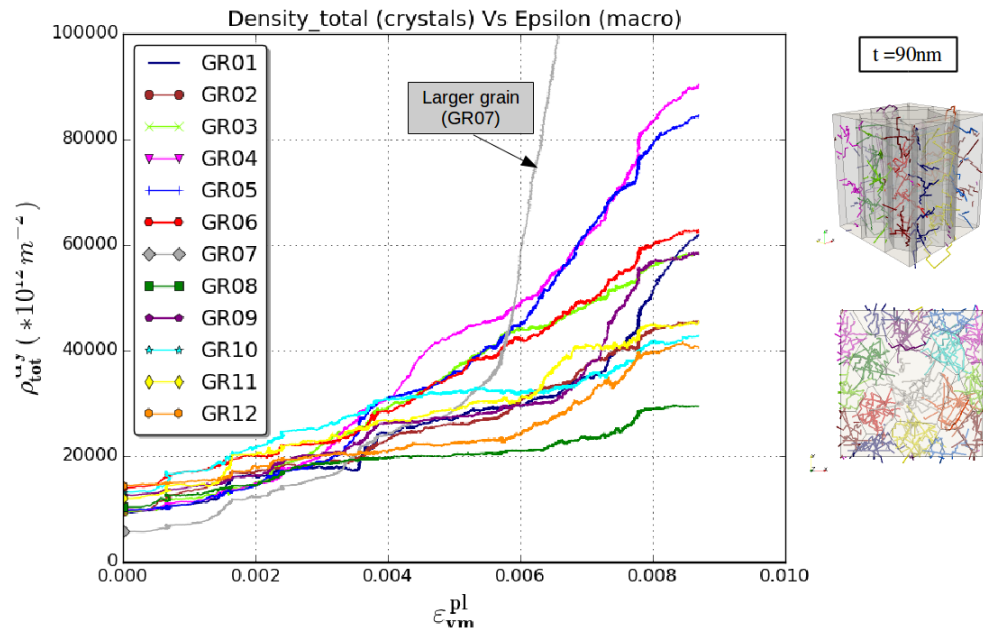


Figure 6.37 – Dislocation density evolution in each grain of 90nm thick film

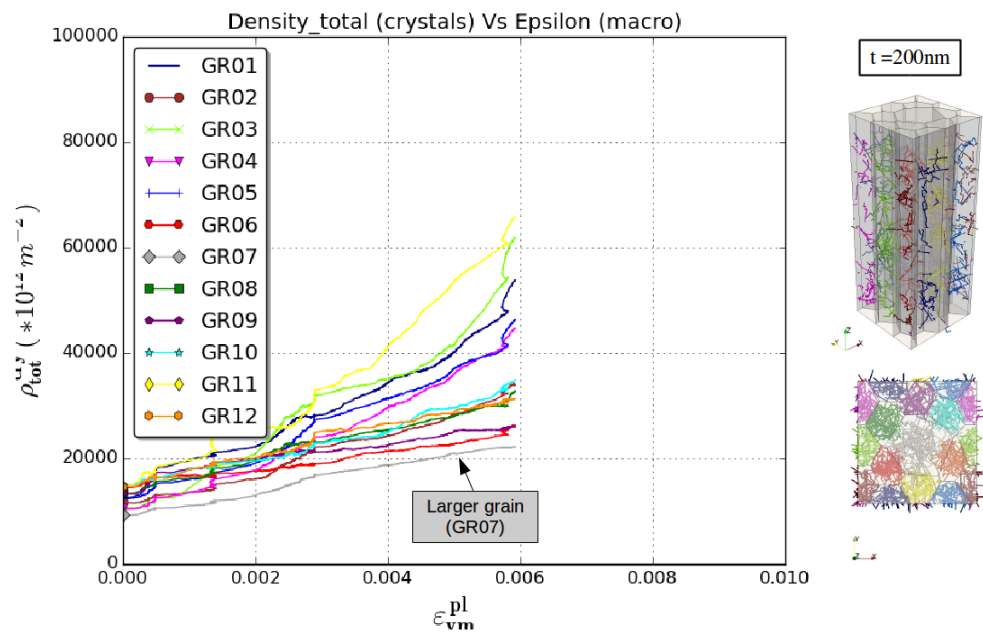


Figure 6.38 – Dislocation density evolution in each grain of 200nm thick film

Chapter 6. Collective influence of grain and dislocation density parameters on plasticity of thin films

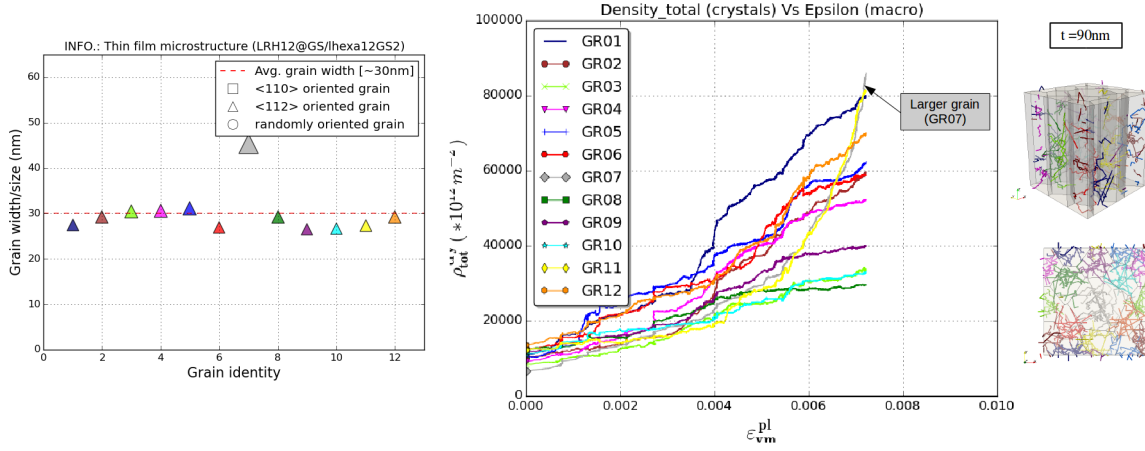


Figure 6.39 – (a) Microstructure details and (a) Dislocation density evolution in each grain of 90nm thick film

Grain size (extreme)	t=90nm	t=200nm	t=480nm
Largest grain=45nm	$AR_{90}^{min} = 2.0$	$AR_{200}^{min} = 4.5$	$AR_{480}^{min} = 10.67$
Smallest grain=25nm	$AR_{90}^{max} = 3.6$	$AR_{200}^{max} = 8.0$	$AR_{480}^{max} = 19.2$

Table 6.3 – Variation of grain aspect ratios with film thicknesses

Observations made in this section further emphasize the impact of grain aspect ratio on dislocation activity. Here, the variation of grain aspect ratio which is inherently present in polycrystal due to grain size distribution create changes in the dislocation density evolution/concentration between films of 90nm and 200nm thickness, respectively.

6.4.4.3 Combined influence of grain size and dislocation density distribution

Results in Section 6.4.4.2 have been useful for understanding the influential role of grain size distribution dictating the deformation behavior in Pd thin films. To probe further on the collective influence of grain size and dislocation density distribution, polycrystal with few grains considerably smaller in size than their counter-parts is modeled. The idea here is to use a cut-off value of the grain size. Below this cut-off value, the probability of finding dislocation sources in the grain will be very low in the thinnest film [10]. That is, in 90nm thick film, grains with no initial dislocation sources will be accounted during the initial dislocation density generation. The initial dislocation densities in 200nm and 480nm thick

films are accordingly adjusted. The Side and Top views of the as generated FRs in 90nm, 200nm and 480nm thick films are shown in Figure 6.40, respectively. Correspondingly, the thin film microstructure is also presented in Figure 6.41(b).

The stress-strain response of the three films has been plotted along with the experimental results of 200nm thick film (green) for reference. A clear indication of the influence of film thickness ($t=90\text{nm}$ and 200nm) is observed. Due to the presence of few grains with no initial dislocation, the 90nm thick film shows an almost elastic response (*cf.* closer to the slope given by the Young's modulus). As already mentioned, size effects are not pronounced due to two reasons:

1. Initial dislocation density was scaled to make it computationally possible to run the simulations for few loading steps especially for the thickest film. Still, it is clearly seen that 480nm thick film takes very long time to reach 0.5% strain.
2. The analysis is confined to a region of low strains $\varepsilon < 1.0\%$. The size effect observed in experiments is highlighted as red box in Figure 6.42.

The main observation here is that considerable size effects are observed when a polycrystal is modeled with certain grain size distribution. Different initial dislocation densities (grain with no initial dislocation sources in 90nm thick film) in films of different thickness can also influence the behavior of thin films accordingly.

Chapter 6. Collective influence of grain and dislocation density parameters on plasticity of thin films

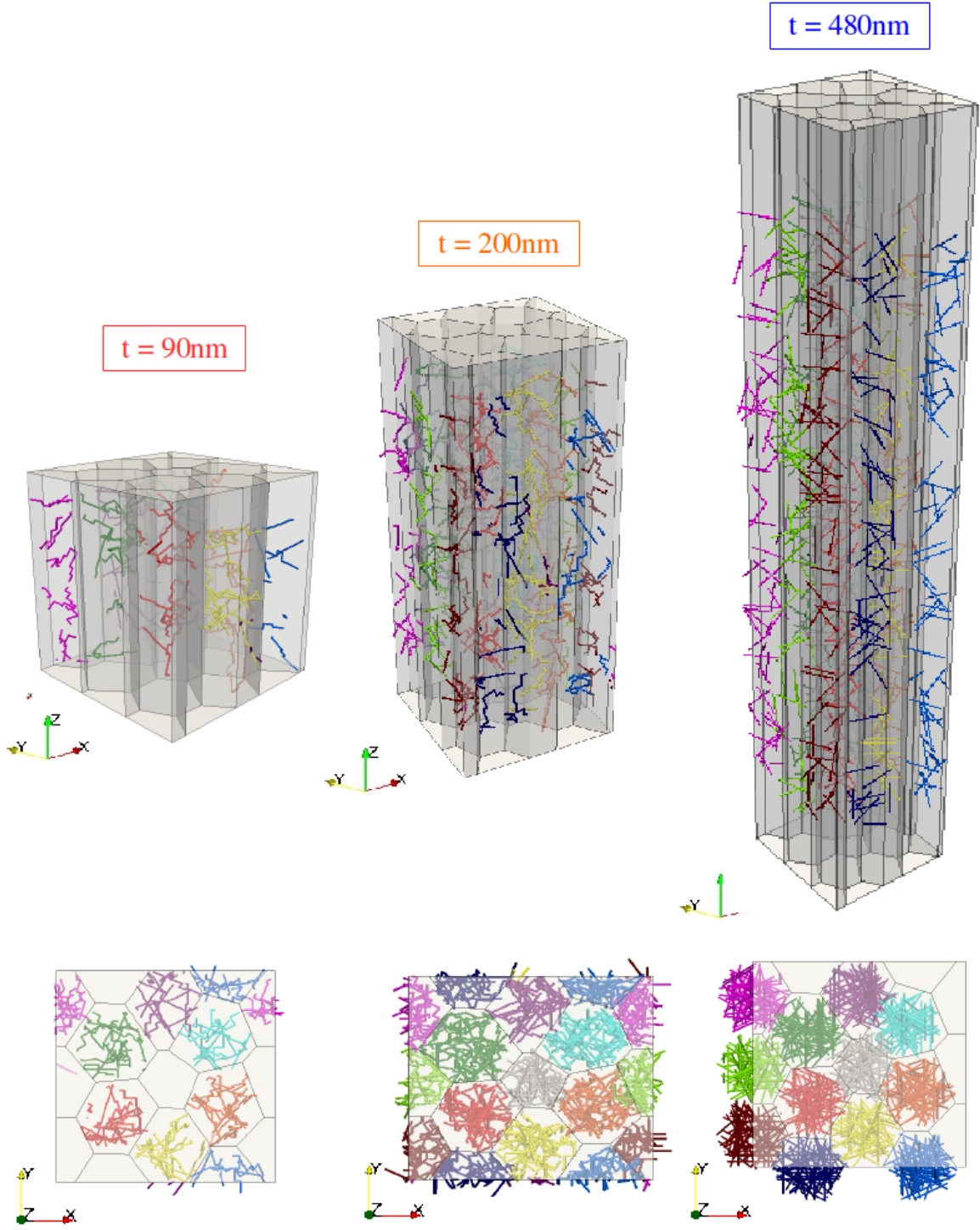


Figure 6.40 – Side and Top views of 90nm, 200nm and 480nm thick films with respective initial dislocation microstructures

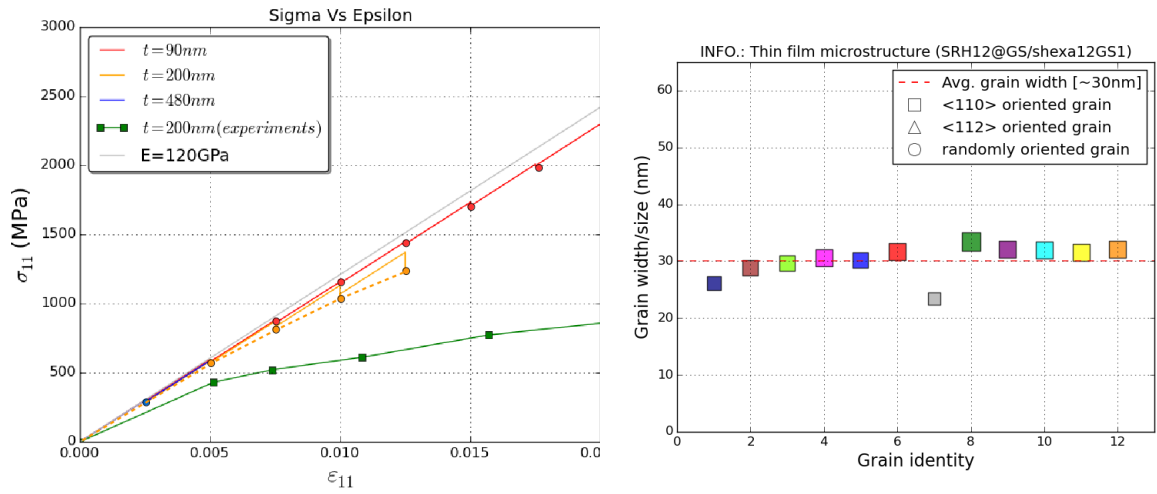


Figure 6.41 – (a) Stress-strain response and (b) Microstructure details of polycrystal with a smaller grain at the center of the film

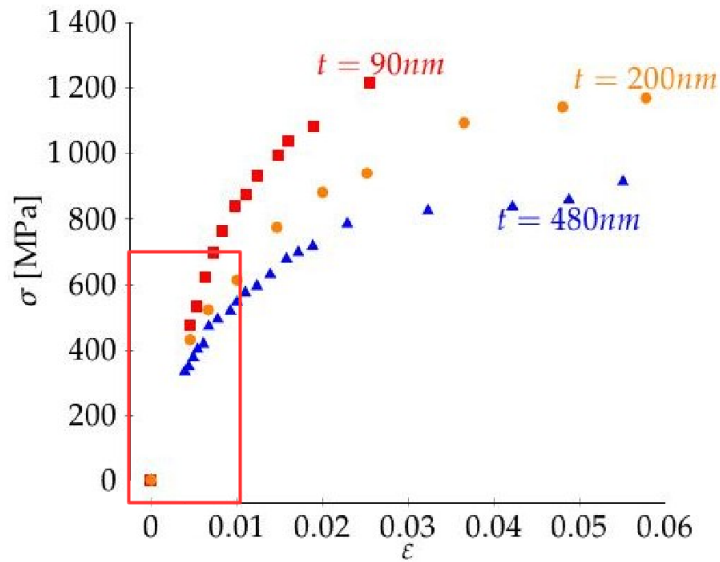


Figure 6.42 – Experimental stress-strain response of 90nm, 200nm and 480nm thick films with $\epsilon < 1.0\%$ region highlighted in red

6.5 Discussion

6.5.1 Anisotropic plastic response

Plastic deformation is generally deemed to be anisotropic. Enhancement of plastic anisotropy in elongated/columnar grains (with high aspect ratios) will prevent plastic strain localization in the grain and will avoid premature failure [40]. Results from polycrystal setup with larger grain at the center are used for further anisotropic analysis. As a reminder, it is again emphasized that all the grains in the polycrystal setup are oriented along $\langle 110 \rangle$ direction (*cf.* Figure 6.43 (a),(c)) which is also the dominant texture for which experimentally high ductility was observed (*cf.* Figure 6.43(b)).

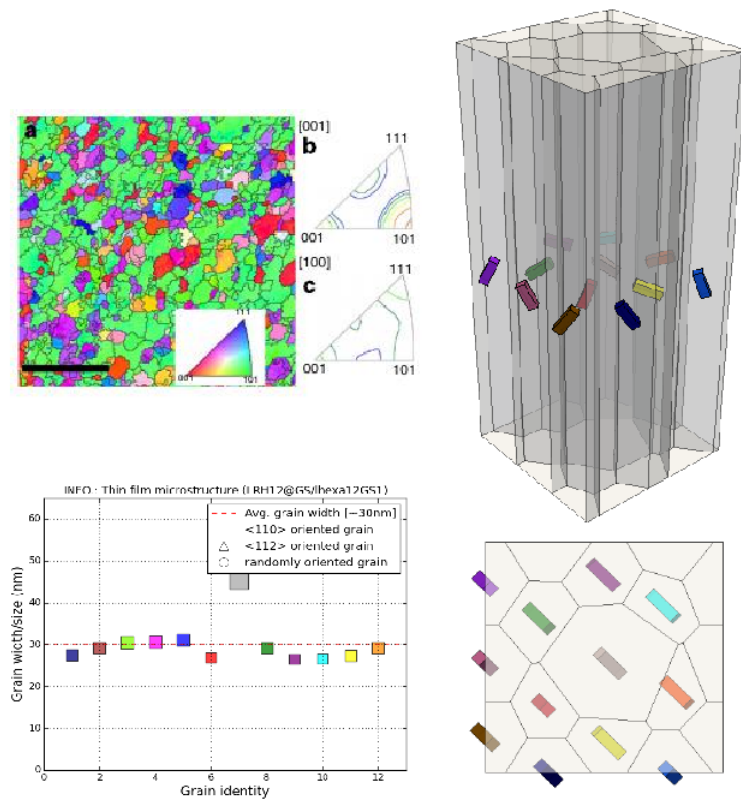


Figure 6.43 – (a) Texture map of Pd thin film showing moderate $\langle 110 \rangle$ texture (b) Polycrystal setup information and (c,d) Top and Side views of polycrystal with coloured texture object

To measure the anisotropic response of thin films, different plastic strain components are plotted against equivalent plastic strain (ε_{11}^{pl}) and are shown in

Figure 6.44. The plastic strain along the loading direction $\varepsilon_{11}^{plastic}$ is comparatively less than the $\varepsilon_{12}^{plastic}$ and $\varepsilon_{33}^{plastic}$. Apparently, $\varepsilon_{12}^{plastic}$ and $\varepsilon_{33}^{plastic}$ components of plastic strain are observed to contribute more to the overall plastic response in both 90nm and 200nm thick films.

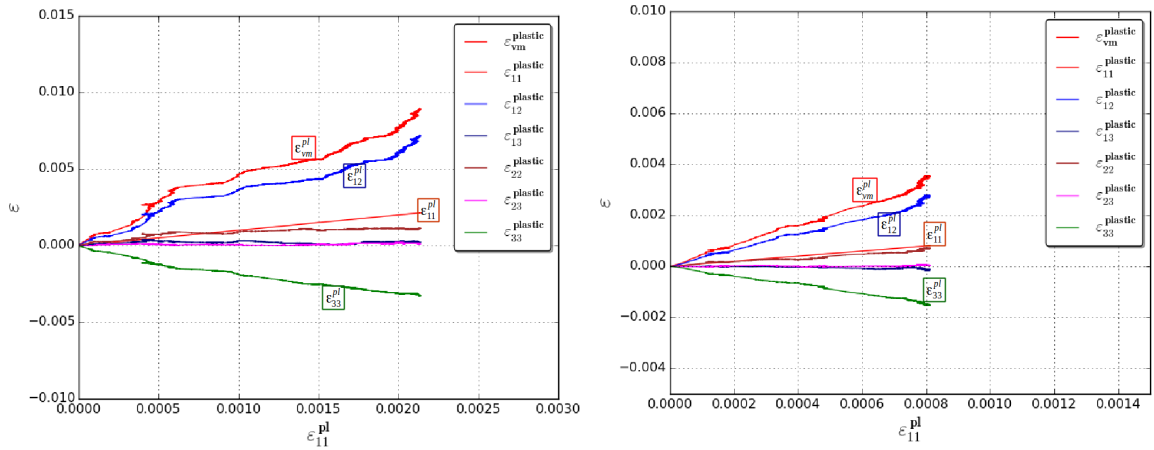


Figure 6.44 – Different plastic strain components and Von Mises plastic strain plotted against equivalent plastic strain (ε_{11}^{pl}) in (a) 90nm and (b) 200nm thick films, respectively

To understand the reason for such a plastic response, a cubic grain with columnar axis aligned along $\langle 110 \rangle$ direction is considered. Similar to the applied loading in the polycrystal simulations, a strain increment is applied along X-direction on a 1 micron cubic grain as shown in Figure 6.45. Due to elastic anisotropic, the stresses developed along Y- and Z- directions (*cf.* Figure 6.46) are sufficient to create considerable plastic strain along these directions.

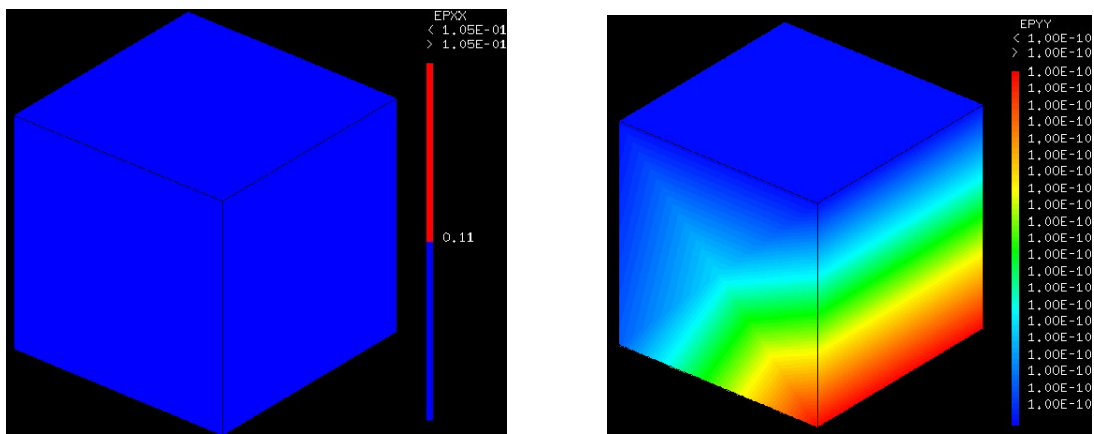


Figure 6.47(a) can now be used as reference to understand the different directions in the polycrystalline thin film setup. With a huge difference in grain

Chapter 6. Collective influence of grain and dislocation density parameters on plasticity of thin films

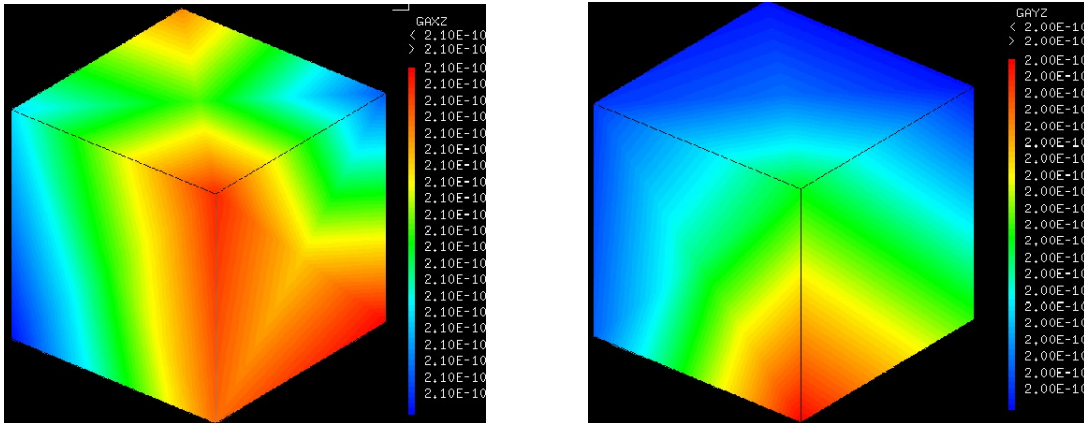
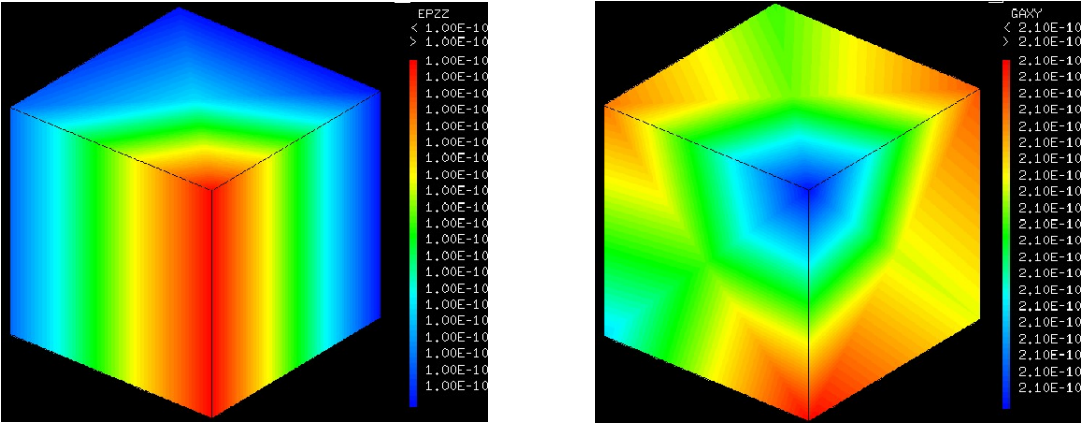
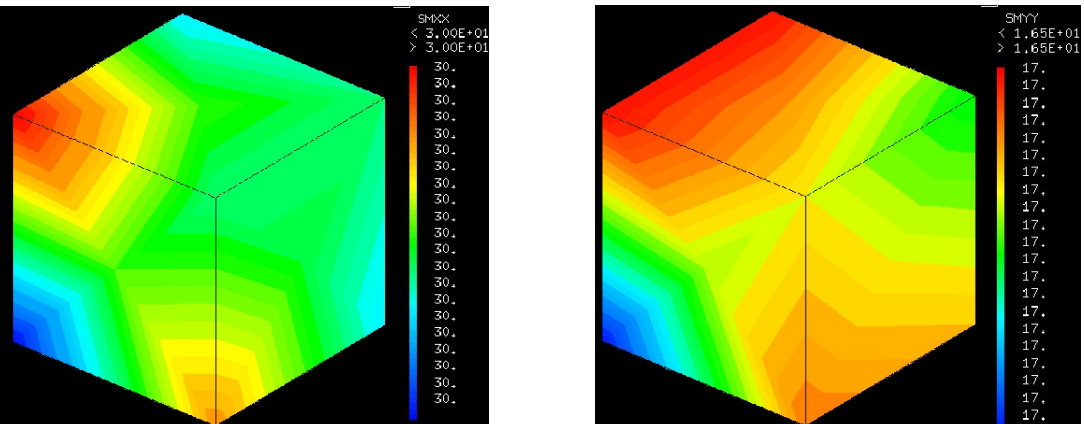


Figure 6.45 – Strain tensor applied on the reference cubic grain



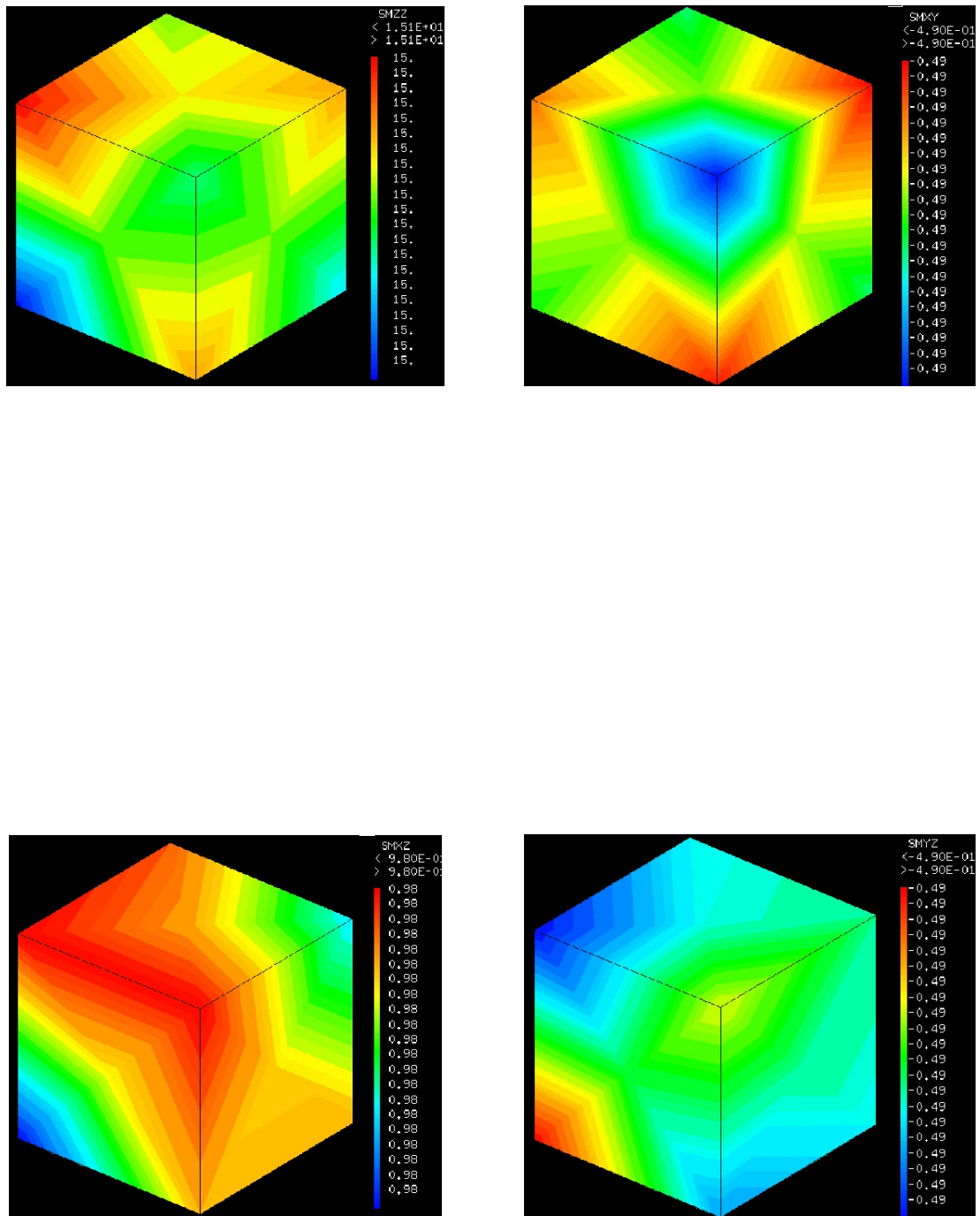


Figure 6.46 – Resultant stress tensor on the reference cubic grain

Chapter 6. Collective influence of grain and dislocation density parameters on plasticity of thin films

dimensions along X-/ Y- and Z- (thickness) directions, the are traced by the slip planes which are aligned almost parallel to the columnar axis (*cf.* Figure 6.47(b)) are large and also contribute to the plastic strain components other than equivalent plastic strain ($\varepsilon_{11}^{plastic}$). The anisotropic coefficient ($r = \frac{\varepsilon_{33}^{plastic}}{\varepsilon_{22}^{plastic}}$) in 90nm thick film suggests that the plastic anisotropy is $r \sim 2.5$. Such high anisotropy values will prevent localization of plastic deformation along the smallest dimension.

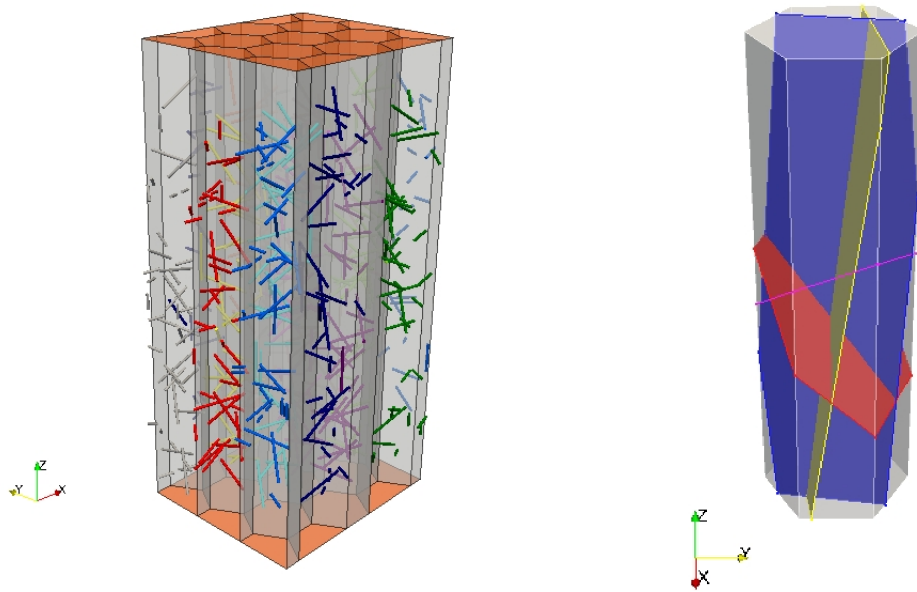


Figure 6.47 – (a) A 200nm thick film with free surface highlighted in orange (b) Direction of (111) glide planes in $\langle 110 \rangle$ textured single grain

6.5.2 Distribution of internal stresses

DD results clearly showed a very high impact of grain size distribution on plastic response. Internal stress distribution influenced by the grain size distribution will be non-negligible. To estimate a measure of heterogeneous distribution of internal stresses,

1. Firstly, analysis is carried out on 90nm thick film with larger grain in the center. Influence of localization of plastic deformation in the largest grain is assessed using an internal stress map (Results from *cf.* Section 6.4.4.2).
2. Further, the heterogeneities in internal stresses arising due to the presence

of grains with no initial dislocations in 90nm thick film is analysed (Results from Section 6.4.4.3).

For both the analysis, internal stresses at $\varepsilon_{11} = 1.0\%$ (*cf.* Figures 6.48(a) and 6.48(b)) are plotted on a plane placed at half-way along the thickness direction.

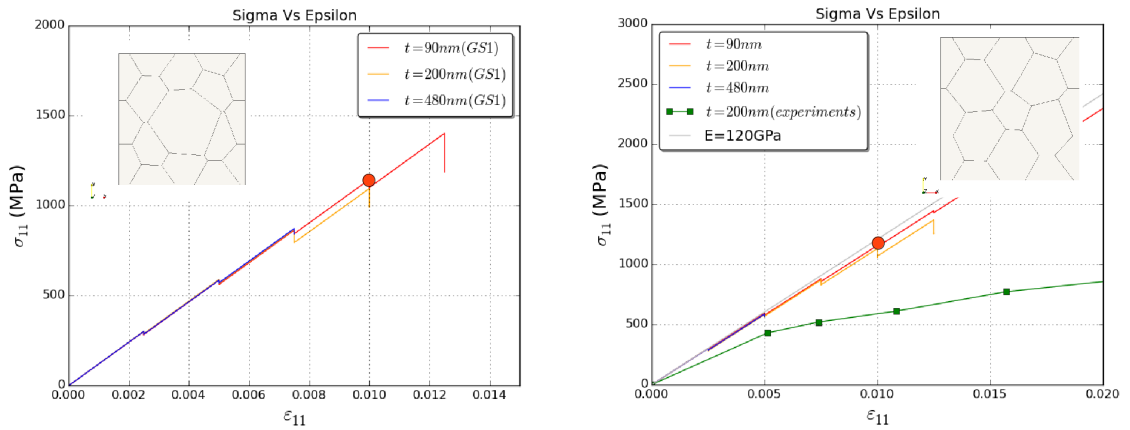


Figure 6.48 – Red marker showing the point analysis point on the (a) stress-strain curve with larger grain at center (b) smaller grain at the center of the polycrystal, respectively

6.5.2.1 Larger grain at the center of the polycrystal

Side and Top views of the internal stress field (σ_{11}^a) are shown in Figures 6.49(a) and 6.49(b). Here, a in the superscript of σ_{11}^a refers to stress field includes contribution from all the grains. The very first observation is that in smaller grains the dislocation concentrates mostly at the grain boundaries. This is due to the confinement of grain size in smaller grains. Whereas in larger grain, the dislocations run freely all over the grain and internal stresses are distributed also at the center of the grain.

To have a clearer picture of internal stress field in the largest grain, only the stress contribution arising from the central grain (σ_{11}^c) is plotted and the Side and Top views are shown in Figure 6.50(a) and 6.50(b). The stress field from the larger central grain is observed to be very intense and even spreads over two neighbouring grains on the right side as shown in Figure 6.50(b). The reason for such a long range influence is due to the fact that the low density of dislocations in smaller grains are mostly concentrated at the grain boundary. Particularly in this case, the stress concentration in smaller grains on the extreme right was observed not to be mutually cancelled (*i.e.*, no screening effect).

Chapter 6. Collective influence of grain and dislocation density parameters on plasticity of thin films

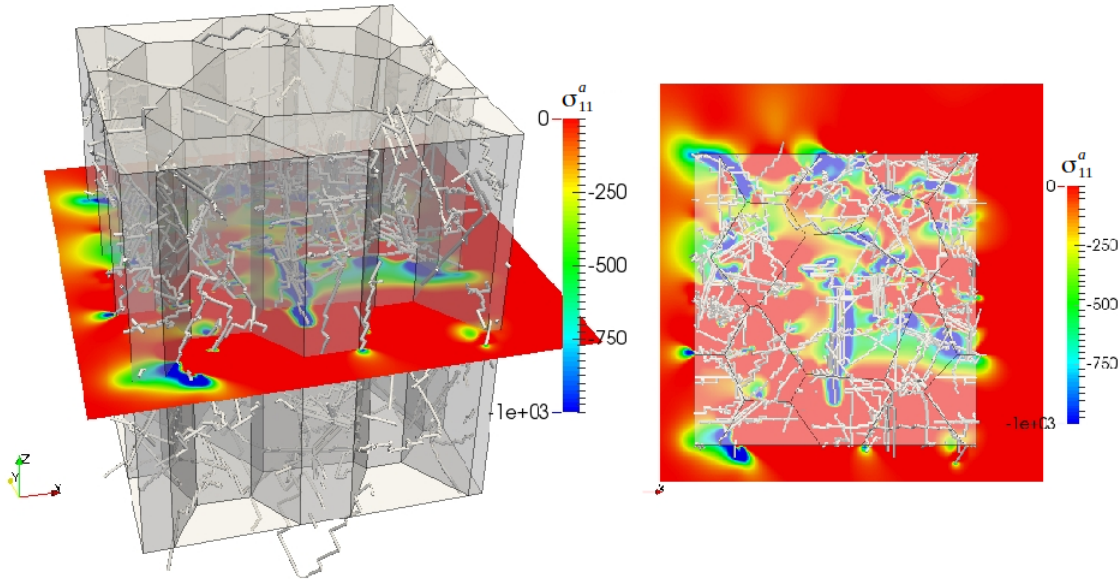


Figure 6.49 – (a) Side and (b) Top views of the internal stress field contribution from all the grains plotted on a square plane placed half-way along 90nm thick film

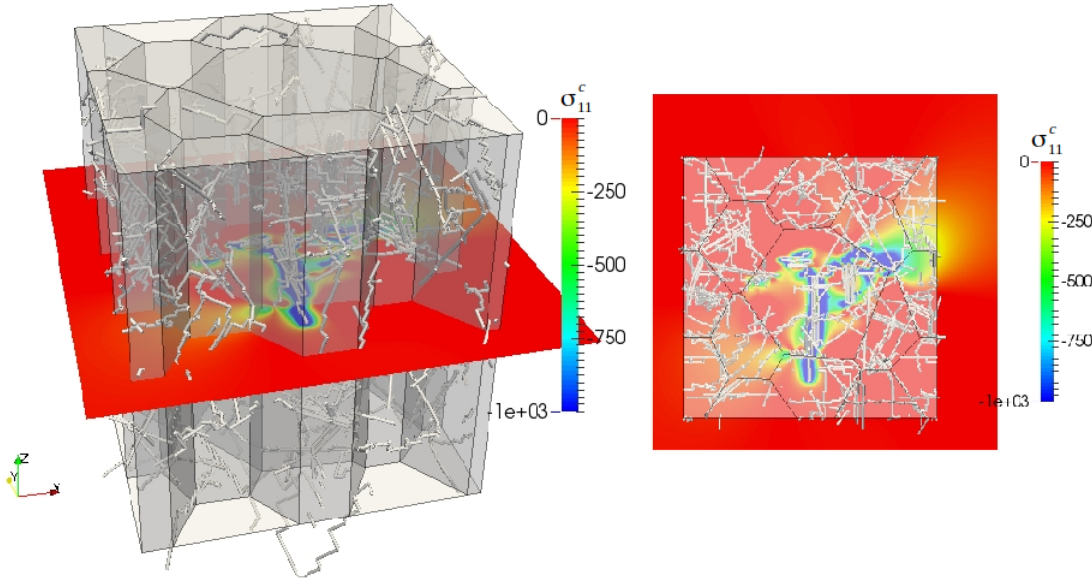


Figure 6.50 – (a) Side and (b) Top views of the internal stress field contribution from only central grain plotted on a square plane placed half-way along 90nm thick film

Similarly, to support the above argument, the internal stress contribution arising from the rest of the grain (σ_{11}^r) is plotted. In other words, the stress contribution from the central grain is not accounted for. Further, the Side and Top views of the stress map are shown in Figures 6.51(a) and 6.51(b). It is observed that the argument initiated during the analysis of internal stress field from central grain holds true even in this case. That is, grains acting as neighbours to the central larger grain will have an influential contribution on the stress field due to their concentration at the grain boundaries. This further promotes deformation in the larger grain.

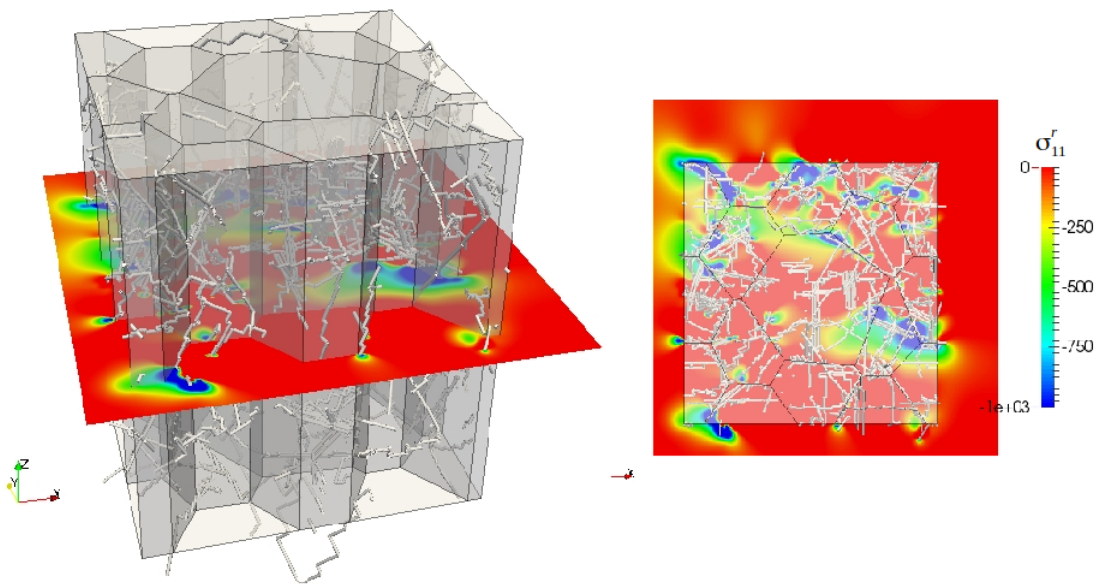


Figure 6.51 – (a) Side and (b) Top views of the internal stress field contribution from all grains except the central grain plotted on a square plane placed half-way along 90nm thick film

6.5.2.2 Effect of the presence of a dislocation free small grain among large grains

Internal stress field of a polycrystal with smaller grain at the center is plotted on a plane and is shown as Side and Top views in Figures 6.52.

Analysis of the internal stress field indicates that it will be quite difficult for the grain with no initial dislocation sources to withstand the stress concentration at the grain boundaries. Ultimately, new dislocations should be nucleated at the grain boundary point with high stress concentration. Such dislocation nucleations mechanisms are required to maintain compatible deformation among different

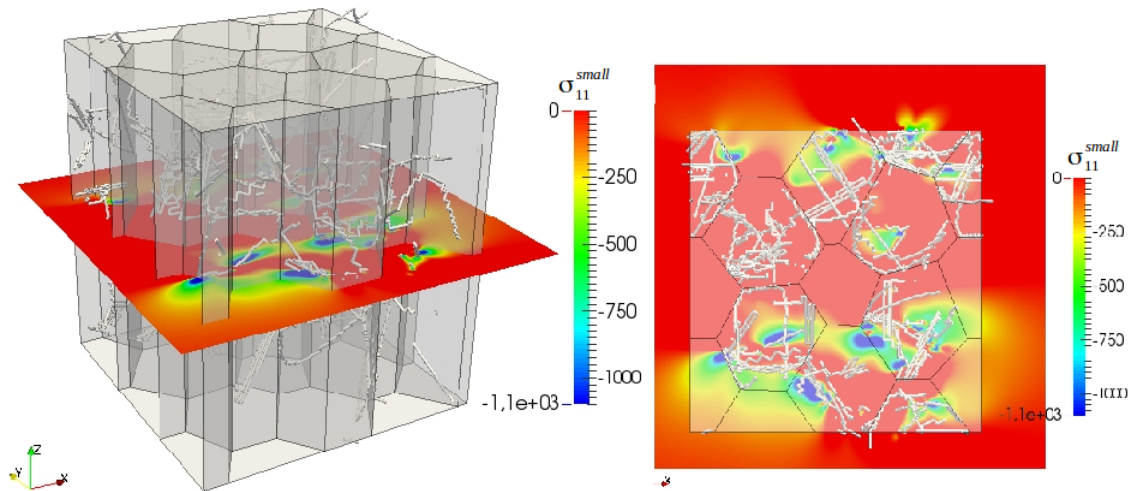


Figure 6.52 – (a) Side and (b) Top views of the internal stress field contribution from all grains except the central grain plotted on a square plane placed half-way along 90nm thick film

grains in a polycrystal [170]. Understanding such dislocation nucleation from GBs is of interest for the materials modeling community at continuum scale. Such studies can be performed using the line tension model [104] in DD simulations. This work has not been carried out and is only presented to highlight a perspective study planned.

6.6 Conclusions

Polycrystalline DD simulations provide an elegant way to study the elementary deformation mechanisms responsible for the strain hardening response of nanocrystalline thin films. An interface with Gmsh software has been developed to model not only the grain size distribution in polycrystals but also to generate the corresponding meshes used while solving the BVP. The simulation setup used for performing uniaxial tensile test on Pd thin films is presented along-with the adapted DD-FEM algorithm based on superposition principle. Major conclusions drawn from the present study are:

- The strain hardening response and the evolution of total dislocation density of 200nm thick film is captured using DD simulations with 4-grains in the polycrystal. The initial dislocation density used during the DD simulations is in close agreement with experiments. This emphasizes that the dominant

deformation mechanism is still dislocation mediated.

- Reasonable size effects were observed from the DD results with no grain size distribution.
- Further, considerable size effects (*cf.* Figure 6.53) were observed only with the model involving grains with no initial dislocation sources in the thinnest film.

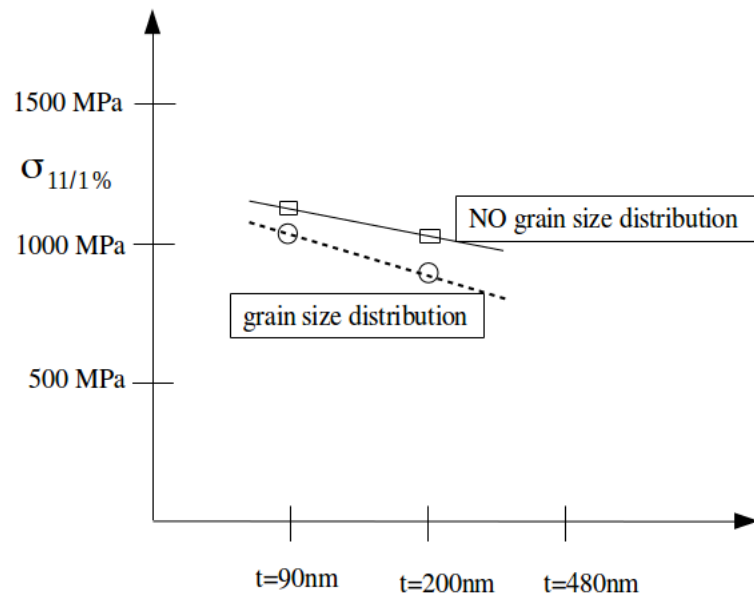


Figure 6.53 – Comparing equivalent stress (σ_{11}) at equivalent strain ($\varepsilon_{11} = 1\%$) in different (90nm, 200nm and 480nm) films with and without grain size distribution

- Anisotropic behavior of polycrystal is very very strong when grains are aligned in a preferential orientation.
- Internal stress fields plotted in polycrystal with larger grain at the center also highlight the localization of plastic deformation changes with the internal aspect ratio specific to a grain size distribution.

PART - IV

DDD simulations in DC crystals

7 Modeling electrostatic dislocations

SEMICONDUCTING materials have been the corner stone to the success of the present-day microelectronics industry. Almost all the opto-electronic devices which are produced using semiconducting materials show the presence of lattice defects, mainly dislocations. The density of dislocations in the range $10^7 - 10^{11} \text{ cm}^{-2}$ is considered relatively low to influence the properties. But, a substantial decrease in the overall performance of solar cells is observed due to the presence of dislocations [77]. This is due to the fact that the carrier lifetime, which determines the efficiency of the solar cell, is significantly affected by the opto-electric features carried by dislocations and other point defects.

The main objective of this chapter is to establish a link between electric properties and dislocations in semiconductors. This chapter introduces some interesting electric features of dislocations in semiconducting materials. A review of one of the earliest and most widely used electrostatic model is carried out. Finally, implementation of Read's model is carried out for the first time in a DD model. This is followed by application of the *electrostatic* model to semiconductors.

7.1 Introduction

In the photovoltaic (PV) industry, conventional crystalline Si based technology still has a dominant market share when compared to the newly developed/developing thin film technology. Availability in abundance, low cost and ease of growing Si wafer constitute few reasons which may have restricted the industry to completely shift towards thin film technology. Another side of the story is more lattice defects based. Si PV wafers cut from single crystal Si cylinders are often free from lattice defects such as dislocations. Inherent defect free nature has been found to be clearly advantageous in terms of overall efficiency of the PV wafer. But, the polycrystalline PV wafer does not provide the same advantage as the single crystal

PV wafers. In polycrystalline PV wafer, dislocations are often generated from grain boundary sources during solidification process [100]. The dislocations may leave some residual dislocations behind during their motion away from the source. Such residual dislocations rearrange into low-energy configurations forming sub-grain boundaries, or often addressed in the PV research community as *dislocation clusters*. A specific DD study had been carried out explaining the reason for forming such low energy configuration.

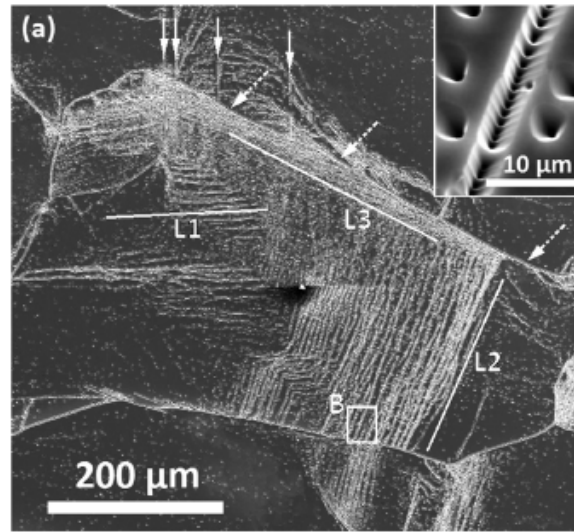


Figure 7.1 – SEM image showing rearrangement of dislocations in Si [100]

GaN thin films produced using various vapour deposition techniques, are impacted by different kind of dislocations, called *misfit dislocations*, which develop due to lattice mismatch at the interface between the S or SiC substrate and GaN layer. These dislocations can with ease glide along the GaN layer and are categorized as *threading dislocations*. A schematic view of GaN layer grown on Si substrate is shown in Figure 7.2 and a TEM image of GaN with AlN buffer layer on a Si substrate can be seen in Figure 7.3. The **B**, **N** and **T** in the image identify the dislocation blocked by the AlN layer, the dislocation produced by the AlN layer and the dislocation threading the interlayer, respectively. Dislocations produced of any kind are observed to have detrimental effects on the electrical performance.

Alexander was among the first to address the important influence of dislocations not only on the plastic deformation but also on the electric behaviour of semiconductors [2]. To address the electrically negative charged nature carried by dislocations, electron paramagnetic resonance (EPR) has been used to estimate the unpaired electrons along a dislocation line in Ge [82]. Though, all EPR spectras

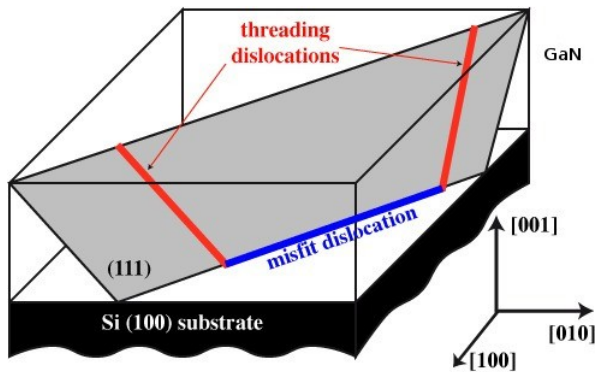


Figure 7.2 – A schematic view of misfit and threading dislocations in GaN layer over Si substrate

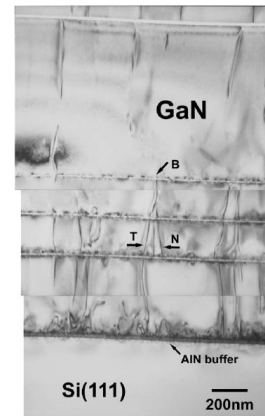


Figure 7.3 – Cross-section TEM images of GaN epilayer with AlN buffer layer with dislocations [73]

came from dangling bond type defects, there was no evidence of 1D conduction along the dislocation line as hypothesized by Shockley¹. The recorded EPR spectra were believed to be due to dislocation debris that are left from dislocation motion. This was confirmed by the clear difference observed between the spectra coming from point-defect clusters and dislocation cluster. As a conclusion, the density of well-defined paramagnetic sites was suggested to be very low in Ge [2]. In other words, only one in hundred or more sites along the dislocation line were occupied by electrons yielding a very low density. Few authors argued that the lack of paramagnetic sites is due to the defective dislocation core² [89] and others did not agree that dislocations can act as electron acceptors. But, Alexander further suggested that the dislocation core should have been predominantly reconstructive in nature which avoid rows of dangling bonds being formed. No conclusive evidence of electric signature carried by dislocations has been found, atleast in Ge and Si.

If reconstruction is the reason for not observing rows of dangling bonds, then one needs to see what would be the stable structure of dislocations in Si. In diamond cubic crystals such as Si, dislocations predominantly align along $\langle 110 \rangle$ direction due to low Peierls energy in that direction. So, the basic type of dislocations were screw and 60° dislocations because of $\langle 110 \rangle$ direction in (111) planes. Dislocations in Si were observed to be dissociated into partials, which is evident from the difference in the velocities of dislocations. The dissociation of a perfect dislocation

¹Shockley's hypothesis has been used by Read to develop an electrostatic model for dislocations in semiconductors which is reviewed in Section 7.2 of this Chapter.

²A defective dislocation core generally contains kinks and jogs along the dislocation line

in Si follows:

1. Screw dislocation is divided into two Shockley partials
2. 60° dislocation is divided into a 30° partial and a 90° partial

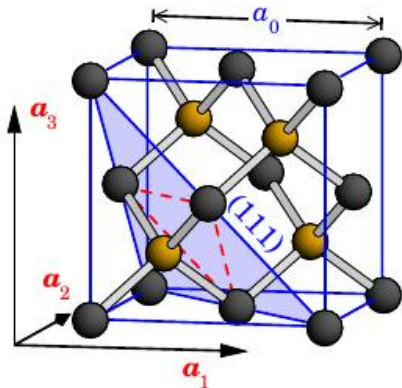


Figure 7.4 – Diamond cubic lattice structure of Si [14]

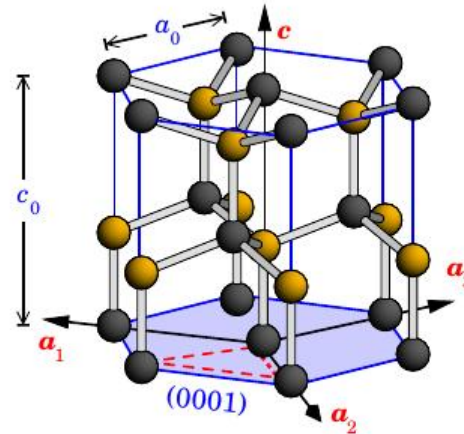


Figure 7.5 – Hexagonal wurtzite lattice structure of GaN [14]

Whereas, GaN which shows a wurtzite crystal structure (example of hexagonal crystal system), mostly perfect dislocations, of a-type (edge), c-type (screw) and $\langle a+c \rangle$ type (mixed) are observed. A good evidence of these dislocations being electrically highly charged is found experimentally [29]. With the above discussion moving in the direction of the dislocation type, it is interesting to understand the behavior of electrically charged perfect dislocation in GaN and maybe, in the future, to extend the concept of electrically charged dislocation to Si or Ge. This will be a challenging task as it requires proper treatment of dislocation characters (Eg: 60° dislocation, dislocation dissociation into partials) in DD codes. Nodal codes such as *NuMoDis* [30] will serve a great deal in this aspect. In the coming sections, a review of electrostatic model proposed by Read is reviewed and further implemented as a post-processing tool in the DD code (TRIDIS).

7.2 Review: Read's electrostatic model

The famous schematic view of a diamond cubic lattice [152] with and without an extra half plane (edge dislocation) are shown below. In Figure 7.7, the row of

7.2. Review: Read's electrostatic model

atoms above the slip plane has no neighbours in the plane below. Dangling bonds can be formed by these atoms which do not have any neighbours. These dangling bonds are believed to be the basis for electrical effects in semiconductors.

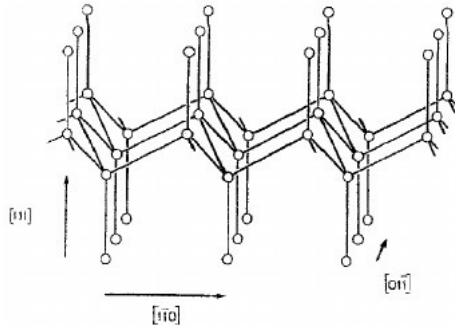


Figure 7.6 – The diamond cubic lattice structure [152]

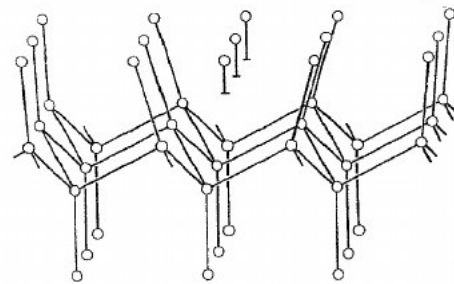


Figure 7.7 – A dislocation lying on a (111) plane at 60° to the Burgers vector [152]

Shockley was the first to put forward the concept of edge dislocation having a one dimensional arrangement of dangling bonds in the dislocation core at the edge of inserted half plane [188]. But, the very first theory pertaining to electrical properties of dislocations was proposed by Read [152]. The statistics of occupation of dislocation states taking into account the Coulomb interactions between accepted electrons was derived [151]. It was also found that dislocations in semiconductors effectively scatter the charge carriers in semiconductors due to two reasons:

1. **Deformation potential** due to the long range distortion field around the dislocation line
2. **Electrostatic potential** due to electric field around a charged dislocation line

The dangling bonds, which act as electron acceptors along an edge dislocation, builds a negative line charge along the dislocation line. In this model, Read introduced a term called *filling fraction*, which would give an idea on whether the acceptor site is filled by electron or not. The filling fraction in n-type germanium was calculated by considering the straight-line array of single traps for an edge dislocation lying on a (111) plane. The *filling fraction* f , which varies between [0,1] is then given by

$$f = \frac{\beta}{\alpha} \quad (7.1)$$

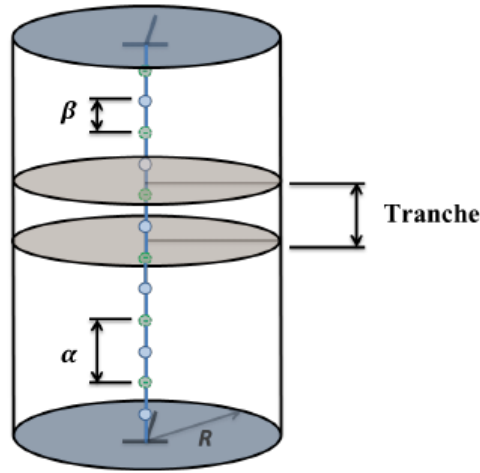


Figure 7.8 – An edge dislocation showing acceptor centres and electron trapping sites

where α is the spacing between trapped electrons or occupied sites, and β is the spacing between dangling bonds. The value $f=0$ represent that none of the acceptor sites are filled with electrons. In contrast, $f=1$ represents that all the acceptor sites are filled with electrons. Figure 7.8 shows a schematic view of every alternate site being filled with an electron, correlating to $f=0.5$.

The trapped electrons are coming from an ionized donor near the edge dislocations. The attached electrons build up a negative charge on the dislocation. Every negatively charged edge dislocation should be compensated by a spatial charge distribution of the opposite polarity. Due to this, a positively charged cylinder with a radius R surrounds every negatively charged dislocation. The radius of the cylinder, R was found from the below neutrality condition:

$$q\pi R^2(N_D - N_A) = \frac{q}{\alpha} \quad (7.2)$$

here, q is the magnitude of the electron charge and N_D, N_A which depend of doping concentration, are the number of donors and acceptors, respectively. When the contribution of carriers to space charge is negligible at low temperatures, and for very large R compared to α , the potential, ϕ is given by the formula:

$$\phi = \frac{-q^2}{\kappa\alpha} \left[1 - \frac{r^2}{R^2} + \ln \frac{R^2}{r^2} \right] \quad (7.3)$$

7.3. Modelling a charged dislocation

where, q is the magnitude of the electron charge, κ is the dielectric constant, α is the spacing between trapped electrons and $\alpha < r \leq R$ is the distance from the dislocation. For $r < a$, one needs to account for the discrete nature of the charges on the dislocation line. For the region outside the space charge cylinder, the potential $\phi = 0$ and the potential varies with r inside the cylinder. The change in the potential for different filling fraction values is presented in the Figure 7.9.

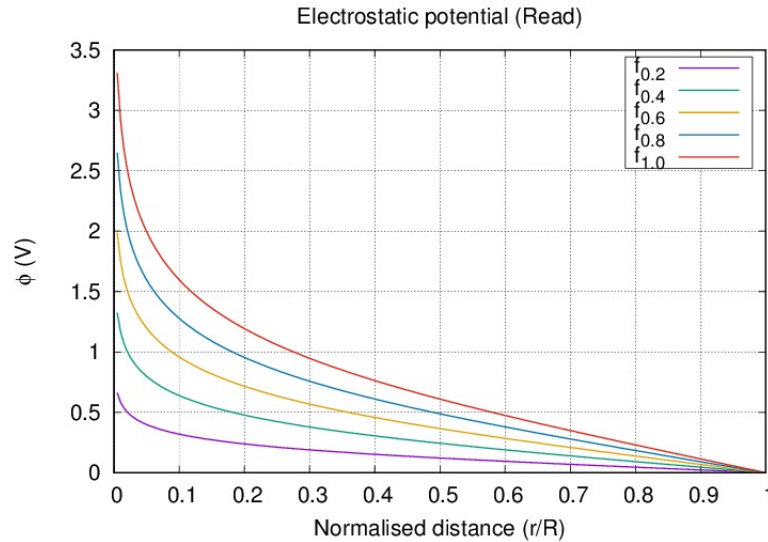


Figure 7.9 – Variation of electric potential with distance r inside the cylinder of radius R for different filling fractions f

7.3 Modelling a charged dislocation

To model an electrically charged dislocation, the charges need to be distributed along every edge dislocation line, according to the *filling fraction*. To efficiently distribute charges along an edge dislocation line, we firstly divide the dislocation line into several *tranches* as shown in Figure 7.10. To avoid modelling empty sites and filled sites (occupied by electron) differently, an effective charge is calculated depending on the number of empty and filled sites in every tranche on the dislocation line. Each *tranche* is then given an effective charge at the center as shown in Figure 7.11.

Since, the potential was observed to decay exponentially when going far away from the dislocation core (cf. Figure 7.9), the influence of each tranche charge can be visualized as a spherical region of radius R (same as the cylinder radius as explained by Read) around the charge.

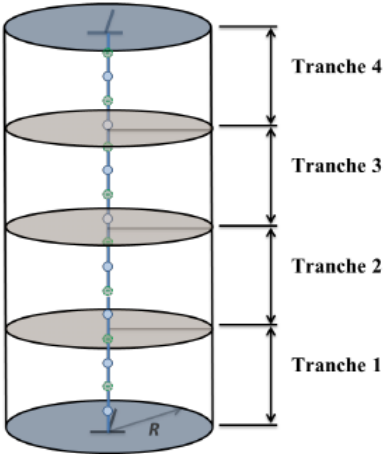


Figure 7.10 – Building tranches along an edge dislocation line

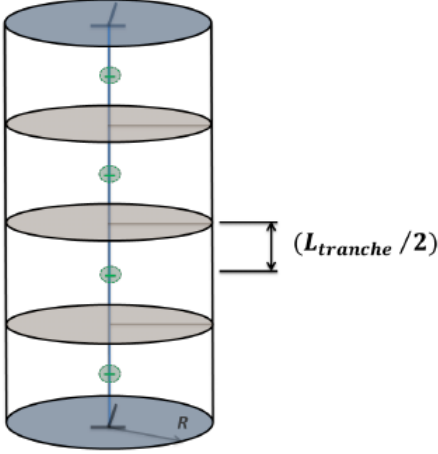


Figure 7.11 – Representation of the effective charge in each tranche

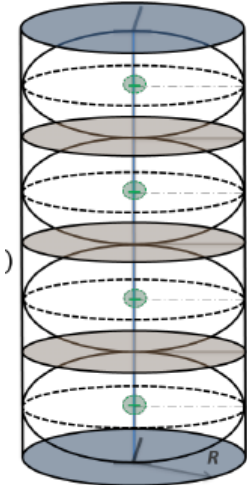


Figure 7.12 – Estimated influence of tranche charge

7.3.1 Application: charged dislocation in GaN

A straight edge dislocation with Burgers vector aligned along $[-1-1\ 0]$ direction is placed in a cubic grain of side 1000nm can be seen in Figure 7.13. The magnitude of Burgers vectors is considered to be 4\AA . The two end (pinning) points of the Frank-Read source are placed on the opposite sides of the cube to resemble an infinitely long dislocation. The distribution of tranche charges along the dislocation line was carried out according to the filling fraction ($f=0.65$) and is shown in the Figure 7.14.

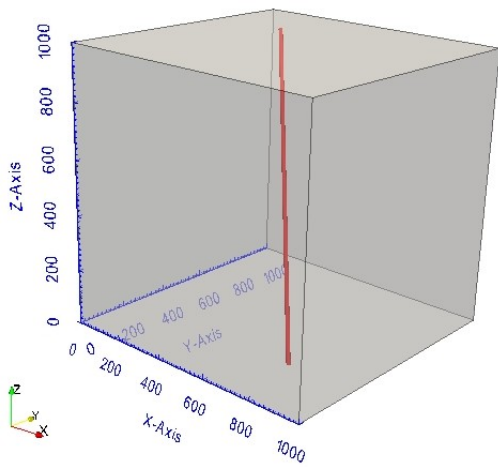


Figure 7.13 – Infinitely long edge dislocation line in a cubic grain

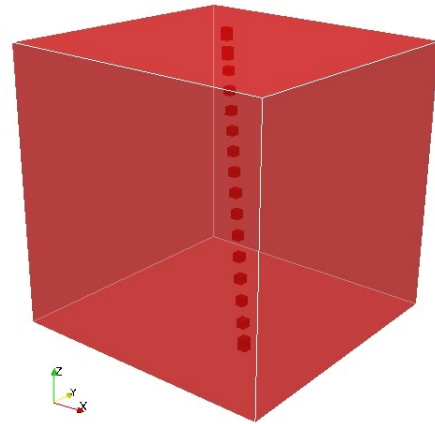


Figure 7.14 – Tranche charges along the corresponding edge dislocation in Figure 7.13

7.4 Solving an electrostatic problem

After constructing a charged dislocation, the problem scales down to a simple electrostatic boundary value problem assuming boundary conditions to be known. The solution of the Poisson equation (*cf.* Equation 7.7) yields electrostatic potential, ϕ for a given charge distribution, ρ . The Poisson equation in electrostatics is derived from Gauss's law:

$$\Delta \cdot \vec{E} = \frac{\rho}{\varepsilon_0} \quad (7.4)$$

where \vec{E} is the electric field, ε_0 is the electric constant and ρ is the total electric charge density (charge per unit volume).

For a linear, isotropic and homogeneous material, in the absence of changing magnetic field, \mathbf{B} , the curl of electric field is zero (cf. Equation 7.6) and can be written as

$$\vec{E} = -\Delta\phi, \quad (7.5)$$

$$\Delta \times \vec{E} = \frac{\partial \vec{B}}{\partial t} = 0 \quad (7.6)$$

where t is the time.

Substituting Equation 7.5 in Equation 7.4, leads to:

$$\Delta^2\phi = -\frac{\rho}{\epsilon_o}. \quad (7.7)$$

Instead of using a simple superposition method to find the effective electrostatic potential due to the accumulated charge in the sample, a more general approach of using a Poisson solver can be followed. The numerical solutions for the differential equation 7.7 can be found by either an iterative FEM-based Poisson solver or a direct FFT-based Poisson solver. For solving the present electrostatic problem of a single negatively charged dislocation in a cubic grain, we use **PoisFFT**, a FFT-based Poisson solver [72]. One advantage of using this particular solver is that, the solver has been elegantly written to adapt to any possible boundary conditions (Periodic, Dirichlet or Neumann). Another advantage is the use of PFFT software library [143] for computing FFT [71] in parallel using message passing interface [132].

7.4.1 Validation of the PoisFFT solver

A simple 2D electrostatic problem is setup to test/validate the applicability of the PoisFFT solver. In the 2D problem, a point charge of 10 Cb is placed at the center of a square surface of unit side. A unique solution is obtained by designating the potential ($\phi = 0$) on the border of the unit square. The solution obtained from PoisFFT solver is shown as a 2D electric potential map in Figure 7.15.

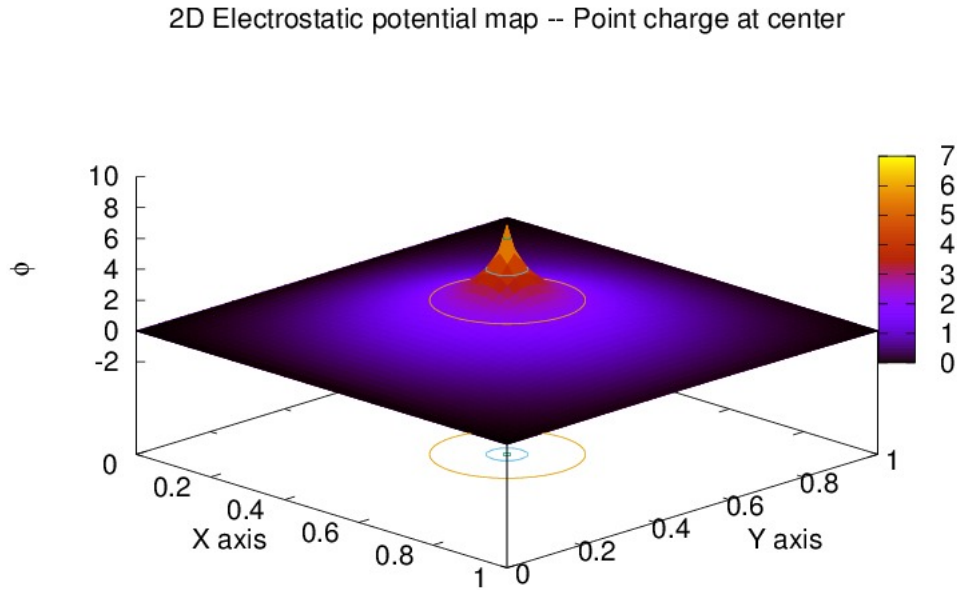


Figure 7.15 – Validation of the PoisFFT solver; Electric potential for a point charge at the center of a unit square

7.5 Results and discussion

For solving the electrostatic boundary value problem, a FFT grid of size 128 has been used. Results were also observed to be consistent for grid sizes 256 and 512. So, these results have not been presented here. Figure 7.16 shows the FFT grid on a cubic grains with tranche charges along the dislocation line.

Upon solving the differential equation with a Dirichlet boundary condition ($\phi_{boundary} = 0$), the electrostatic potential map is shown in Figure 7.17. A cut-off value of 100nm has been used to show the 3D shape of the potential map. It is observed that the potential which takes the shape of an elongated sphere can be closely be manifestation with the Read's positively charged cylindrical region around a dislocation. A filling fraction of $f=0.65$ chosen in Section 7.3.1 indicates that every sites at a distance of $\sim 52\text{nm}$ along the dislocation line is occupied by a tranche electron. In total, 16 tranche electrons were generated on the edge dislocation presented in this setup. For this minimum value of f , the electrostatic potential on the boundary of the cubic grain shows a magnitude of 2.5V. This magnitude of the electrostatic potential for $f=0.65$ is in close agreement with the potential shift measured due to threading edge dislocation in GaN [29].

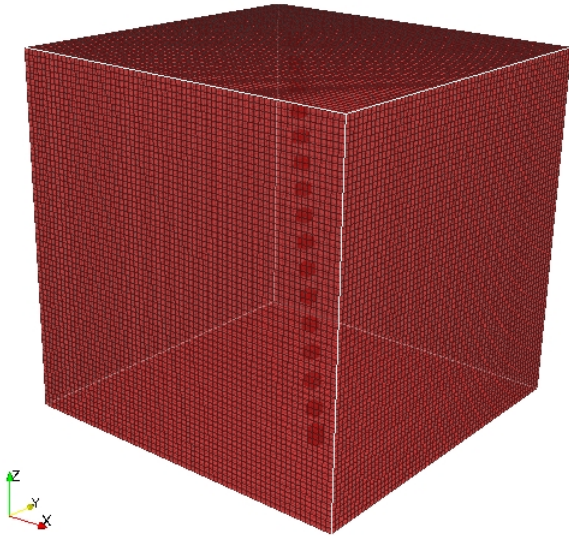


Figure 7.16 – Cubic grain with tranche charges highlighting the FFT grid of size 128^3

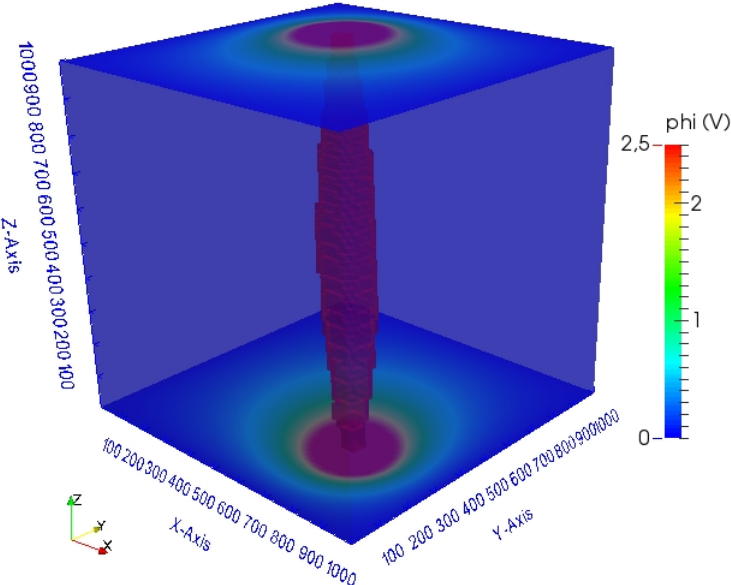


Figure 7.17 – Electrostatic potential surface around an edge dislocation in Figure 7.13 and influence of the potential on the boundary surfaces of the cubic grain

7.6 Conclusions

This chapter presented a review of the very first and widely used electrostatic model for a dislocation. Further, the model has been successfully implemented as a post-processing tool in the DD code. A FFT based Poisson solver has been used to solve the electrostatic boundary value problem with Dirichlet boundary condition. The magnitude of potential measured on the boundary surface of a cubic grain is in close agreement with the one observed in literature.

The electrically charged dislocation model can be also be extended to Si. In that case, the dissociation of a perfect dislocation into partials, as depicted in Section 7.1, should be modeled in the DD codes to accurately predict the influence of a electrically charged dislocations in Si. The easy dissociation of perfect dislocations into partial will present some interesting views in regard to electro-plastic effects due to dislocations (Eg: On the mobility of a dislocation) in Si. Also keeping in mind the potential influence of electrostatic interaction among dislocations, a systematic study need to be carried out to estimate the influence of dislocation-dislocation interactions on the overall electrostatic potential in a single Si crystal. Since it is now understood that both the deformation and electrostatic potentials (*cf.* Section 7.2) are inherent properties of dislocations in semiconductors, the electron scattering capabilities and the mobility of dislocations in semiconductors needs to be addressed together. Moving in a perspective similar direction, recently, a standard piezoelectric framework for linear elastic solids by accounting for the presence and motion of dislocation fields had been published [172]. With this framework, the overall impact on the piezoelectric properties was assessed in the presence of dislocations, which follow a more continuous representation of the overall dislocation density via Nye's tensor [138]. An electro-mechanical coupling needs to be established in the discrete dislocation framework to further understand the behavior (Ex: mobility) of dislocations in semiconductors.

Due to the lack of strong experimental evidence on a dislocation being electrically charged in Si, no further attempt had been made to extend the present implementation to Si. But, preliminary work on GaN has motivated to advance further in the direction of defects-based research in Si. The newly developed electron holography can serve the purpose of diagnostics in Si technology and research [174].

PART - V

Conclusions and perspectives

8 Conclusions and perspectives

Our knowledge of crystalline materials behavior has always been limited to single crystals. This is due to the fact that understanding the mechanics of polycrystalline materials is challenging. The unavoidable presence of GBs and their complex interplay with dislocations will dictate the response of polycrystalline material. One such example is in the field of *flexible electronics*, where, a better understanding of mechanics of the materials along with the knowledge of dislocations in the materials is necessary to develop materials with enhanced properties. As a first step in studying such materials, emphasis had been placed in the present thesis to correctly model grain boundaries i.e., *columnar shape of the grains*.

In the first chapter of the thesis, different types of interfaces which are generally found in crystalline materials are reviewed. Different dislocation-grain boundary models proposed in the literature are revisited. Knowledge of such models will further guide us in developing new and efficient materials modeling tools. In the second chapter, the state-of-the-art *on-chip* tensile test technique developed at UCL has been introduced. This new experimental technique has enhanced our understanding of polycrystalline metallic films. It is technically difficult but not impossible to conduct a detailed study on different types of GBs using this method. The present understanding is confined to external polycrystalline parameters such as, overall dislocation density, film thickness, grain size distribution, grain orientation and the presence of twin in the polycrystalline material. Numerical modeling tools such as, molecular dynamics at atomic scale and crystal plasticity models at continuum scale always provide a useful interpretation of the materials behavior. But, the extent to which these models can be used is limited. For example, local rules used in phenomenological crystal plasticity based models need to be verified or validated. To do this, the use of atomic scale simulation pose strong limitations in predicting materials response under the collective behavior of defects and limited feasibility in modeling complex grain boundary morphologies.

A polycrystalline version of dislocation dynamics (DD) code can bypass the

forth mentioned limitations. An advanced polycrystalline DD model used in the thesis has its roots from the single crystal version of the DD code. A strong background of physics at single crystal level in the DD codes is an added advantage. But, DD codes generally pose a critical stress field computational issue. A new GPU optimised subroutines for stress field computation of dislocations has been added to the polycrystalline DD code. Although, the accuracy of the GPU version has been validated against a single crystal version, the acceleration achieved by this method can still be optimised. In addition to the local hardening rules at single crystal level in DD code, additional dislocation-GB interaction rules are introduced to model slip transmission across GBs. But, this version has not been used for addressing thin films as there is still a long way to go for creating a reasonable GB-based DD model.

Accurate representation of GBs at continuum level is a critical issue which is addressed in Chapter 5 of the thesis. Plastic deformation behavior of the grains of same volumes but different aspect ratios are compared. Change in the aspect ratio of the grain was observed to change systematically change the pileup behavior inside the grains and thereby, the back stress developed. Back stress is quantified by calculating the slope of the unloading part of the stress-strain curve. Results incorporated into an analytical formulation will be useful for phenomenological crystal plasticity models. Plastic deformation behavior in polycrystals with sub-micron sized grains is studied in Chapter 6. GBs were assumed to be infinitely strong obstacles to dislocations but the long-range stress field of dislocations is still felt across GBs. This idea was used to perform first-of-the-kind DD simulations to study the influence of grain size distribution in a polycrystal. Results show a promising future for more polycrystalline DD simulation based studies.

Finally, the basic idea of electrically charged dislocation influencing the mobility of charge carriers in semiconductors is addressed by implementing Read's model as a post-processing tool in DD code. Eventhough, the first-of-this-kind study is limited to a static dislocation case, it opens a wide range of possibilities in developing a discrete piezoelectric models to further study semiconductors.

The present thesis, with a good amalgamation of fundamental studies, emphasizes the role of grain morphology on plastic deformation behavior of polycrystalline materials. In addition, electrostatic study carried out in the last part of the thesis is a good starting point for addressing critical issues in flexible electronic components in a more fundamental way.

A Appendix: Review of Depres's pileup model

THE analytical expression to predict stress strain response of a single grain for equiaxed shapes of dislocation pileups as presented by Depres [43,44] is reviewed in this Appendix.

A.1 Introduction

If $\tau^{(s)}$ is assumed to be the stress required to move a single dislocation at any point during the deformation. Depres divided the stress ($\tau^{(s)}$) as the sum of initial stress ($\tau_i^{(s)}$), which is the stress required to move the dislocation unaffected by other dislocations and dislocation hardening stress ($\tau_d^{(s)}$), which is the stress required to overcome the stress field due to all other dislocations in the grain. The initial stress ($\tau_i^{(s)}$) of a single dislocation is further divided into contributions of the lattice friction (τ_{fr}) and stress required to move a dislocation of certain length ($\frac{\mu b}{l_{source}}$). The mathematical representation of the stress contributions is shown below.

$$\tau^{(s)} = \tau_i^{(s)} + \tau_d^{(s)} \quad \text{avec : } \begin{cases} \tau_i^{(s)} = \left[\tau_{fr} + \frac{\mu b}{l_{source}} \right] \text{sign}(\gamma_p^{(s)}) \\ \tau_d^{(s)} = \left[\frac{1}{k_1} \frac{\mu}{(1-\nu)} \right] \gamma_p^{(s)} \end{cases}$$

The form factor (k_1), which theoretically gives the slope of the hardening curve.

A.1.1 Idealised double-ended pileup

A standard integral expression to find total number of dislocations of either sign in a pileup was derived by considering individual dislocations in the pileup to be in equilibrium. This equilibrium state leads to a condition where the forces produced by external stress, τ_{app} and the one caused by interaction with the other

Appendix A. Appendix: Review of Depres's pileup model

dislocations to be balanced [Kubin 1982].

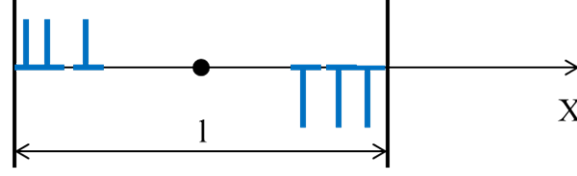


Figure A.1 – Double ended pileup of edge dislocations

Solving the balance equation would lead to the below equation for dislocation density of a double ended pileup, $n(x)$.

$$n(x) = \frac{2(1 - \nu)\tau_{app}}{\mu b} \frac{x}{\sqrt{(\frac{l}{2})^2 - x^2}} \quad (\text{A.1})$$

where,

μ = Shear modulus

ν = Poisson's ratio

b = Burgers vector

l = Grain size (length)

x = position of the dislocation segment (in the pileup) from the center of the grain.

Integration of the dislocation density $n(x)$, over the grain size l , leads to the equation for estimating the total number of dislocations (in a double ended pileup).

$$N = 2 \int_0^{\frac{l}{2}} n(x) dx = \frac{2(1 - \nu)l\tau_{app}}{\mu b} \quad (\text{A.2})$$

A.1.2 Extension to 2D pileup

The total number of dislocations in the pileup is found by integrating $n(x)dx$, which gives the number of dislocations in the interval $[x, x + dx]$, over the length of the slip plane. Here, the length of slip plane is assumed to l in a homogenization surface S .

The total number of dislocations in the pileup turns out to be same as in the

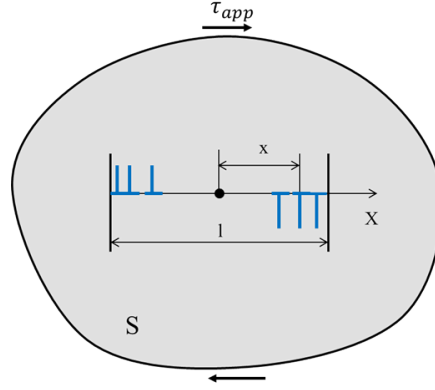


Figure A.2 – Double ended pileup of edge dislocations in homogenization surface S

case of a 1D pileup.

$$\begin{aligned}
n_{2d}^{pu} &= 2 \int_0^{\frac{l}{2}} n(x) dx \\
&= 2 \int_0^{\frac{l}{2}} \frac{2(1-\nu)\tau_{app}}{\mu b} \frac{x}{\sqrt{(\frac{l}{2})^2 - x^2}} dx \\
&= \frac{4(1-\nu)\tau_{app}}{\mu b} \int_0^{\frac{l}{2}} \frac{x}{\sqrt{(\frac{l}{2})^2 - x^2}} dx \\
&= \frac{2(1-\nu)l\tau_{app}}{\mu b}
\end{aligned}$$

The total density of dislocations (ρ_{2d}^{pu}) is given as the ratio of total length of dislocations divided by the homogenization volume (V). If the out-of-plane dimension ($L = 1$) is a constant, then $V = L \cdot S$, where, S is the homogenization surface of the grain. in the pileup to the homogenization surface. The area swept by the dislocations is $A = L \cdot x \cdot n(x) dx$.

The total density of dislocations (ρ_{2d}^{pu}) in a homogenization surface S is:

$$\begin{aligned}
\rho_{2d}^{pu} &= \frac{1}{S} n_{2d}^{pu} \\
&= \frac{1}{S} \frac{2(1-\nu)l\tau_{app}}{\mu b} \\
&= 2 \frac{(1-\nu)}{\mu b S} l \tau_{app}
\end{aligned}$$

Appendix A. Appendix: Review of Depres's pileup model

The average plastic deformation (Υ_{2d}^{pu}) of the volume V due to the dislocation slip is:

$$\begin{aligned}
 \Upsilon^{pu} &= \frac{bA}{V} \\
 \Upsilon_{2d}^{pu} &= b \frac{2 \int_0^{\frac{l}{2}} Lx n(x) dx}{S.L} \\
 &= \frac{4b(1-\nu)\tau_{app}}{S \mu b} \int_0^{\frac{l}{2}} \frac{x^2}{\sqrt{(\frac{l}{2})^2 - x^2}} dx \\
 &= \frac{4(1-\nu)\tau_{app}}{\mu S} \frac{\pi l^2}{16} \\
 &= \frac{\pi(1-\nu)}{4} \frac{l^2 \tau_{app}}{\mu S}
 \end{aligned}$$

A.1.3 Extension to 3D pileup

Let $n(x)$ gives the density of dislocations in the interval $[x, x + dx]$ on a slip plane in a grain of homogenization volume V . The total density of dislocations (ρ_{3d}^{pu}) and plastic deformation (Υ_{3d}^{pu}) of the grain are calculated by including the expression for actual length of the dislocation loop, $\zeta(x)$ and actual area covered by the dislocation loop, $A(x)$ situated at a distance x from the source respectively.

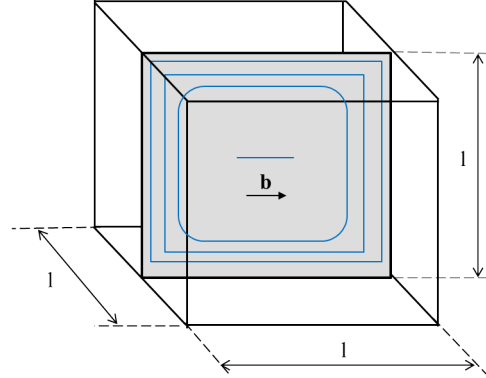


Figure A.3 – Pileup of dislocations on a slip plane passing through the center of the cube

Resistance to dislocation glide is influenced by the shape of the dislocation loop. The shape of the dislocation loop, which effectively changes the area swept, will depend on the orientation of the slip plane w.r.t columnar axis and distance of the slip plane from the center of the grain. In this section, we start our analysis by

assuming only a single dislocation being active on a slip plane passing through the center of the grain. The slip plane normal is perpendicular to the vertical axis of the grain (*cf.* Figure A.3).

A.1.3.1 Form 1 (line)

When the pileup on a slip plane takes the shape of a line (hypothetically), the grain would take the shape similar to the slip plane. This shape of the dislocation loop would lead to similar expressions as in the case of a 2D pileup [Section A.1.2]. The figure below shows the length of a loop at a distance x from source is $\zeta(x) = l$.

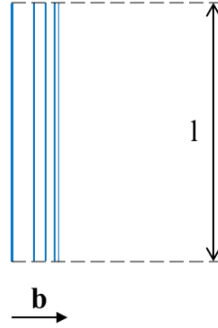


Figure A.4 – Pileup of dislocations on slip plane (form-line)

The total density of dislocations in a homogenization volume V is given by

$$\begin{aligned}
 \rho_{3d}^{pu} &= \frac{2}{V} \int_0^{\frac{l}{2}} \zeta(x)n(x)dx \\
 &= \frac{2}{V} \int_0^{\frac{l}{2}} l \frac{2(1-\nu)\tau_{app}}{\mu b} \frac{x}{\sqrt{(\frac{l}{2})^2 - x^2}} dx \\
 &= \frac{4(1-\nu)l\tau_{app}}{\mu V b} \int_0^{\frac{l}{2}} \frac{x}{\sqrt{(\frac{l}{2})^2 - x^2}} dx \\
 &= \frac{4}{V} \frac{(1-\nu)l\tau_{app}}{\mu b} \frac{l}{2} \\
 &= 2 \frac{(1-\nu)}{\mu V b} l^2 \tau_{app}
 \end{aligned}$$

If $A(x) = lx$ is the area swept by the dislocation loop located at a distance x from the source, and if only a single slip plane is active; then the total area swept

Appendix A. Appendix: Review of Depres's pileup model

by all dislocations in the grain is

$$A = 2 \int_0^{\frac{l}{2}} A(x)n(x)dx$$

The plastic deformation of the grain, Υ_{3d}^{pu} then becomes:

$$\begin{aligned} \Upsilon_{3d}^{pu} &= \frac{bA}{V} \\ &= \frac{2b \int_0^{\frac{l}{2}} A(x)n(x)dx}{V} \\ &= \frac{2b}{V} \int_0^{\frac{l}{2}} lx \frac{2(1-\nu)\tau_{app}}{\mu b} \frac{x}{\sqrt{(\frac{l}{2})^2 - x^2}} dx \\ &= \frac{2b}{V} \frac{2(1-\nu)l\tau_{app}}{\mu b} \int_0^{\frac{l}{2}} \frac{x^2}{\sqrt{(\frac{l}{2})^2 - x^2}} dx \\ &= \frac{4}{V} \frac{(1-\nu)l\tau_{app}}{\mu} \frac{\pi l^2}{16} \\ &= \frac{\pi}{4} \frac{(1-\nu)}{\mu V} l^3 \tau_{app} \end{aligned}$$

A.1.3.2 Form 2 (square)

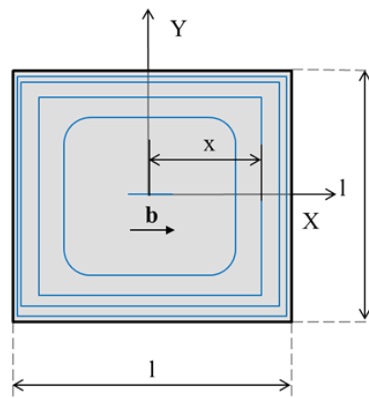


Figure A.5 – Pileup of dislocations on a slip plane (form-square)

If the dislocation loops which pileup on a slip plane takes the shape of a square, the total length of the loop, at the shortest distance x from the position of the

source (center of the plane), is $\zeta(x) = 8x$.

The total density of dislocations in a homogenization volume V is given by

$$\begin{aligned}
 \rho_{3d}^{pu} &= \frac{1}{V} \int_0^{\frac{l}{2}} \zeta(x)n(x)dx \\
 &= \frac{1}{V} \int_0^{\frac{l}{2}} 8x \frac{2(1-\nu)\tau_{app}}{\mu b} \frac{x}{\sqrt{(\frac{l}{2})^2 - x^2}} dx \\
 &= \frac{16(1-\nu)\tau_{app}}{V \mu b} \int_0^{\frac{l}{2}} \frac{x^2}{\sqrt{(\frac{l}{2})^2 - x^2}} dx \\
 &= \frac{16(1-\nu)\tau_{app}}{V \mu b} \frac{\pi l^2}{16} \\
 &= \pi \frac{(1-\nu)}{\mu V b} l^2 \tau_{app}
 \end{aligned}$$

If $A(x) = 4x^2$ is the area swept by the dislocation loop that piles up at a distance x from the source, then the total area swept by all dislocations is A .

$$A = \int_0^{\frac{l}{2}} A(x)n(x)dx$$

The plastic deformation, Υ_{3d}^{pu} then becomes:

$$\begin{aligned}
 \Upsilon_{3d}^{pu} &= \frac{bA}{V} \\
 &= \frac{b \int_0^{\frac{l}{2}} A(x)n(x)dx}{V} \\
 &= \frac{b}{V} \int_0^{\frac{l}{2}} 4x^2 \frac{2(1-\nu)\tau_{app}}{\mu b} \frac{x}{\sqrt{(\frac{l}{2})^2 - x^2}} dx \\
 &= \frac{8b(1-\nu)\tau_{app}}{V \mu b} \int_0^{\frac{l}{2}} \frac{x^3}{\sqrt{(\frac{l}{2})^2 - x^2}} dx \\
 &= \frac{8(1-\nu)\tau_{app}}{V \mu} \frac{l^3}{12} \\
 &= \frac{2(1-\nu)}{3 \mu V} l^3 \tau_{app}
 \end{aligned}$$

Appendix A. Appendix: Review of Depres's pileup model

A.1.3.3 Form 3 (circle)

Similarly, when the dislocation pileup on a slip plane takes the shape of a circle, the length of a loop piled up at a distance x from source is $\zeta(x) = 2\pi x$.

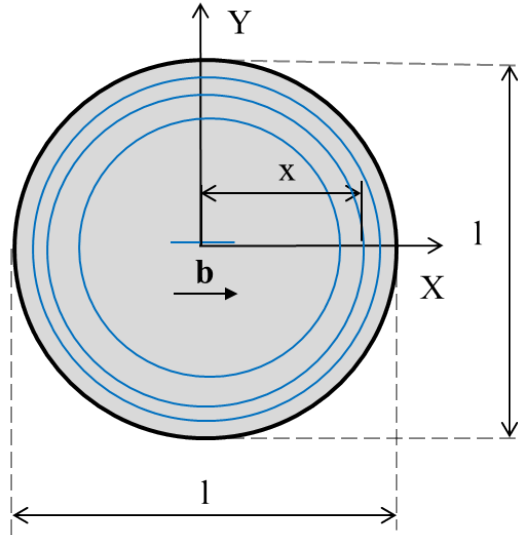


Figure A.6 – Pileup of dislocations on a slip plane (form-circle)

The total density of dislocations in a homogenization volume V is given by

$$\begin{aligned}
 \rho_{3d}^{pu} &= \frac{1}{V} \int_0^{\frac{l}{2}} \zeta(x) n(x) dx \\
 &= \frac{1}{V} \int_0^{\frac{l}{2}} 2\pi x \frac{2(1-\nu)\tau_{app}}{\mu b} \frac{x}{\sqrt{(\frac{l}{2})^2 - x^2}} dx \\
 &= \frac{4\pi(1-\nu)\tau_{app}}{V\mu b} \int_0^{\frac{l}{2}} \frac{x^2}{\sqrt{(\frac{l}{2})^2 - x^2}} dx \\
 &= \frac{4\pi(1-\nu)\tau_{app}}{V\mu b} \frac{\pi l^2}{16} \\
 &= \frac{\pi^2(1-\nu)}{4} \frac{l^2 \tau_{app}}{\mu V b}
 \end{aligned}$$

Since $A(x) = \pi x^2$ is the area swept by the dislocation loop located at a distance

x from the source, the total area swept by all dislocations is A .

$$A = \int_0^{\frac{l}{2}} A(x)n(x)dx$$

The plastic deformation, Υ_{3d}^{pu} then becomes

$$\begin{aligned} \Upsilon_{3d}^{pu} &= \frac{bA}{V} \\ &= \frac{b \int_0^{\frac{l}{2}} A(x)n(x)dx}{V} \\ &= \frac{b}{V} \int_0^{\frac{l}{2}} \pi x^2 \frac{2(1-\nu)\tau_{app}}{\mu b} \frac{x}{\sqrt{(\frac{l}{2})^2 - x^2}} dx \\ &= \frac{\pi b}{V} \frac{2(1-\nu)\tau_{app}}{\mu b} \int_0^{\frac{l}{2}} \frac{x^3}{\sqrt{(\frac{l}{2})^2 - x^2}} dx \\ &= \frac{2\pi}{V} \frac{(1-\nu)\tau_{app}}{\mu} \frac{l^3}{12} \\ &= \frac{\pi}{6} \frac{(1-\nu)}{\mu V} l^3 \tau_{app} \end{aligned}$$

The expressions for total density, plastic deformation of a pileup can be expressed in a generalized form by introducing two variables k_1 and k_2 ,

$$\begin{aligned} \Upsilon_{pu} &= k_1 \frac{(1-\nu)}{\mu V} l^3 \tau_{app} \\ \rho_{pu} &= k_2 \frac{(1-\nu)}{\mu b V} l^2 \tau_{app} \\ \rho_{pu} &= \frac{k_2}{k_1} \frac{1}{bl} \Upsilon_{app} \end{aligned}$$

The variables k_1 and k_2 change according to the shape of the pileup. This highlights the possibility of an unique kinematic hardening which depends on the shape of the dislocation pileup on a slip plane. The table below confirms the same on different shapes of dislocation loops [43].

Form	$\zeta(x)$	$A(x)$	k_1	k_2
<i>line</i>	l	lx	$\frac{\pi}{4}$	2
<i>square</i>	$8x$	$4x^2$	$\frac{2}{3}$	π
<i>circle</i>	$2\pi x$	πx^2	$\frac{\pi}{6}$	$\frac{\pi^2}{4}$

A.2 Hardening due to 'n' similar parallel slip planes in a grain

In reality, dislocation pileup on a single slip plane could never exist. Even if this case is possible, the force on the leading dislocation due to the pileup will easily be high enough for the dislocation segment to cross-slip or cross the grain boundary. Assuming that the dislocation cross-slipped multiple times onto n parallel parallel slip planes which are separated by a distance λ , Depres observed the kinematic hardening to be still linear in an equiaxed cubic grain of $l = D_g$ dimension.

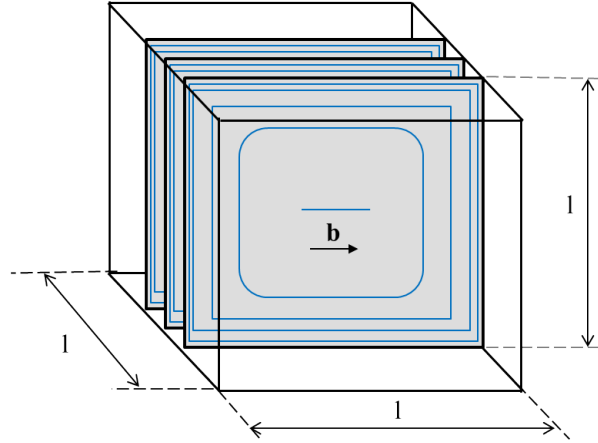


Figure A.7 – Cubic grain with n parallel slip planes

Plastic deformation expression depending on the number of parallel slip planes separated by a distance λ is

$$\tau_d^{(s)} = \frac{1}{k_1} \frac{\mu}{(1 - \nu)} \left[\frac{1 + \exp(-k \frac{\lambda}{D_g})}{2 + (n - 2)(1 - \exp(-k \frac{\lambda}{D_g}))} \right] \Upsilon_p^{(s)}$$

By neglecting the exponential part when the spacing between the parallel slip planes is large, Depres arrive to the below mentioned approximated equation which

inversely depends on the number of parallel slip planes.

$$\tau_d^{(s)} \simeq \frac{1}{n} \frac{1}{k_1} \frac{\mu}{(1-\nu)} \Upsilon_p^{(s)}$$

Plots shown in Figure A.9(b) confirm the decrease in the slope with increasing number of similar parallel planes. The term 'similar' refers to the slip planes having same dimensions all over the grain (irrespective of the slip plane position from the center of the grain and the angle made by the slip plane with respect to the columnar axis).

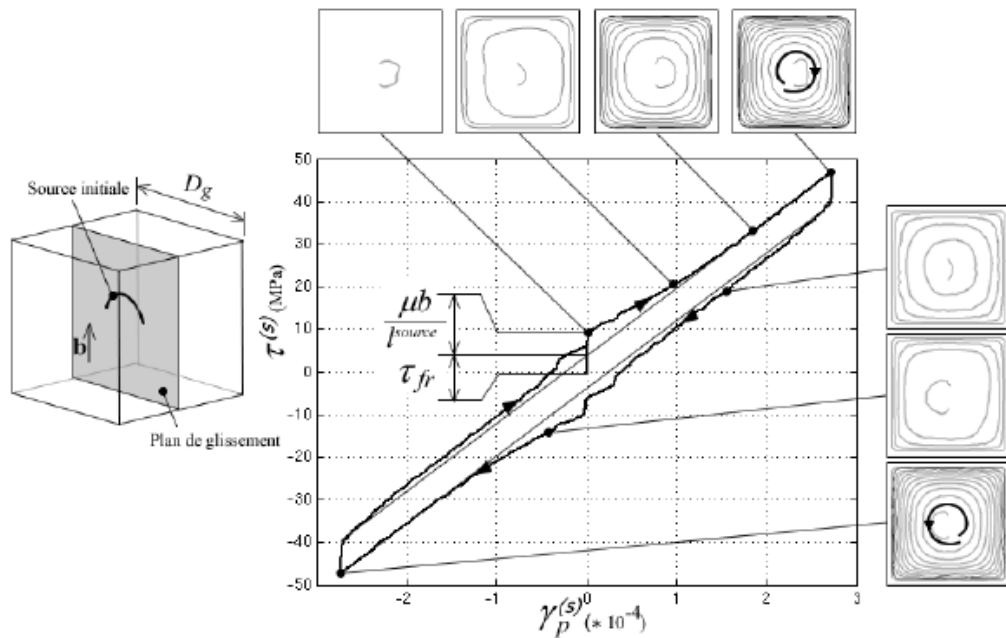


Figure A.8 – Pileup of dislocations on single slip plane [43]

A.3 Conclusions

Following conclusions were drawn from the work carried out by Depres using the 3D extension of the pileup model.

- In the case of a single dislocation pileup, theoretical slopes were exactly found to match the slopes of the work hardening curves from 3D DDD simulations.
- The hardening rate was found to be purely kinematic and linear.

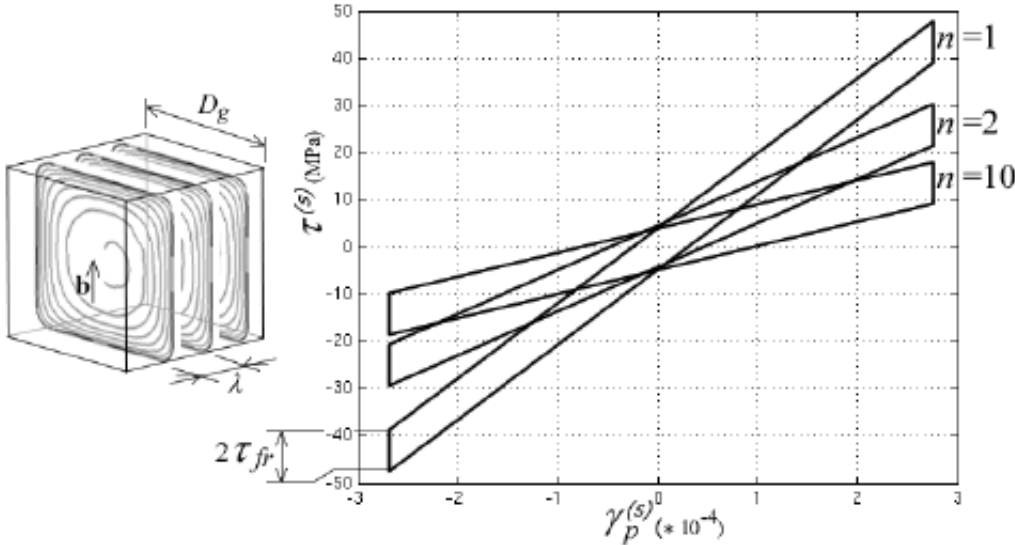


Figure A.9 – Pileup of dislocations on multiple parallel slip planes [43]

- The hardening rate only changed with the shape of the dislocation pileup.
- In the case of pileup on n similar slip plane in an equiaxed grain, the hardening rate was found still to be linear; and inversely proportional to the number of n active similar slip planes.

B Appendix: Non-equiaxed shape of dislocation pileups

THE pileup formula [43], which has been reviewed in Appendix A, considers only the cases where the shape of dislocation loops are equiaxed. The predictions of kinematic hardening values from the formula becomes invalid when a dislocation is present on a slip plane which is not perpendicular to the long axis of the grain (which is generally the case). This section deals with the extension of the work to account not only for the non-equiaxed shape of the dislocation loops in a pileups but also the angle the slip plane normal makes with the columnar axis (long axis in elongated grains). This model which is an extension of the pileup model is hereby referred to as "*extended pileup model*".

B.1 Introduction

In non-equiaxed grains (*cf.* Figure B.5), the shape of the dislocation loop changes from a circle (when slip plane normal is aligned parallel to the long axis of the grain) to an ellipse (when slip plane normal is perpendicular to the long axis of the grain) with same aspect ratio as of the non-equiaxed grain. We derive a formula which can predict the hardening rate on any slip plane in a non-equiaxed grain by taking into account only the aspect ratio of the grain (β) and angle (θ) a slip plane makes with respect to the long axis of the grain. Unless mentioned, local yielding criteria such as cross-slip are not considered in the formulations.

B.1.1 Form 4a (ellipse - longest)

Consider the pileup on a slip plane with shortest diameter l , takes the shape of an ellipse. If the dislocation loop is assumed to have its effect felt even when it is at a longest distance x from the source, $\zeta(x)$ is expressed in a generalized form to account for slip plane geometry which depends on the angle the slip plane normal makes with the long axis of the grain.

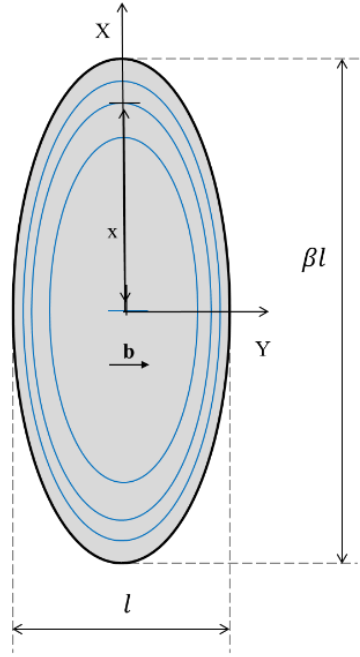


Figure B.1 – Pileup of dislocations on a slip plane (form-ellipse longest)

$$\begin{aligned}\zeta(x) &= \pi(a+b)\left(1 + \frac{h}{4} + \frac{h^2}{64} + \frac{h^3}{256} + \frac{25h^4}{16384} + \frac{49h^5}{65536} + \dots\right) \\ &= \pi(a+b)f(h)\end{aligned}$$

where,

$$f(h) = 1 + \frac{h}{4} + \frac{h^2}{64} + \frac{h^3}{256} + \frac{25h^4}{16384} + \frac{49h^5}{65536} + \dots$$

$$h = \frac{(a-b)^2}{(a+b)^2} \text{ with,}$$

$a = x$ and $b = \beta_s x$ are the generalized half minor and major axes respectively.

β = aspect ratio of the grain

$\beta_s = \frac{\beta}{\sqrt{(\sin\theta)^2 + (\beta\cos\theta)^2}}$, is the aspect ratio of the slip plane.

θ = angle made by the slip plane normal with respect to the long axis of the grain.

The total density of dislocations in a homogenization volume V is given by

$$\begin{aligned}\rho_{3d}^{pu} &= \frac{1}{V} \int_0^{\beta_s \frac{l}{2}} \zeta(x)n(x)dx \\ &= \frac{1}{V} \int_0^{\beta_s \frac{l}{2}} \pi(a+b)f(h) \frac{2(1-\nu)\tau_{app}}{\mu b} \frac{x}{\sqrt{(\frac{l}{2})^2 - x^2}} dx\end{aligned}$$

$$\begin{aligned}
 \rho_{3d}^{pu} &= \frac{\pi}{V} f(h)(1 + \beta_s) \frac{2(1 - \nu)\tau_{app}}{\mu b} \int_0^{\beta_s \frac{l}{2}} \frac{x^2}{\sqrt{(\frac{l}{2})^2 - x^2}} dx \\
 &= \frac{\pi}{V} f(h)(1 + \beta_s) \frac{2(1 - \nu)\tau_{app}}{\mu b} \frac{1}{8} \left[l^2 \tan^{-1} \left(\frac{1}{\sqrt{(\frac{1}{\beta_s})^2 - 1}} \right) - \frac{\beta l^2}{\beta_s} \sqrt{1 - (\beta_s)^2} \right] \\
 &= \frac{\pi}{4V} f(h)(1 + \beta_s) \left[\tan^{-1} \left(\frac{1}{\sqrt{(\frac{1}{\beta_s})^2 - 1}} \right) - \beta_s \sqrt{1 - (\beta_s)^2} \right] \frac{(1 - \nu) l^2 \tau_{app}}{\mu b}
 \end{aligned}$$

If $A(x) = \pi ab$ is the area swept by the dislocation loop located at a distance x from the source, then the total area swept by all the dislocation loops on the slip plane is A .

$$A = \int_0^{\beta_s \frac{l}{2}} A(x) n(x) dx$$

The plastic deformation, Υ_{3d}^{pu} then becomes

$$\Upsilon_{3d}^{pu} = \frac{bA}{V}$$

$$\begin{aligned}
 \Upsilon_{3d}^{pu} &= \frac{b}{V} \int_0^{\beta_s \frac{l}{2}} A(x) n(x) dx \\
 &= \frac{b}{V} \int_0^{\beta_s \frac{l}{2}} \pi ab \frac{2(1 - \nu)\tau_{app}}{\mu b} \frac{x}{\sqrt{(\frac{l}{2})^2 - x^2}} dx \\
 &= \frac{b}{V} \int_0^{\beta_s \frac{l}{2}} \pi x \beta_s x \frac{2(1 - \nu)\tau_{app}}{\mu b} \frac{x}{\sqrt{(\frac{l}{2})^2 - x^2}} dx \\
 &= \frac{2\pi b}{V} \beta_s \frac{(1 - \nu)}{\mu b} \tau_{app} \int_0^{\beta_s \frac{l}{2}} \frac{x^3}{\sqrt{(\frac{l}{2})^2 - x^2}} dx \\
 &= \frac{2\pi}{V} \beta_s \frac{(1 - \nu)}{\mu} \tau_{app} \left[1 - \sqrt{1 - \beta_s^2} \left(1 + \frac{1}{2} \beta_s^2 \right) \right] \frac{l^3}{12}
 \end{aligned}$$

$$\Upsilon_{3d}^{pu} = \frac{\pi}{6} \beta_s \left[1 - \sqrt{1 - \beta_s^2} \left(1 + \frac{1}{2} \beta_s^2 \right) \right] \frac{(1 - \nu) l^3 \tau_{app}}{\mu V} \quad (\text{B.1})$$

B.1.2 Form 4b (ellipse - shortest)

Consider the pileup on a slip plane with shortest diameter l , takes the shape of an ellipse. If the dislocation loop is assumed to have its effect felt only when it is at a shortest distance x from the source, $\zeta(x)$ is expressed in a generalized form to account for slip plane geometry which depends on the angle it's normal makes with the long axis of the grain.

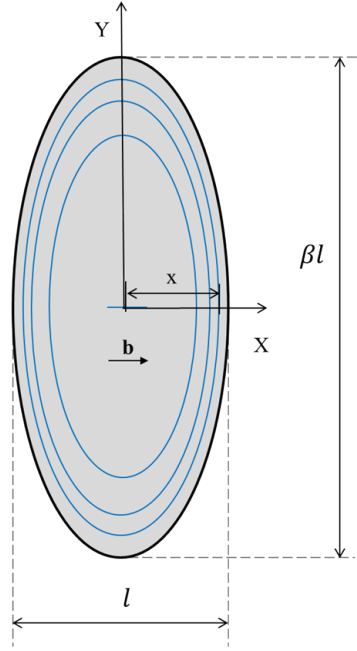


Figure B.2 – Pileup of dislocations on a slip plane (form-ellipse shortest)

$$\begin{aligned}\zeta(x) &= \pi(a+b)\left(1 + \frac{h}{4} + \frac{h^2}{64} + \frac{h^3}{256} + \frac{25h^4}{16384} + \frac{49h^5}{65536} + \dots\right) \\ &= \pi(a+b)f(h)\end{aligned}$$

where,

$$f(h) = 1 + \frac{h}{4} + \frac{h^2}{64} + \frac{h^3}{256} + \frac{25h^4}{16384} + \frac{49h^5}{65536} + \dots$$

$$h = \frac{(a-b)^2}{(a+b)^2} \text{ with,}$$

$a = x$ and $b = \beta_s x$ are the generalized half minor and major axes respectively.

β = aspect ratio of the grain

$$\beta_s = \frac{\beta}{\sqrt{(\sin\theta)^2 + (\beta\cos\theta)^2}}, \text{ is the aspect ratio of the slip plane.}$$

θ = angle made by the slip plane normal with respect to the long axis of the grain.

The total density of dislocations in a homogenization volume V is given by

$$\begin{aligned}
 \rho_{3d}^{pu} &= \frac{1}{V} \int_0^{\frac{l}{2}} \zeta(x)n(x)dx \\
 &= \frac{1}{V} \int_0^{\frac{l}{2}} \pi(a+b)f(h) \frac{2(1-\nu)\tau_{app}}{\mu b} \frac{x}{\sqrt{(\frac{l}{2})^2 - x^2}} dx \\
 &= \frac{\pi}{V} f(h)(1+\beta_s) \frac{2(1-\nu)\tau_{app}}{\mu b} \int_0^{\frac{l}{2}} \frac{x^2}{\sqrt{(\frac{l}{2})^2 - x^2}} dx \\
 &= \frac{\pi}{V} f(h)(1+\beta_s) \frac{2(1-\nu)\tau_{app}}{\mu b} \left[\frac{\pi l^2}{16} \right] \\
 &= \frac{\pi^2}{8V} f(h)(1+\beta_s) \frac{(1-\nu)}{\mu b} l^2 \tau_{app}
 \end{aligned}$$

If $A(x) = \pi ab$ is the area swept by the dislocation loop located at a distance x from the source, then the total area swept by all the dislocation loops on the slip plane is A .

$$A = \int_0^{\beta_s \frac{l}{2}} A(x)n(x)dx$$

The plastic deformation, Υ_{3d}^{pu} then becomes

$$\begin{aligned}
 \Upsilon_{3d}^{pu} &= \frac{bA}{V} \\
 &= \frac{b}{V} \int_0^{\frac{l}{2}} A(x)n(x)dx \\
 &= \frac{b}{V} \int_0^{\frac{l}{2}} \pi ab \frac{2(1-\nu)\tau_{app}}{\mu b} \frac{x}{\sqrt{(\frac{l}{2})^2 - x^2}} dx \\
 &= \frac{b}{V} \int_0^{\frac{l}{2}} \pi x \beta_s x \frac{2(1-\nu)\tau_{app}}{\mu b} \frac{x}{\sqrt{(\frac{l}{2})^2 - x^2}} dx \\
 &= \frac{2\pi b}{V} \frac{\beta_s}{\beta_s} \frac{(1-\nu)}{\mu b} \tau_{app} \int_0^{\frac{l}{2}} \frac{x^3}{\sqrt{(\frac{l}{2})^2 - x^2}} dx \\
 &= \frac{2\pi}{V} \beta_s \frac{(1-\nu)}{\mu} \tau_{app} \left[\frac{l^3}{12} \right]
 \end{aligned}$$

$$\Upsilon_{3d}^{pu} = \frac{\pi}{6} \beta_s \frac{(1-\nu)}{\mu V} l^3 \tau_{app} \quad (\text{B.2})$$

B.2 Extended pileup theory Vs DD simulations

The form factor table [Appendix A] for different dislocation pileup loop shapes is now extended to a non-equiaxed shape like ellipse.

Form	$\zeta(x)$	$A(x)$	k_1	k_2
<i>line</i>	l	lx	$\frac{\pi}{4}$	2
<i>square</i>	$8x$	$4x^2$	$\frac{2}{3}$	π
<i>circle</i>	$2\pi x$	πx^2	$\frac{\pi}{6}$	$\frac{\pi^2}{4}$
<i>ellipse(l)</i>	$\pi x(1 + \beta_s)f(h)$	$\pi x^2 \beta_s$	$\frac{\pi}{6} \beta_s f_1(\beta)$	$\frac{\pi}{4} f(h)(1 + \beta_s)f_2(\beta)$
<i>ellipse(s)</i>	$\pi x(1 + \beta_s)f(h)$	$\pi x^2 \beta_s$	$\frac{\pi}{6} \beta_s$	$\frac{\pi^2}{8} f(h)(1 + \beta_s)$

here,

$h = \frac{(a-b)^2}{(a+b)^2}$ where $a = x$ and $b = \beta_s x$ being the half the length of minor and major axes respectively.

$$f(h) = 1 + \frac{h}{4} + \frac{h^2}{64} + \frac{h^3}{256} + \frac{25h^4}{16384} + \frac{49h^5}{65536} + \dots$$

$$f_1(\beta) = \left[1 - \sqrt{1 - \beta_s^2} \left(1 + \frac{1}{2} \beta_s^2 \right) \right]$$

$$f_2(\beta) = \left[\tan^{-1} \left(\frac{1}{\sqrt{(\frac{\beta_s}{\beta})^2 - 1}} \right) - \beta_s \sqrt{1 - (\beta_s)^2} \right]$$

$$\beta_s = \frac{\beta}{\sqrt{(\sin\theta)^2 + (\beta \cos\theta)^2}} \quad (\beta = \text{aspect ratio of the ellipse})$$

$\theta =$ angle made by the slip plane normal with respect to the long axis of the grain.

B.2.1 Single dislocation pileup (non-centred)

The configuration of dislocation pileup loop is changed when a slip plane which is non-centred is active. Such changes are introduced by introducing a variable l' , which defines the effective shortest radius of a slip plane which is at a distance z from the center of the grain.

$$\frac{l'}{2} = \frac{\beta}{\beta_s} \sqrt{\left(\frac{\beta}{\beta_s} \frac{l}{2} \right)^2 - z^2} \quad (\text{B.3})$$

B.2. Extended pileup theory Vs DD simulations

If $A(x) = \pi ab$ is the area swept by the dislocation loop located at a distance x from the source, then the total area swept by all the dislocation loops on the slip plane is A .

$$A = \int_0^{\beta_s \frac{l}{2}} A(x) n(x) dx$$

The plastic deformation, Υ_{3d}^{pu} is only calculated in this case.

$$\begin{aligned} \Upsilon_{3d}^{pu} &= \frac{bA}{V} \\ &= \frac{b}{V} \int_0^{\frac{l'}{2}} A(x) n(x) dx \\ &= \frac{b}{V} \int_0^{\frac{l'}{2}} \pi ab \frac{2(1-\nu)\tau_{app}}{\mu b} \frac{x}{\sqrt{(\frac{l'}{2})^2 - x^2}} dx \\ &= \frac{b}{V} \int_0^{\frac{l'}{2}} \pi x \beta_s \frac{2(1-\nu)\tau_{app}}{\mu b} \frac{x}{\sqrt{(\frac{l'}{2})^2 - x^2}} dx \\ &= \frac{b}{V} \pi \beta_s \frac{2(1-\nu)\tau_{app}}{\mu b} \int_0^{\frac{l'}{2}} \frac{x^3}{\sqrt{(\frac{l'}{2})^2 - x^2}} dx \\ \\ \Upsilon_{3d}^{pu} &= \frac{\pi \beta_s}{V} \frac{2(1-\nu)\tau_{app}}{\mu} \int_0^{\frac{\beta}{\beta_s} \sqrt{(\frac{\beta}{\beta_s} \frac{l}{2})^2 - z^2}} \frac{x^3}{\sqrt{(\frac{\beta}{\beta_s} \sqrt{(\frac{\beta}{\beta_s} \frac{l}{2})^2 - z^2})^2 - x^2}} dx \\ &= \frac{\pi \beta_s}{V} \frac{2(1-\nu)\tau_{app}}{\mu} \int_0^{\frac{\beta}{\beta_s} \sqrt{(\frac{\beta}{\beta_s} \frac{l}{2})^2 - z^2}} \frac{x^3}{\sqrt{(\frac{\beta}{\beta_s})^2 \left[(\frac{\beta}{\beta_s} \frac{l}{2})^2 - z^2 \right] - x^2}} dx \\ &= \frac{\pi \beta_s}{V} \frac{2(1-\nu)\tau_{app}}{\mu} \int_0^{\frac{\beta}{\beta_s} \sqrt{(\frac{\beta}{\beta_s} \frac{l}{2})^2 - z^2}} \frac{x^3}{\sqrt{(\frac{l}{2})^2 - (\frac{\beta_s z}{\beta})^2 - x^2}} dx \\ \\ \Upsilon_{3d}^{pu} &= \frac{4\pi \beta_s (1-\nu)}{3} \frac{1}{\mu V} \left[\left(\frac{l}{2} \right)^2 - \left(\frac{\beta_s z}{\beta} \right)^2 \right]^{\frac{3}{2}} \tau_{app} \end{aligned} \tag{B.4}$$

Appendix B. Appendix: Non-equiaxed shape of dislocation pileups

Substituting $z=0$ in Equation B.4, we arrive to the plastic deformation equation as in Equation B.2 which has already been validated against DD simulations in Section 5.4.2.1 of Chapter 5.

B.3 Hardening due to 'n' non-similar parallel slip planes in a grain

B.3.1 Equiaxed (spherical) grain

In a spherical grain, the perimeter and area of the dislocation loop on a slip plane changes with respect to the distance from the center of the grain. In the below figure, the slip plane normals is at an angle of 0° with the vertical (Z) axis of the spherical grain. To accurately calculate the average hardening rate (slope) on a slip system (n non-similar parallel slip planes) in a spherical grain, we should also account for.

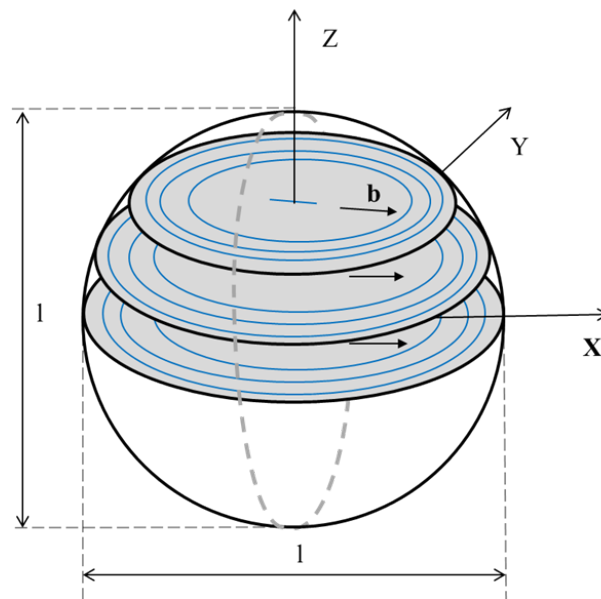


Figure B.3 – Pileup of dislocations on multiple parallel slip plane in a spherical grain

The total density of dislocation due to a single plane passing through the center

B.3. Hardening due to 'n' non-similar parallel slip planes in a grain

of the sphere in a homogenization volume V is

$$\begin{aligned}\rho_{3d}^{pu} &= \frac{1}{V} \int_0^{\frac{l}{2}} \zeta(x)n(x)dx \\ &= \frac{1}{V} \int_0^{\frac{l}{2}} 2\pi x \frac{2(1-\nu)\tau_{app}}{\mu b} \frac{x}{\sqrt{(\frac{l}{2})^2 - x^2}} dx\end{aligned}$$

The total density of dislocations due to n non-similar parallel slip planes in a homogenization volume V is found by changing the limits in the X-direction and then integrating the result over the length of the spherical grain in Z-direction.

$$\begin{aligned}\rho_{3d}^{pu} &= \frac{2}{Vl} \int_{z=0}^{\frac{l}{2}} \int_{x=0}^{\sqrt{(\frac{l}{2})^2 - z^2}} \zeta(x)n(x)dx dz \\ &= \frac{2}{Vl} \int_{z=0}^{\frac{l}{2}} \int_{x=0}^{\sqrt{(\frac{l}{2})^2 - z^2}} 2\pi x \frac{2(1-\nu)\tau_{app}}{\mu b} \frac{x}{\sqrt{(\frac{l}{2})^2 - x^2}} dx dz \\ &= \frac{4\pi}{Vl} \frac{2(1-\nu)\tau_{app}}{\mu b} \int_{z=0}^{\frac{l}{2}} \int_{x=0}^{\sqrt{(\frac{l}{2})^2 - z^2}} \frac{x^2}{\sqrt{(\frac{l}{2})^2 - x^2}} dx dz\end{aligned}$$

Appendix B. Appendix: Non-equiaxed shape of dislocation pileups

$$\begin{aligned}
\rho_{3d}^{pu} &= \frac{8\pi(1-\nu)\tau_{app}}{Vl\mu b} \int_{z=0}^{\frac{l}{2}} \frac{1}{8} \left[l^2 \tan^{-1}\left(\frac{x}{\sqrt{(\frac{l}{2})^2 - x^2}}\right) - 4x\sqrt{(\frac{l}{2})^2 - x^2} \right]_{x=0}^{\sqrt{(\frac{l}{2})^2 - z^2}} dz \\
&= \frac{\pi(1-\nu)\tau_{app}}{Vl\mu b} \int_{z=0}^{\frac{l}{2}} \left[l^2 \tan^{-1}\left(\frac{\sqrt{(\frac{l}{2})^2 - z^2}}{z}\right) - 4z\sqrt{(\frac{l}{2})^2 - z^2} \right] dz \\
&= \frac{\pi(1-\nu)\tau_{app}}{Vl\mu b} \left[\int_{z=0}^{\frac{l}{2}} l^2 \tan^{-1}\left(\frac{\sqrt{(\frac{l}{2})^2 - z^2}}{z}\right) dz - \int_{z=0}^{\frac{l}{2}} 4z\sqrt{(\frac{l}{2})^2 - z^2} dz \right] \\
&= \frac{\pi(1-\nu)\tau_{app}}{Vl\mu b} \left[\left(l^2 z \tan^{-1}\left(\frac{\sqrt{(\frac{l}{2})^2 - z^2}}{z}\right) - l^2 \sqrt{(\frac{l}{2})^2 - z^2} \right)_{z=0}^{\frac{l}{2}} - \left(\frac{-1}{6} (l^2 - 4z^2)^{\frac{3}{2}} \right)_{z=0}^{\frac{l}{2}} \right] \\
&= \frac{\pi(1-\nu)\tau_{app}}{Vl\mu b} \left[\frac{l^3}{2} - \frac{l^3}{6} \right] \\
&= \frac{\pi(1-\nu)\tau_{app}}{Vl\mu b} \frac{l^3}{3} \\
&= \frac{\pi(1-\nu)}{3} \frac{l^2 \tau_{app}}{\mu V b}
\end{aligned}$$

The total plastic deformation due to a single slip plane passing through the center of the sphere of homogenization volume V is

$$\begin{aligned}
\Upsilon_{3d}^{pu} &= \frac{bA}{V} \\
&= \frac{b \int_0^{\frac{l}{2}} A(x)n(x)dx}{V}
\end{aligned}$$

The total plastic deformation due to n non-similar parallel slip planes will be

$$\begin{aligned}
\Upsilon_{3d}^{pu} &= \frac{2b}{Vl} \int_{z=0}^{\frac{l}{2}} \int_{x=0}^{\sqrt{(\frac{l}{2})^2 - z^2}} A(x)n(x) dx dz \\
&= \frac{2b}{Vl} \int_{z=0}^{\frac{l}{2}} \int_{x=0}^{\sqrt{(\frac{l}{2})^2 - z^2}} \pi x^2 \frac{2(1-\nu)\tau_{app}}{\mu b} \frac{x}{\sqrt{(\frac{l}{2})^2 - x^2}} dx dz \\
&= \frac{4b\pi(1-\nu)\tau_{app}}{Vl\mu b} \int_{z=0}^{\frac{l}{2}} \int_{x=0}^{\sqrt{(\frac{l}{2})^2 - z^2}} \frac{x^3}{\sqrt{(\frac{l}{2})^2 - x^2}} dx dz
\end{aligned}$$

B.3. Hardening due to 'n' non-similar parallel slip planes in a grain

$$\begin{aligned}
\Upsilon_{3d}^{pu} &= \frac{4b\pi(1-\nu)\tau_{app}}{Vl\mu b} \int_{z=0}^{\frac{l}{2}} \left[\frac{-1}{3} \left(\frac{l^2}{2} + x^2 \right) \sqrt{\left(\frac{l}{2} \right)^2 - x^2} \right]_{x=0}^{\sqrt{\left(\frac{l}{2} \right)^2 - z^2}} dz \\
&= \frac{-4b\pi(1-\nu)\tau_{app}}{3Vl\mu b} \int_{z=0}^{\frac{l}{2}} \left[z(l^2 - z^2) - \frac{l^3}{4} \right] dz \\
&= \frac{-4b\pi(1-\nu)\tau_{app}}{3Vl\mu b} \int_{z=0}^{\frac{l}{2}} \left[l^2 z - z^3 - \frac{l^3}{4} \right] dz \\
&= \frac{-4b\pi(1-\nu)\tau_{app}}{3Vl\mu b} \left[\frac{l^2 z^2}{2} - \frac{z^4}{4} - \frac{l^3 z}{4} \right]_{z=0}^{\frac{l}{2}} \\
&= \frac{-4b\pi(1-\nu)\tau_{app}}{3Vl\mu b} \left[\frac{l^4}{8} - \frac{l^4}{64} - \frac{l^4}{8} \right] \\
&= \frac{4b\pi(1-\nu)\tau_{app}}{3Vl\mu b} \frac{l^4}{64} \\
&= \frac{\pi(1-\nu)\tau_{app}}{V\mu} \frac{l^3}{48} \\
&= \frac{\pi(1-\nu)}{48\mu V} l^3 \tau_{app}
\end{aligned}$$

Substituting the values of $V = \frac{\pi D_g^3}{6}$ and $l = D_g$ in the above equation gives an average hardening value for a single slip system located anywhere in the sphere.

$$\begin{aligned}
\Upsilon_p^{(s)} &= \frac{\pi(1-\nu)}{48\mu V} l^3 \tau_d^{(s)} \\
&= \frac{\pi(1-\nu)}{48\mu} \frac{D_g^3}{\frac{\pi D_g^3}{6}} \tau_d^{(s)} \\
&= \frac{\pi(1-\nu)}{48\mu} \frac{6}{\pi} \tau_d^{(s)} \\
&= \frac{1(1-\nu)}{8\mu} \tau_d^{(s)}
\end{aligned}$$

The average kinematic hardening of a sphere with hardening contribution from a total of eleven non-similar parallel slip planes is 0.73. The average kinematic hardening can drastically change with the cross-slip mechanism. Here, we just show the importance of cross-slip mechanism by lowering the probability(i.e., increasing the critical stress for cross-slip(CSCS)) with which the cross-slip can occur. A much detailed study would be required to understand the importance of cross-slip

Appendix B. Appendix: Non-equiaxed shape of dislocation pileups

mechanism on kinematic hardening.

$$\tau_d^{(s)} \simeq \frac{8}{11} \frac{\mu}{(1-\nu)} \Upsilon_p^{(s)}$$

$$\tau_d^{(s)} \simeq 0.73 \frac{\mu}{(1-\nu)} \Upsilon_p^{(s)}$$

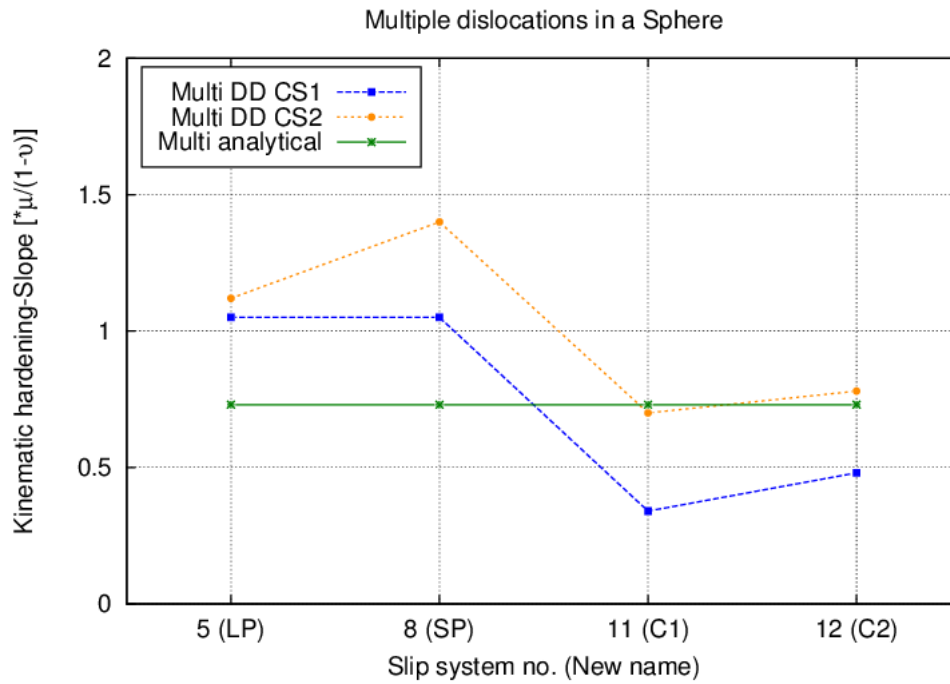


Figure B.4 – KH slope of Sphere @ CSCS= 32MPa(CS1), @ CSCS= 80MPa(CS2) and analytical

B.3.2 Non-equiaxed (spheroidal) grain

In a spheroidal grain, the perimeter and area of a dislocation loop on a slip plane changes not only with respect to the distance from the center of the grain but also with to the orientation of the slip plane normal with respect to the long axis of the grain.

The total density of dislocation due to a single plane passing through the center

B.3. Hardening due to 'n' non-similar parallel slip planes in a grain

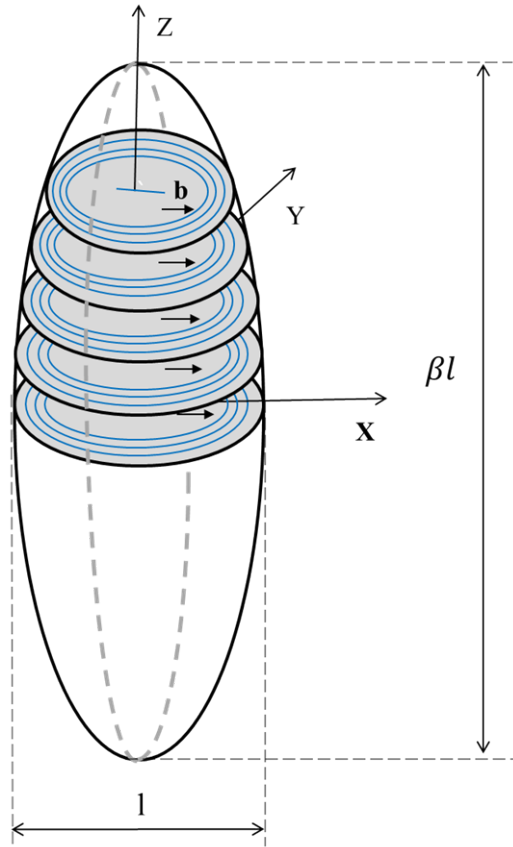


Figure B.5 – Parallel planes in a non-equiaxed (spheroidal/elongated grain

of the spheroid in a homogenization volume V is

$$\begin{aligned}\rho_{3d}^{pu} &= \frac{1}{V} \int_0^{\frac{l}{2}} \zeta(x)n(x)dx \\ &= \frac{1}{V} \int_0^{\frac{l}{2}} \pi(a+b)f(h) \frac{2(1-\nu)\tau_{app}}{\mu b} \frac{x}{\sqrt{(\frac{l}{2})^2 - x^2}} dx\end{aligned}$$

where,

$h = \frac{(a-b)^2}{(a+b)^2}$ where $a = x$ and $b = \beta_s x$ are the generalized half minor and major axes respectively.

$$f(h) = 1 + \frac{h}{4} + \frac{h^2}{64} + \frac{h^3}{256} + \frac{25h^4}{16384} + \frac{49h^5}{65536} + \dots$$

β = aspect ratio of the grain

$\beta_s = \frac{\beta}{\sqrt{(\sin\theta)^2 + (\beta\cos\theta)^2}}$, is the aspect ratio of the slip plane.

θ = angle made by the slip plane normal with respect to the long axis of the grain.

Appendix B. Appendix: Non-equiaxed shape of dislocation pileups

The total density of dislocations due to n non-similar parallel slip planes in a homogenization volume V is found by using the same formula as in the case of ellipse shaped dislocation loops and changing the limits as below.

$$\begin{aligned}
\rho_{3d}^{pu} &= \frac{2}{Vl\beta_s} \int_{z=0}^{\frac{\beta_s l}{2}} \int_{x=0}^{\frac{\beta_s}{\beta} \sqrt{(\beta_s \frac{l}{2})^2 - z^2}} \zeta(x)n(x) dx dz \\
&= \frac{2}{Vl\beta_s} \int_{z=0}^{\frac{\beta_s l}{2}} \int_{x=0}^{\frac{1}{\beta_s} \sqrt{(\beta_s \frac{l}{2})^2 - z^2}} \pi(a+b)f(h) \frac{2(1-\nu)\tau_{app}}{\mu b} \frac{x}{\sqrt{(\frac{l}{2})^2 - x^2}} dx dz \\
&= \frac{2}{Vl\beta_s} \int_{z=0}^{\frac{\beta_s l}{2}} \int_{x=0}^{\frac{1}{\beta_s} \sqrt{(\beta_s \frac{l}{2})^2 - z^2}} \pi(x + \beta_s x)f(h) \frac{2(1-\nu)\tau_{app}}{\mu b} \frac{x}{\sqrt{(\frac{l}{2})^2 - x^2}} dx dz \\
&= \frac{4\pi}{Vl\beta_s} (1 + \beta_s) \frac{(1-\nu)\tau_{app}}{\mu b} \int_{z=0}^{\frac{\beta_s l}{2}} \int_{x=0}^{\frac{1}{\beta_s} \sqrt{(\beta_s \frac{l}{2})^2 - z^2}} \frac{x^2}{\sqrt{(\frac{l}{2})^2 - x^2}} dx dz \\
&= \frac{4\pi}{Vl\beta_s} (1 + \beta_s) \frac{(1-\nu)\tau_{app}}{\mu b} \int_{z=0}^{\frac{\beta_s l}{2}} \frac{1}{8} \left[l^2 \tan^{-1} \left(\frac{x}{\sqrt{(\frac{l}{2})^2 - x^2}} \right) - 4x \sqrt{(\frac{l}{2})^2 - x^2} \right]_{x=0}^{\frac{1}{\beta_s} \sqrt{(\beta_s \frac{l}{2})^2 - z^2}} dz \\
&= \frac{\pi}{2Vl\beta_s} (1 + \beta_s) \frac{(1-\nu)\tau_{app}}{\mu b} \left[\int_{z=0}^{\frac{\beta_s l}{2}} l^2 \tan^{-1} \left(\frac{\sqrt{(\beta_s \frac{l}{2})^2 - z^2}}{z} \right) dz - \int_{z=0}^{\frac{\beta_s l}{2}} 4z \sqrt{(\beta_s \frac{l}{2})^2 - z^2} dz \right] \\
&= \frac{\pi}{2Vl\beta_s} (1 + \beta_s) \frac{(1-\nu)\tau_{app}}{\mu b} \left[\left(l^2 z \tan^{-1} \left(\frac{\sqrt{(\beta_s \frac{l}{2})^2 - z^2}}{z} \right) - l^2 \sqrt{(\beta_s \frac{l}{2})^2 - z^2} \right)_{z=0}^{\frac{\beta_s l}{2}} - \left(\frac{-1}{6} \left(\left(\frac{\beta l}{\beta_s} \right)^2 - 4z^2 \right)^{\frac{3}{2}} \right)_{z=0}^{\frac{\beta_s l}{2}} \right] \\
&= \frac{\pi}{2Vl\beta_s} (1 + \beta_s) \frac{(1-\nu)\tau_{app}}{\mu b} \left[\left(l^2 z \tan^{-1} \left(\frac{\sqrt{(\beta_s \frac{l}{2})^2 - z^2}}{z} \right) \right)_{z=0}^{\frac{\beta_s l}{2}} - \left(l^2 \sqrt{(\beta_s \frac{l}{2})^2 - z^2} \right)_{z=0}^{\frac{\beta_s l}{2}} - \left(\frac{-1}{6} \left(\left(\frac{\beta l}{\beta_s} \right)^2 - 4z^2 \right)^{\frac{3}{2}} \right)_{z=0}^{\frac{\beta_s l}{2}} \right]
\end{aligned}$$

B.3. Hardening due to 'n' non-similar parallel slip planes in a grain

$$\begin{aligned}
\rho_{3d}^{pu} &= \frac{\pi}{2Vl\beta_s}(1 + \beta_s) \frac{(1 - \nu)\tau_{app}}{\mu b} \\
&\quad \left[\left(\frac{l^3 \beta_s}{2} \tan^{-1} \left(\frac{\sqrt{(\beta_s)^2 - (\beta_s)^2}}{\beta_s} \right) \right) - \left(\frac{l^3}{2} \sqrt{(\beta_s)^2 - (\beta_s)^2} - \frac{l^3}{2} \beta_s \right) - \frac{l^3}{6} \left((\beta_s^2 - \beta_s^2)^{\frac{3}{2}} - \frac{\beta^3}{\beta_s^3} \right) \right] \\
&= \frac{\pi}{2Vl\beta_s}(1 + \beta_s) \frac{(1 - \nu)\tau_{app}}{\mu b} \frac{l^3}{2} \\
&\quad \left[\left(\frac{\beta_s}{2} \tan^{-1} \left(\frac{\sqrt{(\beta_s)^2 - (\beta_s)^2}}{\beta_s} \right) \right) - \left(\sqrt{(\beta_s)^2 - (\beta_s)^2} - \beta_s \right) - \frac{1}{3} \left((\beta_s^2 - \beta_s^2)^{\frac{3}{2}} - \frac{\beta^3}{\beta_s^3} \right) \right] \\
&= \frac{\pi}{2Vl\beta_s}(1 + \beta_s) \frac{(1 - \nu)\tau_{app}}{\mu b} \frac{l^3}{2} \\
&\quad \left[\frac{\beta_s}{2} \tan^{-1} \left(\frac{\sqrt{(\beta_s)^2 - (\beta_s)^2}}{\beta_s} \right) - \sqrt{(\beta_s)^2 - (\beta_s)^2} + \beta_s - \frac{1}{3} (\beta_s^2 - \beta_s^2)^{\frac{3}{2}} + \frac{1}{3} \frac{\beta^3}{\beta_s^3} \right]
\end{aligned}$$

The total plastic deformation due to a single slip plane passing through the center of the spheroid of homogenization volume V is

$$\begin{aligned}
\Upsilon_{3d}^{pu} &= \frac{bA}{V} \\
&= \frac{b \int_0^{\frac{l}{2}} A(x)n(x)dx}{V}
\end{aligned}$$

The total plastic deformation due to n non-similar parallel slip planes will be

$$\begin{aligned}
\Upsilon_{3d}^{pu} &= \frac{2b}{Vl\beta_s} \int_{z=0}^{\frac{\beta_s l}{2}} \int_{x=0}^{\frac{1}{\beta_s} \sqrt{(\beta_s \frac{l}{2})^2 - z^2}} A(x)n(x)dx dz \\
&= \frac{2b}{Vl\beta_s} \int_{z=0}^{\frac{\beta_s l}{2}} \int_{x=0}^{\frac{1}{\beta_s} \sqrt{(\beta_s \frac{l}{2})^2 - z^2}} \pi ab \frac{2(1 - \nu)\tau_{app}}{\mu b} \frac{x}{\sqrt{(\frac{l}{2})^2 - x^2}} dx dz \\
&= \frac{2b}{Vl\beta_s} \int_{z=0}^{\frac{\beta_s l}{2}} \int_{x=0}^{\frac{1}{\beta_s} \sqrt{(\beta_s \frac{l}{2})^2 - z^2}} \pi x^2 \beta_s \frac{2(1 - \nu)\tau_{app}}{\mu b} \frac{x}{\sqrt{(\frac{l}{2})^2 - x^2}} dx dz \\
&= \frac{4b\pi}{Vl} \frac{\beta}{\beta_s^2} \frac{(1 - \nu)\tau_{app}}{\mu b} \int_{z=0}^{\frac{\beta_s l}{2}} \int_{x=0}^{\frac{1}{\beta_s} \sqrt{(\beta_s \frac{l}{2})^2 - z^2}} \frac{x^3}{\sqrt{(\frac{l}{2})^2 - x^2}} dx dz
\end{aligned}$$

Appendix B. Appendix: Non-equiaxed shape of dislocation pileups

$$\begin{aligned}
\Upsilon_{3d}^{pu} &= \frac{4b\pi}{Vl} \frac{\beta}{\beta_s^2} \frac{(1-\nu)\tau_{app}}{\mu b} \int_{z=0}^{\frac{\beta_s l}{2}} \left[\frac{-1}{3} \left(\frac{l^2}{2} + x^2 \right) \sqrt{\left(\frac{l}{2} \right)^2 - x^2} \right]_{x=0}^{\frac{1}{\beta_s} \sqrt{(\beta_s \frac{l}{2})^2 - z^2}} dz \\
&= \frac{4b\pi}{Vl} \frac{\beta}{\beta_s^2} \frac{(1-\nu)\tau_{app}}{\mu b} \int_{z=0}^{\frac{\beta_s l}{2}} \left[\frac{\beta_s^3}{3\beta^3} z^3 - \frac{l^2}{3} \frac{1}{\beta_s} z + \frac{l^3}{12} \right] dz \\
&= \frac{4b\pi}{Vl} \frac{\beta}{\beta_s^2} \frac{(1-\nu)\tau_{app}}{\mu b} \left[\frac{\beta_s^3}{3\beta^3} \int_{z=0}^{\frac{\beta_s l}{2}} z^3 dz - \frac{l^2}{3} \frac{1}{\beta_s} \int_{z=0}^{\frac{\beta_s l}{2}} z dz + \frac{l^3}{12} \int_{z=0}^{\frac{\beta_s l}{2}} dz \right] \\
&= \frac{4b\pi}{Vl} \frac{\beta}{\beta_s^2} \frac{(1-\nu)\tau_{app}}{\mu b} \left[\frac{\beta_s^3}{3\beta^3} \left(\frac{z^4}{4} \right)_{z=0}^{\frac{\beta_s l}{2}} - \frac{l^2}{3} \frac{1}{\beta_s} \left(\frac{z^2}{2} \right)_{z=0}^{\frac{\beta_s l}{2}} + \frac{l^3}{12} (z)_{z=0}^{\frac{\beta_s l}{2}} \right] \\
&= \frac{4b\pi}{Vl} \frac{\beta}{\beta_s^2} \frac{(1-\nu)\tau_{app}}{\mu b} \left[\frac{\beta_s^3}{3\beta^3} \frac{(\beta_s l)^4}{4 \cdot 2^4} - \frac{l^2}{3} \frac{1}{\beta_s} \frac{(\beta_s l)^2}{2 \cdot 2^2} + \frac{l^3}{12} \frac{\beta_s l}{2} \right] \\
&= \frac{4b\pi}{Vl} \frac{\beta}{\beta_s^2} \frac{(1-\nu)\tau_{app}}{\mu b} \left[\frac{\beta_s^3}{\beta^3} \frac{(\beta_s)^4}{192} l^4 - \frac{1}{\beta_s} \frac{(\beta_s)^2}{24} l^4 + \frac{\beta_s}{24} l^4 \right] \\
&= \frac{4b\pi}{Vl} \frac{\beta}{\beta_s^2} \frac{(1-\nu)}{\mu b} l^3 \tau_{app} \left[\frac{\beta_s^3}{\beta^3} \frac{(\beta_s)^4}{192} - \frac{1}{\beta_s} \frac{(\beta_s)^2}{24} + \frac{\beta_s}{24} \right] \\
&= \frac{4\pi}{V} \frac{\beta}{\beta_s^2} \frac{(1-\nu)}{\mu b} l^3 \tau_{app} \left[\frac{\beta_s^3}{\beta^3} \frac{(\beta_s)^4}{192} - \frac{1}{\beta_s} \frac{(\beta_s)^2}{24} + \frac{\beta_s}{24} \right] \\
&= \pi \left[\frac{\beta_s^5}{48\beta^2} - \frac{\beta_s}{6} + \frac{\beta}{6\beta_s} \right] \frac{(1-\nu)}{\mu V} l^3 \tau_{app}
\end{aligned}$$

Substituting the values of $V = \frac{\pi l^3 \beta_s}{6}$ and $l = f_1(l)$ (cf. Section B.1.2) in the above equation gives an average hardening value for a single slip system located anywhere in the spheroid.

$$\begin{aligned}
\Upsilon_p^{(s)} &= \pi \left[\frac{\beta_s^5}{48\beta^2} - \frac{\beta_s}{6} + \frac{\beta}{6\beta_s} \right] \frac{(1-\nu)}{\mu V} l^3 \tau_d^{(s)} \\
&= \pi \left[\frac{\beta_s^5}{48\beta^2} - \frac{\beta_s}{6} + \frac{\beta}{6\beta_s} \right] \frac{(1-\nu)}{\mu} \frac{\beta_s l^3}{\frac{\pi l^3 \beta_s}{6}} \tau_d^{(s)} \\
&= \pi \left[\frac{\beta_s^5}{48\beta^2} - \frac{\beta_s}{6} + \frac{\beta}{6\beta_s} \right] \frac{(1-\nu)}{\mu} \frac{6}{\pi} \tau_d^{(s)} \\
&= \left[\frac{\beta_s^5}{8\beta^2} - \beta_s + \beta_s \right] \frac{(1-\nu)}{\mu} \tau_d^{(s)}
\end{aligned}$$

The average kinematic hardening on different slip systems in a spheroid with hardening contribution from a total of eleven non-similar parallel slip planes in

B.3. Hardening due to 'n' non-similar parallel slip planes in a grain

each is plotted against the predictions from DD simulations.

$$\tau_d^{(s)} \simeq \frac{1}{11} \left[\frac{8\beta^2\beta_s}{8\beta^3 - 8\beta^2\beta_s^2 + \beta_s^6} \right] \frac{\mu}{(1-\nu)} \Upsilon_p^{(s)}$$

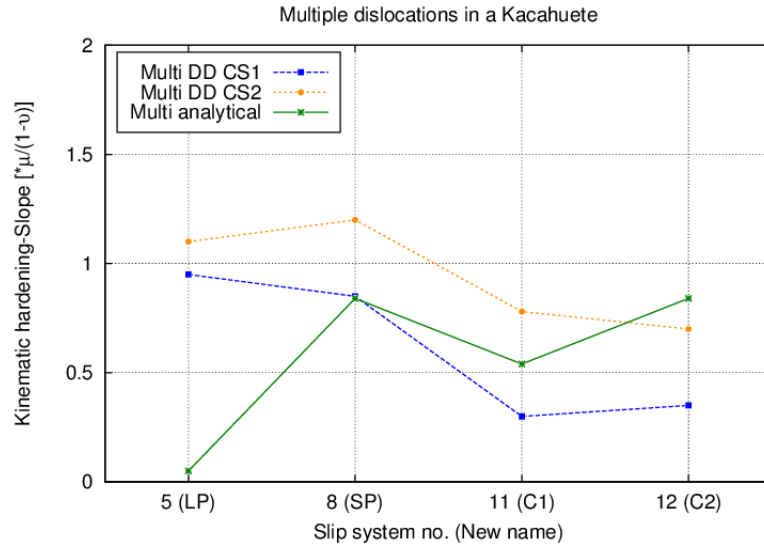


Figure B.6 – KH slope of Kaca @ CSCS= 32MPa(CS1), @ CSCS= 80MPa(CS2) and analytical

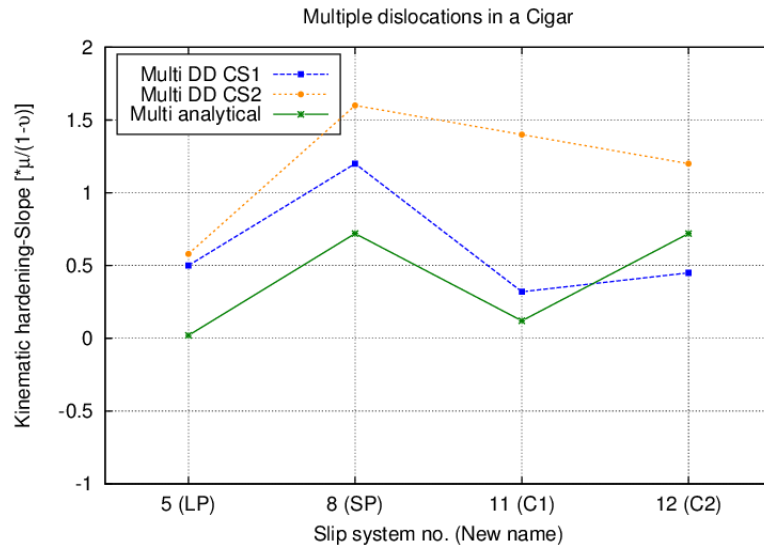


Figure B.7 – KH slope of Cigar @ CSCS= 32MPa(CS1), @ CSCS= 80MPa(CS2) and analytical

B.4 Conclusion

- Depres's work on pileup model had been extended to a more general case of non-equiaxed shape of dislocation loops.
- Analytical formula so developed had been validated against results from DD simulations for grains of aspect ratios from 1.0 to 5.0.
- Cross slip mechanism is observed to change the dislocation slip activity and inturn back stress. This effect can be accounted in analytical formulations by considering primary and its respective deviate systems in pairs. Wherein, the back stress developed on the slip system pair (primary or deviate) can be distributed according to the Schmid factors.

Bibliography

- [1] *LAMMPS database*.
- [2] H. ALEXANDER, *Dislocations in Semiconductors*, Springer Proceeding in Physics, 54 (1991).
- [3] ANDRE PINEAU, A. A. BENZERGA, AND T. PARDOEN, *Failure of metals III. Fracture and fatigue of nanostructured metallic materials*, Acta Materialia, 1 (2015).
- [4] A. ARSENLIS, *Crystallographic aspects of geometrically- necessary and statistically-stored dislocation density*, Acta Materialia, 47 (1999), pp. 1597–1611.
- [5] A. ARSENLIS, W. CAI, M. TANG, T. OPPELSTRUP, G. HOMMES, T. G. PIERCE, V. V. BULATOV, AND M. RHEE, *Enabling strain hardening simulations with dislocation dynamics*, Modelling and Simulation in Materials Science and Engineering, 15 (2007), pp. 553–595.
- [6] A. ARSENLIS AND D. M. PARKS, *Modeling the evolution of crystallographic dislocation density in crystal plasticity*, Journal of the Mechanics and Physics of Solids, 50 (2001), pp. 1979–2009.
- [7] R. J. ASARO AND A. NEEDLEMAN, *Texture development and strain hardening in rate dependent polycrystals*, Acta Metallurgica, 33 (1985), pp. 923–953.
- [8] M. F. ASHBY, *The deformation of plastically non-homogeneous materials*, Philosophical Magazine, 21 (1970), pp. 399–424.
- [9] M. G. BAYLEY, C J, W. A. M. BREKLEMANS, *A comparison of dislocation induced back stress formulations in strain gradient crystal plasticity*, International Journal of Solids and Structures, 43 (2006), pp. 7268–7286.
- [10] A. A. BENZERGA AND N. F. SHAVER, *Scale dependence of mechanical properties of single crystals under uniform deformation*, Scripta Materialia, 54 (2006), pp. 1937–1941.

Bibliography

- [11] N. BERTIN, *On the role of lattice defects interactions on strain hardening: a study from discrete dislocation dynamics to crystal plasticity modelling*, PhD thesis, University of Metz, 2015.
- [12] N. BERTIN, M. V. UPADHYAY, C. PRADALIER, AND L. CAPOLUNGO, *A FFT-based formulation for efficient mechanical fields computation in isotropic and anisotropic periodic discrete dislocation dynamics*, Modelling and Simulation in Materials Science and Engineering, 065009 (2015), p. 65009.
- [13] I. J. BEYERLEIN, X. ZHANG, AND A. MISRA, *Growth Twins and Deformation Twins in Metals*, Annual Review of Materials Research, 44 (2014).
- [14] A. T. BLUMENAU, *The Modelling of Dislocations in Semiconductor Crystals*, PhD thesis, 2002.
- [15] A. P. BRAHME, K. INAL, R. K. MISHRA, AND S. SAIMOTO, *The backstress effect of evolving deformation boundaries in FCC polycrystals*, International Journal of Plasticity, 27 (2011), pp. 1252–1266.
- [16] Y. BRÉCHET, L. P. KUBIN, B. DEVINCRE, M. CONDAT, V. PONTIKIS, AND G. CANOVA, *Dislocation Microstructures and Plastic Flow: A 3D Simulation*, in Non Linear Phenomena in Materials Science II, vol. 23 of Solid State Phenomena, Trans Tech Publications, 1992, pp. 455–472.
- [17] S. BROCHARD AND P. BEAUCHAMP, *Dislocation nucleation from surface steps: Atomistic simulation in aluminium*, Philosophical Magazine A, 80 (2000), pp. 503–524.
- [18] M. J. BUEHLER, A. HARTMAIER, M. A. DUCHAINEAU, F. F. ABRAHAM, AND H. GAO, *The dynamical complexity of work-hardening: a large-scale molecular dynamics simulation*, Acta Mechanica Sinica, 1 (2005), pp. 103–111.
- [19] V. BULATOV AND S. YIP, *Connecting atomistic and mesoscale simulations of crystal plasticity*, Letters to nature, 391 (1998).
- [20] V. V. BULATOV, L. L. HSIUNG, M. TANG, A. ARSENLIS, M. C. BARTELT, W. CAI, J. N. FLORANDO, M. HIRATANI, M. RHEE, G. HOMMES, T. G. PIERCE, AND T. D. DE LA RUBIA, *Dislocation multi-junctions and strain hardening.*, Nature, 440 (2006), pp. 1174–8.
- [21] H.-J. BUNGE, *Texture analysis in Materials science*, digital ed., 1982.

-
- [22] H. J. BUNGE, R. KIEWEL, T. REINERT, AND L. FRITSCHÉ, *Elastic properties of polycrystals - influence of texture and stereology*, Journal Of The Mechanics And Physics Of Solids, 48 (2000), pp. 29–66.
- [23] W. CAI, A. ARSENLIS, C. R. WEINBERGER, AND V. V. BULATOV, *A non-singular continuum theory of dislocations*, Journal of the Mechanics and Physics of Solids, 54 (2006), pp. 561–587.
- [24] CAMBRIDGE, *Cambridge Materials Selector Database*.
- [25] A. CAO, Y. WEI, AND E. MA, *Grain boundary effects on plastic deformation and fracture mechanisms in Cu nanowires: Molecular dynamics simulations*, Physical Review B, 77 (2008), p. 195429.
- [26] CEA, *Cast3M*, 2016.
- [27] CHAN-SUN SHIN, *3d discrete dislocation dynamics applied to dislocation-precipitate interactions*, phd_thesis, INP Grenoble, 2004.
- [28] M. CHASSAGNE, M. LEGROS, AND D. RODNEY, *Atomic-scale simulation of screw dislocation/coherent twin boundary interaction in Al, Au, Cu and Ni*, Acta Materialia, 59 (2011), pp. 1456–1463.
- [29] D. CHERNS, *Electron Holography Studies of the Charge on Dislocations in GaN*, Physica status solidi, 930 (2002), pp. 924–930.
- [30] CNRS AND CEA, *Numodis-OptiDis: a parallel large scale Dislocation Dynamics simulation code.*, 2016.
- [31] M. COLLA, H. IDRISSE, L. MALET, S. GODET, J. RASKIN, D. SCHRYVERS, AND T. PARDOEN, *Dislocation-mediated relaxation in nanograined columnar palladium films revealed by on-chip time-resolved HRTEM testing*, Nature Communications, 6 (2015), pp. 1–8.
- [32] M.-S. COLLA, *Plasticity and creep in thin free-standing nanocrystalline Pd films*, PhD thesis, Université catholique de Louvain, 2014.
- [33] M.-S. COLLA, B. WANG, H. IDRISSE, D. SCHRYVERS, J.-P. RASKIN, AND T. PARDOEN, *High strength-ductility of thin nanocrystalline palladium films with nanoscale twins: On-chip testing and grain aggregate model*, Acta Materialia, 60 (2012), pp. 1795–1806.

Bibliography

- [34] M. COULOMBIER, G. GUIBBIERS, M.-S. COLLA, R. VAYRETTE, J.-P. RASKIN, AND T. PARDOEN, *On-chip stress relaxation testing method for freestanding thin film materials.*, The Review of scientific instruments, 83 (2012), p. 105004.
- [35] CRAY, CAPS, NVIDIA, AND PGI, *OpenACC Homepage*, 2015.
- [36] W. C. J. D AND D. G. RETHWISCH, *Materials science and engineering an introduction*, Wiley, eighth ed., 2009.
- [37] D. WOLF, *A read-shockley model for high-angle grain boundaries*, Scripta Metallurgica, 23 (1989).
- [38] M. S. DE BOER, M. P., DELRIO, F. W., AND BAKER, *On-chip test structure suite for free-standing metal film mechanical property testing, part i - analysis.*, Acta Materialia, 56 (2008), pp. 3344–3352.
- [39] R. DE WIT, *Some Relations for Straight Dislocations*, Physica status solidi, 20 (1967), pp. 567–573.
- [40] L. DELANNAY AND M. R. BARNETT, *Modelling the combined effect of grain size and grain shape on plastic anisotropy of metals*, International Journal of Plasticity, 32-33 (2012), pp. 70–84.
- [41] L. DELANNAY, R. E. LOGÉ, Y. CHASTEL, AND P. VAN HOUTTE, *Prediction of intergranular strains in cubic metals using a multisite elastic-plastic model*, Acta Materialia, 50 (2002), pp. 5127–5138.
- [42] L. DELANNAY, M. A. MELCHIOR, J. W. SIGNORELLI, J. REMACLE, AND T. KUWABARA, *Influence of grain shape on the planar anisotropy of rolled steel sheets – evaluation of three models*, Computational Materials Science, 45 (2009), pp. 739–743.
- [43] C. DÉPRÉS, *A 3D Discrete Dislocation Dynamics modeling of the early fatigue cycles in 316L Austenitic stainless steel*, phd_thesis, Institut National Polytechnique de Grenoble, 2004.
- [44] C. DÉPRÉS, M. FIVEL, AND L. TABOUROT, *A dislocation-based model for low-amplitude fatigue behaviour of face-centred cubic single crystals*, Scripta Materialia, 58 (2008), pp. 1086–1089.
- [45] B. DEVINCRE, *Three dimensional stress field expressions for straight dislocation segments*, Solid state Communications, 93 (1995), pp. 875–878.

-
- [46] B. DEVINCRE AND L. KUBIN, *Scale transitions in crystal plasticity by dislocation dynamics simulations*, Comptes Rendus Physique, 11 (2010), pp. 274–284.
- [47] B. DEVINCRE, L. KUBIN, AND T. HOC, *Collinear superjogs and the low-stress response of fcc crystals*, Scripta Materialia, 57 (2007), pp. 905–908.
- [48] B. DEVINCRE, L. P. KUBIN, C. LEMARCHAND, AND R. MADEC, *Mesosopic simulations of plastic deformation*, Materials Science and Engineering, 310 (2001), pp. 211–219.
- [49] M. P. DEWALD AND W. A. CURTIN, *Multiscale modeling of dislocation/grain-boundary interactions: III. 60degree dislocations impinging on sigma3, sigma9 and sigma11 tilt boundaries in Al*, Philosophical Magazine, 87 (2007), pp. 4615–4641.
- [50] L. DEZERALD, D. RODNEY, E. CLOUET, AND L. VENTELON, *Plastic anisotropy and dislocation trajectory in BCC metals*, Nature Communications, 7 (2016).
- [51] J. DROUET, L. DUPUY, F. ONIMUS, AND F. MOMPIOU, *A direct comparison between in-situ transmission electron microscopy observations and Dislocation Dynamics simulations of interaction between dislocation and irradiation induced loop in a zirconium alloy*, Scripta Materialia, 119 (2016), pp. 71–75.
- [52] E. SCHMID AND W. BOAS, *Kristallplastizität*, 1935.
- [53] I. ERTÜRK, J. A. W. VAN DOMMELEN, AND M. G. D. GEERS, *Gradient crystal plasticity modelling of anelastic effects in particle strengthened metallic thin films*, Meccanica, 49 (2014), pp. 2657–2685.
- [54] B. ESCAIG AND B. ESCAIG, *A study of cross-slip activation parameters in pure copper*, Acta Metallurgica et Materialia, 36 (1988), pp. 1989–2002.
- [55] H. D. ESPINOSA, M. PANICO, S. BERBENNI, AND K. W. SCHWARZ, *Discrete dislocation dynamics simulations to interpret plasticity size and surface effects in freestanding FCC thin films*, International journal of mech. Sci, 22 (2006), pp. 2091–2117.
- [56] H. D. ESPINOSA, B. C. PROROK, AND M. FISCHER, *A methodology for determining mechanical properties of freestanding thin films and MEMS materials*, 51 (2003), pp. 47–67.

Bibliography

- [57] L. P. EVERS AND D. M. PARKS, *Crystal plasticity model with enhanced hardening by geometrically necessary dislocation accumulation*, Journal of the Mechanics and Physics of Solids, 50 (2002), pp. 2403–2424.
- [58] H. FAN, S. AUBRY, A. ARSENLIS, AND J. A. EL-AWADY, *The role of twinning deformation on the hardening response of polycrystalline magnesium from discrete dislocation dynamics simulations*, Acta Materialia, 92 (2015), pp. 126–139.
- [59] F. FERRONI, E. TARLETON, AND S. FITZGERALD, *GPU accelerated dislocation dynamics*, Journal of Computational Physics, 272 (2014), pp. 619–628.
- [60] F. FEYEL AND J.-L. CHABOCHE, *FE2 multiscale approach for modelling the elastoviscoplastic behaviour of long fibre SiC/Ti composite materials*, Computer Methods in Applied Mechanics and Engineering, 183 (2000), pp. 309–330.
- [61] J. E. FINNIS, M. W., SINCLAIR, *A simple empirical N-body potential for transition metals*, Philosophical Magazine A, 50 (1984), pp. 45–55.
- [62] M. FIVEL, *Etudes numériques à différentes échelles de la déformation plastique des monocristaux de structure cfc*, PhD thesis, INP Grenoble, 1997.
- [63] M. FIVEL AND C. DÉPRÉS, *An easy implementation of displacement calculations in 3D discrete dislocation dynamics codes*, Philosophical Magazine, 94 (2014), pp. 3206–3214.
- [64] M. C. FIVEL, *Simulations de la plasticité cristalline et transitions de échelles*, habilitation, INP Grenoble, 2008.
- [65] N. A. FLECK, M. F. ASHBY, AND J. W. HUTCHINSON, *The role of geometrically necessary dislocations in giving material strengthening*, Scripta Materialia, 48 (2003), pp. 179–183.
- [66] J. N. FLORANDO AND W. D. NIX, *A microbeam bending method for studying stress-strain relations for metal thin films on silicon substrates*, Journal of the Mechanics and Physics of Solids, (2004), pp. 1–31.
- [67] D. L. M. FOILES, STEPHEN M, ELIZABETH A. HOLM, DAVID L. OLMSTED, LUKE N, BREWER, DAVID M. FOLLSTAEDT, KHALID M. HATTAR, JAMES A. KNAPP, MARK A. RODRIGUEZ, BLYTHE G. CLARK, *Science at the Interface: Grain Boundaries in Nanocrystalline Metals*, Tech. Rep. September, 2009.

-
- [68] A. J. E. FOREMAN, *The bowing of a dislocation segment*, Philosophical Magazine, (2006), pp. 37–41.
- [69] S. FOREST, R. SIEVERT, AND E. C. AIFANTIS, *Strain gradient crystal plasticity : thermomechanical formulations and applications*, Journal of the Mechanical Behavior of Materials, 13 (2002), pp. 219–232.
- [70] P. FRANCIOSI, *The concepts of latent hardening strain hardening in metallic single crystals*, Acta Materialia, 33 (1985), pp. 1601–1612.
- [71] M. FRIGO AND S. G. JOHNSON, *The Design and Implementation of FFTW3*, Proceedings of the IEEE, 93 (2005), pp. 216–231.
- [72] V. FUKA, *PoisFFT - A Free Parallel Fast Poisson Solver*, Applied Mathematics and Computation, (2014).
- [73] Z. W. G. CONG, Y. LU, W. PENG, X. LIU, X. WANG, *Design of the low-temperature AlN interlayer for GaN grown on Si (1 1 1) substrate*, Journal of Crystal Growth, 276 (2005), pp. 381–388.
- [74] S. GAO, M. FIVEL, A. MA, AND A. HARTMAIER, *Influence of misfit stresses on dislocation glide in single crystal superalloys: A three-dimensional discrete dislocation dynamics study*, Journal of the Mechanics and Physics of Solids, 76 (2015), pp. 276–290.
- [75] C. GEUZAIN AND J.-F. REMACLE, *Gmsh: a three-dimensional finite element mesh generator with built-in pre- and post-processing facilities*, International Journal for Numerical methods in Engineering, 0 (2009), pp. 1–24.
- [76] D. S. GIANOLA, D. H. WARNER, J. F. MOLINARI, AND K. J. HEMKER, *Increased strain rate sensitivity due to stress-coupled grain growth in nanocrystalline Al*, Scripta Materialia, 55 (2006), pp. 649–652.
- [77] A. GOODRICH, P. HACKE, Q. WANG, B. SOPORI, R. MARGOLIS, T. L. JAMES, AND M. WOODHOUSE, *A wafer-based monocrystalline silicon photovoltaics road map: Utilizing known technology improvement opportunities for further reductions in manufacturing costs*, Solar Energy Materials and Solar Cells, 114 (2013), pp. 110–135.
- [78] S. GRAVIER, M. COULOMBIER, A. SAFI, N. ANDRÉ, A. BOÉ, J. P. RASKIN, AND T. PARDOEN, *New on-chip nanomechanical testing laboratory - Applications to aluminum and polysilicon thin films*, Journal of Microelectromechanical Systems, 18 (2009), pp. 555–569.

Bibliography

- [79] J. R. GREER AND W. D. NIX, *Nanoscale gold pillars strengthened through dislocation starvation*, Physical Review B - Condensed Matter and Materials Physics, 73 (2006), pp. 1–6.
- [80] S. GROH, *Computational Materials Science*, 2013.
- [81] P. GUMBSCH, K. ALBE, K. LU, H. HAHN, AND H. GLEITER, *The interaction mechanism of screw dislocations with coherent twin boundaries in different face-centred cubic metals*, Scripta Materialia, 54 (2006), pp. 1163–1168.
- [82] W. S. H. ALEXANDER, R. LABUSCH, *No*, Solid state Communications, 3 (1965), p. 357.
- [83] H. HAHN, P. MONDAL, AND K. PADMANABHAN, *Plastic deformation of nanocrystalline materials*, Nanostructured Materials, 9 (1997), pp. 603–606.
- [84] C. S. HAN, H. GAO, Y. HUANG, AND W. D. NIX, *Mechanism-based strain gradient crystal plasticity - II. Analysis*, Journal of the Mechanics and Physics of Solids, 53 (2005), pp. 1204–1222.
- [85] C.-S. HAN, H. GAO, Y. HUANG, AND W. D. NIX, *Mechanism-based strain gradient crystal plasticity—I. Theory*, Journal of the Mechanics and Physics of Solids, 53 (2005), pp. 1188–1203.
- [86] B. L. HANSEN, C. A. BRONKHORST, AND M. ORTIZ, *Dislocation subgrain structures and modeling the plastic hardening of metallic single crystals*, Modelling and Simulation in Materials Science and Engineering, 18 (2010), p. 42.
- [87] B. A. HARTMAIER, M. J. BUEHLER, AND H. GAO, *Multiscale Modeling of Deformation in Polycrystalline Thin Metal Films on Substrates*, Advanced Engineering Materials, (2005), pp. 1–5.
- [88] A. J. HASLAM, D. MOLDOVAN, V. YAMAKOV, D. WOLF, S. R. PHILLPOT, AND H. GLEITER, *Stress-enhanced grain growth in a nanocrystalline material by molecular-dynamics simulation*, Acta Materialia, 51 (2003), pp. 2097–2112.
- [89] P. B. HIRSCH, *Electronic and Mechanical Properties of Dislocations in Semiconductors*, MRS Proceedings, 2 (1980), pp. 3–12.

-
- [90] H. HONNEFF, H. AND MECKING, *A method for the determination of the active slip systems and orientation changes during single crystal deformation*, Proceeding of ICOTOM5, (1978), p. 265.
- [91] A. M. HUSSEIN, S. I. RAO, M. D. UCHIC, D. M. DIMIDUK, AND J. A. EL-AWADY, *Microstructurally based cross-slip mechanisms and their effects on dislocation microstructure evolution in fcc crystals*, Acta Materialia, 85 (2015), pp. 180–190.
- [92] HUNG-JUN CHANG, *Analysis of Nano indentation Size effect based on Dislocation Dynamics and Crystal Plasticity*, PhD thesis, INP Grenoble, 2009.
- [93] H. IDRISSE, B. WANG, J. P. RASKIN, D. SCHRYVERS, AND T. PARDOEN, *Ultrahigh Strain Hardening in Thin Palladium Films with Nanoscale Twins*, Materials Views, (2011), pp. 2119–2122.
- [94] F. IKER, N. ANDRE, T. PARDOEN, AND J. P. RASKIN, *Three-Dimensional Self-Assembled Sensors in Thin-Film SOI Technology*, Journal of Microelectromechanical Systems, 15 (2006), pp. 1687–1697.
- [95] J. A. RAYNE, *Elastic Constants of Palladium from 4.2-300K*, Magnetic properties of Tm metal, 502 (1960).
- [96] J. W. CHRISTIAN AND S. MAHAJAN, *Deformation twinning*, Progress in Materials Science, 39 (1995), pp. 1–157.
- [97] K. JONNALAGADDA, N. KARANJGAOKAR, I. CHASIOTIS, J. CHEE, AND D. PEROULIS, *Strain rate sensitivity of nanocrystalline Au films at room temperature*, Acta Materialia, 58 (2010), pp. 4674–4684.
- [98] P. D. & M. F. JULIETTE CHEVY , FRANÇOIS LOUCHET, *Creep behaviour of ice single crystals loaded in torsion explained by dislocation cross-slip*, Philosophical Magazine Letters, (2012), pp. 262–269.
- [99] J. KACHER, B. P. EFTINK, B. CUI, AND I. M. ROBERTSON, *Dislocation interactions with grain boundaries*, Current Opinion in Solid State & Materials Science, 18 (2014), pp. 227–243.
- [100] M. M. KIVAMBE, G. STOKKAN, T. ERVIK, B. RYNINGEN, AND O. LOHNE, *The microstructure of dislocation clusters in industrial directionally solidified multicrystalline silicon*, Journal of Applied Physics, 110 (2011).

Bibliography

- [101] U. KOCKS AND C. H., *Slip geometry in partially constrained deformation*, Acta Metallurgica et Materialia, 30 (1982), p. 695.
- [102] U. F. KOCKS AND H. MECKING, *Physics and phenomenology of strain hardening: the FCC case*, Progress in Materials Science, 48 (2003), pp. 171–273.
- [103] U. F. KOCKS, C. N. TOMÉ, AND H.-R. WENK, *Texture and Anisotropy*, Cambridge university press, second ed., 1998.
- [104] M. D. KONING, R. J. KURTZ, V. V. BULATOV, C. H. HENAGER, R. G. HOAGLAND, W. CAI, AND M. NOMURA, *Modeling of dislocation–grain boundary interactions in FCC metals*, 323 (2003), pp. 281–289.
- [105] M. KOSŁOWSKI, *Effect of grain size distribution on plastic strain recovery*, Physical Review B, 82 (2010), pp. 1–5.
- [106] L. KUBIN, B. DEVINCRE, AND T. HOC, *Modeling dislocation storage rates and mean free paths in face-centered cubic crystals*, Acta Materialia, 56 (2008), pp. 6040–6049.
- [107] L. KUBIN, B. DEVINCRE, AND T. HOC, *Toward a physical model for strain hardening in fcc crystals*, Materials Science and Engineering: A, 483–484 (2008), pp. 19–24.
- [108] R. V. KUKTA, *PhD thesis*, PhD thesis, Brown University, 1998.
- [109] K. S. KUMAR, H. V. SWYGENHOVEN, AND S. SURESH, *Mechanical behavior of nanocrystalline metals and alloys*, Acta Materialia, 51 (2003), pp. 5743–5774.
- [110] R. KUMAR, F. SZÉKELY, AND E. V. D. GIESSEN, *Modelling dislocation transmission across tilt grain boundaries in 2D*, Computational Materials Science, 49 (2010), pp. 46–54.
- [111] A. N. L. NICOLA, Y. XIANG, J.J. VLASSAK, E. VAN DER GIESSEN, *Plastic deformation of freestanding thin films: Experiments and modeling*, Journal of the Mechanics and Physics of Solids, 54 (2006), pp. 2089–2110.
- [112] L. ZHANG AND C. LU, *A review on atomistic simulation of grain boundary behaviors in face-centered cubic metals*, Computational Materials Science, 118 (2016), pp. 180–191.

-
- [113] R. A. LEBENSOHN, *N-site modeling of a 3D viscoplastic polycrystal using Fast Fourier Transform*, Acta Materialia, 49 (2001), pp. 2723–2737.
- [114] R. A. LEBENSOHN, A. K. KANJARLA, AND P. EISENLOHR, *An elasto-viscoplastic formulation based on fast Fourier transforms for the prediction of micromechanical fields in polycrystalline materials*, International Journal of Plasticity, 32-33 (2012), pp. 59–69.
- [115] R. A. LEBENSOHN AND C. N. TOMÉ, *A self-consistent viscoplastic model: prediction of rolling textures of anisotropic polycrystals*, Materials Science and Engineering A, 175 (1994), pp. 71–82.
- [116] S.-W. LEE, S. AUBRY, W. D. NIX, AND W. CAI, *Dislocation junctions and jogs in a free-standing FCC thin film*, Modelling and Simulation in Materials Science and Engineering, (2010), pp. 1–28.
- [117] M. LEGROS, D. S. GIANOLA, AND K. J. HEMKER, *In situ TEM observations of fast grain-boundary motion in stressed nanocrystalline aluminum films*, Acta Materialia, 56 (2008), pp. 3380–3393.
- [118] P. LEJČEK AND S. HOFMANN, *Thermodynamics of Grain Boundary Segregation and Applications to Anisotropy, Compensation Effect and Prediction*, Critical Reviews in Solid State and Materials Sciences, 33 (2008), pp. 133–163.
- [119] G. LEMOINE, L. DELANNAY, H. IDRISSE, AND T. PARDOEN, *Dislocation and back stress dominated viscoplasticity in freestanding sub-micron Pd films*, Acta Materialia, 111 (2016), pp. 10–21.
- [120] R. LESAR AND J. M. RICKMAN, *Multipole expansion of dislocation interactions: Application to discrete dislocations*, Physical Review B, 65 (2002), p. 144110.
- [121] Z. LI, C. HOU, M. HUANG, AND C. OUYANG, *Strengthening mechanism in micro-polycrystals with penetrable grain boundaries by discrete dislocation dynamics simulation and Hall–Petch effect*, Computational Materials Science, 46 (2009), pp. 1124–1134.
- [122] L. LIM AND R. RAJ, *Interaction between lattice and grain boundary dislocations and their role in mechanical properties of interfaces*, Journal of Physics, 46 (1985), pp. 581–595.

Bibliography

- [123] B. LIU, P. EISENLOHR, F. ROTERS, AND D. RAABE, *Simulation of dislocation penetration through a general low-angle grain boundary*, Acta Materialia, 60 (2012), pp. 5380–5390.
- [124] J. P. H. LOTHE AND JENS, *Theory of dislocations*, Krieger Pub. Co., Malabar, FL, 1992.
- [125] L. J. C. M., *Stress field of a dislocation segment*, Philosophical Magazine, 10 (1964), pp. 1097–1098.
- [126] M. COULOMBIER, *Nanomechanical lab on-chip for testing thin film materials and application to Al and Al (Si)*, PhD thesis, Université catholique de Louvain, 2012.
- [127] M. PEACH AND J. S. KOEHLER, *The forces exerted on dislocations and stress fields produced by them*, Physical Review, 80 (1950), pp. 436–439.
- [128] M. A. MEYERS, A. MISHRA, AND D. J. BENSON, *Mechanical properties of nanocrystalline materials*, Progress in Materials Science, 51 (2006), pp. 427–556.
- [129] D. MORDEHAI, Y. ASHKENAZY, I. KELSON, AND G. MAKOV, *Dynamic properties of screw dislocations in Cu: A molecular dynamics study*, Physical Review B, 67 (2003), pp. 1–9.
- [130] J. W. MORRIS, *Chapter 4 : Defects in Crystals*, Materials Science, (2007), pp. 76–107.
- [131] C. MOTZ, D. WEYGAND, J. SENGER, AND P. GUMBSCH, *Initial dislocation structures in 3-D discrete dislocation dynamics and their influence on microscale plasticity*, Acta Materialia, 57 (2009), pp. 1744–1754.
- [132] MPI FORUM, *Message Passing Interface (MPI) Forum*. <http://www.mpi-forum.org>, 2009.
- [133] N. OHNO AND D. OKUMURA, *Higher-order stress and grain size effects due to self-energy of geometrically necessary dislocations*, Journal of the Mechanics and Physics of Solids, 55 (2007), pp. 1879–1898.
- [134] A. NEEDLEMAN AND ERIK VAN DER GIESSEN, *Discrete dislocation plasticity: a simple planar model*, Modelling and Simulation in Materials Science and Engineering, 3 (1995), pp. 689–735.

-
- [135] J. NICKOLLS, I. BUCK, M. GARLAND, AND K. SKADRON, *Scalable parallel programming with CUDA*, AMC Queue, 6 (2008), pp. 40–53.
- [136] L. NICOLA, E. VAN DER GIESSEN, AND A. NEEDLEMAN, *Plasticity in polycrystalline thin films: A 2D dislocation dynamics approach*, (2003), pp. 159–163.
- [137] NOBUHIRO TSUJI, *Bulk nanostructured metals*.
- [138] F. NYE, *Some geometrical relations in Dislocated crystals*, Acta Materialia, 1 (1952).
- [139] T. PARDOEN, *Size and rate dependent necking in thin metallic films*, Journal of the Mechanics and Physics of Solids, 62 (2014), pp. 81–98.
- [140] T. PARDOEN AND T. J. MASSART, *Interface controlled plastic flow modelled by strain gradient plasticity theory*, Comptes Rendus Mecanique, 340 (2012), pp. 247–260.
- [141] T. A. PARTHASARATHY, S. I. RAO, D. M. DIMIDUK, M. D. UCHIC, AND D. R. TRINKLE, *Contribution to size effect of yield strength from the stochastics of dislocation source lengths in finite samples*, Scripta Materialia, 56 (2007), pp. 313–316.
- [142] J. PHILIBERT, *Dislocations et d’eformation plastique (Ecole d’ete d’Yrivals)*, 1979.
- [143] M. PIPPIG, *PFFT-An extension of FFTW to massively parallel architectures*, SIAM Journal on Scientific Computing, 35 (2013), pp. 213–236.
- [144] A. PRAKASH, S. M. WEYGAND, AND H. RIEDEL, *Computational Materials Science*, Compu, 45 (2009), pp. 744–750.
- [145] W. PU, *Models for dislocation cross-slip in close-packed crystal structures: a critical review*, Progress in Materials Science, 47 (2002), pp. 415–461.
- [146] A. RAHMAN AND F. H. STILLINGER, *Propagation of sound in water. a molecular-dynamics study*, Phys. Rev. A, 10 (1974), pp. 368–378.
- [147] V. RANDLE, *Overview no. 127 the role of the grain boundary plane in cubic polycrystals*, 46 (1997), pp. 1459–1480.

Bibliography

- [148] S. RAO, D. DIMIDUK, J. EL-AWADY, T. PARTHASARATHY, M. UCHIC, AND C. WOODWARD, *Spontaneous athermal cross-slip nucleation at screw dislocation intersections in FCC metals and L1 2 intermetallics investigated via atomistic simulations*, Philosophical Magazine, 93 (2013), pp. 3012–3028.
- [149] S. RAO, T. A. PARTHASARATHY, AND C. WOODWARD, *Atomistic simulation of cross-slip processes in model fcc structures*, Philosophical Magazine A, 79 (1999), pp. 1167–1192.
- [150] S. I. RAO, D. M. DIMIDUK, T. A. PARTHASARATHY, J. EL-AWADY, C. WOODWARD, AND M. D. UCHIC, *Calculations of intersection cross-slip activation energies in fcc metals using nudged elastic band method*, Acta Materialia, 59 (2011), pp. 7135–7144.
- [151] W. J. READ, *CXXIV. Statistics of the occupation of dislocation acceptor centres*, Philosophical Magazine and Journal of Science, 45 (1954), pp. 1119–1128.
- [152] J. READ, W.T, *Theory of dislocations in germanium*, Philosophical Magazine Series 7, 7 (1954), pp. 775–796.
- [153] B. D. RONAN MADEC, L.P. KUBIN, *Dislocation Intersections and Reactions in FCC and BCC Crystals*, Materials Research Society, 779 (2003), pp. 1–12.
- [154] F. ROTERS, *Advanced Material Models for the Crystal Plasticity Finite Element Method*, PhD thesis, 2011.
- [155] W. P. K. A. A. RYAN B. SILLS AND W. CAI, *Fundamentals of Dislocation Dynamics Simulations*.
- [156] I. RYU, W. CAI, W. D. NIX, AND H. GAO, *Anisotropic Size-Dependent Plasticity in Face-Centered Cubic Micropillars Under Torsion*, Journal of Mineral, Metals and Materials Society, 68 (2016), pp. 253–260.
- [157] SATYENDRA, *Twinning induced plasticity steels*, 2014.
- [158] R. SCHWAIGER, B. MOSER, M. DAO, N. CHOLLACOOP, AND S. SURESH, *Some critical experiments on the strain-rate sensitivity of nanocrystalline nickel*, Acta Materialia, 51 (2003), pp. 5159–5172.
- [159] J. SENGER, D. WEYGAND, P. GUMBSCH, AND O. KRAFT, *Discrete dislocation simulations of the plasticity of micro-pillars under uniaxial loading*, Scripta Materialia, 58 (2008), pp. 587–590.

-
- [160] J. SENGER, D. WEYGAND, C. MOTZ, P. GUMBSCH, AND O. KRAFT, *Aspect ratio and stochastic effects in the plasticity of uniformly loaded micrometer-sized specimens*, Acta Materialia, 59 (2011), pp. 2937–2947.
- [161] J. G. SEVILLANO, I. ALDAZABAL, A. LUQUE, AND J. ALDAZABAL, *Atomistic simulation of the elongation response of a $\langle 011 \rangle$ oriented columnar nano-grain bcc Fe polycrystalline sample*, Meccanica, 51 (2016), pp. 401–413.
- [162] R. SHARPE, W.N., J., YUAN, B., AND EDWARDS, *A new technique for measuring the mechanical properties of thin films.*, Journal of Microelectromechanical Systems, 6 (1997), pp. 193–199.
- [163] Z. SHEN, R. H. WAGONER, AND W. A. T. CLARK, *Dislocation and grain boundary interactions in metals*, Acta Materialia, 36 (1988), pp. 3231–3242.
- [164] C. S. SHIN, M. C. FIVEL, M. VERDIER, AND S. C. KWON, *Numerical methods to improve the computing efficiency of discrete dislocation dynamics simulations*, 215 (2006), pp. 417–429.
- [165] S. S. SHISHVAN AND E. V. D. GIESSEN, *Distribution of dislocation source length and the size dependent yield strength in freestanding thin films*, Journal of the Mechanics and Physics of Solids, 58 (2010), pp. 678–695.
- [166] S. M. SPEARING, *Materials issues in microelectromechanical systems (MEMS)*, Acta Materialia, 48 (2000), pp. 179–196.
- [167] M. STRICKER AND D. WEYGAND, *Dislocation multiplication mechanisms - Glissile junctions and their role on the plastic deformation at the microscale*, Acta Materialia, 99 (2015), pp. 130–139.
- [168] Y. SUN AND J. A. ROGERS, *Inorganic semiconductors for flexible electronics*, Advanced Materials, 19 (2007), pp. 1897–1916.
- [169] R. W. SUTTON, A. P., & BALLUFFI, *Interfaces in crystalline materials*, Clarendon Press, Oxford, 1995.
- [170] H. V. SWYGENHOVEN AND D. CARO, A FARKAS, *A molecular dynamics study of polycrystalline fcc metals at the nanoscale: grain boundary structure and its influence on plastic deformation*, Materials Science and Engineering, A309-310 (2001), pp. 440–444.
- [171] H. V. SWYGENHOVEN AND J. R. WEERTMAN, *Deformation in nanocrystalline metals*, Review feature, 9 (2006), pp. 24–31.

Bibliography

- [172] V. TAUPIN, C. FRESSENGEAS, P. VENTURA, M. LEBYODKIN, AND V. GORNAKOV, *A field theory of piezoelectric media containing dislocations*, Journal of Applied Physics, 115 (2014).
- [173] G. I. TAYLOR, *Plastic strain in metals*, tech. rep., 1938.
- [174] I. TECHNOLOGIEPARK AND T. UNIVERSIT, *Potential and Limitations of Electron Holography in Silicon Research P. Formanek 1,2*, Solid state Phenomena, 109 (2005), pp. 603–608.
- [175] N. THOMPSON, *Dislocation Nodes in Face-Centred Cubic Lattices*, Proceedings of the Physical Society. Section B, 66 (1953), pp. 481–492.
- [176] D. D. TJAHAJANTO, S. TURTELTAUB, A. S. J. SUIKER, AND S. VAN DER ZWAAG, *Modelling of the effects of grain orientation on transformation-induced plasticity in multiphase carbon steels*, Modelling and Simulation in Materials Science and Engineering, 14 (2006), p. 617.
- [177] H. A. M. TRAN H-S, TUMMALA H, DUCHÊNE L., PÉRON-LÜHRS V., FIVEL M., *Interaction between Dislocation and Coherent Twin Boundary by QuasiContinuum model*, in XIII International Conference on Computational Plasticity. Fundamentals and Applications COMPLAS XIII, D. P. E. Oñate, D.R.J. Owen and M. C. (Eds), eds., 2015.
- [178] M. D. UCHIC, D. M. DIMIDUK, J. N. FLORANDO, AND W. D. NIX, *Sample dimensions influence strength and crystal plasticity*, Science, 305 (2004), pp. 986–989.
- [179] M. D. UCHIC, P. A. SHADE, AND D. M. DIMIDUK, *Plasticity of Micrometer-Scale Single Crystals in Compression*, Annual Review of Materials Research, 39 (2009), pp. 361–386.
- [180] UNIVERSITY OF LIVERPOOL, www.matter.org.uk.
- [181] P. VAN HOUTTE, L. D. AND, AND I. SAMAJDAR, *Quantitative prediction of cold rolling textures in lo-carbon steel by means of the lamel model*, Textures and Microstructures, 31 (1999), pp. 109–149.
- [182] P. VAN HOUTTE AND L. DELANNAY, *Influence of Local Lattice Orientation on Grain Subdivision in 40% Cold-Rolled Aluminium*, in Local Lattice Rotations and Disclinations in Microstructures of Distorted Crystalline Materials, vol. 87 of Solid State Phenomena, Trans Tech Publications, 2002, pp. 157–162.

-
- [183] P. VAN HOUTTE, A. K. KANJARLA, A. VAN BAEL, M. SEEFELDT, AND L. DELANNAY, *Multiscale modelling of the plastic anisotropy and deformation texture of polycrystalline materials*, European Journal of Mechanics, A/Solids, 25 (2006), pp. 634–648.
- [184] A. VATTRÉ, B. DEVINCRE, F. FEYEL, R. GATTI, S. GROH, O. JAMOND, AND A. ROOS, *Modelling crystal plasticity by 3D dislocation dynamics and the finite element method: The Discrete-Continuous Model revisited*, Journal of the Mechanics and Physics of Solids, 63 (2014), pp. 491–505.
- [185] M. VERDIER, *Une étude de la restauration dans des alliages Al-Mg*, PhD thesis, INP Grenoble, 1996.
- [186] M. VERDIER, M. M. FIVEL, AND I. GROMA, *Mesosopic scale simulation of dislocation dynamics in fcc metals: Principles and applications*, Modelling and Simulation in Materials Science and Engineering, 6 (1998), pp. 755–770.
- [187] B. VON BLANCKENHAGEN, E. ARZT, AND P. GUMBSCH, *3D simulation of the dislocation dynamics in polycrystalline metal thin films*, Materials Research Society, 779 (2003), pp. 1–12.
- [188] W. T. READ AND W. SHOCKLEY, *Dislocation models of crystal grain boundaries*, Physical Review, 75 (1950).
- [189] B. WANG, H. IDRISI, M. GALCERAN, M. S. COLLA, S. TURNER, S. HUI, J. P. RASKIN, T. PARDOEN, S. GODET, AND D. SCHRYVERS, *Advanced TEM investigation of the plasticity mechanisms in nanocrystalline freestanding palladium films with nanoscale twins*, International Journal of Plasticity, 37 (2012), pp. 140–156.
- [190] B. WANG, H. IDRISI, H. SHI, M. S. COLLA, S. MICHOTTE, J. P. RASKIN, T. PARDOEN, AND D. SCHRYVERS, *Texture-dependent twin formation in nanocrystalline thin Pd films*, Scripta Materialia, 66 (2012), pp. 866–871.
- [191] Z. WANG, N. GHONIEM, AND R. LESAR, *Multipole representation of the elastic field of dislocation ensembles*, Physical Review, 69 (2004), pp. 1–7.
- [192] D. WEYGAND, L. H. FRIEDMAN, E. VAN DER GIESSEN, AND A. NEEDLEMAN, *Discrete dislocation modeling in three-dimensional confined volumes*, Materials Science and Engineering A, 309-310 (2001), pp. 420–424.

Bibliography

- [193] D. WEYGAND, J. SENGER, C. MOTZ, W. AUGUSTIN, AND V. HEUVELINE, *High Performance Computing and Discrete Dislocation Dynamics : Plasticity of Micrometer sized specimens*.
- [194] D. WOLF, V. YAMAKOV, S. R. PHILLPOT, A. MUKHERJEE, AND H. GLEITER, *Deformation of nanocrystalline materials by molecular-dynamics simulation: relationship to experiments?*, *Acta Materialia*, 53 (2005), pp. 1–40.
- [195] Z. X. WU, Y. W. ZHANG, AND D. J. SROLOVITZ, *Dislocation–twin interaction mechanisms for ultrahigh strength and ductility in nanotwinned metals*, *Acta Materialia*, 57 (2009), pp. 4508–4518.
- [196] V. YAMAKOV, D. WOLF, S. R. PHILLPOT, AND H. GLEITER, *Grain-boundary diffusion creep in nanocrystalline palladium by molecular-dynamics simulation*, *Acta Materialia*, 50 (2002), pp. 61–73.
- [197] S. YEFIMOV AND E. VAN DER GIESSEN, *Multiple slip in a strain-gradient plasticity model motivated by a statistical-mechanics description of dislocations*, *International Journal of Solids and Structures*, 42 (2005), pp. 3375–3394.
- [198] N. YOSHINAGA, N. SUGIURA, S. HIWATASHI, K. USHIODA, AND O. KADA, *Deep Drawability of Electro-deposited Pure Iron Having an Extremely Sharp $\langle 111 \rangle$ //ND Texture*, *ISIJ International*, 48 (2008), pp. 667–670.
- [199] S. X. M. Z. SHAN, E. A. STACH, J. M. K. WIEZOREK, J. A. KNAPP, D. M. FOLLSTAEDT, *Grian Boundary-mediated Plasticity in Nanocrystalline Nickel*, Tech. Rep. July, 2004.
- [200] H. M. ZBIB, M. RHEE, AND J. P. HIRTH, *On plastic deformation and the dynamics of 3D dislocations*, *International journal of mech. Sci*, 40 (1998), pp. 113–127.
- [201] X. ZHANG, H. WANG, R. O. SCATTERGOOD, J. NARAYAN, AND C. C. KOCH, *Evolution of microstructure and mechanical properties of in situ consolidated bulk ultra-fine-grained and nanocrystalline Zn prepared by ball milling*, *Materials Science and Engineering A*, 344 (2003), pp. 175–181.
- [202] C. ZHOU AND R. LESAR, *Dislocation dynamics simulations of plasticity in polycrystalline thin films*, *International Journal of Plasticity*, 30-31 (2012), pp. 185–201.

- [203] L. ZHU, H. RUAN, X. LI, M. DAO, H. GAO, AND J. LU, *Modeling grain size dependent optimal twin spacing for achieving ultimate high strength and related high ductility in nanotwinned metals*, *Acta Materialia*, 59 (2011), pp. 5544–5557.
- [204] Y. T. ZHU, X. Z. LIAO, AND X. L. WU, *Deformation twinning in nanocrystalline materials*, *Progress in Materials Science*, 57 (2012), pp. 1–62.

Nomenclature

$\Delta\theta$	misorientation
2D DDD	Two Dimensional Discrete Dislocation Dynamics
3D DDD	Three Dimensional Discrete Dislocation Dynamics
Å	Angstrom
ACOM TEM	Automated Crystallographic Orientation indexation in a TEM
Al	aluminium
API	Application Program Interface
BCC	Body Centered Cubic
BVP	Boundary Value Problem
CP	Crystal Plasticity
CTB	Coherent Twin Boundary
DC	Diamond Cubic
DD	Dislocation Dynamics
DFT	Density Function Theory
DOF	Degrees of Freedom
EPR	Electron Paramagnetic Resonance
FC	Fully Constraint
FCC	Face Centered Cubic
FFT	Fast Fourier Transform
FIB	Focused Ion Beam

Bibliography

FMM	Fast Multi-pole Method
FR	Frank-Read
GB	Grain Boundary
GPU	Graphical Processing Unit
HAGB	High Angle Grain Boundary
HCP	Hexagonal Close Packed
HRTEM	High Resolution TEM
LAGB	Low Angle Grain Boundary
LPCVD	Low Pressure Chemical Vapour Deposition
MD	Molecular Dynamics
micron	micrometer
MPI	Message Passing Interface
Ni	nickel
nm	nanometer
NPT	constant number(N), pressure(P), and temperature(T)
NVE	constant number(N), volume(V), and energy(E)
NVT	constant number(N), volume(V), and temperature(T)
OpenMP	Open Multi-Processing
PBC	Periodic Boundary Condition
Pd	palladium
PECVD	Plasma Enhanced Chemical Vapour Deposition
PV	Photo Voltaic
QC	Quasicontinuum
RC	Relaxed Constraint

RDL	Resultant Dislocation Loop
sccm	Standard Cubic Centimetres per Minute
SGCP	Strain gradient crystal plasticity
Si	silicon
VPSC	Visco-Plastic Self Consistent

List of Figures

1.1	Slip traces on the free surface of a bicrystal with (a) $\Delta\theta = 0^\circ$; (b) $\Delta\theta = 20^\circ$ [122]	9
1.2	Schematic representation of (a) coherent, (b) semi-coherent and (c) incoherent interfaces, respectively [180]	10
1.3	(a) Grain boundaries in a polycrystal; (b) An example atomic arrangement at triple junction [137]	11
1.4	Crystallography of a grain boundary [118]	12
1.5	Schematic representation of a pure tilt and a pure twist boundary in a bicrystal [118]	13
1.6	Grain boundary energy versus disorientation angle in Ni [67]	14
1.7	Stacking sequence of a perfect crystal and a twinned crystal <i>modified from</i> [157]	15
1.8	Sketches of possible dislocation mechanisms for slip propagation across interface [163]	16
1.9	Schematic view of dislocation transmission explained using de Koning's line tension model [202]	18
1.10	(a) A low angle symmetric tilt boundary represented as a wall of edge dislocations; (b) dislocation spacing vs misorientation angle [188]	19
1.11	A 60° boundary showing equivalence of $\psi = 0^\circ$ and $\psi = 45^\circ$ models and relationship to imperfect (210) surfaces [188]	20
2.1	Schematics of on-chip tensile testing technique [33]	26
2.2	Steps involved in the fabrication of Pd thin film	27

List of Figures

2.3	Test specimen of different lengths on a substrate	29
2.4	Stress-strain curves of (a) 80nm, (b) 160nm and (c) 310 nm, respectively	29
2.5	Stress-strain curves after smoothing and interpolation, the Pd films are covered with a few nm thick Cr layer	30
2.6	Stress-strain curves of free-standing, unpassivated films (90, 200, 410 nm thickness)	30
2.7	Microstructure of the as-deposited Pd film [31]	31
2.8	Grain width distribution and grain height distribution derived from the cross-section analysis of three film thickness [31]	31
2.9	(a) Average dislocation density vs time; (b-d) Changes in the dislocation positions with time [31]	32
2.10	Twin boundary thickness evolution upon relaxation [31]	33
3.1	Different numerical tools at different length- and time- scales [80] .	37
3.2	Different numerical models for thin film modeling (a) atomistics [161], (b) dislocation dynamics and (c) 2D crystal plasticity model [119], respectively	38
3.3	Schmid law explained using a cylindrical grain deformed under tension along the tensile axis [180]	40
3.4	Schematic representation of reference, intermediate and current configurations based on multiplicative decomposition of the deformation gradient tensor	42
4.1	Edge-Screw based discretization of a curved dislocation line [27] . .	51
4.2	Notation adapted for calculating stress field of a dislocation	52
4.3	A Frank-Read source in a 2D system with periodic boundary condition	54
4.4	Superposition principle used to deal with complex boundary conditions	55

4.5	Dislocation motion by breaking and making bonds [36]	57
4.6	Schematics of neighbouring segments (orange color) used to find the angle between Burgers vector and line vector; which inturn is used for line tension calculating	58
4.7	Annihilation: Dislocation i detects dislocation j of same Burgers vector but opposite sign (vice-versa possible)	60
4.8	Cross-slip of a screw segment	61
4.9	Bicrystal with grains in different orientations separated by grain boundary; lattice orientation being represented by a coloured texture object	62
4.10	Pileup of dislocations against a grain boundary	62
4.11	Schematic view of a Glissile loop being placed at corresponding lattice point in Grain2 (to mimic transmission) after hitting the grain boundary	64
4.12	Schematic view CTB setup with texture objects representing the lattice orientation of grains	64
4.13	Schematic view slip planes corresponding to \mathbf{b}_1 in Grain1 and Grain2 of the Bicrystal	64
4.14	Thompson tetrahedron representing all the slip planes and vectors in a FCC crystal	65
4.15	Schematic view of a double Thompson tetrahedron with (111) common slip plane	65
4.16	Pileup against the CTB (for $RSS < \tau_{gb}^c$) at step P	66
4.17	Stress field on the CTB due to pileup at step P	66
4.18	Slip transmission across CTB (for $RSS > \tau_{gb}^c$) at step P+T₁	66
4.19	Stress field on the CTB after transmission at step P+T₁	66
4.20	Slip transmission across CTB (for $RSS > \tau_{gb}^c$) at step P+T₂	67

List of Figures

4.21	Stress field on the CTB after transmission at step $P+T_2$	67
4.22	Slip transmission across CTB (for $RSS > \tau_{gb}^c$) at step $P+T_3$	67
4.23	Stress field on the CTB after transmission at step $P+T_3$	67
4.24	Distance between subsequent loops in a pileup (Edge and Screw segments in red and blue colors, respectively)	68
4.25	Slip transmission across CTB at step $P+T_1$	68
4.26	Slip transmission across CTB at step $P+T_2$	68
4.27	Slip transmission across CTB at step $P+T_3$	69
4.28	Slip transmission across CTB at step $P+T_4$	69
4.29	Directionality test with initial dislocation source of Burgers vector ($\mathbf{b} = \mathbf{b}_1^{(1)}$) in Grain1	70
4.30	Directionality test with initial dislocation source of Burgers vector ($\mathbf{b} = \mathbf{b}_1^{(2)}$) in Grain1	70
4.31	Directionality test with initial dislocation source of Burgers vector ($\mathbf{b} = \mathbf{b}_1^{(3)}$) in Grain2	71
4.32	Directionality test with initial dislocation source of Burgers vector ($\mathbf{b} = \mathbf{b}_1^{(4)}$) in Grain2	71
4.33	<i>In situ</i> TEM image showing the absorption and emission of dislocation across CTB in Cu [28]	72
4.34	Bicrystal indicating the introduced general convention of the grain size (D) and dislocation segment length (DL)	73
4.35	Comparison of number of loops in pileup (modified pileup-based formula Vs DDD results) [177]	74
4.36	<i>In situ</i> TEM image showing dislocation propagation across CTB in $\alpha - Ti$ [99]	75

4.37 Schematic view highlighting the interface padding region of a general width= $iPad$	75
4.38 Snapshots taken during first and second transmission (for $iPad=10.xl$) along with the corresponding points on the stress-strain plots are also indicated	76
4.39 Snapshots taken during and after the third transmission (for $iPad=10.xl$) along with the corresponding points on the stress-strain plots are also indicated	77
4.40 <i>In situ</i> TEM image showing succession of cross slip events indicated by directional arrow ($a-e$) and final transmission across grain boundary in f in $\alpha - Ti$ [99])	77
4.41 First dislocation loop attached to the grain boundary; whereas the subsequent dislocation loops (2nd and 3rd) begin cross slipped	78
4.42 Dislocation transmission across CTB after subsequent cross slip events in the parent grain	79
4.43 3D dislocation dynamics algorithm explained based on a bicrystal geometry	81
4.44 Schematic view of the 2D box approach to segregate short- and long-range dislocation interactions	82
4.45 Side and Top views of the initial static configuration considered, respectively	84
4.46 Side and Top views of σ_{xx} component of the internal stress field	84
4.47 Side and Top views of σ_{xy} component of the internal stress field	85
4.48 Side and Top views of σ_{yy} component of the internal stress field	85
4.49 Side and Top views of σ_{zz} component of the internal stress field	86
4.50 Comparison of different components of stress field calculated at the center of each segments in the dislocation loop shown in Figure 4.45	86

List of Figures

4.51 (a) Activation stress of an edge dislocation as a function of the discretization ratio (b) Activation stress as a function of the source length with discretization ratio of 10 [155]	87
4.52 Swept area by a dislocation segment of length l	88
5.1 Cross-sectional TEM image of a 310-nm-thick Pd film [93]	94
5.2 Sphere (AR=1.0); Kacahuete (AR=2.5) and Cigar (AR=5.0)	98
5.3 Schematic shows a.) a Cigar grain in rotated configuration inside a cubic simulation volume in reference frame and b.) the Cigar grain with the axes data imported from crystal plasticity	99
5.4 Stress tensor imported from CP model being expressed in principle axes	100
5.5 Dislocation activity without cross slip in Sphere	101
5.6 Dislocation activity with cross slip in Sphere	101
5.7 Schematics of slip systems "Long path" (LP) and "Collinear1" (CP1) in Sphere (AR=1.0); Kachuete (AR=2.5) and Cigar (AR=5.0) grains, respectively	103
5.8 Randomized initial dislocation source realization (RR 05) in Sphere (AR=1.0); Kacahuete (AR=2.5) and Cigar (AR=5.0) grains with only the four most active slip systems being highlighted	104
5.9 Tangential hyperbolic monitoring (change in stress increment and stress with no.of steps)	105
5.10 Snapshot of dislocation slip activity on four most active slip systems in Sphere grain at $\varepsilon_{eq}^p = 4.10^{-4}$	106
5.11 Different dislocation slip activity on four most active slip systems in Sphere grain	106
5.12 Schematics showing (a) Short-range and long-range contributions; (b) Directionality of long-range interaction [43]	107

5.13 Single dislocation source on "Long path" located at the center of Sphere grain 108

5.14 Long-range stress field due to dislocations in the pileup hindering further activation of the initial dislocation source on "Long path" located at the center of Sphere grain 109

5.15 Kinematic hardening slope of the unloading part of the stress-strain curve as a measure of backstress on "Long path" in Sphere grain . . 110

5.16 Plastic response of sphere, kachahute and cigar with no cross slip . . 111

5.17 Schematic drawing of a slip plane of "long path" (blue) and "deviate of long path" (red) passing through the center of the Cigar grain . . 112

5.18 Dislocation microstructure at step 1070 in Cigar grain 113

5.19 Region of interest at step 1070 in Cigar grain 113

5.20 Evolution of dislocation microstructure on "long path" and "deviate of long path" in Cigar grain 113

5.21 Comparison of equivalent stress versus plastic strain response in (a) Sphere, (b) Kacahuete and (c) Cigar grains, respectively at different critical cross slip stresses (CS1, CS2 and CS3) 116

5.22 (a) Comparison of equivalent plastic strain of Sphere, Kacahuete and Cigar at equivalent stress $\sigma_{eq} = 50MPa$; (b) Extraction of equivalent plastic strain values for Cigar grain 116

5.23 Comparison of plastic deformation behavior on highly active slip systems and their corresponding deviates in Sphere at CS1 and CS3, respectively 118

5.24 Comparison in terms of plastic deformation behavior on highly active slip systems and their corresponding deviates in Cigars at CS1 and CS3, respectively 119

5.25 Variation of σ_{eq} with γ_p involving an unloading step to quantify back stress whose magnitude is represented by the slope on "long path" (blue) of Sphere, Kacahuete and Cigar grains 120

List of Figures

5.26	Average back stresses on slip system of interest in Sphere, Kacahuete and Cigar grains at CS3; Labels are presented as abbreviation of the prescribed new names along with the Schmid factor, primary and deviate angles triad	121
5.27	Rearranged average back stresses on slip system of interest in Sphere, Kacahuete and Cigar grains at CS3	121
5.28	Dislocation microstructure in Cigar grain at critical cross slip stress of CS3=160MPa in "long path", "short path" and "collinear1" and their respective deviates	122
5.29	Average back stresses on slip system of interest in sphere, kacahuete and cigar at CS2; Labels are presented as abbreviation of the prescribed new names along with the Schmid factor, primary and deviate angles triad	123
5.30	Rearranged average back stresses on slip system of interest in sphere, kacahuete and cigar at CS2	124
5.31	Comparison of DD (centred) results against extended pileup model a.) without cross-slip and b.) with cross-slip	126
5.32	Non-centred plane with cross-slip(CS2=80MPa)	126
5.33	Comparison of DD (non-centred) results against extended pileup model	126
6.1	Model plot showing transition in deformation mechanisms when changing the grain size	130
6.2	(a.) Bright field image obtained on the cross-sectional FIB sample; (b.) Region of interest for modeling thin film behavior being highlighted in red [31,93]	133
6.3	(a.) Side view and (b.) Top view of the periodic (X- and Y-directions) polycrystal microstructure generated by Gmsh using Voronoi tessellation	134

6.4	(a.) Side view and (b.) Top view of the periodic (X- and Y-directions) polycrystal representing GBs as <i>facets</i>	135
6.5	Refined mesh created by Gmsh shown (a.) after importing to CASTEM (snapshot of the mesh from CASTEM) and (b.) corresponding mesh viewed using Paraview	136
6.6	(a.) Side view and (b.) Top view of the polycrystal with larger grain at the center of the film	136
6.7	(a.) Side view and (b.) Top view of the polycrystal with smaller grain at the center of the film	137
6.8	(a.) Side view and (b.) Top view of the polycrystal with cuboid-shaped texture objects representing the lattice orientation of each grain on which respective dislocations move	137
6.9	(a.) Side view and (b.) Top view of the polycrystal with initial dislocation configuration as Frank-Read sources of same length . . .	138
6.10	Total dislocation density plotted against number of steps during relaxation test	139
6.11	(a.) Side view and (b.) Top view of the polycrystal with relaxed dislocation configuration extracted at relaxation simulation step no.250 (<i>cf.</i> highlighted in Figure 6.10)	140
6.12	Top view of the initial FRs configuration in polycrystal with four hexagonal grains	143
6.13	Top view snapshots at different simulations steps showing validity of the grain identity scheme (PBC) in DD simulations	143
6.14	Side view of the (a) Actual polycrystal, (b) Showing only GBs in the polycrystal and (c) Free surfaces in the polycrystal being highlighted in orange color	144
6.15	Description of the (a) Full problem; Applying superposition principle to solve (b) DD sub-problem and (c) FE sub-problem	145
6.16	Adapted DD-FEM algorithm using superposition principle	148

List of Figures

6.17 Von Mises plastic strain monitored for every stress increment during the simulations	149
6.18 (a.) Side view and (b.) Top view of the polycrystal with cuboid-shaped texture objects representing the oriented lattices of each grain	150
6.19 Plot representing size and orientation details about each grain in the polycrystal	151
6.20 (a.) Stress-Strain curve (original) and (b.) Stress-Strain curve (resultant) for the reference simulation of the polycrystal	151
6.21 (a.) Side view and (b.) Top view of the polycrystal with initial relaxed dislocation microstructure	152
6.22 (a) Stress-Strain curve (resultant) and (b) Evolution of total dislocation density during the reference simulations of the polycrystal	152
6.23 Stress-plastic strain response of two simulations with different boundary conditions	153
6.24 (a) Stress-Strain response and (b) Dislocation density evolution of two simulations with different numbers of grains in the RVE, respectively	155
6.25 Stress-Strain response for different loading increments	156
6.26 Strain hardening behavior (actual and resultant) of thin film with different initial dislocation densities	157
6.27 Evolution of dislocation density in thin film with initial dislocation density $\rho_{initial}^{exp} \sim 3.5 \times 10^{+16} m^{-2}$ [31]	157
6.28 Initial dislocation microstructure corresponding to $\rho_{initial}^{sim} = \rho_{10} = 3.5 \times 10^{+16} m^{-2}$ in 200nm thick film with four grains	158
6.29 Side and Top views of 90nm, 200nm and 480nm thick films with respective initial dislocation microstructures	160

6.30 (a) Comparison of stress-strain (actual) response in 90nm, 200nm and 480nm thick films (b) Corresponding microstructure details of the polycrystal configuration (color coding followed for grains)	161
6.31 (a) Comparison of stress-plastic strain response and (b) Total dislocation density evolution in 90nm, 200nm and 480nm thick films with $\langle 110 \rangle$ texture	161
6.32 (a) Comparison of stress-plastic strain response and (b) Total dislocation density evolution in 90nm, 200nm and 480nm thick films with $\langle 112 \rangle$ texture	162
6.33 (a) Comparison of stress-plastic strain response in 90nm, 200nm and 480nm thick films (b) Corresponding microstructure details of the polycrystal configuration (color coding followed for grains)	162
6.34 (a) Comparison of stress-plastic strain response in 90nm, 200nm and 480nm thick films (b) Corresponding microstructure details of the polycrystal configuration with $\langle 110 \rangle$ texture (color coding followed for grains)	163
6.35 (a) Side and (b) Top views of 200nm thick film with a large grain surrounded by small grains in the polycrystalline film	163
6.36 (a) Stress-strain response and (b) Microstructure details of polycrystal with a large grain surrounded by small grains in the polycrystalline film	164
6.37 Dislocation density evolution in each grain of 90nm thick film	165
6.38 Dislocation density evolution in each grain of 200nm thick film	165
6.39 (a) Microstructure details and (a) Dislocation density evolution in each grain of 90nm thick film	166
6.40 Side and Top views of 90nm, 200nm and 480nm thick films with respective initial dislocation microstructures	168
6.41 (a) Stress-strain response and (b) Microstructure details of polycrystal with a smaller grain at the center of the film	169

List of Figures

6.42	Experimental stress-strain response of 90nm, 200nm and 480nm thick films with $\varepsilon < 1.0\%$ region highlighted in red	169
6.43	(a) Texture map of Pd thin film showing moderate $\langle 110 \rangle$ texture (b) Polycrystal setup information and (c,d) Top and Side views of polycrystal with coloured texture object	170
6.44	Different plastic strain components and Von Mises plastic strain plotted against equivalent plastic strain (ε_{11}^{pl}) in (a) 90nm and (b) 200nm thick films, respectively	171
6.45	Strain tensor applied on the reference cubic grain	172
6.46	Resultant stress tensor on the reference cubic grain	173
6.47	(a) A 200nm thick film with free surface highlighted in orange (b) Direction of (111) glide planes in $\langle 110 \rangle$ textured single grain	174
6.48	Red marker showing the point analysis point on the (a) stress-strain curve with larger grain at center (b) smaller grain at the center of the polycrystal, respectively	175
6.49	(a) Side and (b) Top views of the internal stress field contribution from all the grains plotted on a square plane placed half-way along 90nm thick film	176
6.50	(a) Side and (b) Top views of the internal stress field contribution from only central grain plotted on a square plane placed half-way along 90nm thick film	176
6.51	(a) Side and (b) Top views of the internal stress field contribution from all grains except the central grain plotted on a square plane placed half-way along 90nm thick film	177
6.52	(a) Side and (b) Top views of the internal stress field contribution from all grains except the central grain plotted on a square plane placed half-way along 90nm thick film	178
6.53	Comparing equivalent stress (σ_{11}) at equivalent strain ($\varepsilon_{11} = 1\%$) in different (90nm, 200nm and 480nm) films with and without grain size distribution	179

7.1	SEM image showing rearrangement of dislocations in Si [100]	184
7.2	A schematic view of misfit and threading dislocations in GaN layer over Si substrate	185
7.3	Cross-section TEM images of GaN epilayer with AlN buffer layer with dislocations [73]	185
7.4	Diamond cubic lattice structure of Si [14]	186
7.5	Hexagonal wurtzite lattice structure of GaN [14]	186
7.6	The diamond cubic lattice structure [152]	187
7.7	A dislocation lying on a (111) plane at 60° to the Burgers vector [152]	187
7.8	An edge dislocation showing acceptor centres and electron trapping sites	188
7.9	Variation of electric potential with distance r inside the cylinder of radius R for different filling fractions f	189
7.10	Building tranches along an edge dislocation line	190
7.11	Representation of the effective charge in each tranche	190
7.12	Estimated influence of tranche charge	190
7.13	Infinitely long edge dislocation line in a cubic grain	191
7.14	Tranche charges along the corresponding edge dislocation in Figure 7.13	191
7.15	Validation of the PoisFFT solver; Electric potential for a point charge at the center of a unit square	193
7.16	Cubic grain with tranche charges highlighting the FFT grid of size 128^3	194
7.17	Electrostatic potential surface around an edge dislocation in Figure 7.13 and influence of the potential on the boundary surfaces of the cubic grain	194

List of Figures

A.1	Double ended pileup of edge dislocations	202
A.2	Double ended pileup of edge dislocations in homogenization surface S	203
A.3	Pileup of dislocations on a slip plane passing through the center of the cube	204
A.4	Pileup of dislocations on slip plane (form-line)	205
A.5	Pileup of dislocations on a slip plane (form-square)	206
A.6	Pileup of dislocations on a slip plane (form-circle)	208
A.7	Cubic grain with n parallel slip planes	210
A.8	Pileup of dislocations on single slip plane [43]	211
A.9	Pileup of dislocations on multiple parallel slip planes [43]	212
B.1	Pileup of dislocations on a slip plane (form-ellipse longest)	214
B.2	Pileup of dislocations on a slip plane (form-ellipse shortest)	216
B.3	Pileup of dislocations on multiple parallel slip plane in a spherical grain	220
B.4	KH slope of Sphere @ CSCS= 32MPa(CS1),@ CSCS= 80MPa(CS2) and analytical	224
B.5	Parallel planes in a non-equiaxed (spheroidal/elongated grain)	225
B.6	KH slope of Kaca @ CSCS= 32MPa(CS1),@ CSCS= 80MPa(CS2) and analytical	229
B.7	KH slope of Cigar @ CSCS= 32MPa(CS1),@ CSCS= 80MPa(CS2) and analytical	229

List of Tables

4.1	Number of loops before 1 st slip transmission as predicted by DDD simulations	73
5.1	Slip system information along with Schmid factors and angle made with respect to the long axis of the grain, respectively	100
5.2	Four most active slip system	101
5.3	Material parameters of Ni	104
5.4	Deviates of four most active slip system	112
6.1	Material parameters of Pd	140
6.2	Material parameters of Pd	141
6.3	Variation of grain aspect ratios with film thickensses	166

Hareesh Tummala | Curriculum Vitae

Batiment EULER (Bureau A.218),

Avenue Georges Lemaitre 4, 1348 Louvain-la-Neuve, Belgium

Mobile: +32 (0) 465662406 E-mail: tummala_hari@yahoo.com



EDUCATION:

Doctoral studies in micromechanics of materials

PhD title: 3D discrete dislocation dynamic simulations of polycrystalline films and silicon electrostatics

UGA, France and UCL, Belgium (2013 –2016)

Masters in Computational Materials Science

TU Bergakademie Freiberg, Germany (2011 –2013)

Grade: 2.7

Bachelors in Mechanical Engineering

Nagarjuna University, Guntur, India (2006 -2010)

Percentage: 7.4

AWARDS & FELLOWSHIPS:

Erasmus mundus scholarship for Doctoral studies

International doctoral school (IDS) in Functional Materials (FunMat) (2013-2016)

German academic exchange service (DAAD) - STIBET grant

Awarded semi-annually to outstanding final year Masters students (2012-2013)

ORAL PRESENTATIONS:

H. Tummala, M. Fivel, T. Pardoen, L. Delannay, “*Collective influence of texture, grain shape, grain size and dislocation density on the plasticity of polycrystalline thin films*” at 8th International conference on Multiscale Materials Modelling (MMM2016), Dijon, France (J5, 12th Oct, 2016)

H. Tummala, M. Fivel, T. Pardoen, L. Delannay, “*Collective influence of texture, grain shape, grain size and dislocation density on the plasticity of polycrystalline thin films*” at European Mechanics of Materials conference (EMMC15), Brussels, Belgium (8th Sept, 2016)

H. Tummala, L. Delannay, M. Fivel, T. Pardoen, “*Influence on grain shape on intra-granular back-stresses*” at IAP semi-annual meeting P7/21, UCL, Belgium (17th May, 2015)

POSTER PRESENTATIONS:

- “*Grain shape influence on plastic anisotropy*” at EUROMECH Colloquium 570, Houffalize, Belgium (20th -23rd Oct, 2015)
- “*Grain shape influence on plastic anisotropy*” at Colloque Plasticite 2015, Annecy, France (28th -30th April, 2015)
- “*Plastic anisotropy due to grain shape*” at International DD workshop, Saclay, France (10th -12th Dec, 2014)

PUBLICATIONS / REPORTS:

- [1] **H. Tummala**, L. Delannay, M. Fivel, T. Pardoen. *3D discrete dislocation dynamics simulations on the influence of grain shape on intra-granular back-stress predictions in single grain* [paper to be submitted]
- [2] **H. Tummala**, M. Fivel, T. Pardoen, L. Delannay. *An advanced polycrystalline dislocation dynamics model for predicting behaviour of free-standing thin films* [paper to be submitted]
- [3] **H. Tummala**, M. Fivel, T. Pardoen. *Harnessing the power of GPUs for 3D discrete dislocation dynamics simulations* [report]
- [4] **H. Tummala**, M. Fivel, T-W-Lin, H. Johnson. *Relevance of [110] traces on polarized light-emission of Silicon wafers* [report]
- [5] **H. Tummala**, M. Fivel. *Modelling electrostatic behaviour of dislocations: Linking dislocations to electrical properties of semiconductors* [report]
- [6] H. S. Tran, **H. Tummala**, L. Duchene, M. Fivel, A. M. Habraken. *Interaction between dislocation and coherent twin boundary* [COMPLAS XIII]

CONFERENCE / MEETING (Participation):

5th Semi-annual IAP P7/21 meeting at UCL, Belgium

Organizers : promoters of IAP P7/21

Topic : Mechanics of interface-dominated materials

Period : 17th May, 2016

2nd Schoental symposium on ‘Dislocation based plasticity’ at Schoental, Germany

Organizers : DFG research group 1650

Topic : Advances in dislocation based plasticity modelling

Period : 29th, February – 04th March, 2016

EUROMECH Colloquium 570 at Houffalize, Belgium

Organizers : Laurent Duchene, Aude Simar, Rafael Estevez

Topic : Multiscale analysis of impact of microstructure on plasticity and fracture in interface-dominated materials

Period : 20th – 23rd October, 2015

Colloque Plasticite 2014 at Autrans, France

Organizers : J. B. Vogt
Topic : National (French) annual meeting; recent advances in plasticity
Period : 28th -30th April, 2014

4th Semi-annual IAP P7/21 meeting at Royal Military Academy, Brussels, Belgium

Organizers : promoters of IAP P7/21
Topic : Mechanics of interface-dominated materials
Period : 17th -18th Nov, 2014

3rd Semi-annual IAP P7/21 meeting at Ghent, Belgium

Organizers : promoters of IAP P7/21
Topic : Mechanics of interface-dominated materials
Period : 12th – 13th May, 2014

Plasticite 2015 at Autrans, France

Organizers : Marc Fivel, Emilie Ferrie, Guillaume, Christophe Depres, Michel Perez, Dome Tanguy
Topic : National (French) annual meeting; recent advances in plasticity
Period : 28th -30th April, 2015

2nd Semi-annual IAP P7/21 meeting at UCL, Belgium

Organizers : promoters of IAP P7/21
Topic : Mechanics of interface-dominated materials
Period : 14th -15th Nov, 2013

TRAINING SCHOOLS (Participation):

6th IDS-FunMat Training school at Bordeaux, France

Organizers : IDS FunMat
Topic : Annual doctoral training school; 7 scientific lectures; workshop on transferable skills
Period : 13th -18th March, 2016

5th Les Houches School in computational physics at Les Houches, France

Organizers : David Rodney, Jean-Louis Barrat, Ralf Everaers
Topic : Multiscale modelling of materials
Period : 11th -22th May, 2015

5th IDS-FunMat Training school at Koblenz, Germany

Organizers : IDS FunMat
Topic : Annual doctoral training school; 7 scientific lectures; workshop on transferable skills
Period : 15th -20st March, 2015

International workshop in Dislocation Dynamics at Saclay, France

Organizers : Marc Bletry, Olivier Coulaud, Laurent Dupuy, Marc Fivel
Topic : Recent progress in modelling and simulation of dislocation dynamics
Period : 10th -12th December, 2014

Short course on crystal plasticity modelling at UCL, Belgium

Organizers : Laurent Delaunay and Thierry J. Massart
Topic : Introduction to crystal plasticity modelling
Period : 4th -5th November, 2013

4th IDS-FunMat Training school at Spa, Belgium

Organizers : IDS FunMat
Topic : Annual doctoral training school; 7 scientific lectures; workshop on transferable skills
Period : 16th -21st March, 2014

CONFERENCE / MEETING (Organisation):

Plasticite 2015 at Autrans, France

Designation : Student co-ordinator
Topic : National (French) annual meeting; recent advances in plasticity
Period : 28th -30th April, 2015

International workshop in Dislocation Dynamics at Saclay, France

Designation : Student co-ordinator (Lodging and Transportation)
Topic : Recent progress in modelling and simulation of dislocation dynamics
Period : 10th -12th December, 2014

PROFESSIONAL EXPERIENCE:

Research assistant at TU Bergakademie Freiberg, Germany

Institute : Institute for Mechanics and Fluid Dynamics
Period : April 2012 – June 2012

Trainee Mechanical Engineer in Dredging section

Organisation : Ocean Sparkle Limited, Hyderabad, India
Period : August 2010 – April 2011

OTHER PROJECTS:

Master thesis, TU Bergakademie Freiberg, Germany

Mentors : Jun. Prof. Dr. S. Groh and Prof. M. Kuna
Topic : Modelling of fracture using two dimensional dislocation dynamics framework
Period : April 2013 – September 2013

Programming Project, TU Bergakademie Freiberg, Germany

Mentors : Jun. Prof. Dr. S. Groh
Topic : A concurrent multiscale coupling of a finite element method and molecular statics using Quasi-continuum approach
Period : October 2012 - March 2013

Bachelor Thesis, Modal analysis of turbine rotor shafts

Mentors : Dr. Venkata Ramana Kavuluri

Topic : Modal analysis of turbine rotor shafts using a finite elements method

Period : December 2009 – April 2010

POSITIONS HELD:

- International students in Schools (ISIS) project at TU Bergakademie Freiberg
- Member of student council (Computational Materials science) at TU Bergakademie Freiberg
- Member of AKAS (student organisation) at TU Bergakademie Freiberg
- Member of Indian red cross society

COMPUTER SKILLS:

Languages : C, C++, Fortran, Python

Commercial packages : MATLAB, ABAQUS, Microsoft Office

Open source softwares : Para View, Latex, Gnu plot, Matplot, LAMMPS, OVITO

User developed codes : PoisFFT, TRIDIS, microMegas

Other packages : Doxygen (documentation), GitHub (version control)

Operating Systems : Linux-based (Ubuntu, Mint), Windows (7, Vista, Xp)

LANGUAGE SKILLS:

- English (Fluent in speaking, writing and listening)
- Telugu (Native language)
- Hindi (Native language)
- German and French (Basic User)

HOBBIES:

Gardening, Sketching, Badminton, Judo and Mountain biking

REFERENCES:

Available upon request